



The  
University  
Of  
Sheffield.

# Combustion Instabilities in Alternative Fuels

Abdullah Mohammad **Alsharif**

A thesis submitted in partial fulfilment of the requirements for the degree of  
Doctor of Philosophy

The University of Sheffield  
Faculty of Engineering  
Department of Mechanical Engineering

December 2021

## **DEDICATION**

**To my parents**

**To my lovely wife, Hanan**

**To my son, Mohammad**

**To my brothers and sisters**

## **ACKNOWLEDGEMENTS**

To my Almighty God, who gave me strength and confidence and made this research possible.

I would like to express my gratitude to the following people, without whom I would not have accomplished this research or made it through my PhD degree.

I would like to express my sincere thanks to my supervisor Dr. Robert Woolley for his support and advice throughout the research. I would also like to thank Nazrein Amaludin, Houshi Jiang, and Oliver Cooper for their guidance and help in conducting the experiments.

Special appreciation to my lovely wife Hanan and my lovely son Mohammad, for their support and patience throughout my studies.

My biggest thanks and appreciation to my father, mother, brothers, sisters, and all my friends for their support and encouragement.

Finally, my appreciation goes to the Ministry of Education Saudi Arabia and also to Taibah University who provided me with a scholarship and financial support.

## ABSTRACT

The experiments in this study used premixed flames that propagated in a vertical tube with one end open, the other end closed, and a pilot flame as the ignition source. Various methane-air and propane-air flames were examined for equivalence ratios ranging from 0.8 to 1.5 and with varying addition of hydrogen ( $R_H = 0 - 0.4$ ). Furthermore, for the methane-air flames, the study used the volumetric method for equivalence ratios of  $\phi = 0.8$  to 1.5 and a range of hydrogen additions (10% $H_2$  - 40% $H_2$ ). The flame propagation was captured using high-speed cameras. The flames' shape and propagation rate were found to be influenced by several mechanisms, including pressure and velocity. Specifically, significant differences in flame behaviour were observed in line with the hydrogen content, with the flame area decreasing with increasing hydrogen concentration. Meanwhile, slower flames showed higher underlying flame speeds and maximum pressure, as well as a larger flame surface area. This suggests that the dominant mechanism of acoustic instability in downward propagating flames is velocity coupling. However, despite the increase in the laminar burning velocity by an almost double magnitude, the peak pressure and underlying speed remained constant. Most flames with a high burning velocity presented more pronounced  $\sim 400$  Hz oscillation than flames with a low burning velocity. Comparing the methane and propane flames using the  $R_H$  method revealed a close correlation in terms of their behaviour. For the methane-hydrogen fuels, a further comparison between the  $R_H$  and volumetric methods unveiled a similar behaviour.

# TABLE OF CONTENTS

<b>DEDICATION</b> .....	<b>i</b>
<b>ACKNOWLEDGEMENTS</b> .....	<b>ii</b>
<b>ABSTRACT</b> .....	<b>iii</b>
<b>LIST OF TABLES</b> .....	<b>vii</b>
<b>LIST OF FIGURES</b> .....	<b>viii</b>
<b>DECLARATION</b> .....	<b>xviii</b>
<b>NOMENCLATURE</b> .....	<b>xix</b>
<b>1 INTRODUCTION</b> .....	<b>1</b>
<b>2 LITERATURE REVIEW</b> .....	<b>3</b>
<b>2.1 Flame instabilities in premixed combustion</b> .....	<b>3</b>
2.1.1 Hydrodynamic (Darrieus-Landau) instabilities .....	3
2.1.2 Thermo-diffusive instabilities .....	5
2.1.3 Body-force instabilities .....	9
<b>2.2 Thermo-acoustic instability</b> .....	<b>18</b>
<b>2.3 History of premixed flame instabilities</b> .....	<b>19</b>
<b>2.4 Effect of tube configuration on instabilities</b> .....	<b>32</b>
2.4.1 Flame propagation in a tube closed at both ends.....	32
2.4.2 Flame propagation in a tube closed at the ignition end, open at the other end.....	34
2.4.3 Flame propagation in a tube open at the ignition end, closed at the other end.....	35
2.4.4 Flame propagation in a tube open at both ends.....	38
<b>2.5 Experimental and theoretical studies on primary and secondary instabilities in downward propagating flames</b> .....	<b>39</b>
<b>2.6 Fuel composition</b> .....	<b>44</b>
2.6.1 Effect of fuel composition on instability .....	44
2.6.2 Equivalence ratio .....	48
2.6.3 Background of hydrocarbons and hydrogen fuel blends .....	52
2.6.4 Effect of hydrogen addition on the laminar burning velocity.....	53
2.6.5 Effect of hydrogen addition on combustion instability .....	55
<b>2.7 Spectral analysis</b> .....	<b>56</b>

2.7.1	Fast Fourier transform (FFT).....	59
2.7.2	Synchrosqueezed wavelet transform .....	64
2.7.3	Phase study.....	69
<b>3</b>	<b>EXPERIMENTAL METHODOLOGIES .....</b>	<b>72</b>
<b>3.1</b>	<b>Rig setup .....</b>	<b>72</b>
<b>3.2</b>	<b>Data acquisition.....</b>	<b>77</b>
3.2.1	High-speed camera.....	77
3.2.2	Pressure measurement .....	77
3.2.3	The synchronisation of optical and pressure data.....	78
<b>3.3</b>	<b>Fuel.....</b>	<b>82</b>
3.3.1	Fuel type.....	82
3.3.2	Calculation of rig volume.....	82
3.3.3	Calculation of fuel volume.....	84
<b>3.4</b>	<b>Experimental errors .....</b>	<b>87</b>
3.4.1	Systematic errors.....	87
3.4.2	Random errors .....	88
3.4.3	Measurement errors.....	88
<b>4</b>	<b>POST-PROCESSING .....</b>	<b>90</b>
<b>4.1</b>	<b>Introduction.....</b>	<b>90</b>
<b>4.2</b>	<b>Classification of flames .....</b>	<b>91</b>
<b>4.3</b>	<b>Preparation of raw video .....</b>	<b>91</b>
4.3.1	Cropping and conversion of video.....	91
<b>4.4</b>	<b>Flame front, tail, thickness and area tracking.....</b>	<b>92</b>
4.4.1	Analysis of flame front .....	94
<b>4.5</b>	<b>MATLAB analysis of frequency .....</b>	<b>98</b>
4.5.1	Synchrosqueezed wavelet transform (SST) .....	99
4.5.2	Phase study.....	106
<b>5</b>	<b>EXPERIMENTAL RESULTS.....</b>	<b>111</b>
<b>5.1</b>	<b>R<sub>H</sub> method .....</b>	<b>111</b>
5.1.1	The effect of hydrogen addition .....	111
5.1.2	The effect of equivalence ratio .....	139
5.1.3	Lean flame with hydrogen addition .....	159

5.2	<b>Volumetric method</b> .....	162
5.2.1	The effect of hydrogen addition .....	162
6	<b>DISCUSSION</b> .....	168
6.1.	Overall flame behaviour.....	168
6.2.	Comparison between methane and propane flames using $R_H$ method.....	169
6.3.	Overarching discussion .....	182
7	<b>CONCLUSION</b> .....	191
7.1.	Future work .....	192
	<b>REFERENCES</b> .....	193
	<b>APPENDICES</b> .....	208
	Appendix A: Optical calibration.....	208
	Appendix B: Pressure measurement settings .....	209
	Appendix C: Fuel collection procedure .....	210
	Appendix D: Experimental Procedures .....	212
	Appendix E: Procedure for selecting the presented run .....	213
	Appendix F: Procedure for selecting reference velocity .....	214
	Appendix G: MATLAB code for SST and ISST .....	215

## LIST OF TABLES

Table 2.1: Reactive mixtures' laminar flame velocity, expansion ratio, and laminar spatial velocity. Reproduced from [103].....	45
Table 2.2: The range of hydrogen mole fractions for $R_H$ method, Bradley method, and volumetric method.....	52
Table 2.3: Parameters for three different waves.....	57
Table 3.1: Synchronisation test results.....	81
Table 3.2: The readings of pressure and volume.....	84
Table 3.3: Tabulated laminar burning velocity, mole fraction, volume for methane – air mixtures with hydrogen addition, $R_H$ and the standard deviation .....	86
Table 4.1: The properties of the low-pass finite impulse response filter.....	96
Table 6.1: Summary of methane behaviour based on the peak pressure and laminar burning velocity .....	190
Table 6.2: Summary of propane behaviour based on the peak pressure and minimum underlying speed.....	190

## LIST OF FIGURES

Figure 2.1: Deviation of flow lines that generate Darrieus-Landau instability. Reproduced from [14].....	5
Figure 2.2: The structure of a wrinkled premixed flame. Reproduced from [15].....	6
Figure 2.3: DL and TD instability development following planar flame perturbation. The relative changes in the unburned gas pressure are indicated by + and – between the perturbed streamlines. The arrowed solid lines located at the wave crest show the deficient reactant diffusion, and the arrowed dotted lines show thermal conduction [17].....	8
Figure 2.4: Visualisation of an unstable Rayleigh-Taylor configuration. Reproduced from [23].....	11
Figure 2.5: Schematic flow patterns showing how unstable two-dimensional flows evolve in RT. The heavy fluid is penetrated by the light fluid during acceleration in the direction of the heavy fluid in every condition. Reproduced from [26].....	13
Figure 2.6: Pre- and post-schematics of a shock as it passes through a fluid interface. The incident shock was planar, but the transmitted/reflected shocks were corrugated. Reproduced from [30].....	15
Figure 2.7: Two forms of Rayleigh-Taylor instability, a) gravity-driven, b) pressure driven, segmented into three phases: i) undisturbed interface, ii) disturbed interface, iii) interface at time, $t$ . Reproduced from [34].....	17
Figure 2.8: The feedback loop responsible for the appearance of thermoacoustic instabilities. Reproduced from [40].....	18
Figure 2.9: Vibration modes for a tube open at both ends: a) first harmonic, b) second harmonic, c) third harmonic, where A represents the velocity antinodes and N indicates velocity nodes. Reproduced from [52].....	23
Figure 2.10: The mechanism for the initiation and propagation of a tulip flame. Reproduced from [54].....	24
Figure 2.11: Formation of (a) distorted tulip flame, (b) classical tulip flame. Reproduced from [56].....	24
Figure 2.12: Sequence of numerical schlieren presenting the evolution of premixed stoichiometric hydrogen–air flame. Reproduced from [55].....	27

Figure 2.13: Flame behaviours induced by vibration of flame structure. Reproduced from [7] .....	29
Figure 2.14: Regions of unstable pulsation and oscillation induced by vibration as a function of different dimensionless parameters: frequency, $\Omega$ , velocity amplitude, $W$ , and wavelength, $\lambda$ . Reproduced from [7] .....	31
Figure 2.15: Stroboscopic flame records. Mixture: 10 parts CO + 1 part O <sub>2</sub> saturated with water vapour at 15 °C, tube closed at both ends; diameter 5 cm; length: (a) 19.5 cm (b) 17 cm (c) 12 cm (d) 9.5 cm. Reproduced from [7] .....	33
Figure 2.16: Example of flame-shape distortions in a closed tube propagation. Reproduced from [6] .....	34
Figure 2.17: Flame position and acoustic pressure of a lean propane-air mixture. Reproduced from [11].....	37
Figure 2.18: High-speed tomography of premixed flames in open-ended ignition at different stages: (a) curved flame at onset of primary instability, (b) flat flame during saturation of primary instability, (c) cellular structure at onset of secondary instability, (d) high amplitude cells during secondary instability development. Reproduced from [70] based on [11].....	38
Figure 2.19: Maximum peak-to-peak pressure amplitudes for n-butane-methane-air mixtures. Fundamental mode, 2 foot tube: Reproduced from [60].....	46
Figure 2.20: Maximum peak-to-peak pressure amplitudes for n-butane-methane-air mixtures. Fundamental mode, 4 foot tube. Reproduced from [60].....	47
Figure 2.21: Set of laminar burning velocity of methane .....	50
Figure 2.22: Effect of hydrogen addition on laminar burning velocity of methane.....	54
Figure 2.23: Three waves, $X_1$ , $X_2$ and $X_3$ plotted in (a) and the combined wave, $X_{total}$ in (b).....	58
Figure 2.24: A discrete Fourier transform from example a) randomly generated time signal, producing b) the 3-dimensional representation of the time-series signal, c) the power spectrum, and finally d) the phase spectrum. Reproduced from [142].....	60
Figure 2.25: Acoustic pressure records for spray flame (decane) in a 1.2 m tube. a) $\phi = 0.9$ , between the frequency change, there is a period of silence, b) $\phi = 1.1$ The instability occurs in three distinct frequencies successively. Reproduced from [8]....	62

Figure 2.26: Fast Fourier transform of the flame position (solid line) and pressure signal (dotted line) for the lean flame at time $t_1 = 0.3$ s, $t_2 = 0.6$ s, and $t_3 = 0.9$ s. Reproduced from [101].....	63
Figure 2.27: Fast Fourier Transform of $X_{total}$ .....	64
Figure 2.28: Fourier spectrograms of a) flame position and b) flame pressure for a lean propane flame. Reproduced from [101].....	65
Figure 2.29: Comparison between a continuous wavelet transform (CWT) and a synchrosqueezed wavelet transform (SST). Reproduced from [147].....	67
Figure 2.30: Phase of the $OH^*$ chemiluminescence against normalised instability strength for all operating conditions. Reproduced from [159].....	71
Figure 3.1: Experimental combustion rig setup.....	73
Figure 3.2: Data acquisition tools.....	74
Figure 3.3: Schematics of downwardly propagating experiment.....	75
Figure 3.4: Methane flame at $\phi = 1.0$ , $R_H = 0.3$ a) the whole pressure signal, b) zoomed in pressure signal from the ignition point and prior to flame observation region, both before cropping.....	76
Figure 3.5: a) Both trigger and pressure synchronisation signals, b) pressure signal magnified, both signals prior to cropping.....	79
Figure 3.6: Video recording to trigger signal synchronisation.....	80
Figure 3.7: The tracked metal plate edge (green line) reverses after coming into contact with the tube.....	81
Figure 3.8: Example of a synchronised flame front position and pressure signals for methane flame at $\phi = 1.0$ , $R_H = 0.2$ .....	82
Figure 3.9: Measuring the recorded distance of the tube.....	89
Figure 4.1: Flame front, tail, and thickness from the filmed images.....	92
Figure 4.2: Image thresholding. (a) Grayscale image. (b) zero threshold. (c) 0.5 threshold. (d) 0.9 threshold.....	93
Figure 4.3: The corresponding flame area at 0, 0.5, and 0.9 levels of thresholding.....	94
Figure 4.4: The influence of different passband frequencies on a) flame position and b) flame distance amplitude and c) underlying flame velocity.....	95
Figure 4.5: The position of the flame front and their derivatives.....	98

Figure 4.6: Synchrosqueezed transform plot for $X_{total}$ , clearly showing the existence of 2 different dominant frequencies.....	100
Figure 4.7: Synchrosqueezed transform contour plot of raw signal.....	101
Figure 4.8: Penalty levels' effect on the frequency ridges formation formed from a) no penalty, b) penalty = 1, and c) penalty = 20.....	102
Figure 4.9: SST contour plot of a pressure signal of a $\phi = 1.0$ , $R_H = 0.3$ methane flame .....	104
Figure 4.10: SST frequency ridges at penalty of 20 of a pressure signal of a $\phi = 1.0$ , $R_H = 0.3$ methane flame .....	104
Figure 4.11: Reconstruction of a) the original pressure signal into b) ~200 Hz pressure component, and c) ~400 Hz pressure component of a $\phi = 1.0$ , $R_H = 0.3$ methane flame .....	105
Figure 4.12: Plots of a) instantaneous phase of $X_2$ and $X_3$ , followed by b) phase difference between both signals.....	107
Figure 4.13: Phase plots for a) ~200 Hz components, b) ~400 Hz components of a $\phi = 1.0$ , $R_H = 0.3$ methane flame.....	108
Figure 4.14: Phase difference plots against time for a) ~200 Hz components, b) ~400 Hz components of a $\phi = 1.0$ , $R_H = 0.3$ methane flame.....	109
Figure 4.15: Phase difference plots against pressure for a) ~200 Hz components, b) ~400 Hz components of a $\phi = 1.0$ , $R_H = 0.3$ methane flame .....	110
Figure 5.1: Effect of hydrogen addition on methane (blue), propane (red) on $\phi = 1.0$ , $R_H = 0 - 0.4$ flames, on a) flame front position, b) flame front position amplitude, c) tube end pressure, and d) flame area.....	112
Figure 5.2: Effect of hydrogen addition on methane (blue), propane (red) on $\phi = 1.0$ , $R_H = 0 - 0.4$ flames, on a) raw flame speed, broken down into b) underlying flame speed, c) ~200 Hz speed component, and d) ~400 Hz speed component.....	114
Figure 5.3: Effect of hydrogen addition on methane (blue), propane (red) on $\phi = 1.0$ , $R_H = 0 - 0.4$ flames, on a) ~200 Hz pressure component, b) ~200 Hz area component, c) phase difference between a) and b), d) ~400 Hz pressure component, e) ~400 Hz flame area component.....	116
Figure 5.4: Flame front position and tube end pressure against time of methane on $\phi = 1.0$ , $R_H = 0$ flame .....	119

Figure 5.5: Underlying flame speed against time of methane on $\phi = 1.0, R_H = 0$ flame	119
Figure 5.6: Representative images for flame behaviour in different regimes of methane on $\phi = 1.0, R_H = 0$ flame. Interval of 1/2000 second increments for each frame downwards.....	120
Figure 5.7: Flame front position and tube end pressure against time of methane on $\phi = 1.0, R_H = 0.1$ flame.....	121
Figure 5.8: Underlying flame speed against time of methane on $\phi = 1.0, R_H = 0.1$ flame .....	121
Figure 5.9: Representative images for flame behaviour in different regimes of methane on $\phi = 1.0, R_H = 0.1$ flame. Interval of 1/2000 second increments for each frame downwards.....	122
Figure 5.10: Flame front position and tube end pressure against time of methane on $\phi = 1.0, R_H = 0.2$ flame .....	124
Figure 5.11: Underlying flame speed against time of methane on $\phi = 1.0, R_H = 0.2$ flame .....	124
Figure 5.12: Representative images for flame behaviour in different regimes of methane on $\phi = 1.0, R_H = 0.2$ flame. Interval of 1/2000 second increments for each frame downwards.....	125
Figure 5.13: Flame front position and tube end pressure against time of methane on $\phi = 1.0, R_H = 0.3$ flame.....	126
Figure 5.14: Underlying flame speed against time of methane on $\phi = 1.0, R_H = 0.3$ flame .....	126
Figure 5.15: Representative images for flame behaviour in different regimes of methane on $\phi = 1.0, R_H = 0.3$ flame. Interval of 1/2000 second increments for each frame downwards.....	127
Figure 5.16: Flame front position and tube end pressure against time of methane on $\phi = 1.0, R_H = 0.4$ flame.....	128
Figure 5.17: Underlying flame speed against time of methane on $\phi = 1.0, R_H = 0.4$ flame .....	128
Figure 5.18: Representative images for flame behaviour in different regimes of methane on $\phi = 1.0, R_H = 0.4$ flame. Interval of 1/2000 second increments for each frame downwards.....	129

Figure 5.19: Tube end pressure against time of methane (blue), and propane (red) on $\phi = 1.0, R_H = 0.1$ flames.....	131
Figure 5.20: Underlying flame speed against time of methane (blue), and propane (red) on $\phi = 1.0, R_H = 0.1$ flames.....	131
Figure 5.21: Representative images for flame behaviour in different regimes of methane (M) and propane (P) on $\phi = 1.0, R_H = 0.1$ flames. Interval of 1/2000 second increments for each frame downwards.....	132
Figure 5.22: Tube end pressure against time of methane (blue), and propane (red) on $\phi = 1.0, R_H = 0.2$ flames.....	133
Figure 5.23: Underlying flame speed against time of methane (blue), and propane (red) on $\phi = 1.0, R_H = 0.2$ flames.....	133
Figure 5.24: Representative images for flame behaviour in different regimes of methane (M) and propane (P) on $\phi = 1.0, R_H = 0.2$ flames. Interval of 1/2000 second increments for each frame downwards.....	134
Figure 5.25: Tube end pressure against time of methane (blue), and propane (red) on $\phi = 1.0, R_H = 0.3$ flames.....	135
Figure 5.26: Underlying flame speed against time of methane (blue), and propane (red) on $\phi = 1.0, R_H = 0.3$ flames.....	135
Figure 5.27: Representative images for flame behaviour in different regimes of methane (M) and propane (P) on $\phi = 1.0, R_H = 0.3$ flames. Interval of 1/2000 second increments for each frame downwards.....	136
Figure 5.28: Tube end pressure against time of methane (blue), and propane (red) on $\phi = 1.0, R_H = 0.4$ flames.....	137
Figure 5.29: Underlying flame speed against time of methane (blue), and propane (red) on $\phi = 1.0, R_H = 0.4$ flames.....	137
Figure 5.30: Representative images for flame behaviour in different regimes of methane (M) and propane (P) on $\phi = 1.0, R_H = 0.4$ flames. Interval of 1/2000 second increments for each frame downwards.....	138
Figure 5.31: Effect of equivalence ratio on methane (blue), propane (red) on $\phi = 0.9-1.2, R_H = 0.1$ flames, on a) flame front position, b) flame front position amplitude, c) tube end pressure, and d) flame area.....	140

Figure 5.32: Effect of equivalence ratio on methane (blue), propane (red) on $\phi = 0.9$ - 1.2, $R_H = 0.1$ flames, on a) raw flame speed, broken down into b) underlying flame speed, c) 200 Hz speed component, and d) 400 Hz speed component.....	142
Figure 5.33: Effect of equivalence ratio on methane (blue), propane (red) on $\phi = 0.9$ - 1.2, $R_H = 0.1$ flames, on a) $\sim 200$ Hz pressure component, b) $\sim 200$ Hz area component, c) phase difference between a) and b), d) $\sim 400$ Hz pressure component, e) $\sim 400$ Hz flame area component.....	143
Figure 5.34: Flame front position and tube end pressure against time of methane on $\phi$ $= 0.9$ , $R_H = 0.1$ flame.....	146
Figure 5.35: Underlying flame speed against time of methane on $\phi = 0.9$ , $R_H = 0.1$ flame .....	146
Figure 5.36: Representative images for flame behaviour in different regimes of methane on $\phi = 0.9$ , $R_H = 0.1$ flame. Interval of $1/2000$ second increments for each frame downwards.....	147
Figure 5.37: Flame front position and tube end pressure against time of methane on $\phi$ $= 1.1$ , $R_H = 0.1$ flame.....	148
Figure 5.38: Underlying flame speed against time of methane on $\phi = 1.1$ , $R_H = 0.1$ flame .....	148
Figure 5.39: Representative images for flame behaviour in different regimes of methane on $\phi = 1.1$ , $R_H = 0.1$ flame. Interval of $1/2000$ second increments for each frame downwards.....	149
Figure 5.40: Flame front position and tube end pressure against time of methane on $\phi$ $= 1.2$ , $R_H = 0.1$ flame.....	150
Figure 5.41: Underlying flame speed against time of methane on $\phi = 1.2$ , $R_H = 0.1$ flame .....	150
Figure 5.42: Representative images for flame behaviour in different regimes of methane on $\phi = 1.2$ , $R_H = 0.1$ flame. Interval of $1/2000$ second increments for each frame downwards.....	151
Figure 5.43: Tube end pressure against time of methane (blue), and propane (red) on $\phi = 0.9$ , $R_H = 0.1$ flames.....	153
Figure 5.44: Underlying flame speed against time of methane (blue), and propane (red) on $\phi = 0.9$ , $R_H = 0.1$ flames.....	153

Figure 5.45: Representative images for flame behaviour in different regimes of methane (M) and propane (P) on $\phi = 0.9$ , $R_H = 0.1$ flames. Interval of 1/2000 second increments for each frame downwards.....	154
Figure 5.46: Tube end pressure against time of methane (blue), and propane (red) on $\phi = 1.1$ , $R_H = 0.1$ flames.....	155
Figure 5.47: Underlying flame speed against time of methane (blue), and propane (red) on $\phi = 1.1$ , $R_H = 0.1$ flame.....	155
Figure 5.48: Representative images for flame behaviour in different regimes of methane and propane on $\phi = 1.1$ , $R_H = 0.1$ flames. Interval of 1/2000 second increments for each frame downwards.....	156
Figure 5.49: Tube end pressure against time of methane (blue), and propane (red) on $\phi = 1.2$ , $R_H = 0.1$ flames.....	157
Figure 5.50: Underlying flame speed against time of methane (blue), and propane (red) on $\phi = 1.2$ , $R_H = 0.1$ flames.....	157
Figure 5.51: Representative images for flame behaviour in different regimes of methane and propane on $\phi = 1.2$ , $R_H = 0.1$ flames. Interval of 1/2000 second increments for each frame downwards.....	158
Figure 5.52: Effect of equivalence ratio on methane on $\phi = 0.8$ , $R_H = 0.4$ flames, on a) flame front position, b) flame front position amplitude, c) Underlying flame speed and d) tube end pressure.....	159
Figure 5.53: Effect of equivalence ratio on methane on $\phi = 0.8$ , $R_H = 0.4$ flames, on a) ~200 Hz speed component, b) ~400 Hz speed component, c) ~200 Hz pressure component and d) ~400 Hz pressure component.....	161
Figure 5.54: Effect of hydrogen addition on methane on $\phi = 1.0$ , 10% $H_2$ - 40% $H_2$ flames, on a) flame front position, b) flame front position amplitude, c) tube end pressure, and d) flame area.....	163
Figure 5.55: Effect of hydrogen addition on methane on $\phi = 1.0$ , 10% $H_2$ - 40% $H_2$ flames, on a) raw flame speed, broken down into b) underlying flame speed, c) 200 Hz speed component, and d) 400 Hz speed component.....	165
Figure 5.56: Effect of hydrogen addition on methane on $\phi = 1.0$ , 10% $H_2$ - 40% $H_2$ flames, on a) ~200 Hz pressure component, b) ~200 Hz area component, c) phase difference	

between a) and b), d) ~400 Hz pressure component, e) ~400 Hz flame area component.....	167
Figure 6.1: Peak pressure against laminar burning velocity scatter plot for methane flames at $\phi = 0.8-1.5$ and $R_H = 0-0.4$ .....	170
Figure 6.2: Peak pressure against minimum underlying speed scatter plot for propane flames at $\phi = 0.8-1.5$ and $R_H = 0-0.4$ .....	170
Figure 6.3: Peak underlying flame speed against laminar burning velocity scatter plot for methane flames at $\phi = 0.8-1.5$ and $R_H = 0-0.4$ .....	172
Figure 6.4: Peak underlying flame speed against minimum underlying speed scatter plot for propane flames at $\phi = 0.8-1.5$ and $R_H = 0-0.4$ .....	172
Figure 6.5: Peak underlying flame speed against peak pressure scatter plot for methane flames at $\phi = 0.8-1.5$ and $R_H = 0-0.4$ .....	174
Figure 6.6: Peak underlying flame speed against peak pressure scatter plot for propane flames at $\phi = 0.8-1.5$ and $R_H = 0-0.4$ .....	174
Figure 6.7: Tube end pressure and underlying flame speed against time of methane on $\phi = 1.4, R_H = 0$ flame.....	176
Figure 6.8: Tube end pressure and underlying flame speed against time of methane on $\phi = 1.5, R_H = 0.1$ flame .....	176
Figure 6.9: Tube end pressure and underlying flame speed against time of methane on $\phi = 1.4, R_H = 0$ flame.....	177
Figure 6.10: Tube end pressure and underlying flame speed against time of propane on $\phi = 1.5, R_H = 0$ flame.....	177
Figure 6.11: Tube end pressure and underlying flame speed against time of propane on $\phi = 1.5, R_H = 0.1$ flame .....	178
Figure 6.12: Tube end pressure and underlying flame speed against time of propane on $\phi = 1.2, R_H = 0.4$ flame .....	178
Figure 6.13: Representative images for flame behaviour in different regimes of methane on $\phi = 1.4, R_H = 0$ flame, $\phi = 1.5, R_H = 0.4$ flame, and $\phi = 1.2, R_H = 0.4$ flame. Interval of 1/2000 second increments for each frame downwards .....	180
Figure 6.14: Representative images for flame behaviour in different regimes of propane on $\phi = 1.5, R_H = 0$ flame, $\phi = 1.5, R_H = 0.1$ flame, and $\phi = 1.2, R_H = 0.4$ flame. Interval of 1/2000 second increments for each frame downwards .....	181

Figure 6.15: Tube end pressure against time of methane flames in region (A) .....	183
Figure 6.16: Tube end pressure against time of methane flames in region (B) .....	184
Figure 6.17: Tube end pressure against time of methane flames in region (C) .....	185
Figure 6.18: Tube end pressure against time of the rest of the methane flames in region (C) .....	186
Figure 6.19: Tube end pressure against time of propane flames in region (A) .....	187
Figure 6.20: Tube end pressure against time of propane flames in region (B) .....	188
Figure 6.21: Tube end pressure against time of propane flames in region (C).....	189

## **DECLARATION**

*I, Abdullah Mohammad Abdullah Alsharif, confirm that this Thesis is my own work. I am aware of the University's guidance on the use of unfair means ([www.sheffield.ac.uk/ssid/unfair-means](http://www.sheffield.ac.uk/ssid/unfair-means)). This work has not been previously presented for an award at this, or any other, university.*

# NOMENCLATURE

## *Latin Letters*

$k$	Wave number of perturbation
$U_L$	Laminar burning velocity
$f$	Positive function
$E$	Gas expansion ratio
$Le$	Lewis number
$D$	Mass diffusivity
$v$	Velocity
$g$	Gravitational acceleration
$p'$	Pressure fluctuation
$q'$	Heat release fluctuation
$T$	Oscillation period
$f$	Frequency
$W$	Dimensionless velocity amplitude
$C_F$	Mole fraction of fuel
$C_A$	Mole fraction of air
$C_H$	Mole fraction of hydrogen
$X_H$	Mole fraction of hydrogen in the fuel mixture
$R_H$	The Relative amount of hydrogen addition to methane is defined according to Equation 2.12
$\bar{x}_F$	Fuel mole fraction
$\bar{x}$	Mole fraction of constituent
$a_s$	Air-fuel ratio
$X_f$	Fourier coefficient
$n$	Number of data points

$x$	Inverse Fourier transform
$A$	Instantaneous amplitude
$t$	Instantaneous time
$W_s$	Wavelet transform
$a$	Scale of mother wavelet
$b$	Time shift of mother wavelet
$T_s$	Synchrosqueezed transform

### ***Greek Letters***

$\alpha$	Thermal diffusivity/ Expansion ratio
$\delta$	Flame thickness
$\vartheta$	Instantaneous phase
$\lambda$	Wavelength
$\xi$	Angular frequency
$\rho$	Density
$\sigma$	Growth rate of hydrodynamic instability
$\phi$	Equivalence ratio
$\phi_F$	Effective fuel/air equivalence ratio defined according to Equation 2.11
$\psi^*$	Mother wavelet in time domain
$\psi^*$	Mother wavelet in frequency domain
$\Omega$	Strouhal number
$\omega_s$	Instantaneous frequency
$\omega_l$	Central frequency

### **Subscripts**

$st$	Stoichiometric
$u$	Unburned gas

<i>b</i>	Burned gas
<i>i</i>	<i>i<sup>th</sup> constituent of fuel mixture</i>
<i>j</i>	<i>j<sup>th</sup> constituent of fuel mixture</i>
<i>n</i>	Number of data points
<i>k</i>	Number of iterations / <i>k<sup>th</sup> component</i>
<i>K</i>	Maximum number of components in signal
<i>s</i>	Instantaneous component of frequency

### **Abbreviations**

DL	Darrieus-Landau instability
TD	Thermal–diffusive instability
RT	Rayleigh-Taylor instability
DTF	Distorted Tulip flame

# 1 INTRODUCTION

Thermo-acoustic instability is an inherent problem in many combustion devices including rocket motors, gas turbine engines, and industrial furnaces. This instability has the potential to change the flame behaviour significantly. If the flame is confined, thermo-acoustic instabilities which become apparent due to the combination of unsteady heat release and pressure oscillations can cause serious structural damage and catastrophic engine failure [1]. The early flame propagation of premixed gas fuel blends in a tube was studied by Mallard and Le Chatelier in 1883 [2]. It was reinvestigated in the following years, generally because of the need to better recognise combustion risks or the need to improve the power of combustion engines. The tube method, which is a convenient method to observe acoustic oscillation, has been used to investigate thermo-acoustic instabilities in order to better understand this unwanted behaviour [3]. Tube study goes back several years, with notable contributions by Mallard and Le Chatelier [2], Mason and Wheeler [4], Coward and Hartwell [5], Guénoche [6], Markstein [7] and Clanet et al. [8]. Despite their work, questions remain regarding the key features associated with propagating flames in tubes. It is important to note that the propagation of the flame is dependent on the design of the rig and the conditions at the boundary, e.g. whether the ends are open or closed, the source of ignition, diameter of the tube, and propagation direction, either vertical or horizontal [7].

Markstein [7] and Guénoche [6] characterised the propagation of premixed flame in open-ended horizontal tubes. After ignition, the shape of the flame is convex to the unburned gas and propagates steadily down the tube faster than its laminar burning velocity. The flame commences a self-induced longitudinal acoustic field at about half the distance down the tube. The frequency of oscillation is dependent on the dimensions of the tube. Initially, the oscillations flatten the shape of the flame, decreasing its speed as a result of the reduction in its surface area. Following several acoustic cycles, the flame can rapidly accelerate, which is associated with violent oscillations and an increased pressure oscillation amplitude.

The flame moving along the tube dampens the oscillation amplitude within the field, ultimately causing the flame to propagate steadily towards the tube's end. Flames in any confined space can spontaneously generate acoustic oscillations [6]. When an oscillation occurs, feedback processes take place whereby the flame's heat release is modulated by the acoustic field, and the flame returns energy to the acoustic wave. The Rayleigh criterion states that acoustic waves will be subject to amplification when the acoustic pressure and heat release fluctuations are in phase with one another [9]. Searby [10], [11] suggested two acoustic instabilities in tubes: primary and secondary. While the behaviour of flames propagating in tubes has long been subject to extensive research, it is still not entirely possible to accurately predict the behaviour of such flames without actually measuring them.

This research aims to investigate the thermo-acoustic instabilities utilising methane and propane flames within a vertical tube which is open at one end and closed at the other. This research has further investigated the addition of hydrogen, which provides an understanding of the effect of hydrogen addition to thermo-acoustic instabilities.

This study focused on the behaviour of premixed methane-hydrogen-air flames, and propane-hydrogen-air flames that propagate vertically through a tube (length = 1.2 m; internal diameter = 0.02 m) with an open ignition end. Methane and propane were tested with an equivalence ratio,  $\phi$ , ranging from 0.8 to 1.5 in 0.1 increments. Using Yu et al.'s [12] method, the amount of hydrogen addition,  $R_H$ , hydrogen was added for each equivalence ratio in 0.1 increments until  $R_H = 0.4$ . In addition, the volumetric method was also used with methane, 10% $H_2$  - 40% $H_2$  in 10% increments. In total, 112 mixtures were tested, with burning and recording carried out three times for each mixture, making 336 runs in total. Adding hydrogen increased the laminar burning velocity; therefore, this study investigated how the laminar burning velocity affects oscillatory flame propagation.

## **2 LITERATURE REVIEW**

This section describes the history of the research into flame propagation instabilities in tubes and gives important definitions to provide a background for the current work. Previous studies have, in particular, emphasised flame tube configuration, flame stability, fuel composition and the spectral analysis of flame propagation.

### **2.1 Flame instabilities in premixed combustion**

The focus of this section is to provide general and background information on premixed flame instability. Premixed flame can ultimately become unstable without any influence from external sources such as flow fields, acoustic sounds or pressure waves. Generally speaking, there are two main categories of instability [13]:

1. Those occurring in combustion chambers (the most common type) as a result of shock and acoustic waves.
2. Those taking place outside a chamber elsewhere in the system.

The most common examples of instability are Darrieus-Landau, thermo-diffusive, and buoyancy or acceleration. These strongly interact with each other in premixed combustion systems and it is, therefore, appropriate to discuss their mechanisms in detail.

#### **2.1.1 Hydrodynamic (Darrieus-Landau) instabilities**

Flame fronts may undergo spontaneous curving due to hydrodynamic instabilities; this was initially proposed by Darrieus and Landau (the DL instability), and this is the main cause of the curvature of the flame front found in a number of experiments [14]. Because this instability has associations with gas expansion with an exothermic reaction, the DL instability is inherent in all flames within gaseous mixtures. The DL instability proposes that flame fronts are surfaces with a thickness of zero that act as a separator between burned and unburned gas, propagation towards unburned gas at the constant normal velocity. This concept states that, as gas expands through a curved flame the flow will undergo divergence at sites where the front has a convex relation with unburned gas, and convergence where the flame has a concave relation with it, as illustrated in Figure 2.1 [14].

The theory of mass conservation suggests that the upstream flow will accelerate or decelerate accordingly, respectively, to whether the flame front is lagging behind or ahead of the mean position. The assumption was made that the front's propagation velocity is constant, unconditional instability occurs within the flame front and it becomes more wrinkled over time: here the DL instability is found. There are four parameters within the analysis: the wavelength  $\lambda$  (or wave number  $k=2\pi/\lambda$ ); laminar burning velocity  $U_L$ ; a positive function of order unity  $f$ ; and, the gas ratio densities  $E = \rho_u/\rho_b$ . Dimensional analysis creates a growth rate of Darrieus–Landau instability,  $\sigma$  (dimensions  $s^{-1}$ ) [15]:

$$\sigma \propto k U_L f \left( \frac{\rho_u}{\rho_b} \right)$$

**Equation 2.1**

Landau [15] gives the precise expression:

$$\sigma = k U_L \frac{E}{E + 1} \left( \sqrt{\frac{E^2 + E - 1}{E}} - 1 \right)$$

**Equation 2.2**

with  $E$  being the gas expansion ratio  $E = \rho_u/\rho_b$ , the expression above is constrained by the linear limit of the wrinkling amplitude much smaller than the wavelength. The DL instability rate is subject to an increase alongside the speed of the flame and the wrinkling's wavenumber. Nevertheless, there cannot be an indefinite increase of growth rate at small wavelengths. Perhaps, the most significant influence when flame thickness and wrinkling wavelength are close is the thermo-diffusive phenomenon [15].

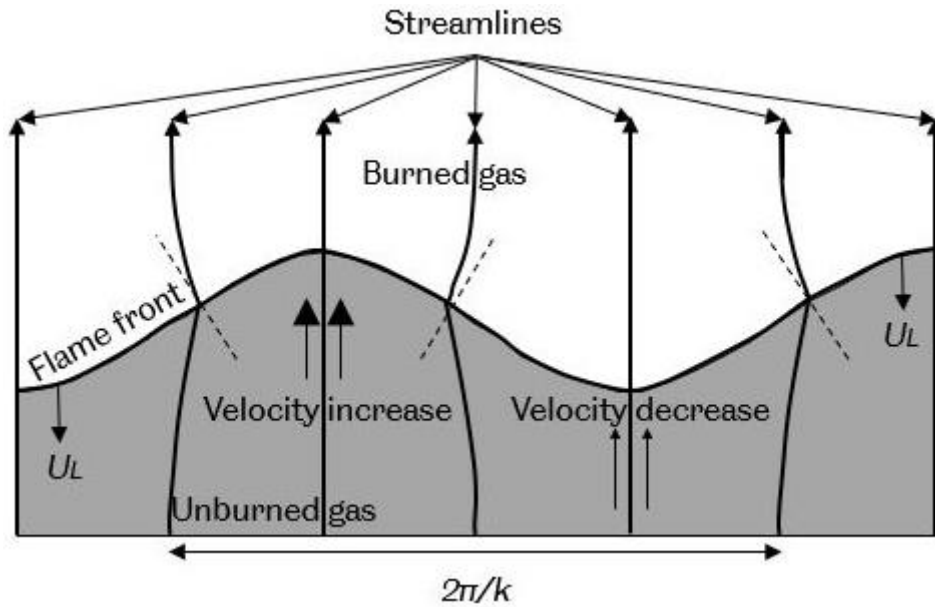
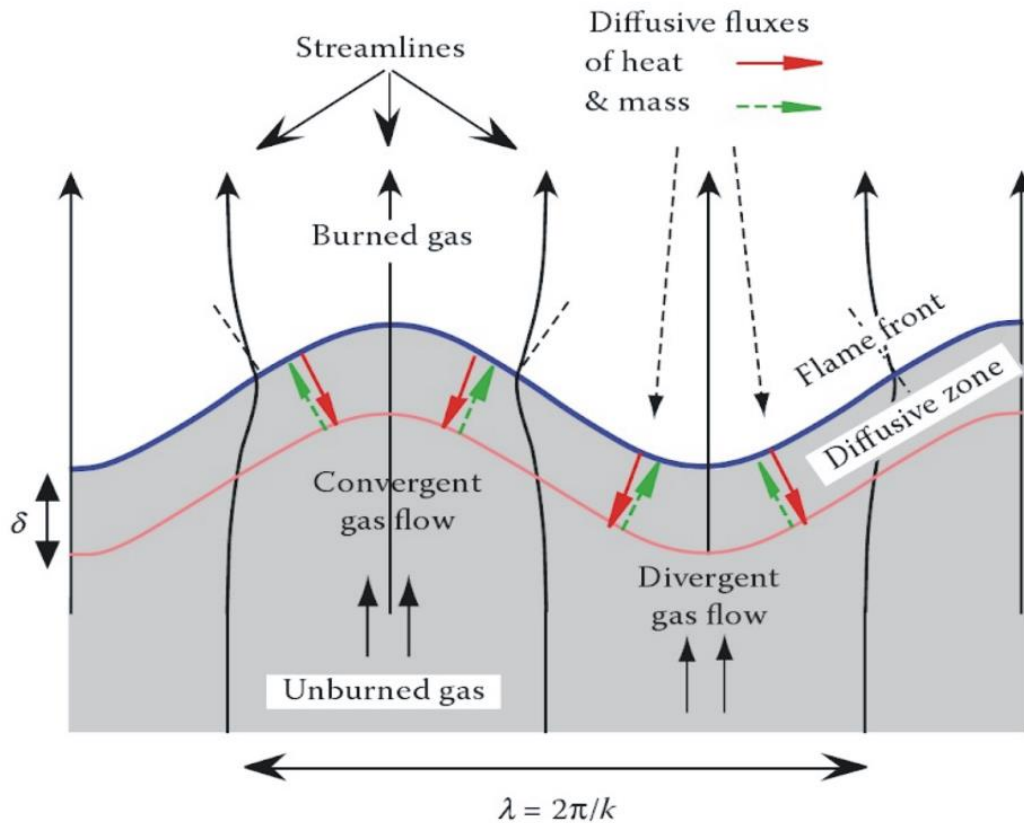


Figure 2.1: Deviation of flow lines that generate Darrieus-Landau instability. Reproduced from [14]

### 2.1.2 Thermo-diffusive instabilities

The way in which the flames propagate depends upon the heat diffusion involving combustion and the flame thickness,  $\delta$ . When flames are curved or wrinkled at the front, species concentration and temperature gradients do not coincide with the propagation's average direction and, thus, there may be variations in local flame velocity. In sites where the flame front is concave towards the unburnt gas, there is local convergence in the heat flux. Because of this, increases occur in local propagation velocities and flame temperatures. Thermal diffusion has the effect of stabilising the wrinkled flame only if  $Le > 1$ . At sites where the flame front has a convex relationship with unburned gas, there is local divergence in heat flux. Because of this, decreases occur in local propagation velocities and flame temperatures. Figure 2.2 shows the thermal diffusion gradient with red arrows and the species concentration gradient with green arrows. The thermal and species gradients can be seen move on opposed paths.



**Figure 2.2: The structure of a wrinkled premixed flame. Reproduced from [15]**

The final outcome of action of the pair of diffusive fluxes is dependent on the ratio between the diffusion coefficients of the thermal  $\alpha$  and species  $D$  diffusion; the ratio represents the Lewis number and has the following definition:

$$Le = \frac{\alpha}{D}$$

**Equation 2.3**

with  $\alpha$  being thermal diffusivity and  $D$  representing the coefficients of species diffusion.

With the equidiffusive flame,  $Le = 1$  (thermal diffusion = mass diffusion), thermal diffusion from the surface of the flame towards the unburned gas is equalled by the mass diffusion of deficient reactant, which results in a constant temperature of flame, which does not affect the perturbation [16].

With the  $Le > 1$  flame (thermal diffusion  $>$  mass diffusion), there is convergence of the thermal diffusion from the flame's concave area in the direction of the unburned gas, which leads to temperature increases ahead of the concave section, and this speeds up the flame. In the convex area of the flame the opposite occurs as the flame slows as a result of a reduction in the flame temperature due to an increase in the heat transfer to the unburnt gas. When both processes are combined, the disturbance will ultimately decrease [16].

Finally, with  $Le < 1$  flame (thermal diffusion  $<$  mass diffusion), increases in mass diffusion for the reactant in the direction of the flame surface results in a temperature increase at the convex section of the flame, which technically causes acceleration. This acceleration results in the convex section achieving deeper penetration within the unburned gas, which destabilises the surface of the flame. Clarke [16] asserted that this process will proceed until the flame becomes cellular, also observing that the process of transforming to a cellular flame would be swifter in comparison to hydrodynamically unstable flames.

In Figure 2.3, the wave-like perturbation effect of the planar front is presented diagrammatically. The developing line interfaces between the burned and unburned gas experience vortices due to the perturbations, whereby rotations emerge close to the streamlines, as indicated by the broken curves. As shown by the streamlines, this phenomenon, combined with the contraction of the expanded hot gases, causes the streamtubes to expand. Relative pressure changes are instigated by these perturbations, as indicated in the area of unburned gas by + and -, and their gradients contribute to the perturbations originally found at the planar front. The hot gas expansion propels the perturbations, and according to the theory, the planar flames demonstrate unconditional instability. As indicated by the model in Figure 2.3, positively stretching the flame sheet would, to some extent, neutralise this instability. In the past, the enhanced elucidation of the structure of laminar flames, including the molecular thermal-diffusive (TD) effects, revealed factors that can alleviate or strengthen the Darrieus-Landau (DL) instability.

These factors include the conductive energy flux between burned and unburned gas, as suggested in Figure 2.3 by the broken arrowed lines situated at the flame's leading edge, and the diffusion flux of deficient reactant from the unburned gas into the reaction zone of the flame, as shown by the solid lines in the same figure [17].

For lean mixtures, the deficient reactant is fuel, while for rich mixtures it is oxygen. Hereby, a key parameter is the Lewis number. If  $Le < 1$ , the flame curvature focuses the diffusion of enthalpy into the flame, as highlighted by arrowed solid lines, therein exceeding the flame's conductive energy loss, indicated by arrowed broken lines. Consequently, there is an increase in the local burning velocity. In the valley, there is the opposite effect, i.e. the local burning velocity diminishes. Hence, there is an additional increase in flame instability. This instability due to TD strengthens that due to DL. Using the same rationale, Lewis numbers above unity have a contrasting and stabilising effect, similar to the viscosity increase due to rising temperature. These two instability forms are linked and are denoted as DLTD in the following. The instability dispersion relation's additional TD term refers to the effects of  $Le$ , the flame stretch rate, the unburned to burned gas density ratio  $\sigma$ , and the reaction's overall activation energy, all of which are valid across a range of wavelengths [17].

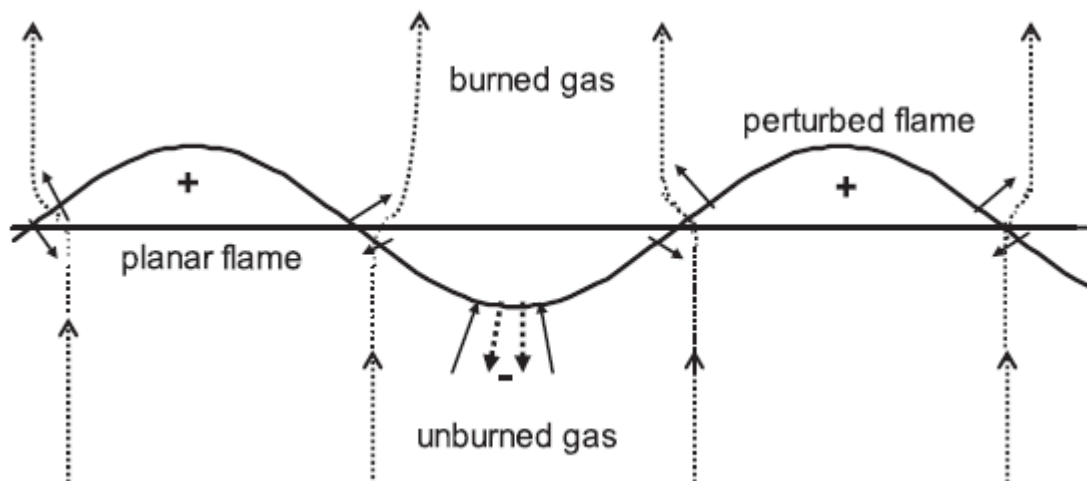


**Figure 2.3: DL and TD instability development following planar flame perturbation. The relative changes in the unburned gas pressure are indicated by + and - between the perturbed streamlines. The arrowed solid lines located at the wave crest show the deficient reactant diffusion, and the arrowed dotted lines show thermal conduction [17]**

In this research, Lewis number calculations for the mixtures employed were not undertaken as it is difficult to calculate Lewis numbers for binary fuel mixtures. Clarke [16] undertook systematic research regarding the Lewis numbers for various hydrocarbons, employing a variety of Lewis number calculations; these hydrocarbons included methane. In the findings of this study, based on the deficient species for pure methane, the Lewis number was estimated to range from 0.87 to 0.95 for equivalence ratios of 0.6-1.4.

Jackson et al. [18] undertook research into the influence of adding hydrogen to lean premixed methane for highest strained flows. They calculated effective Lewis numbers for the fuel mixtures employed, and found that Lewis numbers for hydrogen-enriched methane mixtures were not as high as those for pure methane mixtures, which technically leads to reductions in the sensitivity of the flame to the strain rate. It should be noted that the mixing methodology employed in that research was not the same as that employed in this research (a detailed discussion of the mixing methodology for this research can be found later in section 2.6.2).

### **2.1.3 Body-force instabilities**

If one fluid is placed above another at rest, with the upper fluid having a higher density, gravity will cause buoyant instability, also known as body-force instability [19]. The technical description of gravity is a constant acceleration towards Earth of  $9.81 \text{ m/s}^2$  [20], and so a perpendicular acceleration towards the surface of the flame (that is effectively an interface between denser unburned gas and lower density burned gas) will create instability comparable to the body-force instability detailed above.

If the flame is treated as being a discontinuity that moves at a velocity of  $v_u$  (unburned gas) and  $v_b$  (burned gas) influenced by  $g$  (gravitational acceleration) [21], the characteristic transverse length and growth rate may be estimated for body-force instability as:

$$\text{Characteristic transverse length} \propto \frac{v_u v_b}{g}$$

**Equation 2.4**

$$\text{Growth time} \propto \frac{\sqrt{v_u v_b}}{g}$$

**Equation 2.5**

On the basis of Equation 2.5, as flame speed decreases instability will increase, shortening the growth time, meaning that the instability will develop more quickly. Williams [22] offered a detailed discussion of this phenomenon, concluding that when a flame experiences acceleration perpendicular to the surface, towards the direction of flame propagation, body-force instability will occur; decelerating flames will experience stabilisation.

Two types of fluid instability that can be categorised as body-force are the Rayleigh-Taylor (RT) instability and the Richtmeyer-Meshlov (RM) instability, in which the chief mechanism that produces instability of the fluctuations is acceleration caused by identical fluid forces on regions that have different densities, a condition that generally exists at the surface of the flame.

The Rayleigh-Taylor instability results from the differences in density of a pair of fluids. When two fluids of different densities accelerate perpendicularly to the interface, the stability or instability of the surface is dependent on the direction of acceleration. When the acceleration direction runs from heavy fluids to light fluids, surface stability is present; if it does not, surface instability is present [19]. Instabilities develop when  $\nabla P \cdot \nabla \rho < 0$ . The Rayleigh-Taylor instability can be seen in the way water behaves when it is suspended over oil in Earth's gravity. It may be observed that the Rayleigh-Taylor instability is caused by pressure torque as a result of the differential between density and pressure gradients present at the disturbed interface, as seen in this equation:

$$\frac{D\omega}{Dt} = \frac{1}{\rho^2} \nabla \rho \times \nabla P$$

**Equation 2.6**

With  $\omega$  representing vorticity,  $P$  representing pressure and  $\rho$  representing density. In this instance, acceleration is responsible for the pressure gradient. If the system configuration is not stable, interface torque will create vorticity with a tendency for increased variations in gradient vectors when particular harmonic components of initial disturbance are present. This subsequently leads to supplementary vorticity, which exacerbates the differences between gradient vectors. This can be seen in Figure 2.4 (where  $u$  is velocity,  $\omega$  is vorticity,  $\rho$  is density,  $P$  is pressure, and  $g$  is gravity). The thick circular arrows demonstrate the velocity field produced by the vortex), having two counter-rotating vortices in the perturbed interface with velocity fields that correspond at both peaks and troughs. When the configuration is stable, vorticity, and so also the induced velocity fields, have patterns in movements that lead to a reduction in gradient vector fluctuation and, thus, stabilises the system [23].

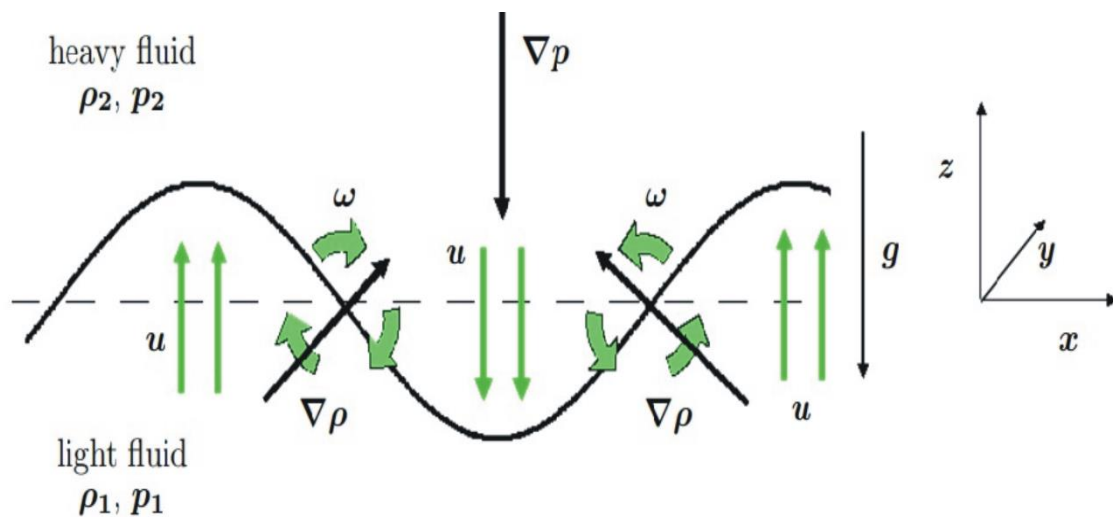


**Figure 2.4: Visualisation of an unstable Rayleigh-Taylor configuration. Reproduced from [23]**

Study of RT instability was carried out theoretically by Rayleigh [24] in 1882, and in 1950, Taylor [19] revived this discovery, and in the same year Lewis [25] provided experimental validation. Lewis' research had found that instability of air-water interfaces experiencing constant gravitational acceleration comprised three phases in succession; these being a) instability growing exponentially, b) bubble formation in a transitional phase, and c) an asymptomatic stage comprising rising air columns. Instability could not be created by accelerating lighter fluid towards heavier fluids.

An outline of the characteristic flow pattern as RT instability evolves is shown in Figure 2.5 [26] where a) represents normal mode disturbance, b) represents free-surface bubbles, c) shows falling spike in negligible density medium, d) represents falling in spike in the medium with finite density, and e) shows the advanced intermixing stage. For every pattern, these fluids were subject to kinematic acceleration from light fluid towards heavy. Shown in Figure 2.5(a) is a sinusoidal surface modulation caused by normal mode disturbances of the horizontal equilibrium surface on the basis of Taylor's theoretical calculations [19]. Because of this acceleration from the left region towards the right, an initially flat interface became sinusoidal as seen in Figure 2.5(a). Instability ultimately expands to the shape shown in Figure 2.5(b), which was seen in experimentation by Lewis [25] and Emmons et al. [27].

Employing the vortex methodology, Baker et al. [28] undertook numerical simulations to find the influence of the Atwood number (non-dimensional number describing density difference between two fluids) on RT instability, reaching the conclusion that the density interface calculation of the Atwood number significantly influences the way in which RT instability spikes form. Figure 2.5(c) shows how spikes are formed for a density influence with an Atwood number of 1. When the Atwood number was below 1, spikes were followed by a rolling of spikes, as illustrated in Figure 2.5(d). Spike rolling was also found by Gardner et al. [29] (theoretically), who described it as representing vortices being shed at the spike's tip.

Richtmeyer [30] made a theoretical study of RM instability in 1960, and Meshkov [31] made experimental studies of the same in 1972. Richtmeyer [30] examined how instability grew during impulsive acceleration, usually meaning that the interface experiences massive acceleration over a brief period, with a subsequent period where little or no deceleration was present, which could be achieved through the application of a pressure wave in the direction of fluid interfaces with varying densities.

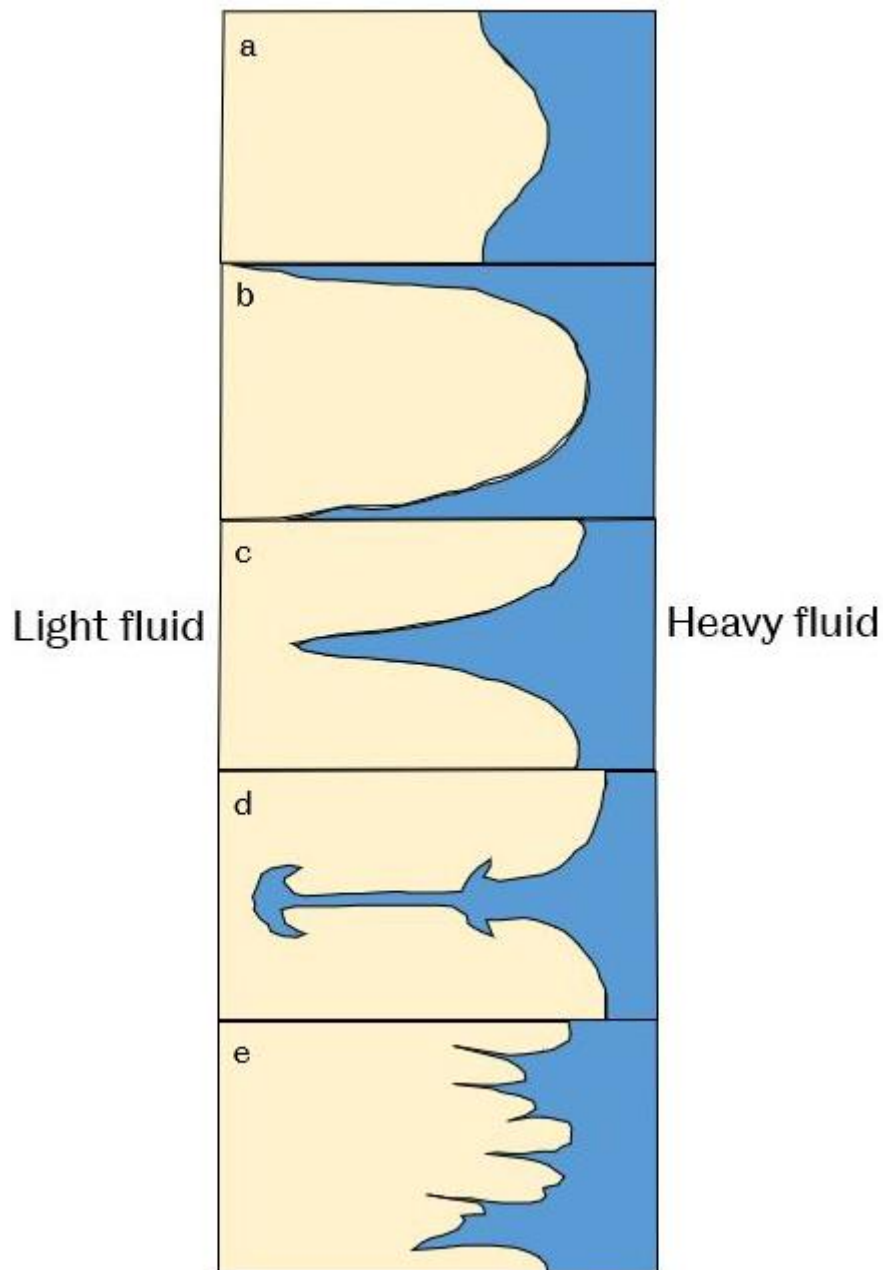


**Figure 2.5: Schematic flow patterns showing how unstable two-dimensional flows evolve in RT. The heavy fluid is penetrated by the light fluid during acceleration in the direction of the heavy fluid in every condition. Reproduced from [26]**

For the transmission of pressure waves within fluids, this form of instability is only observed in gases as they are compressible, meaning that gas is the only material that allows for research into this form of instability. Meshkov [31] employed various combinations of inert gas, e.g., air, helium, freon, and carbon dioxide; he used thin films to separate them and created acceleration by bursting a diaphragm and creating a shock wave. He found that if impulsive acceleration occurs from light gas towards heavy gas, or the other way round, then instability is created in the interface.

Figure 2.6 illustrates the pre- and post-schematics as a shock passes through a fluid interface, as shown by Richtmeyer [30]. Prior to moving through the fluid interface, it was assumed that the shockwave was a plane, producing a pair of varied corrugated shocks, these being a reflected shock and a transmitted shock. In both of these shocks, the correlations were central to the ways in which the fluid interface was destabilised. Looking at Figure 2.6, the interface crest (the point at which the heavy fluid protrudes within the light fluid) expands because the transmitted shock had a moderately converged travel direction, creating a small pressure rise in the heavy fluid, and the reflected shock had a slight divergence, which created a small pressure drop in the light fluid. This creates resistance to the shock's original motion, which makes the crest virtually stationary. The opposite occurred at the interface trough, as these troughs were accelerated into the heavy fluid in the direction of the original shock motion [30].

RM and RT instabilities may look similar but Gardner et al. [32] state that RT instabilities generally are associated with instability caused by constant acceleration, e.g. when honey is suspended over water under constant gravitational acceleration, but RM instabilities are associated with a shorter length scale (impulsive acceleration) acute gradient pressure (shockwaves), which creates larger scale instabilities that have significant vorticity in comparison to RT instabilities, as Cloutman states [33]. For the avoidance of confusion, it should be noted that this research did not detect any shockwaves, just standard pressure waves, which leaves RT instability as the primary body-force instability. It is possible for pressure waves to be moving at the speed of sound, but they could not go supersonic (exceeding the speed of sound), and were unable to create a shockwave as required to form an RM instability.

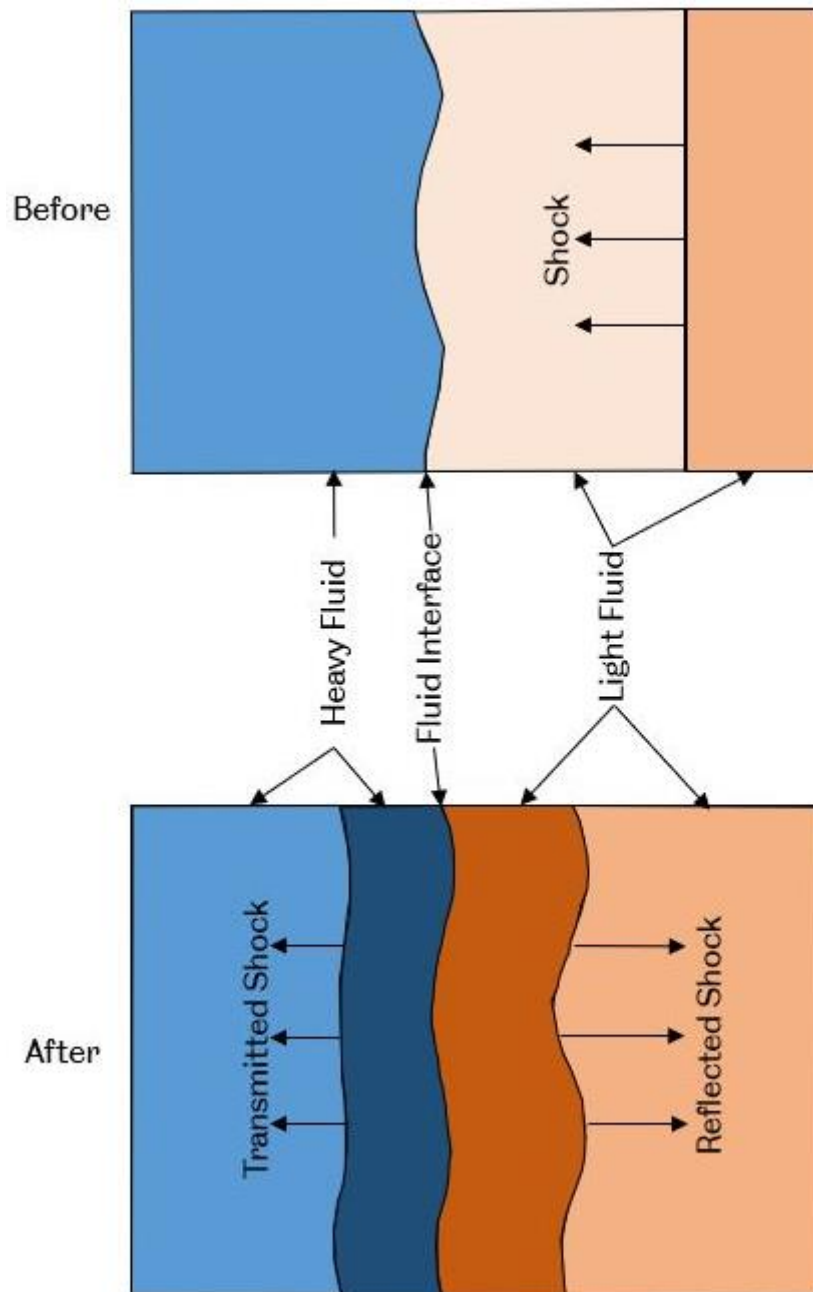


**Figure 2.6: Pre- and post-schematics of a shock as it passes through a fluid interface. The incident shock was planar, but the transmitted/reflected shocks were corrugated. Reproduced from [30]**

Liu et al. [34] undertook numerical studies of pressure wave-flame front interactions or differentiation of pressure-driven RT instabilities and gravity-driven RT instabilities, as illustrated in Figure 2.7. These two forms were virtually identical, but there was a differential related to the growth rates of the interface disturbance's magnitude; in the gravity-driven instability, the increase was exponential, and in the pressure-driven instability, the increase was sub-exponential.

On the basis of Figure 2.7, Liu et al. [34] compared the gravity-driven RT instability with the pressure-driven RT instability in detail. They found that acceleration towards unburned gas from burned gas creates instability in the flame front disturbance; if the process is reversed, stability is introduced in both instances. These differences were noted within the basic flow field, in which the gravity-driven interface remained still because no basic flow velocity was present; in the pressure-driven interface, acceleration was caused by the pressure wave, making the basic flow acquire time-dependent velocity.

As well as finding basic flow-field differences, Liu et al. [34] also stated that there were differences in the time for the expansion of instability. In the gravity-driven instance, this began as soon as gravity began acting upon the interface; in the pressure-driven instance, growth began following compressibility effects caused by the initiation of the pressure wave, which produced differential acceleration in areas of different densities.

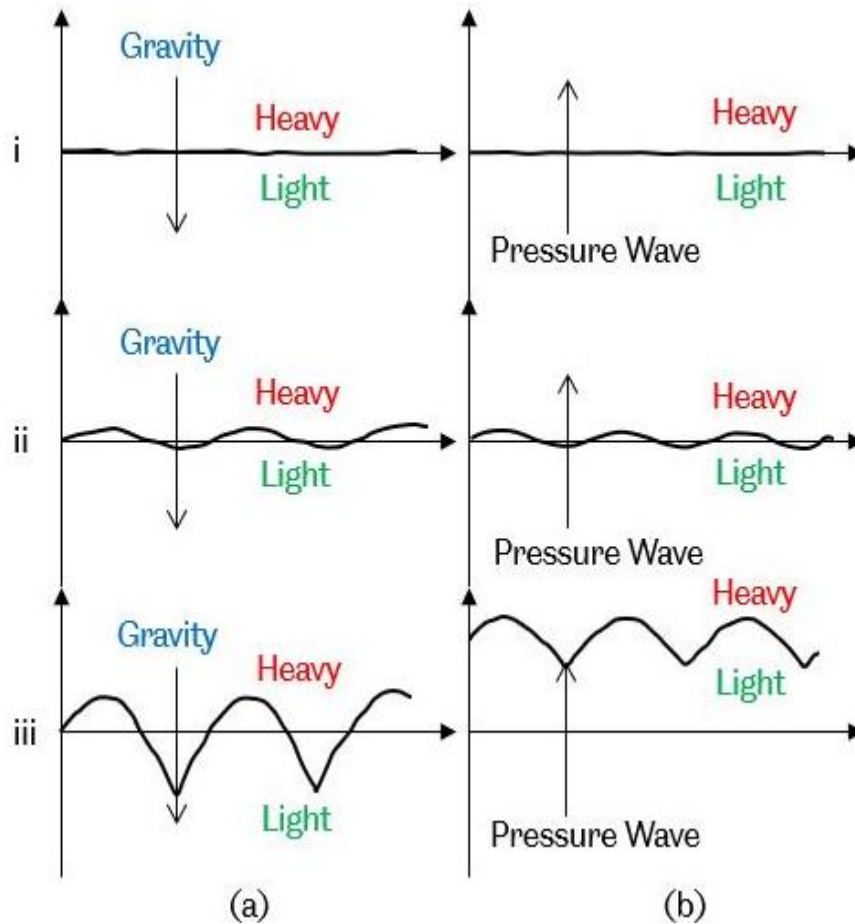


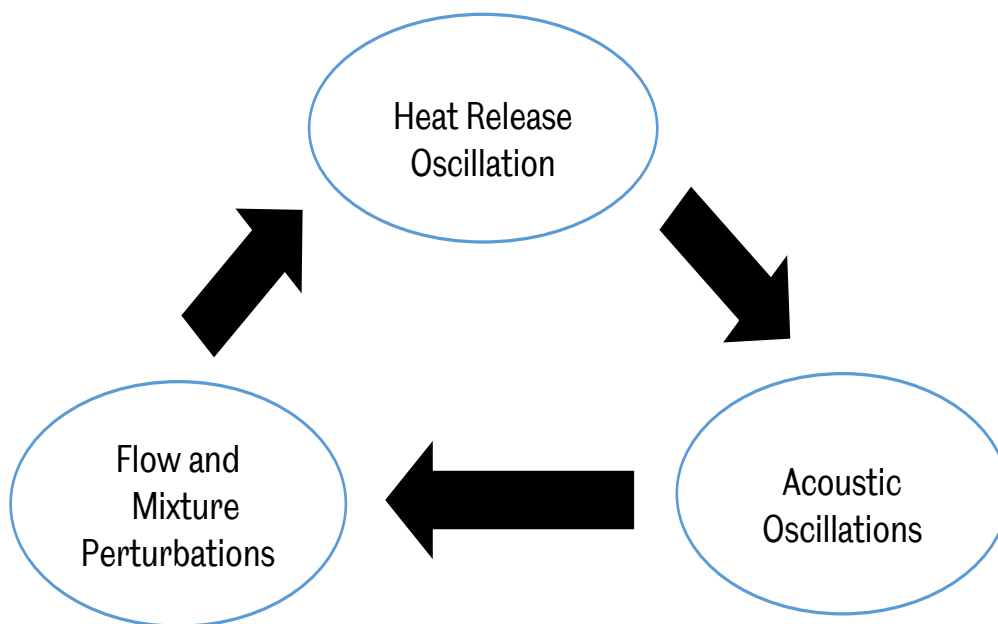
Figure 2.7: Two forms of Rayleigh-Taylor instability, a) gravity-driven, b) pressure driven, segmented into three phases: i) undisturbed interface, ii) disturbed interface, iii) interface at time,  $t$ . Reproduced from [34]

Figure 2.7 makes the interface appear different, but over time both instances will show similarities in their spikes and bubbles. Finally, sinusoidal pressure disturbances initiate oscillation at the flame front, which reduces the overall flame front turbulence level after it has alternated from enhancement to suppression at the flame front disturbance; this was noted experimentally by Tsuruda et al.[35].

It is apparent that the flame shape influences the relationship between the non-flame flow and the flame. For example, Ebieta [36] found that the area of the flame decreases when it is exposed to sinusoidal pressure, eventually causing a flat flame to form. This formation is accompanied by a steady increase in sinusoidal pressure until the non-flame flow is strong enough to cause unburnt gas spikes in the flame. After the emergence of these spikes, the disturbance in the sinusoidal pressure increases significantly. The overall impact of this type of instability in the tube is that highly oscillatory flame propagation has been observed [2][37].

## 2.2 Thermo-acoustic instability

Thermoacoustic instabilities, that may be seen when oscillations in pressure and variable heat release combine, reduce efficiency and raise levels of emissions. Understanding the way in which preservation and unsteadiness of heat release is regarded as one of the fundamental difficulties of investigating combustion instability. The heat release oscillation can occur due to oscillation in pressure, velocity, temperature, and reactants' composition [38]. The principle of thermoacoustic instabilities is that unsteady heat release in the system causes acoustic waves, which are reflected at the system boundaries. The acoustic fluctuations lead to increased flow and mixture perturbations, which in turn influence the flame, resulting in a perturbation of the heat release; thus, a self-exciting loop is created, as shown in Figure 2.8 [39]. These fluctuations are often associated with Thermo-diffusive instability and Rayleigh-Taylor instability.



**Figure 2.8: The feedback loop responsible for the appearance of thermoacoustic instabilities. Reproduced from [40]**

Three main coupling mechanisms can be identified [41]:

- ❖ Pressure coupling is the most basic type. As a result of acoustic waves, changes in gas temperature are brought about by adiabatic compression and this in turn changes the rate of heat release.
- ❖ Velocity coupling is the key mechanism that takes place in a Rijke tube which is a cylindrical tube open at both ends in a vertical position with a disc of wire gauze placed inside it.
- ❖ Acceleration coupling causes primary instability in tubes, where the fluctuation in the flame surface area, caused by periodic flow acceleration, leads to changes in heat release.

### **2.3 History of premixed flame instabilities**

Higgins conducted early work with heat-driven oscillation in 1777. A paper written by Higgins [37] in 1802 describes the 'singing flame' phenomenon, where sound can be produced by placing a diffusion hydrogen flame into a tube. This work was the first observation of sound inside the tube caused by combustion [37]. In 1802 Ernst Chladni [40] demonstrated that the flame excites the tube's fundamental mode, or one of its harmonics. An example of the experiment that has majorly contributed to the comprehension of thermoacoustic instabilities is the Rijke tube. In this tube, the sound was produced by a hot metal gauze, heated by burner or electrically, placed in the lower half of the tube [42]. In 1878, Lord Rayleigh proposed a criterion for heat-driven acoustic oscillation:

*"If heat be given to the air at the moment of greatest condensation, or be taken from it at the moment of greatest rarefaction, the vibration is encouraged. On the other hand, if heat be given at the moment of greatest rarefaction, or abstracted at the moment of greatest condensation, the vibration is discouraged"* [43].

Rayleigh's criterion is a standard tool that is used to predict and investigate combustion instabilities. It also measures the correlation between pressure and heat release. Two combustion systems with acoustical oscillations were investigated by Putnam and Dennis [44]: 1) Premixed flame with (open at both ends) tube, 2) Premixed flame with (closed-open) tube.

From their experiments and analysis, it was concluded that oscillations were enhanced when two criteria were met concurrently:

-Firstly, when the heat-release oscillation component and pressure variation were phased.

-Secondly, when the heat-release point was close to the maximum pressure amplitude point in the combustor.

In 1883, Mallard and Le Chatelier applied early propagation of premixed gas fuel blends in a tube [45]. The experiments employed a horizontal tube configured with an opening close to the ignition port with the further end being sealed. However, the general conclusions drawn were as follows. It was found that a flame that propagates from open to closed ends starts to oscillate as it propagates along the tube. Moreover, photographic experimentation was undertaken on the propagation of flame and it was found that both detonation and oscillation are dependent on the composition of the mixture and how the tube was configured. Coward and Harwell [5] carried out an analysis to explore oscillations in tubes with diameters between 10 and 20 cm. One of the interesting results was that oscillation occurred as the flames travelled from the pressure node to the velocity node within the tube. In 1953 Schimdt et al. [46] researched oscillations in square cross-section tubes using Schlieren photography. It was found that the flame oscillated when it was ignited at the sealed end with the flame travelling towards the tube's opening. Their pictures showed that, with these oscillations, important changes occurred in the shape of the flame front, however, their tests were conducted using only one tube length with a mixture of propane and air.

Further experimental studies in oscillatory flame propagation in tubes were carried out by Kaskan [47] using methane-air mixtures as well as 0.75 and 1.5 inch diameter tubes that were either open or closed. As his aim was to explore how the cyclic addition of heat drives oscillation, he did not experiment with a variety of fuel mixtures, focusing instead on mixtures that generate flat or disk-like flames during propagation. Most oscillations began in the first 1/3 to 1/2 of the tube and ceased at around 5/6 of the tube. The author concluded that two mechanisms may be causing this heat-driven oscillation. The first mechanism is based on the fact that the cyclic temperature and pressure changes cause correlating fluctuations in the flame speed; hence, the rate of heat release changes periodically depending on pressure, thereby fulfilling Rayleigh's criterion.

The second mechanism, which was first proposed by Kaskan [47], relates to the periodic changes in the flame area. The author showed that in the acoustic boundary layer, i.e. the thin region by the wall that is affected by viscosity [48], the flame flattens out at the point of maximum recession, developing a cusped (cellular) form at the point of maximum penetration. This causes the flame to have an increased surface area. The fact that the maximum penetration point is due to a pressure increase meets the driving condition stipulated by Rayleigh. Moreover, he also showed that the pressure amplitude increases in the early propagation stages, which drives the oscillation; as the flame reaches the end, there is a reduction in the velocity amplitude, which in turn reduces the fluctuation of the flame shape until it eventually ceases.

In addition, Markstein [49] later showed evidence that primary acoustic instability resulted from variations in flame area. Lord Rayleigh showed that the phased relationship between heat release and acoustic pressure oscillation had to be considered as one aspect of heat driven oscillation. These criteria had inspired Putnam and Dennis to derive it mathematically and to incorporate Lord Rayleigh's phased relationship [50].

An integral version which is shown in Equation 2.7 is one of the most commonly used forms of the Rayleigh criterion:

$$R = \int_0^T p'(t)q'(t) dt$$

**Equation 2.7**

With  $R$  representing the Rayleigh Index,  $T$  representing the oscillation period, and finally  $p'$  and  $q'$  representing, respectively, the fluctuation in pressure and fluctuation in heat release rate. When the Rayleigh Index is positive, this shows that pressure oscillation has been amplified with fluctuations in heat release; if the index is negative, this shows that the pressure oscillations have been dampened. A positive index does not, however, guarantee pressure oscillation amplification. In order to maintain self-driven thermoacoustic instability it is necessary to overcome pressure dissipation losses, which can be accomplished by coupling the heat release with the pressure oscillation [50].

In 1859, Rijke [51] extensively investigated the thermoacoustic phenomenon outlined by Rayleigh's abovementioned criterion. He demonstrated the phenomenon both theoretically and experimentally using a so-called Rijke tube. When sound waves are propagated within a Rijke tube, they are reflected back inside upon reaching the open end. If a reflected sound wave influences another wave, a standing wave is established in the tube; this standing wave will vary depending on its wavelength, as illustrated in Figure 2.9. This figure shows the first three harmonics with different vibration frequencies.

As can be seen in Figure 2.9(a), an open-ended tube's first harmonic involves pressure nodes at the open ends. These coexist with the antinodes of the velocity fluctuation, implying that, in the tube's lower half, the phase of velocity fluctuation leads that of the pressure oscillation by 90 degrees, while lagging in the top half by the same amount. Upon the introduction of a heat source to the tube, the flow occurring across the tube starts to align with the direction of the heat, i.e. upwards, thanks to the heat-related buoyancy effect. Thus, assuming that upward flow is the positive direction in the case of velocity fluctuation, a heat source located in the tube's lower half will cause

excitation of the flow because the transfer of heat directly relates to the flow velocity. If the heat source is located at the top, then flow damping will occur. As the Rayleigh Index is positive for the tube's lower half and negative for its top half, this is confirmed in theory. This excitation leads to a pressure fluctuation at a characteristic frequency that is in line with the criteria for the configuration of the tube, which in turn produces a thermoacoustic instability feedback mechanism.

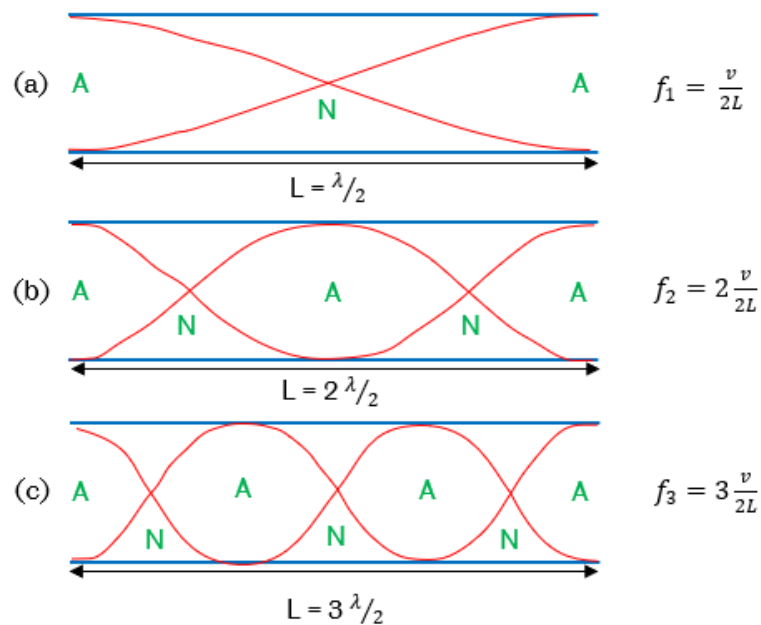


**Figure 2.9: Vibration modes for a tube open at both ends: a) first harmonic, b) second harmonic, c) third harmonic, where A represents the velocity antinodes and N indicates velocity nodes. Reproduced from [52]**

Research on thermoacoustic coupling in systems using lean premixed combustion has found that disturbances in the flow field and reactant mixture composition due to acoustic waves produce changes in the release of local volumetric heat [53]. These changes are frequently related to both thermal diffusive and Rayleigh-Taylor instabilities.

Taniyama et al. [54] showed how tulip-shaped flames' initiation and propagation have a correlation with fluctuation pressures when the flame is confined as illustrated in Figure 2.10. Using the Rayleigh criteria, it can be seen that self-turbulization can occur if pressure fluctuations and heat release exist in phase with each other.

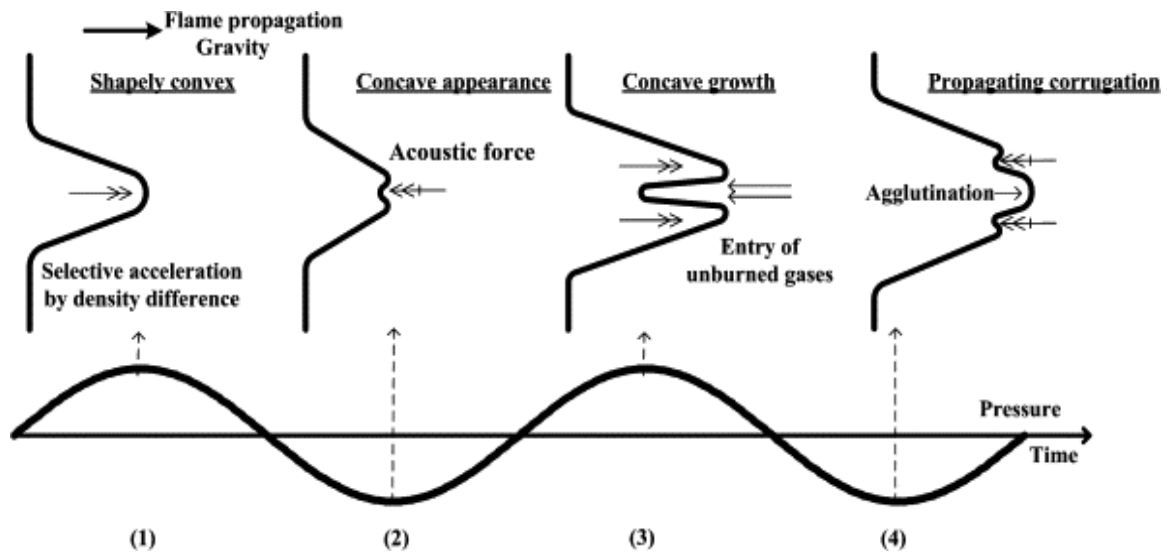


Figure 2.10: The mechanism for the initiation and propagation of a tulip flame. Reproduced from [54]

Xiao [55] has undertaken wide-ranging research into how tulip flames are formed, both with computer modelling and experimentation. This research suggested, and gave a detailed explanation of, the way distorted tulip flames are formed as a result of vortex generation behind the tulip lips, as illustrated in Figure 2.11 where solid lines indicate the initial flame front shape and dashed lines indicate the subsequent flame shape. Arrows indicate a characteristic flow velocity field [56].

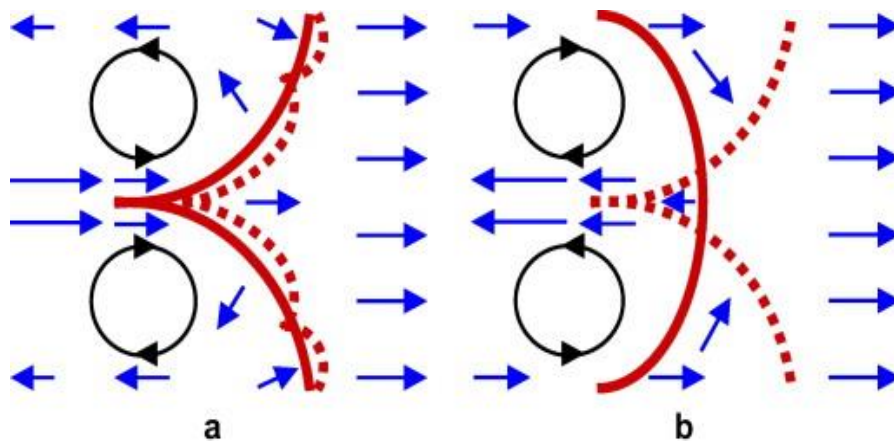


Figure 2.11: Formation of (a) distorted tulip flame, (b) classical tulip flame. Reproduced from [56]

Distorted tulip flames may only be present following the standard formation of a tulip flame. Looking at the way tulip flames are formed, both experimentally and numerically, evidence has suggested that tulip flames form as a result of fluid dynamics rather than instabilities [55] [57].

The following discusses the effects of ignition as well as of the overall behaviour of the thus generated pressure waves, as presented in the computational schlieren image (Figure 2.12) [55]. The pressure waves generated by the ignition process propagate in front of the flame, with the first being reflected by the sidewalls and then propagating along the tube. As the schlieren image shows, these reflections create a set of crisscrossed lines characterized by more intense local pressure. However, they cannot be referred to as a shock train, despite the fact that they possess that form, as they are not strong enough. Upon reaching the right wall, the first pressure waves are reflected, reaching the flame after around 1.4 ms. At this point, they bounce back into the unburned gas or transit through the flame, reaching the burned region. Nonetheless, these acoustic interactions are rather weak and have no noticeable effect on the shape of the flame. Following ignition, the flame front takes on a hemispherical shape that expands briefly; at 0.49 ms, the flame begins to assume a finger shape. During this first stage, it demonstrates free outwards expansion without being affected by the sidewalls. In line with previous research [55], due to the non-slip nature of the boundary conditions, boundary layers form along the walls with the propagation of the flame.

In the second stage, in which the flame has a finger shape, it is substantially elongated along the tube axis, mainly due to the gas expansion confined by the sidewalls of the tube. This was shown by Kurdyumov and Matalon [58] in their examination of flame acceleration in channels that were long, narrow, and open. At the same time, due to boundary layer effects, the flame near the left wall presents an incline and displays an acute angle with the wall, as can be seen at 1.37 ms. There is a change in the flow velocity once the boundary layer begins to take shape, rising from zero near the wall. The flame is stretched by this nonuniform flow, with its various portions entering different background flow environments, causing the flame shape to take on the profile of the flow velocity.

Initially, at around 1.69 ms, the flame contacts the sidewalls near the tube's left corners (not shown), and the sudden loss of flame area, which was an energy source promoting flame expansion, produces pressure waves. As elucidated below in greater detail, a weak rarefaction wave emerges from this interaction between the flame and the wall.

There are small angles between the flame skirt and the sidewalls, whereby the flame evolves until the skirt almost parallels the sidewalls. Then, at 1.95 ms (not shown), the flame skirt touches the sidewalls again, this time reducing the flame surface area more drastically than before. This produces a significantly stronger expansion wave, as illustrated in the schlieren image taken at 1.96 ms. Propagating at the speed of sound, this expansion wave rapidly overtakes the flame front; reaching the flame's leading tip, the expansion causes the flame to suddenly decelerate, and this deceleration is maintained during the third stage, characterized by continued interaction between the flame and the walls. In this third stage, the flame surface area reduction is causing expansion waves to be continuously generated at the sidewalls.

At about 2.72 ms, the flame begins to invert, eventually forming a tulip flame (see 3.05 and 3.31 ms in Figure 2.12). The distortion of the flame begins at around 3.91 ms, following the establishment of a pronounced tulip flame, with secondary cusps forming close to the lips of the original tulip flame (4.14 ms). These secondary cusps travel to the tube's centre, producing a triple tulip flame (see 4.38 ms). Over time, the first DTF vanishes, along with the collapse of the primary cusp of the tulip flame. This collapse process, which produces a comparably strong pressure wave, as visible in the collapse region at 5.81 ms, is elucidated in the following.

Before the first DTF collapses, a second DTF is formed (see, e.g., 5.44 ms). The cusps hereby behave similarly to those of the first DTF. However, before the second DTF vanishes, a third DTF emerges; see 7.03 ms. A series of DTFs emerge, with each one being formed by its predecessor, until the flame's leading tip nears the tube's end. Towards the end of the flame propagation, the flame resumes the classical tulip shape, including small wrinkles across the whole flame front, as exemplified at 9.71 ms. The flame keeps this form until the combustion has finished.

After the formation of the tulip flame, there is vortex motion in the burnt gas, as noticeable in the schlieren images. With the continued evolution of the flame, vortical structures form successively behind the flame front and move opposite to the flame front, creating a street of vortices through the burnt gas. As the schlieren images show, the leading vortex has a mushroom-like structure (e.g., at 7.03 and 8.63 ms). Because of combustion product compression, when the leading front of the flame nears the tube's right-end wall, the leading vortex similarly approaches the left-end wall, as illustrated at 9.71 ms [55].

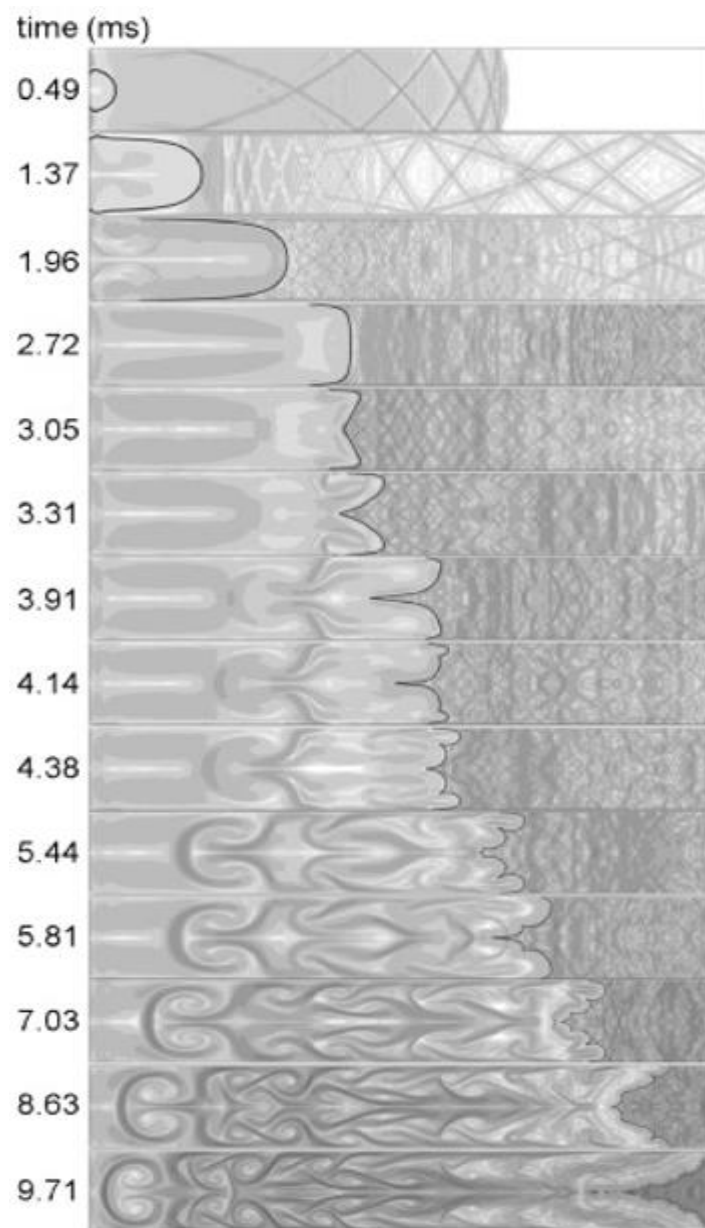


**Figure 2.12: Sequence of numerical schlieren presenting the evolution of premixed stoichiometric hydrogen–air flame. Reproduced from [55]**

However, Markstein attributed more influence to flame structures which he felt had been overlooked by other investigators [59], [60]. He created experiments using n-butane-methane-air mixtures for the fuel. In his research, nitrogen was used to dilute the mixture if propagation speeds were too high. This analysis was divided into two sections:

1. Focus on the cellular structure of the flames that concluded that the limit for a fully developed structure was a mixture of 20% methane to 80% n-butane, whereas no structure was found in the 50% mixture. The mixtures that included methane at levels between 20% and 50% had a non-cellular structure in rich flame and cellular structure in lean flame.

It was a major part of his observations that the difference in flame speed induced differences in flame structure, however, because of the difficulty in stabilising lean flames it was difficult to test the lean mixtures.

2. Focus on the movements of the vibratory flame that found that the frequency, amplitude, wave shape of the pressure records, and flame speed differed in a very complex way during the vibrational movement.

In his final conclusion, it was found that the theoretical and experimental results were in limited agreement. Moreover, theory indicated that excitation of the vibrations was proportional to the burning velocity. In addition, in slow-burning mixtures, amplitudes could be built up to higher values where the flame stayed in regions of the tube favourable to excitation for longer periods of time. Markstein went on to describe two unstable forms of vibratory movement of flame as shown in Figure 2.13.

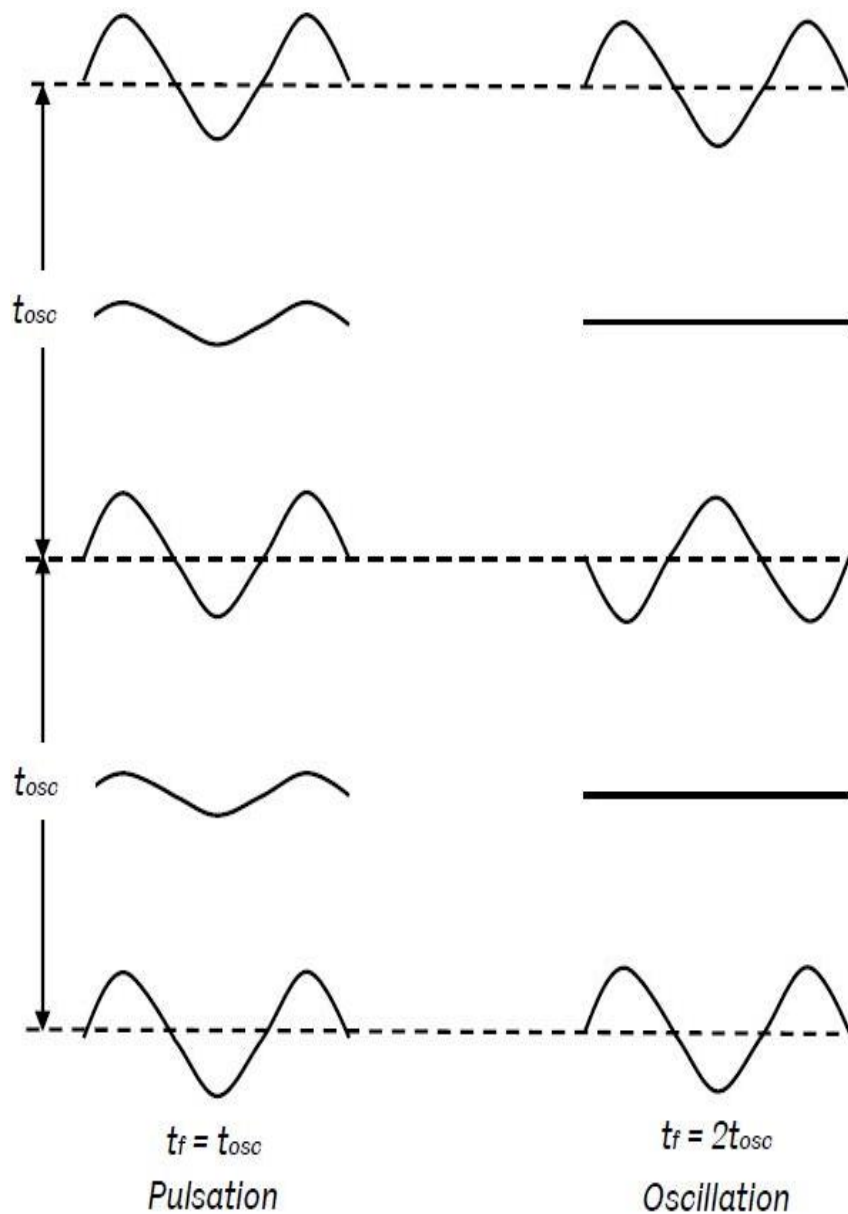


**Figure 2.13: Flame behaviours induced by vibration of flame structure. Reproduced from [7]**

The first mode concerned pulsation and had the same test period as the oscillation but without flame structure inversion, thereby creating a minor difference in the area of the flame. This difference may not have provided the required feedback to satisfy the Rayleigh criterion [61]. The second mode concerned oscillation, with the flames undergoing structural inversion, contributing to a double oscillating cycle of gas oscillation. This inversion made the flame structure shift from a sine wave to a straight line, and increased the possibility for interaction with the acceleration wave via the Rayleigh criterion.

In the case of a single cell, Jost [21] seems to have addressed the difference between pulsation and oscillation of a flame structure within a tube. He highlighted that the average surface area of the flame under pulsation remained unchanged with regard to the steady flame surface, whereas the average area under oscillation was dramatically increased. This was intended to be linked to doubling the time of oscillating flames in Figure 2.13.

Markstein declared that instabilities in the oscillation of flames is heavily influenced by vibration frequencies, finding that the transformation from pulsating flame to oscillating is more easily achieved using low-frequency vibrations, because low velocity amplitudes may result in oscillation instability, whilst triggering unstable oscillations at high frequency vibrations requires high amplitude velocities [7]. The regions of instability for pulsation and oscillation at different dimensionless frequency parameter values  $\Omega$ , Strouhal number (dimensionless number describing the mechanism of an oscillating flow) are shown in Figure 2.14. It was found that the unstable pulsation region was almost independent of the frequency parameter values,  $\Omega$ , and limited to a small dimensionless velocity amplitude,  $W$ . Unlike that of pulsation, the unstable oscillation region was heavily dependent upon the value of the frequency parameter values,  $\Omega$ . Markstein [62]–[63] then used a technique to obtain shadowgraph high-speed motion pictures of the flame structure. The photographs that were taken normal to the axis of the tube were intended to observe the distorted turbulent flame structure. During the early low amplitude of flame propagation, the structure of the cells was found to “fade away and appear periodically”; this in fact has since been observed in a wide range of fuel mixtures. Furthermore, the appearance of these cells did not depend on the existence of a spontaneous cell structure without oscillations.

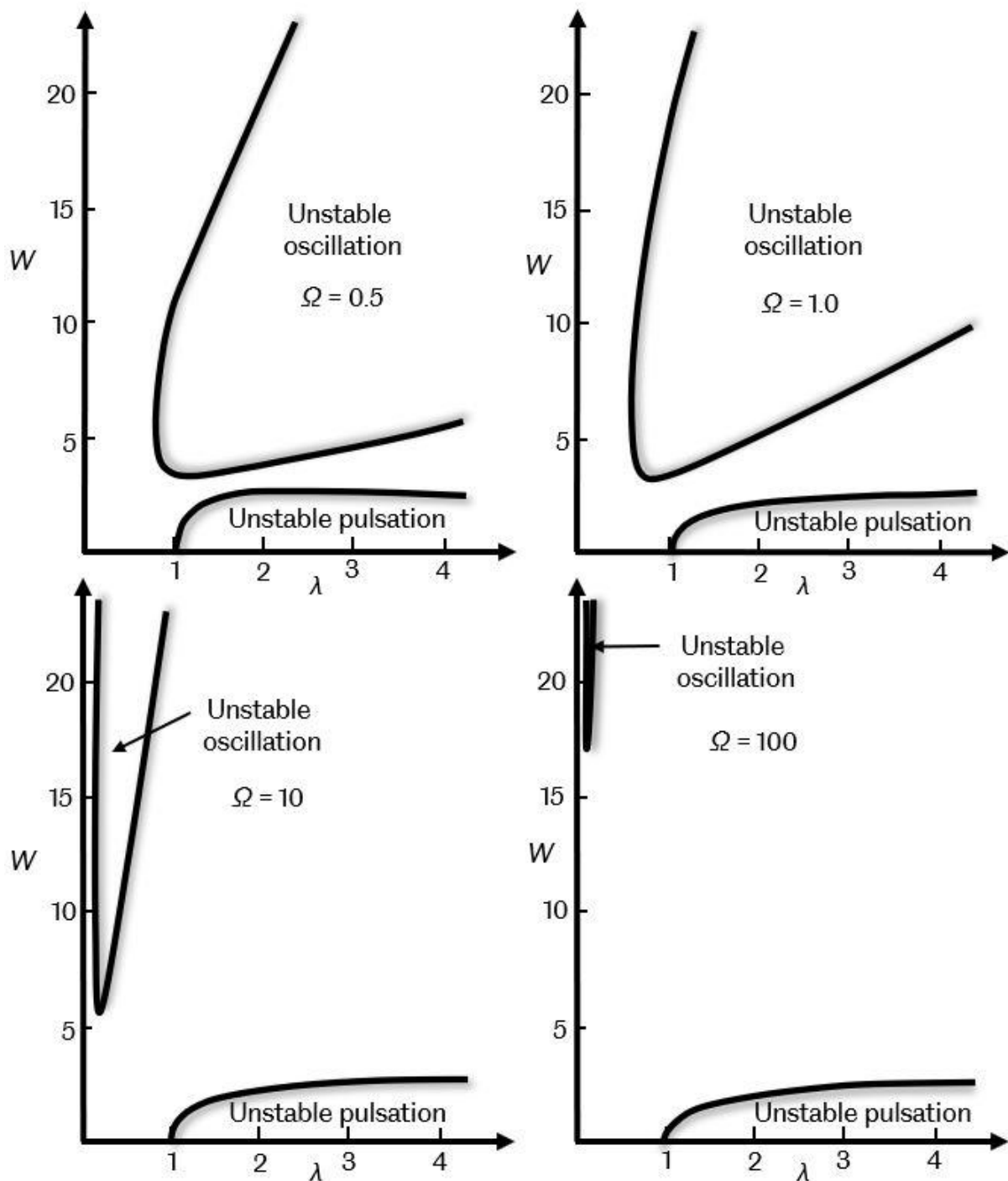


**Figure 2.14: Regions of unstable pulsation and oscillation induced by vibration as a function of different dimensionless parameters: frequency,  $\Omega$ , velocity amplitude,  $W$ , and wavelength,  $\lambda$ . Reproduced from [7]**

Markstein found that, in the unstable pulsation phase, the flame propagation velocity reduces with each pulsation of the flame structure, suggesting that the pressure amplitude is increasing steadily. The transition from pulsation to oscillation depended on the frequency parameter values or Strouhal number,  $\Omega$ , which in turn was dependent upon the characteristic length of a flame,  $L$ , which is today recognised as the Markstein length. This characterises the effect of flame curvature on the flame

speed, and he showed that  $L$  was associated with flame thickness. He further noted that any change to the Strouhal number altered both the dimensionless velocity amplitude range and the dimensionless wavelength at the location of the instability. While Markstein's analysis did not account for the feedback between the pressure pulsations and the flame, in line with Rayleigh's criterion, it did observe phase difference changes in the pressure as well as changes in light intensity between the two modes of instability. However, concerning the pressure reading and flame propagation, it should be noted that, although he measured the pressure at the end of the tube, the flame was situated further along the tube [7].

## **2.4 Effect of tube configuration on instabilities**

Guenoche [6] suggested four possible configurations to investigate the instability of flame propagation in tubes:

- Tubes open at both ends
- Tubes closed at both ends
- Tubes open at the ignition end, closed at the other end
- Tubes closed at the ignition end, open at the other end

These configurations were studied both horizontally and vertically, but more recent studies were carried out on flames that propagated vertically downwards, e.g. Searby [11] and Higuera [64] preferred a flame propagating downwards that stabilised the flame from a body-force instability. In these experiments measurements were performed in tube open at the ignition end, closed at the other end open.

### **2.4.1 Flame propagation in a tube closed at both ends**

Experiments carried out by Ellis [65] into closed tubes of the same diameter, but with different lengths, produced a series of stroboscopic records, and these are shown in Figure 2.15. These revealed that, after ignition, the flame gradually changed, passing from a hemisphere to a shape that was semi-ellipsoid. When the flame then made contact with the side wall, this had the effect of quenching the flame and its area decreased.

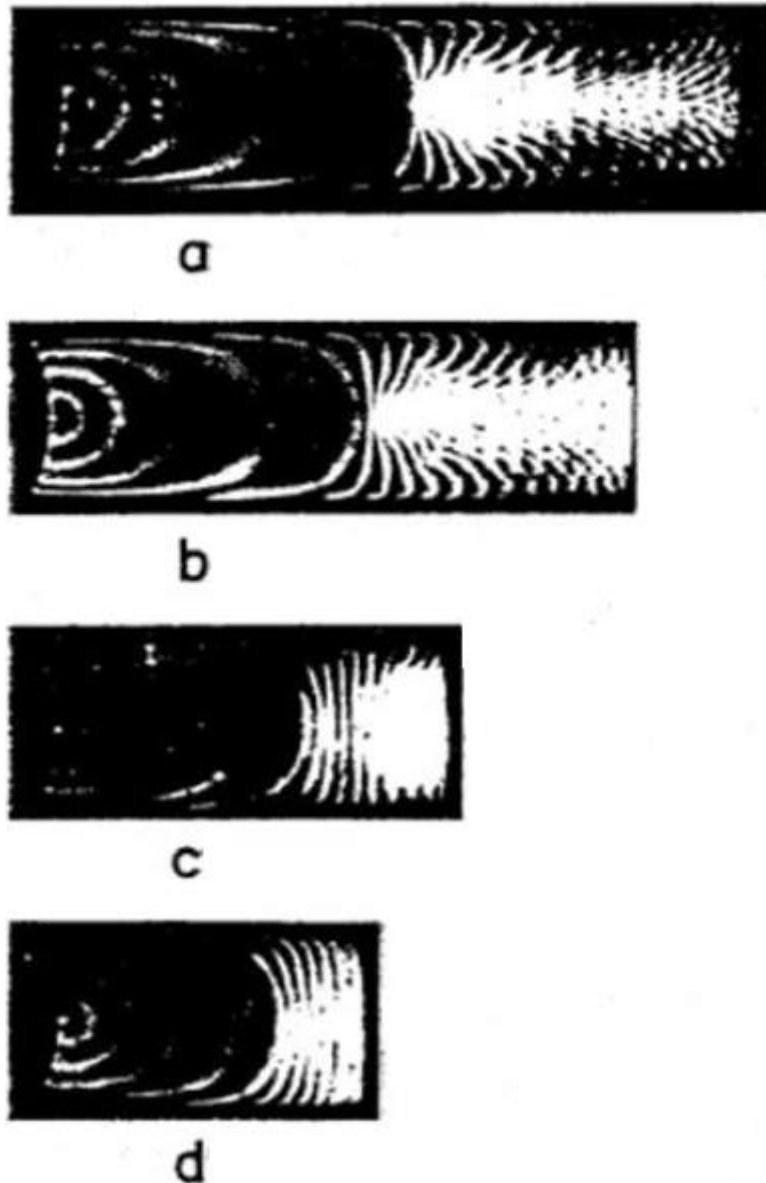


**Figure 2.15: Stroboscopic flame records. Mixture: 10 parts CO + 1 part O<sub>2</sub> saturated with water vapour at 15 °C, tube closed at both ends; diameter 5 cm; length: (a) 19.5 cm (b) 17 cm (c) 12 cm (d) 9.5 cm. Reproduced from [7]**

With the development of the flame surface, the fresh gases' velocity profile progressively changes as the walls start impeding their flow in front of the flame under the continuous expansion of burned gases. Guenoche [6] further offered a description of two-stage propagation within sealed tubes. Firstly, the flame would expand prior to coming into contact with the walls of the tube, and secondly it would be constricted when it reached the walls. In the initial stage, the longer the tube, the longer the flame, and so the flame would have an increased surface area. The surface area of the flame was directly responsible for the flame's speed, which would therefore also rise. In the second stage, concerning the flame that reached the sidewalls, the cylindrical

structure of the flame disappeared, and a decrease in the area of the flame was therefore noted. The rapid drop in the surface area of the flame contributed to a decrease in flame speed. However, this decrease was not seen in the shorter tubes, since the flame did not have time to elongate, and, therefore, it appeared to propagate at an almost constant speed [6]. In the longer tubes, the flame was longer and more rapid changes were detected, contributing to a flame inversion structure, known by some investigators as “tulip” flames [57], [66], [55], [67]. Furthermore, the flame centre accelerated, making the flame convex towards the fresh gas as shown in Figure 2.16.

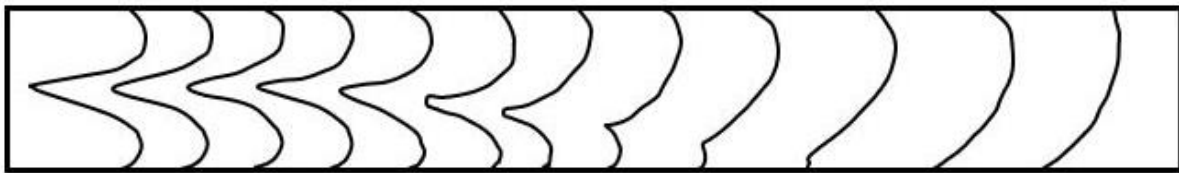


Figure 2.16: Example of flame-shape distortions in a closed tube propagation. Reproduced from [6]

#### 2.4.2 Flame propagation in a tube closed at the ignition end, open at the other end

Guenoche [6] also stated that the first propagation phase was similar to that for the long tube closed at both ends. After the first phase, the propagation was generally different to the phenomenon found in a closed tube, since the fresh gas flow was not impeded. However, the fresh gas expansion resulted in a faster flame making it easier for the flame to become turbulent, leading to an increase in flame area. The flame shape was also prone to distortion, similar to that mentioned in Figure 2.16. According to experiments carried out by Schmidt et al. [46], after the first phase of propagation the flame became indented with a reduction in its propagation velocity. Then the flame centre overtook the edges, similar to that occurring in a closed tube; the propagation velocity increased, which clearly occupied a greater length than in a closed tube, as there was no obstacle to the flow of fresh gas. Under the impact of the reduction of the flame area, the flame again became convex towards the unburned gases and the subsequent thrust reduction of the burned gases.

Additionally, because of the wave system produced within the tube, and finally to a limited extent due to the cooling of the gases, the flame slowed down and became indented again. This process was repeated until the end of the propagation, where an increase was observed in the mean propagation speed. It was later added that this increase in speed was due to turbulence induced by fresh gas expansion and not only from the open end [46]. A flame was also seen to oscillate as a result of flame motion reversal.

### **2.4.3 Flame propagation in a tube open at the ignition end, closed at the other end**

Researchers frequently propagate flames within tubes closed at the far end and open at the ignition end because this is the easiest of the propagation conditions to model. Additionally, because such a configuration offers the longest constant speed propagation this allows for measurement of the flame's laminar burning velocity [6]. It is noted that the oscillatory behaviour is causing the pressure waves to expand across the gaseous medium as a result of expanding disturbance from ignition. This initial disturbance is amplified as a result of the repetition of interactions of pressure disturbances and flame fronts, and it is associated with variations in flame structure. Further studies carried out by Guenoche [6] demonstrated that, as with completely sealed tubes, where flames underwent a decrease in surface area as they reached the side walls, this also happened over a shorter distance than when there was an open end and the burned gases expanded towards it. Because the initial phase was dependent on the size of the ignition source, auxiliary flames that were effective in igniting a complete cross-section simultaneously became important because they minimised the initial perturbation.

Subsequent to this phase, flames propagated for a certain distance with quite uniform movements and constant velocities until the surface was found to vibrate around a mean position. As the gases vibrated this led to a quick reduction in the mean surface region and this in turn decelerated the speed of propagation. Subsequently, still as a result of gas vibration, the surface of the flame was altered to form a cellular structure which accelerated its speed.

The vibration amplitude also increased whilst its frequency became irregular. This amplitude continued and drove the flame to propagate with a mean velocity which reduced rapidly to an almost uniform value.

In conditions where narrow tubes were used, most rich mixtures of hydrocarbons appeared to vibrate, with the exception of methane, hydrogen and acetylene (that will even vibrate with lean mixtures) [68]. Where similar mixtures were used, the amplitude of vibration depended mostly on the tube diameter, so that, for example, a decrease in the diameter caused the vibration to increase slightly. Mixtures with a high burning speed, and particularly when oxygen was the oxidizer, caused flame propagation to have similar features to those occurring in closed tubes, and may also have contributed to the creation of detonation waves.

Coward et al. [69] presented a comparison between tubes that were both cylindrical and square, with regard to vibration, and found that the cylindrical tube vibrated more readily than the square tube. The square tube was also found to produce a slow humming sound, but which was not effective enough to alter the propagating flame's speed or shape. They also added that the tube material was an important factor for damping the vibration. For example, a rubber tube, as opposed to glass, caused instability as it was found to release minimal sound, indicating low amplitude oscillations.

Experimentation by Searby [11] found four particular forms of unstable behaviours from premixed flame fronts that propagate downwards within a tube from its opening towards its closed end. Flame behaviour in these instances is dependent on the rate at which the premixed flame burns and behaviours were as follows:

- Less than 16 cm/s: a curved flame is produced and its propagation to the end of the tube does not produce any sound;
- Between 16 cm/s and 25 cm/s: the propagation of the flame creates sound in the upper section of the tube, followed by primary acoustic instability at the bottom half;
- Over 25 cm/s: there is a primary acoustic instability followed by a violent secondary acoustic instability as the flame moves along the tube;

- Finally, with faster flames, an extremely significant acoustic level is achieved with the violent secondary acoustic instability, and this separates into non-continuous turbulent waves with the levels of sound dropping as illustrated in Figure 2.17.

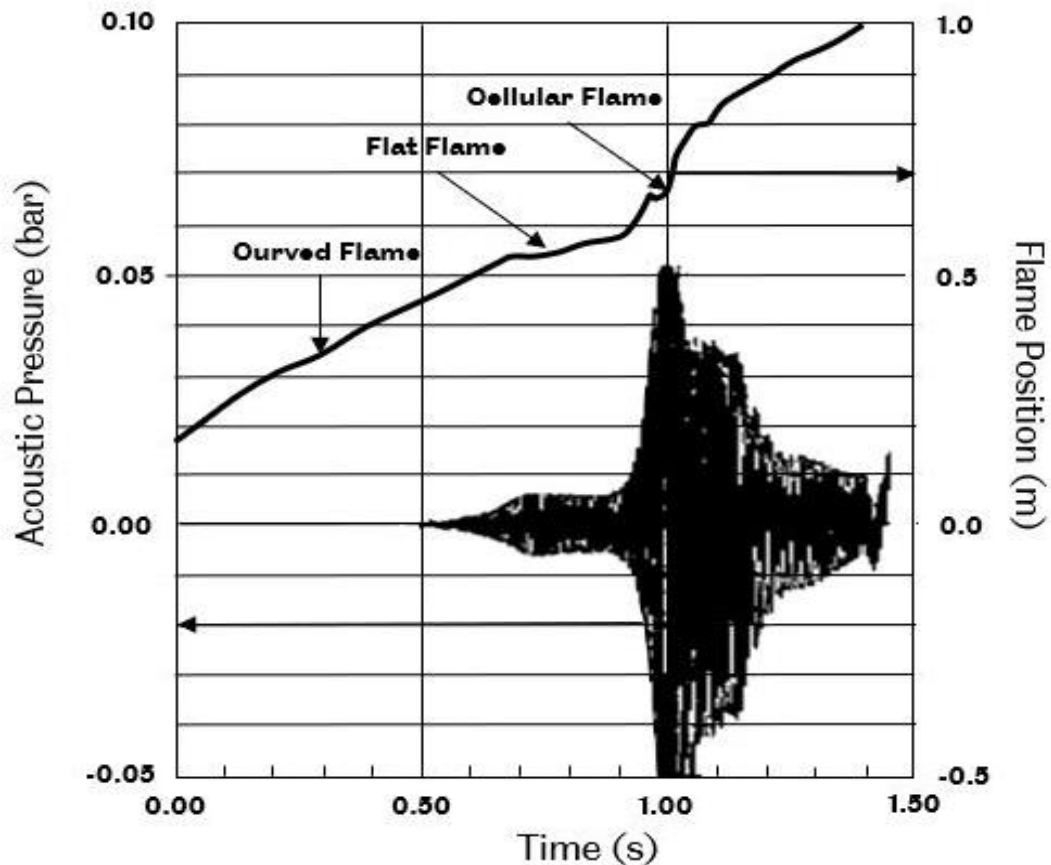
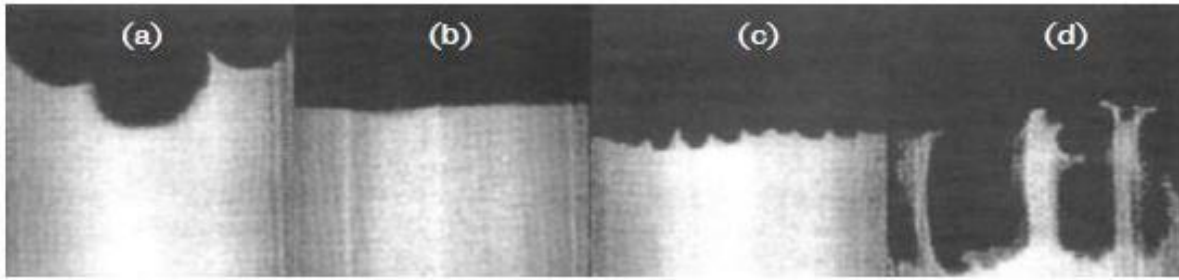


Figure 2.17: Flame position and acoustic pressure of a lean propane-air mixture. Reproduced from [11]

In Figure 2.17, the curved flame results can be seen under extremely minimal acoustic pressures. As the pressure increases, at approximately  $\sim 0.6$  seconds, there is a slightly distorted curved flame as illustrated in Figure 2.18(a). Figure 2.18(b) shows a flat flame shape resulting from primary instability saturation of  $\sim \pm 0.007$  bar at  $\sim 0.7$  seconds. In Figure 2.18(c), it can be seen that cellular structures began to appear on the flat flame surface at the beginning of secondary instability at  $\sim 0.9$  seconds. Finally, these cellular structures caused a rapid increase in oscillation amplitude as shown in Figure 2.18(d), which began decreasing at  $\sim 1.00$  second after hitting a maximum acoustic pressure of  $\sim \pm 0.05$  bar.



**Figure 2.18: High-speed tomography of premixed flames in open-ended ignition at different stages: (a) curved flame at onset of primary instability, (b) flat flame during saturation of primary instability, (c) cellular structure at onset of secondary instability, (d) high amplitude cells during secondary instability development. Reproduced from [70] based on [11]**

#### **2.4.4 Flame propagation in a tube open at both ends**

Guenoche [6] reported that the first phase was similar to that observed in a tube closed at the non-ignition end. The burned gases set the fresh gases in motion which accelerated the flame and caused a higher flame propagation velocity than when closed at the non-ignition end. Furthermore, over a length of  $1/3$  to  $1/2$  the tube length, the flame vibration began, allowing the initially curved flame to flatten and decrease the propagation velocity. Then, under the influence of the amplitude of the gas mass, the velocity of propagation increased, as was discovered by Mason and Wheeler [4]. An experimental study on the propagation of propane-air mixture, in rich conditions, was performed by Yang et al. [71]. They found that self-induced pressure fluctuations resulted in flame oscillations with a maximum amplitude of  $\pm 10$  mm at 220 Hz recorded frequency, which decreased as they travelled towards the end of the tube. It was also observed that the flame propagation was the same as in a tube open at the ignition end, except without a flat flame. In the case of low fluctuations, they were found to travel down the tube with a caterpillar-like movement, where the flame tail stayed anchored and the front of the flame moved forward. Subsequently the flame tail moved forward and the front became stationary. With a significant build-up of oscillation, inversion occurred to the flame shape which was found to be unburned reactant tongues positioned within the product which caused the flame to accelerate rapidly into unburned gas. This inverted shape has similarities with those already mentioned in Figure 2.16 by Guenoche [6].

## 2.5 Experimental and theoretical studies on primary and secondary instabilities in downward propagating flames

Here the primary instability occurs when the flame front's hydrodynamic (D-L) instability is suppressed due to the flame-acoustic interactions, thereby generating sustained pressure oscillations. This in turn produces a secondary instability, along with a parametric instability, which leads to significantly higher growth rates. During parametric instability, the flame front structures oscillate with half the frequency of the acoustic oscillation, as with Faraday instability. Evidence of primary instability is observed in moderately strong mixtures, primary instability is followed by secondary instability in stronger mixtures, whose strength is assessed based on the mixture's laminar burning velocity [3]. Flames propagating in a downward direction in an annulus between two cylinders have been found to show similar behaviour [72]–[75]. Such a downward flame propagation is used here to examine the onset of primary instability via laser irradiation [76]–[78] as well as the impact of the Lewis number,  $Le$  [79]–[81]. Furthermore, the geometrical parameters' effects on thermoacoustic instability are also elucidated [82]. How the geometric parameters, namely length and diameter, affect the thermoacoustic instability in combustion tubes has also been experimentally and analytically examined. Changing the laminar burning velocity,  $U_L$  of the mixture is known to trigger various flame responses. Specifically, an increase in  $U_L$  leads to an increase in flame instability. Furthermore, with the increasing length of the tube, there is a decrease in the minimum  $U_L$  at which instability can be observed, while the flame's instability decreases with increased tube diameter. The effects of  $U_L$  and tube length and diameter have been studied based on the theoretical growth rates calculated via the velocity coupling mechanism. The findings reveal that the velocity coupling mechanism correctly reflects the experimental results in terms of changes to the burning velocity and geometric parameters. Thus, for downward propagating flames in tubes, when cellular flames form, the dominant mechanism dictating the onset of instability is the modulation of the area of the cellular flame through acoustic acceleration [82].

Secondary instability in the context of downward propagating flames is analytically and experimentally assessed here for two different values of  $Le$ . Parametric instability with higher harmonics, which was first noted for flames from gaseous fuel, with a lower  $Le$  leading to stronger instability, is found to cause increased growth rates, producing secondary acoustic instability under pressure oscillations with a high amplitude. A further increase in  $U_L$  leads to secondary instability with higher acoustic modes. Using a velocity coupling mechanism, it is possible to estimate secondary thermoacoustic instability growth rates for flames in a combustion tube [3].

Experiments have shown that a critical diameter exists for the case of secondary instability in downward propagating flames at a minimum  $U_L$ . For the three mixtures used here, this critical diameter is around 10 mm. Surprisingly, unlike other aspects of thermoacoustic instability, such as the growth rate, the  $Le$  of the mixtures appears to have little influence on the critical diameter. Nonetheless, the  $U_L$  of the mixture at which instability is introduced for any given diameter is greater for mixtures with higher  $Le$ . Close to this critical diameter, the primary acoustic instability growth rate reaches a maximum, whereas there is an increase in the secondary instability growth rate and the maximum pressure fluctuation amplitude with increasing diameter. These phenomena and their mechanisms are clarified in this study [83]. An examination of thermoacoustic instability in the context of flames propagating downward through a narrow tube with an 8 mm inner diameter would identify new flame regimes that are specific to such narrow tubes. For instance, the flame's extinction was observed shortly after secondary acoustic instability has occurred. Using a fundamental mode at an  $U_L$  higher than 22.5 cm/s, both the secondary acoustic and parametric instabilities of the flame front can be suppressed. It is further clarified that parametric instability depends on the tube diameter,  $Le$ ,  $U_L$  and frequency [84].

The influence of  $Le$  on the transition to “complete instability”, i.e. when there is no flat flame, is investigated both theoretically and experimentally for downward propagating flames with thermoacoustic instability. The lowest  $U_L$  of the mixture at which complete instability occurs is called the “critical  $U_L$ ”. Flames with a higher  $Le$  have a higher critical  $U_L$  for any given fuel. Theoretical estimations have successfully described the influence of  $Le$ . It is possible to achieve an improved quantitative agreement between the

theoretical and experimental results through the application of a correction factor that is a function of  $\beta$  and  $Le$  and corrects  $Ma$ . By measuring the “critical  $U_L$ ”, it is also possible to estimate  $Ma$  [85].

Specifically, both one-step [86], [87] and two-step chemistry [88] are used to explore the theory of the pressure coupling mechanism, while the influence of pressure is numerically [89] and experimentally [90] investigated for premixed flames. Chemical mechanisms are drawn upon to explore the details of premixed flame-acoustics coupling [91], [92]. Based on a velocity-coupling mechanism that incorporates an artificial modification appropriate for non-linear cells [8], previous experiments have measured primary acoustic instability growth rates that have been matched within a factor of two with the theoretical predictions.

Parametric instability has been explored theoretically through laminar flame theory, and experimentally using a stabilised flame [10]. It was possible to predict the flame cells' wavenumber at the parametric instability onset. An analytical solution has been derived for parametric instability under the limitations of high-frequency acoustic oscillation [93]. Studies have examined flame front parametric instability in  $H_2$ -air mixtures, indicating that the parametric instability growth rate on the flame front is not the same as the acoustic pressure amplitude growth rate observed during secondary acoustic instability in experiments with downward propagating flames due to parametric instability [94], [95]. The growth rate measurement was performed on propagating flames inside a Taylor-Couette combustor [73]. During experiments with downward propagating flames, secondary instability stems from the parametric instability of the flame front as it propagates in the acoustic field. Hereby, once the acoustic fluctuations achieve a critical amplitude, corrugated structures with a certain wavelength form along the flame front. In the event that the tube diameter is close to this critical wavelength, the acoustic parametric instability approaches the limit of its length scale, potentially leading to interesting phenomena. At this scale, the heat loss from the flame to the walls of the tube can also play a role. While thermoacoustic instability has been experimentally investigated in contexts in which neither acoustic nor flame instabilities were influenced by heat loss, little attention has been paid to thermoacoustic instability at the scale where the heat loss from the propagating

flames may become a factor [84]. Such an examination may also offer a significant practical contribution in that it would enhance the knowledge of flame instability in very small combustion devices; a field that has experienced rapid advances thanks to the demand for portable small-scale generators [96], [97]. Heat losses and their effects are significant at a small scale, and various forms of flame instability can be witnessed in both micro and mesoscale combustion processes [96]. Recent research using very lean H<sub>2</sub>-air mixtures has revealed interesting transitions in the flame shape stemming from heat loss and the subsequent propagation in narrow-gap Hele-Shaw cells [98].

It is well-established that heat losses lead to the extinction of flames at small scales. Furthermore, they can also alter flat flames' stability limits, and a heat-loss-driven pulsating instability close to extinction has been predicted [99]. This pulsating instability inevitably has a high  $Le$ , as is found for lean n-butane-oxygen-helium ( $Le \approx 4.0$ ) flames that occur near the lean flammability limit [100]. Similarly, heat losses reduce the critical  $Le$  regarding the observation of pulsating instability, as is revealed for  $Le \approx 1.9$  flames from lean propane-air mixtures [100], [80]. A recent study reported thermoacoustic instability in flames propagating across the small space between plates, i.e. Hele-Shaw cells. While thermoacoustic instability cannot be produced with very narrow spacing, parametric instability is produced for spacings of around 8 to 10 mm [101]. In parametric instability, the dimensions-to-critical-wavelength ratio is important [84].

Theoretical models can be used to predict the corrugated structures' wavenumbers and acoustic velocity amplitude [10], [85]. During parametric instability, the flames' propagation speed and pressure oscillations' amplitude are significantly greater than during primary acoustic instability. Lastly, the cells' amplitude increases, eventually causing a regime of turbulent combustion. While there has been much experimental research on parametric instability in propagating flames, such an instability has also been found in burner-stabilised premixed flames within tubes [10]. If the existing oscillations' amplitudes are sufficiently high for parametric instability to occur, they can, in principle, also emerge in the combustion process of gas turbines, thereby generating very high amplitude oscillations.

The instabilities experimentally revealed by Searby [11] are also observed in methane-air flames that propagate in a Taylor–Couette burner annulus [72], [73]. Meanwhile, Dubey et al. [82], examining the influence of geometric parameters on thermoacoustic instabilities analytically and experimentally, show that the dominant mechanism is velocity coupling. The velocity coupling mechanism relates to changes in the flame area that modulate the released heat and, thus, influence thermoacoustic instability.

Theoretically determining a transfer function for the velocity coupling mechanism, Pelce and Rochwerger [102] used it to establish the thermoacoustic instability growth rate when it is due to the acoustic acceleration of a weak cellular flame front (where  $ak \ll 1$ ,  $a$  is the amplitude,  $k$  is the wavenumber). Subsequently, the findings of Clanet et al. [8], who used a higher aspect ratio for the coupling parameters,  $ak$ , advanced the estimation for realistic flames; are in line with those for propane-air flames. By controlling the structure of the flame, it would be possible to investigate the effect of velocity coupling more accurately. This could be achieved by changing the fuel mixture and the geometry of the tube [82]. It would also be possible by artificially altering the flame shape through laser beam irradiation, such as in prior research which used a CO<sub>2</sub> laser. Although the laser energy is absorbed by the unburnt fuel, this is insignificant compared to the flame's released energy. Thus, specific deformed flame structures can be produced through laser irradiation while leaving the mixture's combustion properties mostly unaffected. This new experimental method to examine how the flame structure interacts with the acoustic field has already been used to examine the onset of primary acoustic instability [78], [76], the impact of  $Le$  on thermoacoustic instability [81], [80], and the parametric instability generation mechanism in flames irradiated by lasers [77], [54]. Geometric parameters determine instability in combustion tubes. Clavin et al. [86] were among the first to analytically show the effect of geometric parameters using a pressure coupling mechanism, thereby proposing that wider and shorter tubes would be less stable. However, experiments have shown that, unlike with pressure coupling predictions, longer (300-700 mm) and narrower (30-70 mm) tubes are less stable [82]. The authors also found that the mechanism of velocity coupling can clarify these results [82]. Searby and Rochwerger's model was used to study the parametric instability of the flame front in H<sub>2</sub>-air mixtures, albeit without conducting any quantitative comparison with the experiments [95].

As such, there is a need for more work to test and verify the quantitative agreements between the theoretical and experimental findings on flat flame stability in acoustic fields for a variety of mixtures and acoustic fields. The prior research only compared the experiments with the theory using the acoustic velocity and the wavenumbers of the flame structure at the onset of parametric instability [73], [10].

## **2.6 Fuel composition**

### **2.6.1 Effect of fuel composition on instability**

In order to understand the impact of fuel composition on every combustion system, it must be appreciated that it is an essential parameter in every such study. The change in the composition of the air-fuel blend modifies its behaviour during propagation, including flame propagation speed and possible instabilities. For decades, several researchers have conducted varying fuel composition tests to analyse instabilities in combustion rigs. Kerampran et al. [103] for example, performed an instability analysis using propane, ethylene and acetylene as the basic fuel in a horizontal flame tube with variable lengths. For each reactive mixture, the equivalence ratio was different to achieve mixtures with a good luminosity and increased laminar burning speed, ranging from 0.38 to 1.38 m/s. The product of the multiplication between expansion ratio and the laminar burning velocity was the laminar spatial velocity, as shown in Table 2.1.

According to Kerampran et al. [103], the oscillating propagation observed is highly dependent on the two parameters of tube length and gaseous composition. For low laminar spatial velocities, the flame is sensitive to acoustic perturbation, making it more likely to experience oscillation when propagating. Furthermore, the average velocity of the flame does not increase in line with tube length. However, flames that have high laminar spatial velocity seem to be more resilient against acoustic perturbations, as demonstrated by non-oscillating propagation with slightly reduced speeds. Here, the average velocity of the flame does rise in line with tube length. The authors surmised that the flame behaviour was a product of the competition between the propagating flame and the oscillating column of gas within the tube.

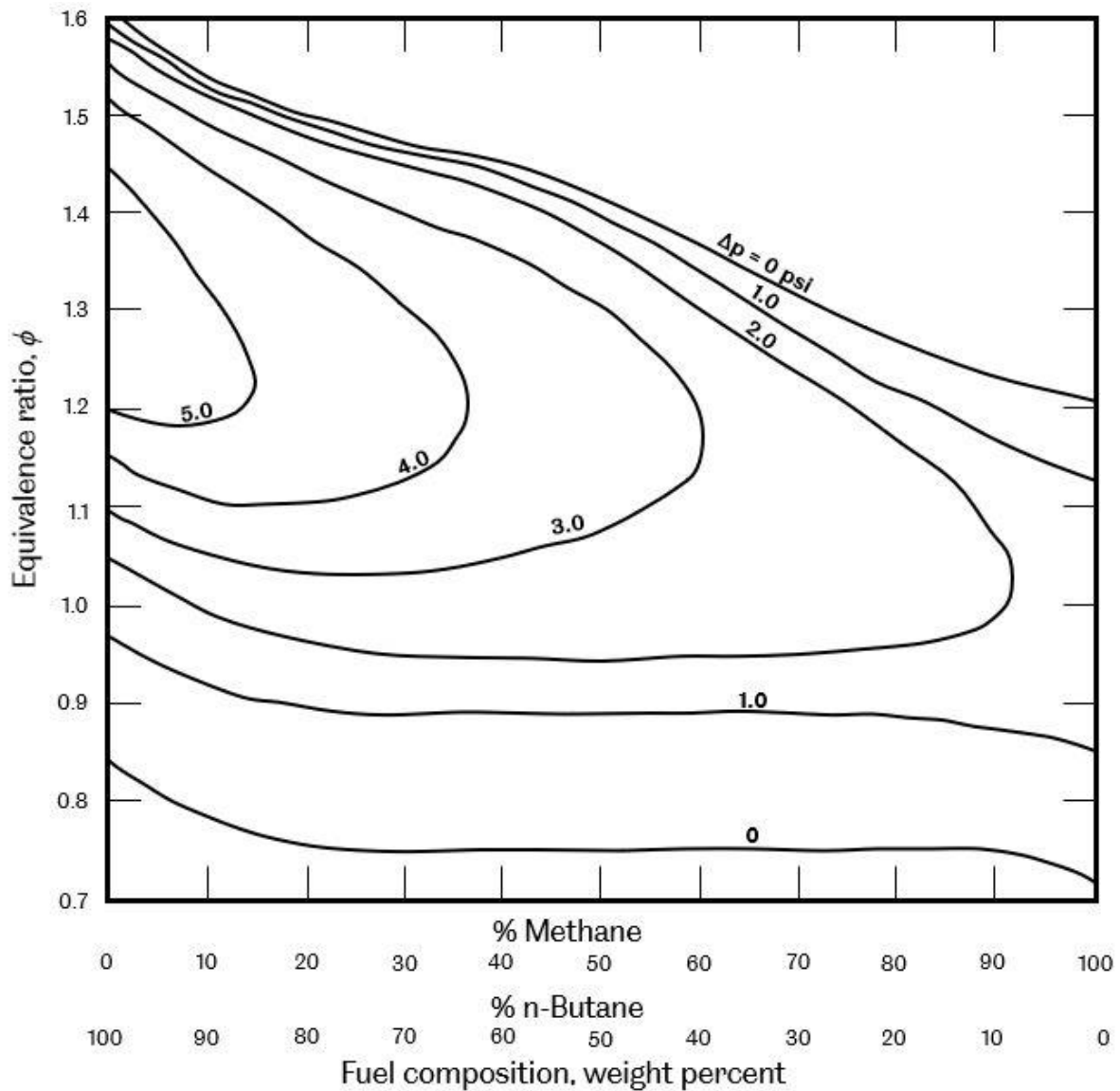
**Table 2.1: Reactive mixtures' laminar flame velocity, expansion ratio, and laminar spatial velocity. Reproduced from [103]**

<b>Reactive Mixture</b>	<b>Equivalence ratio, <math>\phi</math></b>	<b>Laminar burning velocity, <math>U_L(\text{ms}^{-1})</math></b>	<b>Expansion ratio, <math>\alpha</math></b>	<b>Laminar spatial velocity, <math>V</math> (<math>\text{ms}^{-1}</math>)</b>
<b>Propane-air</b>	1.0	0.38	8.0	3.0
	1.2	0.39	8.0	3.1
	1.4	0.24	7.8	1.9
<b>Ethylene-air</b>	1.0	0.64	8.2	5.3
<b>Acetylene-air</b>	0.6	0.65	6.6	4.3
	0.8	1.08	7.9	8.5
	1.0	1.38	8.5	11.7

Markstein and Somers [60] performed experiments using methane and n-butane mixtures in vertical tubes with lengths of 2 and 4 feet, both being 9.15 cm in diameter. They investigated the vibratory propagation by adding methane 15% by weight increment to n-butane. Furthermore, the addition of nitrogen helped to reduce the burning velocity and caused the flames to propagate steadily at the front end of the tube. This technique was suitable for rich flame in order to record the transition to vibratory flame movement, but failed to work effectively with a lean flame since the flame was difficult to stabilise.

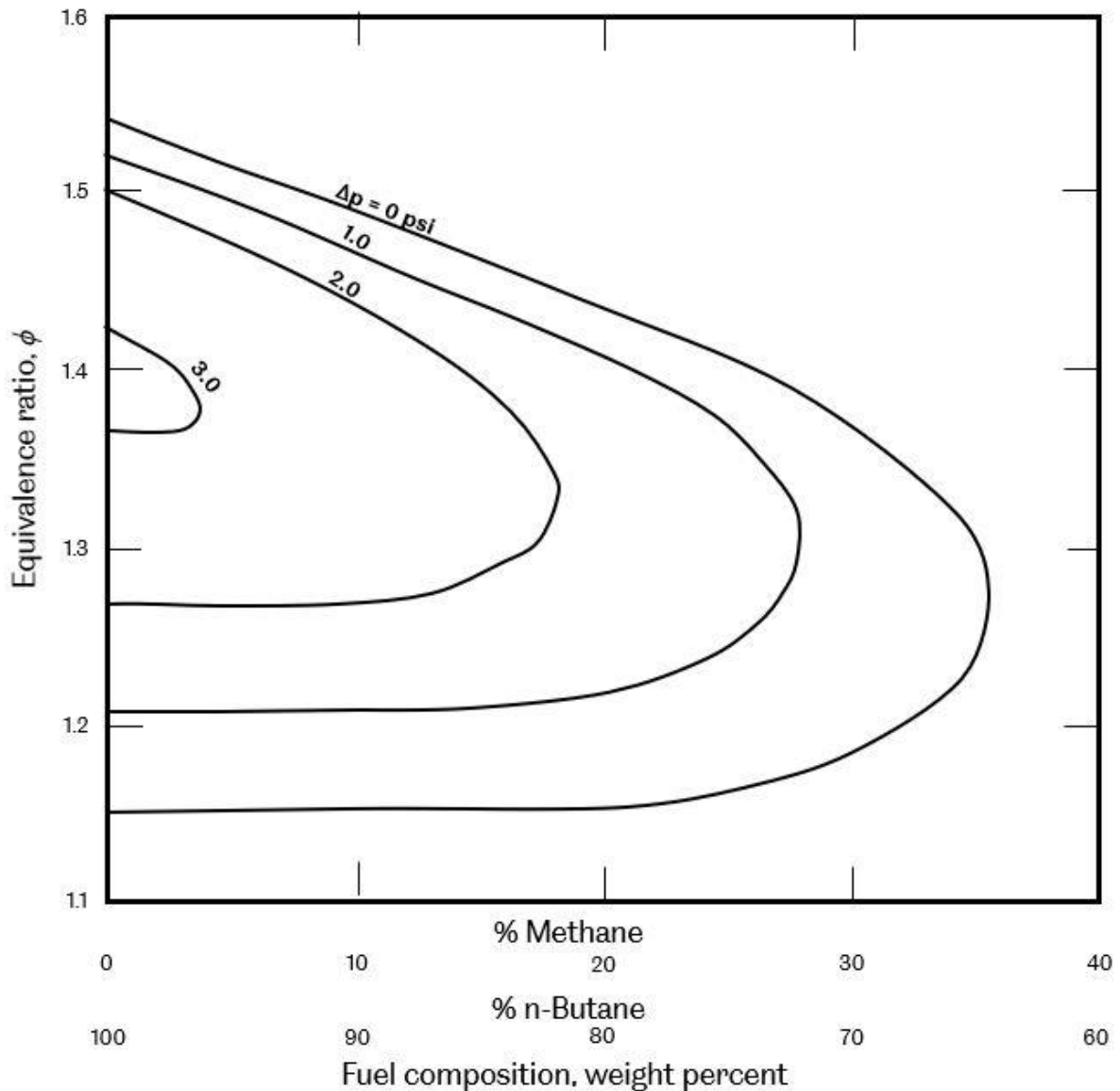
Cellular structures were shown to disappear as the fuel mixture rises above 50% methane. In this case, after the cell structure was formed, the flame developed a complicated vibratory movement that was described as being “beyond the Paper's reach”. The team only analysed the maximum pressure peak-to-peak amplitudes and flame speed during uniform movement.

Figure 2.19 displays these amplitudes of pressure which were seen to oscillate at the fundamental frequency (~270 Hz), occurring in most 2-foot tube mixtures. Based on the contour, the maximum peak pressure amplitudes (5 psi) were formed by the use of pure rich n-butane. These amplitudes were gradually lowered to 1 psi as the concentration of methane increased towards lean pure methane.



**Figure 2.19: Maximum peak-to-peak pressure amplitudes for n-butane-methane-air mixtures. Fundamental mode, 2 foot tube: Reproduced from [60]**

The next stage of the research used an increased tube length of 4 feet. Here it was noticed that the fundamental mode of the tube was high, yet erratic, so that, unlike the first harmonic, it was hard to correlate with the equivalence ratio of the mixtures. Using the increased tube length, the first harmonic was systemically excited with the equivalence ratio, but only for mixtures varying from  $\phi = 1.2-1.5$ , and n-butane weight percentage between  $\sim 70-100\%$  as shown in Figure 2.20. Markstein and Somers [60] observed that the first harmonic excitation, when using the 4 foot tube, was due to the cellular structures. This was considered to be in agreement with Behrens' [68] results, which associated vibration excitation with flame structure but did not show the frequency of excitation.



**Figure 2.20: Maximum peak-to-peak pressure amplitudes for n-butane-methane-air mixtures. Fundamental mode, 4 foot tube. Reproduced from [60]**

Mandilas et al. [104] performed a study on the impact of the addition of hydrogen to methane and iso-octane, in both laminar and turbulent conditions, using spherical bombs. Methane and iso-octane mixtures increased in laminar burning speeds under laminar conditions, with the exception of rich methane mixtures over  $\phi = 1.2$ . They also observed that the addition of hydrogen contributed to earlier laminar flame instabilities. In the case of turbulent conditions, for both methane and iso-octane with hydrogen added, the turbulent burning velocity at the lean limit was nearly doubled. The impact of adding hydrogen became reduced with an increase in the equivalence ratio until “no change” was observed in the turbulent burning velocity at the rich ignition limit for methane and the sooting limit for iso-octane.

In order to systematically research the impact of hydrogen addition, it must be methodically varied together with the equivalence ratio in order to provide a valuable insight into the results. The following sections address the effects of both the equivalence ratio and hydrogen addition.

### 2.6.2 Equivalence ratio

Alternative fuels consisting of a combination of hydrocarbons and hydrogen have become widely used because they produce fewer emissions and lead to improved performance [105]. However, thought has to be given to the air fuel ratio when using this fuel. Here the equivalence ratio was used which compares the ratio of the actual fuel to oxidiser ratio to the stoichiometric case. If this ratio is equal to one ( $\phi = 1$ ; fuel and air are equal), the combustion is stoichiometric. If not, it is either rich ( $\phi > 1$ ; excess of fuel) or lean ( $\phi < 1$ ; excess of air). Since the hydrocarbon-air mixture that is enriched with hydrogen has two fuels and one oxidiser, the system needs two parameters to represent its composition, which are fuel-oxidiser ratio and the amount of hydrogen added. The overall equivalence ratio and the mole fraction of hydrogen in the fuel mixture were used by most previous researchers, respectively defined as:

$$\phi = \frac{C_F/C_A}{(C_F/C_A)_{st}}$$

Equation 2.8

$$X_H = \frac{C_H}{C_H + C_F}$$

Equation 2.9

where,

$C_F$  – Mole concentration of fuel, (mol)

$C_A$  – Mole concentration of air, (mol)

$C_H$  – Mole concentration of hydrogen, (mol)

$X_H$  – Mole fraction of hydrogen in the fuel mixture

The subscript *st* designates the mole concentrations at the stoichiometric condition.

If the mole fraction of fuel, hydrogen and air are respectively  $C_F$ ,  $C_H$ , and  $C_A$ , with

$$C_F + C_H + C_A = 1.$$

**Equation 2.10**

The equations [12] below were used to determine the composition parameters for the mixture.

$$\phi_F = \frac{C_F/[C_A - C_H/(C_H/C_A)_{st}]}{(C_F/C_A)_{st}}$$

**Equation 2.11**

$$R_H = \frac{C_H + [C_H/(C_H/C_A)_{st}]}{C_F + (C_A - C_H/(C_H/C_A)_{st})}$$

**Equation 2.12**

A number of researchers have examined the correlation between laminar burning velocity and equivalence ratios in fuel mixtures. These researchers found a variety of laminar burning velocity values depending upon their experimental methodology. Nevertheless, taken overall, the experiments do illustrate a trend which forms a bell-shaped curve: maximum velocity at the top of the curve is at equivalence ratios approximately 1.0–1.1, and it drops when the mixture becomes more rich or more lean.

A compilation of laminar burning velocities for methane from various studies is shown in Figure 2.21. Various methodologies produced a variety of values for laminar burning velocity. Gu [106] employed a constant volume spherical vessel, Edmondson [107] employed the Bunsen burner method, and Law [108] employed the counter-flow method.

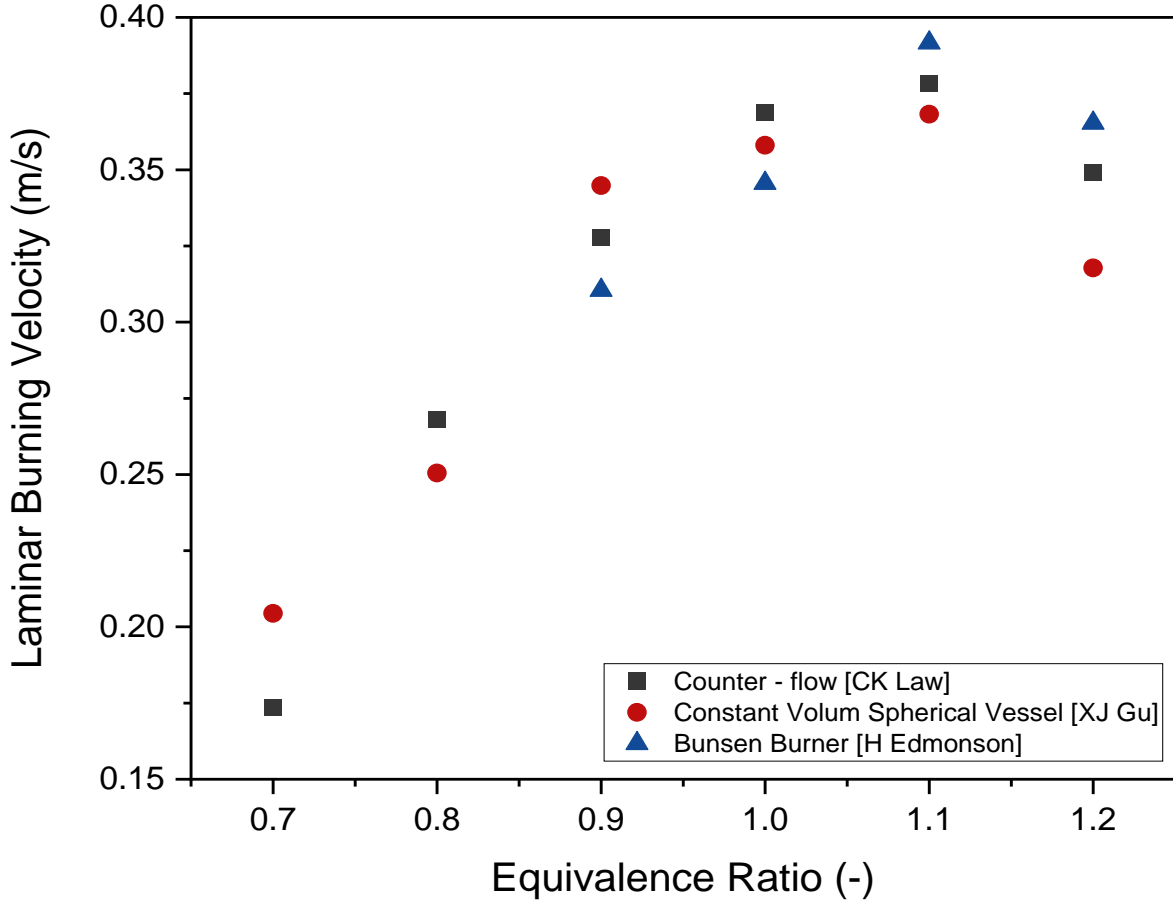


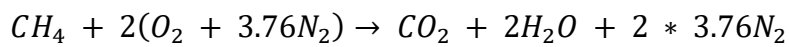
Figure 2.21: Set of laminar burning velocity of methane

Alternatively, Bradley et al. [109] defined an alternative way of determining the fuel composition, using a predetermined equivalence ratio and mole fractions of the combined fuels.  $\bar{x}_{Fi}$  and  $\bar{x}_{Fj}$  are the mole fractions determined based on the total fuel, i.e, for a 20% fuel  $j$  mixture,  $\bar{x}_{Fi} = 0.8$  and  $\bar{x}_{Fj} = 0.2$ . The stoichiometric air-fuel ratios for fuel  $i$  and  $j$ ,  $a_{si}$  and  $a_{sj}$  are 2.387 for hydrogen and 9.547 for methane. The mole fraction of air-fuel mixture,  $\bar{x}_i$  and  $\bar{x}_j$ , will be calculated using the equation:

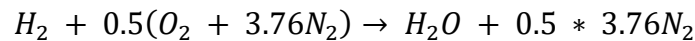
$$\bar{x}_{Fi} = \frac{\left(\frac{\phi}{\phi + a_{si}}\right) \bar{x}_i}{\left[\left(\frac{\phi}{\phi + a_{si}}\right) \bar{x}_i + \left(\frac{\phi}{\phi + a_{sj}}\right) \bar{x}_j\right]}$$

Equation 2.13

The  $R_H$  method was selected for the addition of hydrogen in all equivalence ratios in the present analysis. The key advantage of this method is that the hydrogen amount is independent of the main fuel and equivalence ratio. For example, for an  $R_H = 0.2$  addition to a rig with 1163 ml volume, the amount of hydrogen required to be added would be 57 ml for any equivalence ratio of any fuel. This method also has the advantage of facilitating the comparison of the hydrogen addition effect between two different fuels. Another method that was used in this research was the volumetric method. For the stoichiometric methane-air and hydrogen-air mixture combustion, the chemical formulas were as follows [110]:

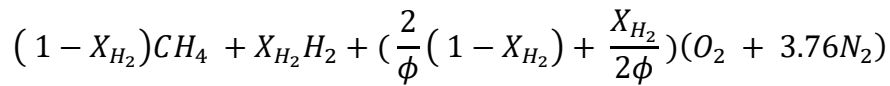


**Equation 2.14**



**Equation 2.15**

To find the mole fraction for methane, hydrogen and air, the mixture can be expressed as:



**Equation 2.16**

Table 2.2 presents a comparison of the three approaches for the mixture of methane-hydrogen, varying equivalence ratio from 0.8-1.5. Regardless of the change in the equivalence ratio, the hydrogen mole fraction was found to be constant in the  $R_H$  method compared with the other methods.

**Table 2.2: The range of hydrogen mole fractions for  $R_H$  method, Bradley method, and volumetric method**

Hydrogen Addition	The range of hydrogen mole fractions		
	$R_H$ Method	Bradley Method	Volumetric Method
0	0	0	0
0.1	0.027	0.033-0.040	0.008-0.015
0.2	0.049	0.071-0.081	0.018-0.031
0.3	0.068	0.120-0.131	0.030-0.050
0.4	0.085	0.170-0.190	0.042-0.073

### 2.6.3 Background of hydrocarbons and hydrogen fuel blends

Combustion is one of the most important sources of energy around the world, providing a significant portion of power. Approximately 80% of energy demand is met by combustion, which means that the world today is heavily dependent on combustion of fossil fuels [111]. Greenhouse gases and carbon emissions produced by the burning of fossil fuels have become severe environmental issues. Thus, more attention is now being paid to alternative fuels, because they provide cleaner and more efficient combustion. Natural gas (of which methane is the major component), which is considered to be one of the most suitable and promising alternative fuels for combustion, has received significant research attention. Hydrogen is also proposed as another alternative fuel, due to its high burn rate during combustion, an absence of carbon (which generates greenhouse gases), and its availability. Methane and hydrogen have both demonstrated that they have the potential to reduce emissions and are more environmentally friendly. However, there are disadvantages to the use of both natural gas and hydrogen. Concerning the use of pure natural gas, the main issues are its low thermal efficiency, its high cycle-to-cycle variation, the lack of lean burn resulting from its slow-burning velocity, and the limitations of its flammability limit. The storage and transportation of hydrogen as a liquid are problematic due to the high-energy cost of liquefaction and a low boiling point [112], [113]. Consequently, using a combination of these two fuels for combustion, i.e. methane with the addition of hydrogen, is considered to be a good way of compensating for the inefficiencies of the two individual fuels [105].

There have been attempts to reduce emissions by adding hydrogen in internal combustion engines [114], [115], however, experimental results have found that both carbon monoxide levels and the number of unburned hydrocarbons could be reduced by adding hydrogen to a dual fuel SI, leading to cleaner combustion and improved performance [114]. Similarly, Lata et al. [115] indicated that the brake thermal efficiency of a dual fuel diesel engine could be improved by adding a mixture of hydrogen and liquid petroleum gas. As a result, specific energy consumption decreases. Moreover, the quantity of unburned hydrocarbons, nitrous oxides, and smoke produced by the engine is reduced.

#### **2.6.4 Effect of hydrogen addition on the laminar burning velocity**

Experiments measuring the laminar burning velocity of hydrogen-hydrocarbon gas mixtures have been performed with different values of pressure, temperature, equivalence ratio, and fuel composition, and within different configurations [12], [116]–[117]. In 1959, Scholte [116] measured the flame speeds of hydrogen-methane and hydrogen-carbon monoxide mixtures using the tube burner method. Milton and Keck [118] used a spherical combustion bomb and were the first to measure laminar burning velocity at the stoichiometric condition of hydrogen, acetylene, propane, residual, and methane mixtures for elevated temperatures and pressures. Yu et al. [12] determined the laminar flame speeds of propane-air mixtures and methane-air with a variation in hydrogen amounts by using symmetrical, adiabatic counterflow. The results showed that the laminar flame speeds increased with hydrogen addition. Halter [117] undertook similar studies employing the constant volume spherical bomb methodology, finding similar trends in methane's laminar burning velocity, however, the figures were lower than those found by Yu. Speed comparisons from the two papers are shown in Figure 2.22.

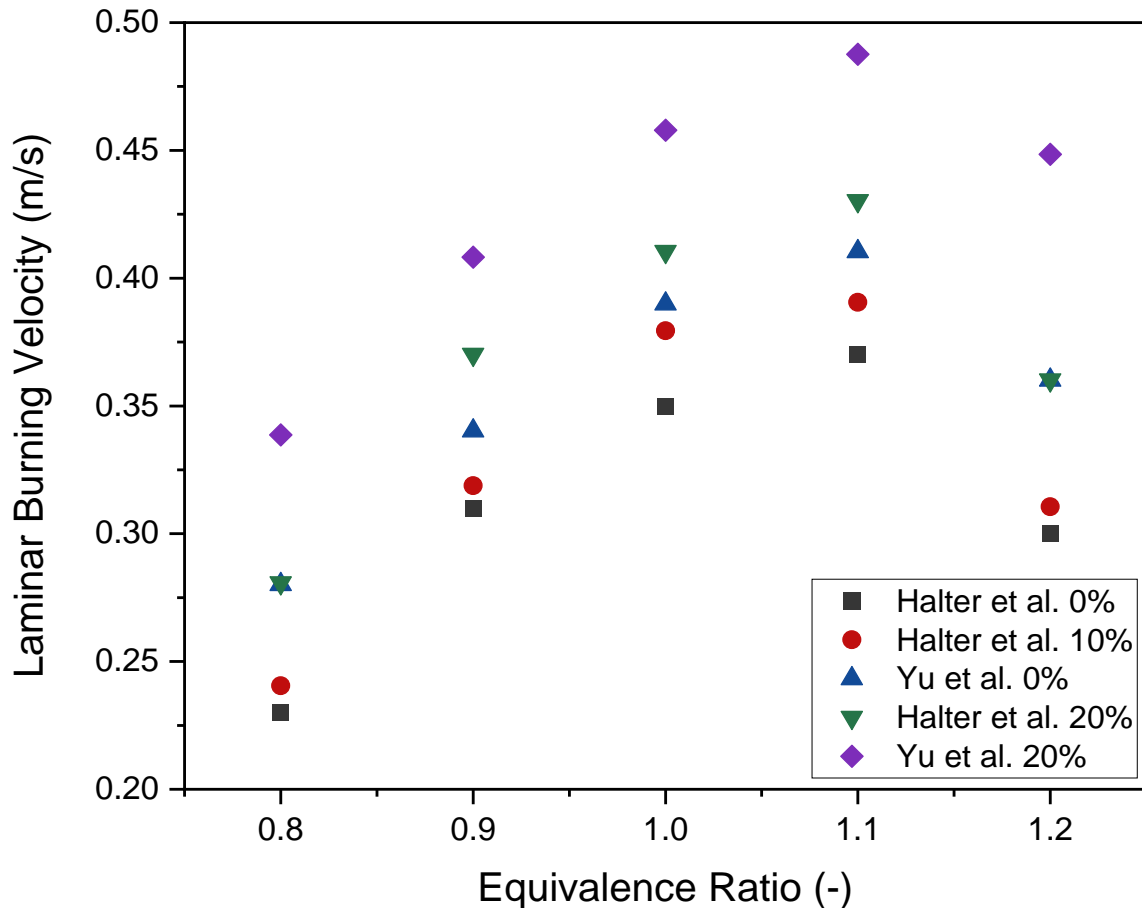


**Figure 2.22: Effect of hydrogen addition on laminar burning velocity of methane**

Hermanns et al. [119] used the heat flux method to report the burning velocities for methane-hydrogen-air mixtures by varying the hydrogen addition up to 30% to the fuel. Halter et al. [117] presented the effect of pressure and hydrogen addition on methane-air premixed laminar flames. The experiment was conducted using a spherical combustion chamber coupled with a classical shadowgraph system. A similar behaviour trend of methane laminar burning velocity was observed, lower compared to the trend observed by Yu. Ren et al. [120] and Huang et al. [121] conducted experimental investigations over a wide range of hydrogen fractions and equivalence ratios in methane-hydrogen-air flames.

From a numerical perspective, simulations of premixed flames have been widely performed [122], [117], [120], [123], [124]. Most of these computations used CHEMKIN to determine the laminar burning velocity. Sarli et al. [125] used the CHEMKIN PREMIX code with the GRI kinetic mechanism to calculate the laminar burning velocities of hydrogen-methane-air mixtures at normal temperature and pressure conditions. The fuel composition and the equivalence ratio varied from pure methane to pure hydrogen, and from lean to rich, respectively.

### **2.6.5 Effect of hydrogen addition on combustion instability**

Studies that have been performed with simplified burners have found that adding hydrogen to methane could enhance energy density [126], increase the laminar burning velocity [127], broaden the flashback limit, alter the characteristics of ignition [128], [129], increase the flame stability, and reduce the emission of NO<sub>x</sub> [130], [131]. The physical and chemical processes evident in the flame are directly influenced by the incorporation of hydrogen. Scholars have put forward different opinions on the correlation between flame instability and the addition of hydrogen.

In a study of the relationship between lean premixed flame dynamics and hydrogen content, Di Sarli [132] found that an increase in hydrogen content correlates with changes to the flame surface area and burning rate. Specifically, Di Sarli observed how an increase in hydrogen content results in the pocket phenomenon and quantitatively influences the flow field. Schefer [133] found that the incorporation of 20% hydrogen content resulted in a higher OH concentration towards the outer shear layer of the lean premixed swirling flame, which subsequently served to increase the burner's stability limits. A study by Yilmaz [134] found that the addition of hydrogen generated a significant modification in the combustion characteristics of the amalgamation and increased the flame compression at various acoustic frequencies. The acoustic response and thermoacoustic coupling phenomenon observed at the flame base exhibit different outcomes depending on whether non-resonant or resonant frequencies are employed.

A study by Kim [135] concluded that the higher diffusivity of hydrogen content speeds up the premixing velocity, thereby reducing the elapsed time of the high-temperature reaction area. García-Armingol [136] examined the correlation between the combustion instabilities of hydrogen-enriched fuels and flashback, and ascertained that the addition of hydrogen could stimulate periodic tempering, which leads to variations in flame fronts and changes in the temperature fluctuations which, in turn, generate increased fluctuations in velocity and thermoacoustic oscillations. However, alternative studies have found that the addition of hydrogen impedes combustion volatility. Taamallah [137] found that the addition of hydrogen reduces the value of the strain rate function and reduces the combustion instability that is observed in the external recirculation zone. Barbosa [138] determined that the addition of hydrogen appreciably increases flame length, reduces the width and heat release of the flame, and reduces combustion instability. Emadi [139], [140] demonstrated that the degree of thermoacoustic oscillation observed at the root position of the mixed gas flame with 40% hydrogen content at an acoustic sound frequency of 135 Hz is substantially lowered. As such, it is widely accepted that adding hydrogen represents an effective method of reducing combustion instability.

## **2.7 Spectral analysis**

Spectral analysis plays a significant role in signal processing studies as it helps researchers to delineate useful insights from raw time-domain signals. Fast Fourier transform (FFT) is a common spectral analysis approach that is employed to visualise signals in the frequency domain as a means of facilitating users to determine the dominant frequencies within the signals. It is also possible to inverse the FFT product as a means of translating a frequency domain signal back to its time-domain signal form. Another method that has attracted increasing attention in recent times is the synchrosqueezed wavelet transform (SST). SST differs from FFT in that it can delineate data that is typically obscured within the Fourier spectrum [141]. The most significant advantage that SST offers in comparison to FFT is that it can reassign a time-domain signal into a time-frequency domain signal. As such, researchers can use the SST approach to pinpoint the instantaneous dominant frequency of a given signal at a precise time point.

A further spectral analysis method that is often used is the Hilbert transform. This technique is particularly useful for extracting a complex signal from one that is limited to only a real part [142]; for instance, a time-domain pressure signal. The current study utilised Hilbert transform to obtain the phase of time-domain signals within a phase analysis. All of the techniques outlined above will be examined in more depth in the subsequent section.

Three waves are employed here to show the capacity of the individual techniques to analyse waves, which are governed by the following equation:

$$X(t) = A \cos(\omega t + \phi)$$

**Equation 2.17**

$$\omega = 2\pi f$$

**Equation 2.18**

In Equation 2.17,  $X(t)$  is the wave function in relation to time,  $A$  is the amplitude,  $\omega$  is the angular frequency, and finally  $\phi$  is the wave phase. The angular frequency,  $\omega$  is directly proportional to the wave frequency,  $f$ , defined by Equation 2.18. The three waves' parameters are given in Table 2.3.

**Table 2.3: Parameters for three different waves.**

<b>Wave</b>	<b>Amplitude, A</b>	<b>Frequency, <math>f</math> (Hz)</b>	<b>Angular frequency, <math>\omega</math> (rad/s)</b>	<b>Phase, <math>\phi</math> (radians)</b>	<b>Duration, (seconds)</b>
$X_1$	10	50	314.2	0	0.2
$X_2$	5	30	188.5	0	0.2
$X_3$	5	30	188.2	$\pi/2$	0.2

The waves are combined to produce the wave  $X_{total}$ ; this is then employed to assess how effectively Fast Fourier Transform (FFT) can identify the dominant frequencies and how well Synchrosqueezed Transform can discern the different frequencies. All parameters of waves  $X_2$  and  $X_3$  are identical, except for their phase, whereby  $X_3$  leads by  $\pi/2$  radians, which is equivalent to  $90^\circ$ . Both waves are used to assess how effectively the Hilbert Transform can identify the phase difference between identical waves that have different phases. Figure 2.23(a) plots the individual waves, and the combined wave,  $X_{total}$ , is presented in Figure 2.23(b).

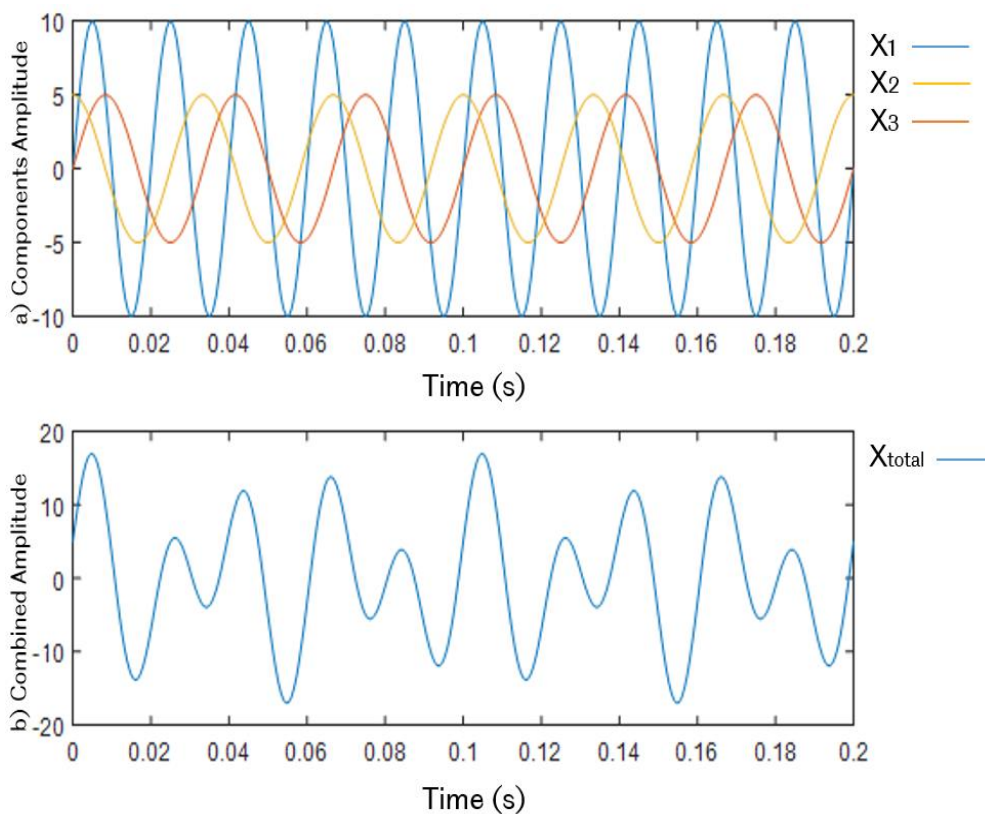


**Figure 2.23: Three waves,  $X_1$ ,  $X_2$  and  $X_3$  plotted in (a) and the combined wave,  $X_{total}$  in (b)**

### 2.7.1 Fast Fourier transform (FFT)

It is possible to obtain the Fourier transform by computing the dot product between a time signal and sine waves of various frequencies [142]. Three specific attributes set sine waves apart from one another:

- 1) Power or amplitude: power is determined by squaring the amplitude.
- 2) Frequency: the number of completed cycles per second.
- 3) Phase: the sine wave timing, as measured in radians or degrees.

The primary purpose of a Fourier transform is to transform a time series signal into a 3D representation that consists of the three attributes described above. A discrete-time Fourier transform is a form of Fourier transform that is constrained by the time-series signal. The number and frequency of the sine waves that are generated are determined by the number of data points in the time-series signal. This is represented by the following equation:

$$X_f = \sum_{k=1}^n x_k e^{-i2\pi f(k-1)n^{-1}}$$

**Equation 2.19**

where  $n$  refers to the number of data points in the time series signal,  $X_f$  represents the Fourier coefficient of the time series variable,  $x$ , which is recorded at a frequency,  $f$ , and  $k$  is the number of iterations in the summation. Figure 2.24(a) presents a time-series signal that has been randomly generated with  $n = 10$ . As can be observed in Figure 2.24(b), applying Equation 2.19 to the data related to the signal produces an outline of the Fourier coefficient; i.e., the frequency, power, and phase. The 3D graph presented in Figure 2.24(c) can be generated from the data related to the power-frequency axis, while the graph in Figure 2.24(d) can be generated from the phase-frequency axis. It is possible to employ the 3D representation to model the time signal by applying an inverse Fourier transform that is derived from the following equation:

$$x_k = \sum_{k=1}^n X_k e^{i2\pi f(k-1)n^{-1}}$$

Equation 2.20

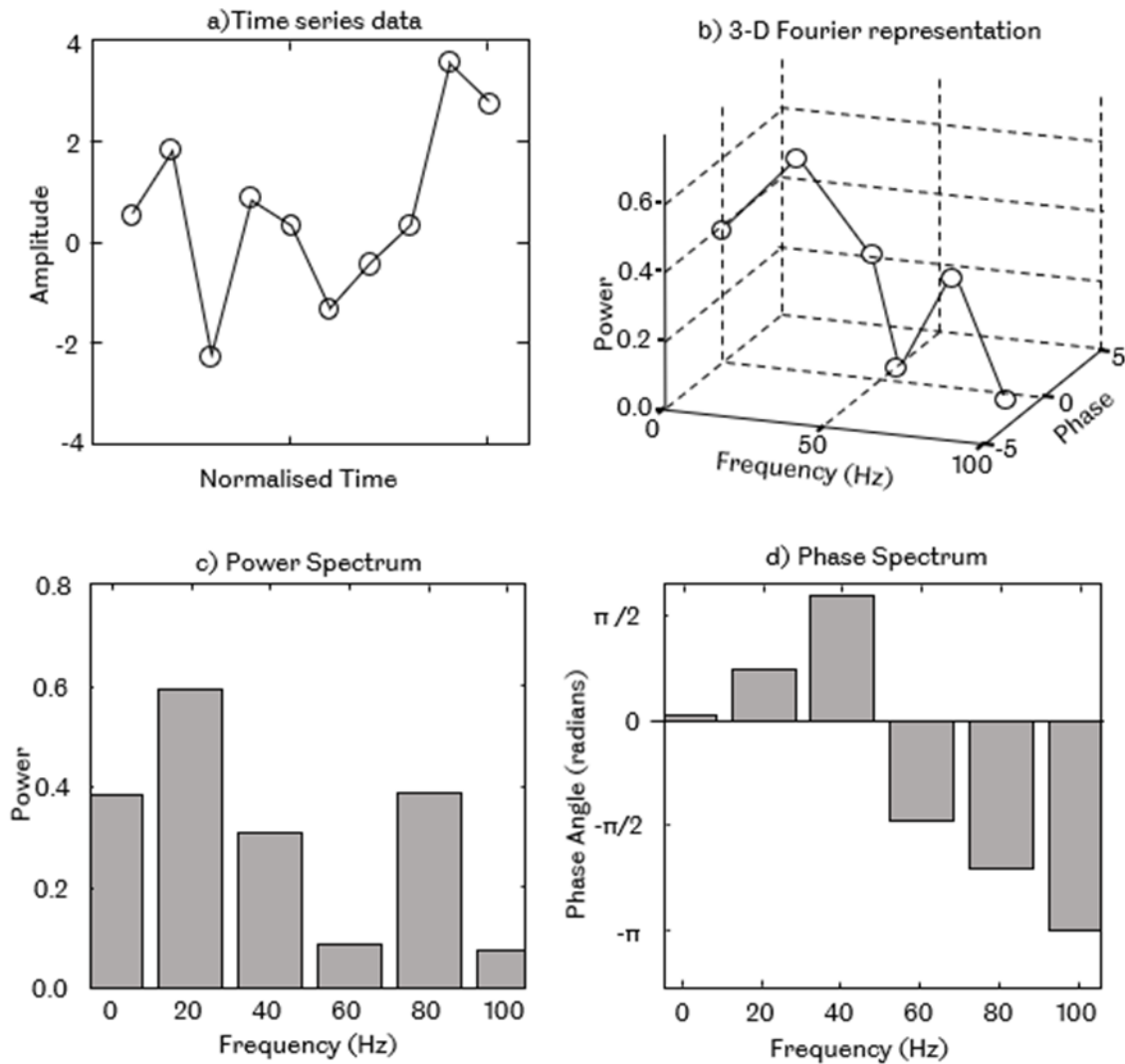


Figure 2.24: A discrete Fourier transform from example a) randomly generated time signal, producing b) the 3-dimensional representation of the time-series signal, c) the power spectrum, and finally d) the phase spectrum. Reproduced from [142]

FFT represents an alternative method of determining the Fourier transform. It involves eradicating the elements that are deemed to be of no use within the original computation without losing critical data [142]. Cohen [142] offers a detailed overview of the Fourier transform and the various forms that it can take. FFT plays a significant role in research into unstable combustion.

Scholars frequently employ it to rapidly identify the frequency aspects of the flame oscillation in accordance with the power-frequency graph presented in Figure 2.24(c). Ebieto et al. [143] employed FFT to determine the dominant frequency of flame oscillations. They concluded that the ~240 Hz determined oscillations were a characteristic of the tube, which transformed slightly in response to an increase in hydrogen content.

Clanet et al. [8] utilised FFT to distinguish various frequency oscillations, which they subsequently ascribed to resonant modes of the tube that was used. Two distinct flames oscillations at different equivalence ratios can be observed in Figure 2.25. Figure 2.25(a) presents a view of a  $\phi = 0.9$  decane flame. A clear silence can be observed after the first harmonic oscillation before the outset of the fundamental mode. As can be seen in Figure 2.25(b), a rise in the equivalence ratio to 1.1 resulted in the commencement of a different set of frequencies. In this scenario, FFT appears to play a useful role in determining which frequency is dominant within the oscillations. However, if the oscillations are overlapping, for instance between the fundamental mode and the parametric instability in Figure 2.25(b), it is more challenging to delineate the frequency. In this case, there would be a requirement to crop the signal into distinct sections so that it is possible to determine the dominant frequency, however, rationalising where to crop would represent a further challenge.

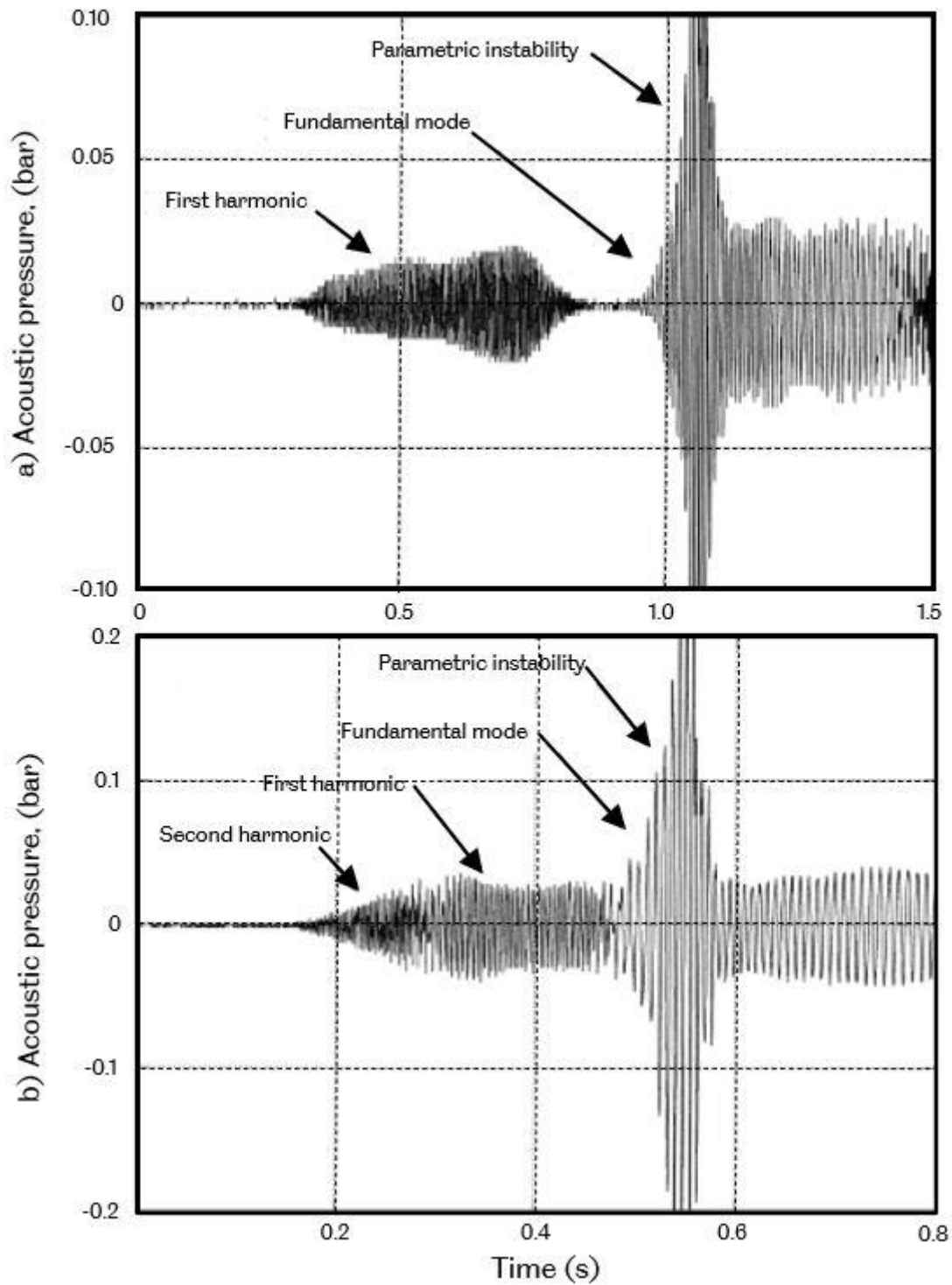
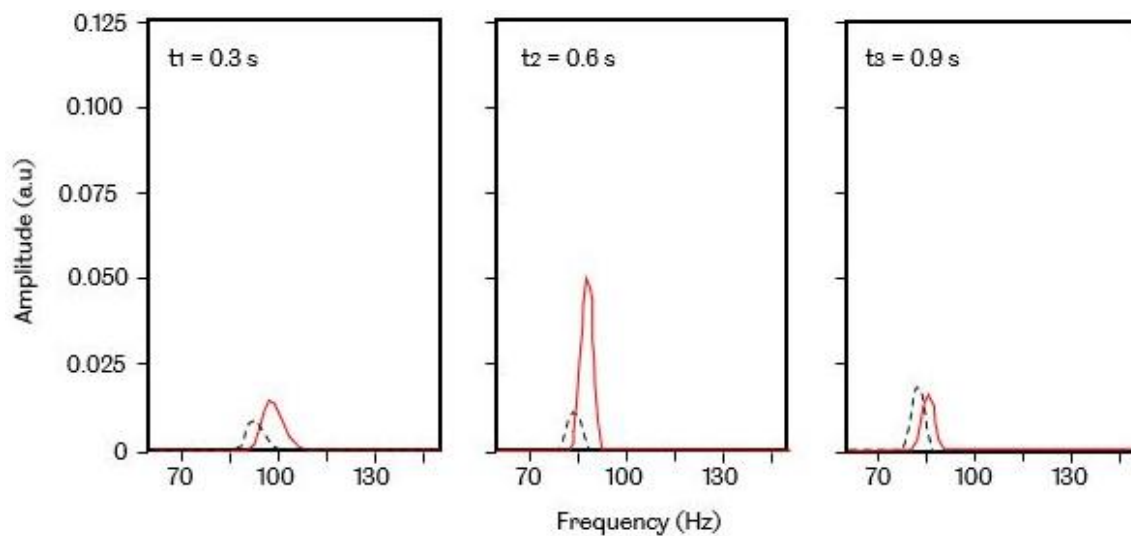


Figure 2.25: Acoustic pressure records for spray flame (decane) in a 1.2 m tube. a)  $\phi = 0.9$ , between the frequency change, there is a period of silence, b)  $\phi = 1.1$  The instability occurs in three distinct frequencies successively. Reproduced from [8]

Veiga-López et al. [101] studied oscillatory premixed flames in a Hele-Shaw cell propagating towards a closed end. They tried to dissect the oscillatory behaviour of the flames by applying FFT on both the pressure and flame position signal and subsequently cropped them in accordance with the way in which the flame structures appeared. The FFT of the flame position and the pressure signal for a lean  $\phi = 0.8$  propane flame, which has been segregated into three sections according to the shape of the flames, can be observed in Figure 2.26. Had the signal not been divided into these three sections, the FFT would have exhibited several peaks. The downside of using FFT is that it lacks the time domain, which hides the time information.



**Figure 2.26: Fast Fourier transform of the flame position (solid line) and pressure signal (dotted line) for the lean flame at time  $t_1 = 0.3$  s,  $t_2 = 0.6$  s, and  $t_3 = 0.9$  s. Reproduced from [101]**

The drawback of employing FFT is that there is no time domain present, meaning that time information cannot be seen. This would make it virtually impossible to discover any points at which a particular frequency is dominant, unless this was found using divided time-series sections, as illustrated by Figure 2.26. However, if there are a number of overlapping components, this method quickly becomes onerous. An alternative means of overcoming this difficulty is the production of time-frequency plots; this will be detailed in the following section.

After performing FFT on  $X_{total}$ , i.e. the summation of the three waves (see Table 2.3), two distinct peaks emerge, as illustrated in Figure 2.27. While wave  $X_1$  produces a peak at 50 Hz, waves  $X_2$  and  $X_3$  generate a single peak at 30 Hz, associated with their respective frequencies, given in Table 2.3.

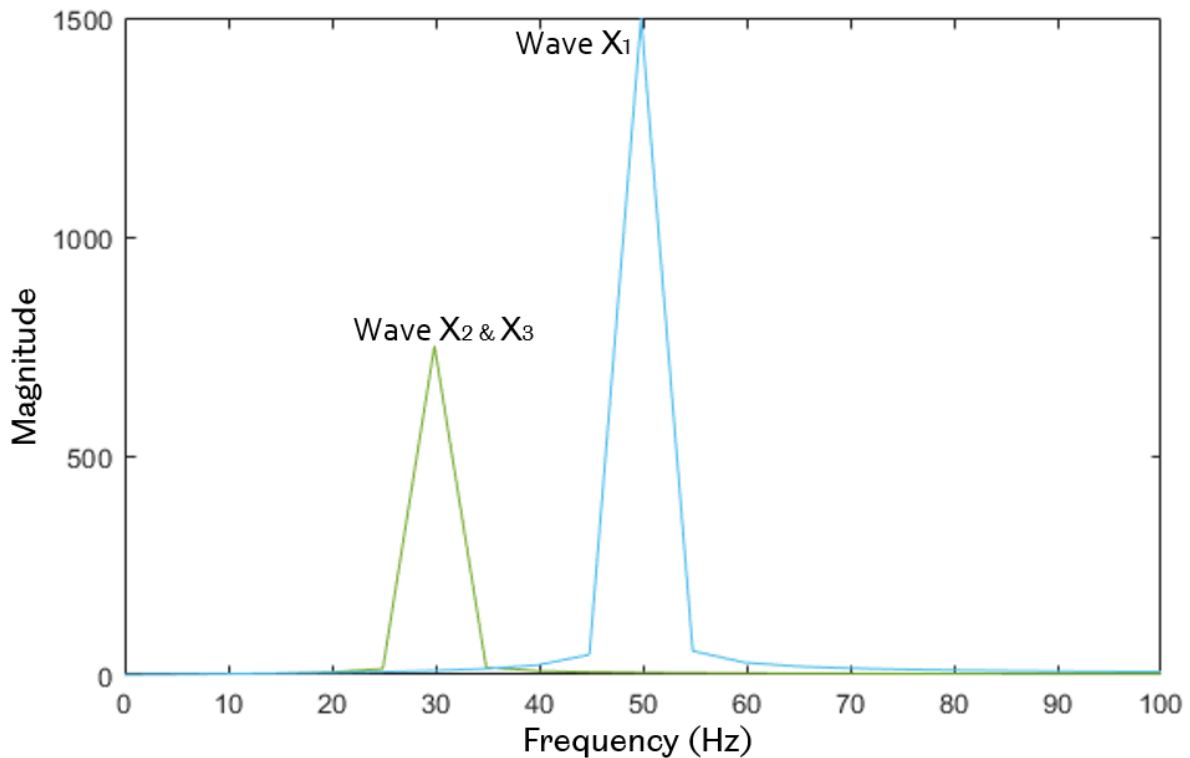
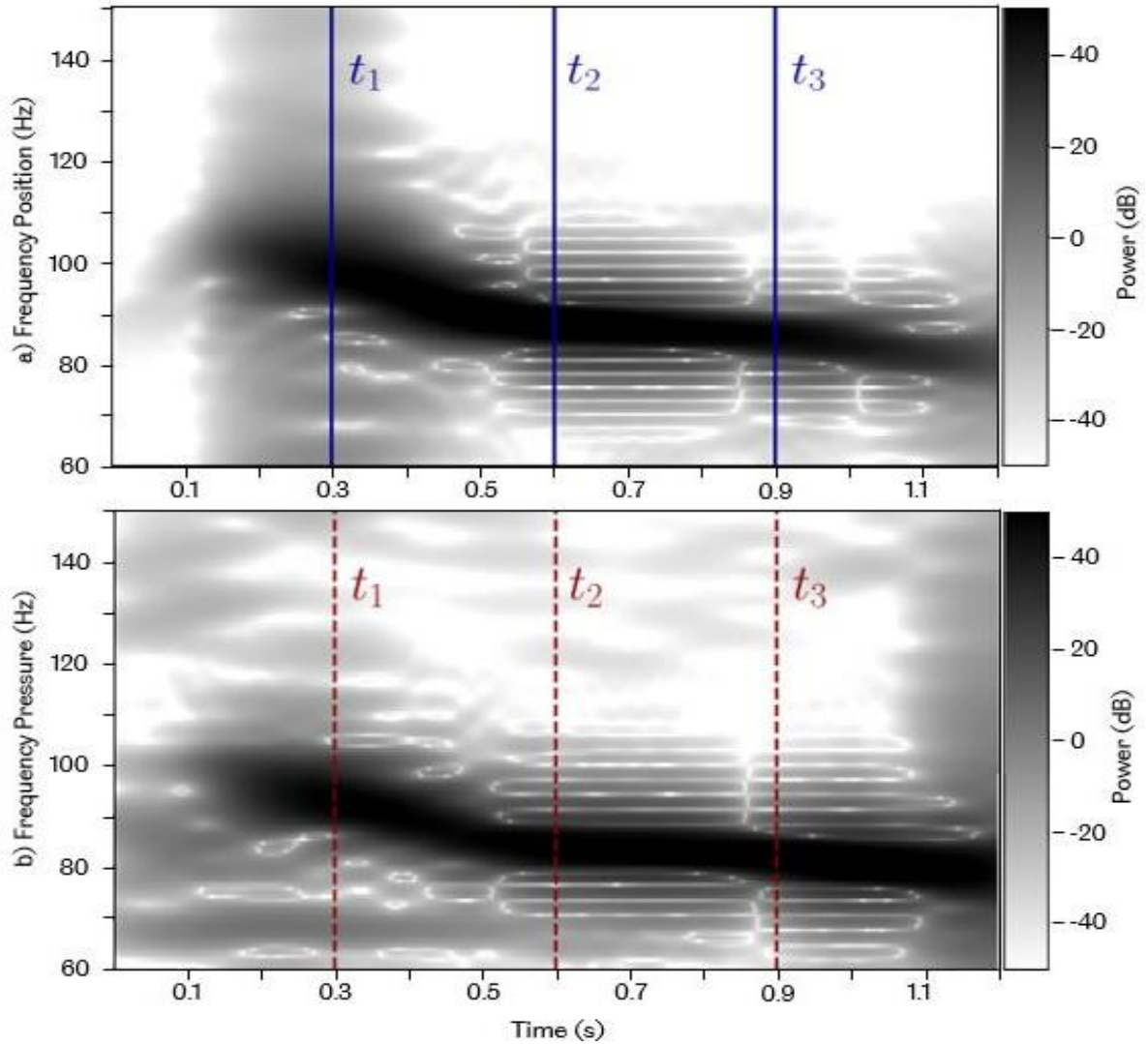


Figure 2.27: Fast Fourier Transform of  $X_{total}$

## 2.7.2 Synchrosqueezed wavelet transform

As can be observed in Figure 2.28, using the same data as that employed to generate the FFT plots presented in Figure 2.26, Veiga-López et al. [101] also sought to generate a time-frequency plot through the use of a Fourier spectrogram. The pressure and position spectrogram plots both clearly show a domain frequency shift. The Fourier spectrogram provides an effective means of observing the shift in the dominant frequency within a single-component signal. If the signal is multi-component and features overlapping frequencies, it would be more challenging to decipher the visualisation and even more so to decompose the signal into specific components.



**Figure 2.28: Fourier spectrograms of a) flame position and b) flame pressure for a lean propane flame. Reproduced from [101]**

The empirical mode decomposition (EMD) approach can be employed to decompose a superposition of signals into their individual signals if they are spectrally and temporally separated in the time-frequency plane. Daubechies et al. [144] performed an in-depth evaluation of various EMD methods. They developed the synchrosqueezed wavelet transform (SST) approach, the purpose of which is to identify the constituent components of time-series signals,  $s(t)$ , that exhibit time-varying harmonic behaviour, as follows [141]:

$$s(t) = \sum_{k=1}^K A_k(t) \cos[\theta_k(t)] + \eta(t)$$

**Equation 2.21**

where  $A_k(t)$  represents the instantaneous amplitude,  $\eta(t)$  represents additive noise,  $K$  is the maximum number of components in one signal, and  $\theta_k(t)$  is the instantaneous phase of the  $k_{th}$  component. The instantaneous phase can be employed to approximate the instantaneous frequency,  $f_k(t)$ , of the  $k_{th}$  component defined by:

$$f_k(t) = \frac{1}{2\pi} \frac{d}{dt} \theta_k(t)$$

**Equation 2.22**

The primary goal of employing SST is to separate a raw signal into  $K$  number components, each of which has an amplitude of  $A_k(t)$  at their respective instantaneous frequency  $f_k(t)$ . Time-series signals in the form of Equation 2.21 are employed in a variety of scientific applications [145]–[146] in which there is a need to assess time-varying spectral properties as a means of better understanding the problem. Similar to FFT, it is possible to use SST to reconstruct the signals back into the time-domain with the additional benefit of reconstructing the time signal into  $K$  number of signals, which becomes the original signal if totalled.

It is possible to reduce the working principle of a synchrosqueezed wavelet transform into three phases. In the first phase, one obtains the continuous wavelet transform (CWT) of a signal through the use of an analytical wavelet as a means of capturing the instantaneous frequency information. In the second phase, the instantaneous frequency is extracted from the CWT output. Finally, the CWT is squeezed over regions with constant phase transform. This squeezing process generates a concentrated instantaneous frequency in the time-frequency plane, similar to the smeared instantaneous frequency that was observed in the Fourier spectrogram that was presented by Veiga-López et al. [101]. Figure 2.29 illustrates a further example that was developed by comparing the SWT and CWT output of the same signal. As can be observed in the figure, the smeared instantaneous frequency line significantly sharpens when SWT is implemented.

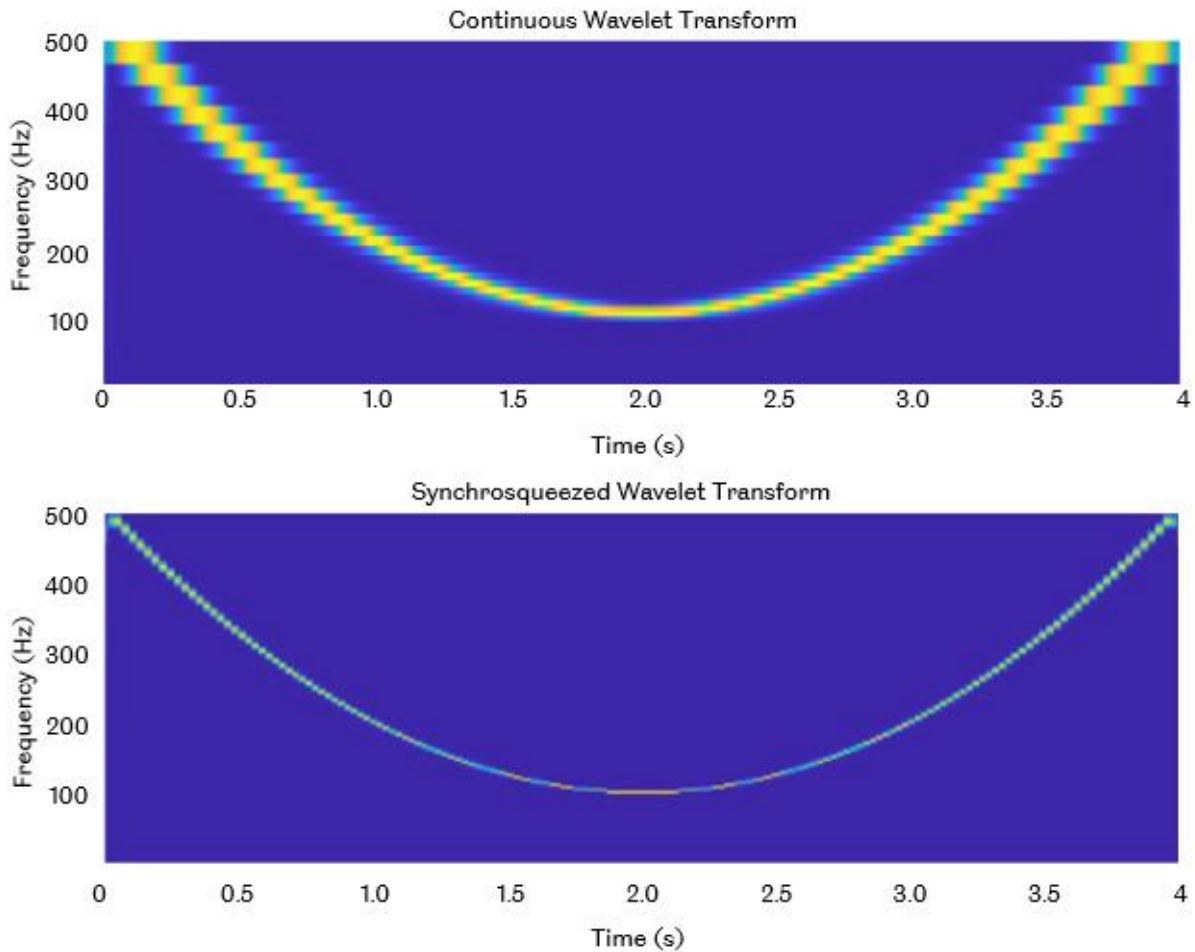


**Figure 2.29: Comparison between a continuous wavelet transform (CWT) and a synchrosqueezed wavelet transform (SST). Reproduced from [147]**

Several steps are involved in generating an SST plot from a CWT of a signal as shown in Equation 2.23. According to Daubechies [148], the CWT of a signal,  $s(t)$ , comprises the complex conjugate of the mother wavelet,  $\psi^*$ , the time shift that is applied to the mother wavelet,  $b$ , and the scale that is applied to the mother wavelet,  $a$ .

$$W_s(a, b) = \frac{1}{\sqrt{a}} \int s(t) \psi^* \left( \frac{t-b}{a} \right) dt$$

**Equation 2.23**

Based on Equation 2.23, the CWT of the signal  $s(t)$ , can be delineated as a cross-correlation between the signal with multiple scaled and time-shifted versions of the mother wavelet [141]. The instantaneous frequency can be obtained using the coefficients obtained from Equation 2.23, producing a CWT plot that is comparable to that presented in Figure 2.29 [144]. Plancherel's theorem can be used to rewrite Equation 2.23 in the frequency domain to produce Equation 2.24:

$$W_s(a, b) = \frac{1}{2\pi} \int \frac{1}{\sqrt{a}} \hat{s}(\xi) \hat{\psi}^*(a\xi) e^{jb\xi} d\xi$$

**Equation 2.24**

where  $j = \sqrt{-1}$ ,  $\xi$  is the angular frequency,  $\hat{\psi}^*(a\xi)$  is the scaled mother wavelet in the frequency domain, and  $e^{jb\xi}$  is the time shift  $b$  in the frequency domain. Equation 2.25 assumes a simple signal:

$$s(t) = A \cos(\omega t)$$

**Equation 2.25**

Applying Equation 2.25 to Equation 2.24 could be simplified into Equation 2.26:

$$W_s(a, b) = \frac{A}{2\sqrt{a}} \hat{\psi}^*(a\omega) e^{jb\omega}$$

**Equation 2.26**

The information obtained via Equation 2.26 can be mapped, however, it typically leads to a blurred/smeared interpretation in the time-scale plane that typically occurs in the scale dimension,  $a$ , which assumes a constant time shift,  $b$ . According to Daubechies and Maes [149], the effect of smearing can be minimised with a derivative of Equation 2.26. The instantaneous frequency,  $\omega_s(a, b)$ , which is represented by Equation 2.27 can be obtained by computing the derivative of Equation 2.26 for all  $W_s(a, b) \neq 0$ :

$$\omega_s(a, b) = \frac{-j}{W_s(a, b)} \frac{\partial}{\partial b} W_s(a, b)$$

**Equation 2.27**

There is a requirement to complete the process by mapping the time-scale information ( $a - b$  plane) to the time-frequency plane ( $\omega_l - b$  plane). This process is known as synchrosqueezing and involves the information being shifted from the form of  $(b, a)$  to  $(b, \omega_s(a, b))$  [144].  $a$  and  $b$  are markedly distinct values. It is possible to compute a scaling step for each  $a_k$ , which is specified as  $\Delta a_k = a_{k-1} - a_k$ , for any  $W_s(a, b)$  value. Since the scale is defined by  $a$ , which serves to alter the frequency of the mother wavelet, the scaling step for  $\omega$  is required to compute the synchrosqueezed transform,

$T_s(\omega_l, b)$ , where only the centre of the instantaneous frequency,  $\omega_l$ , will be computed, within the range of  $(\omega_l - \frac{\Delta\omega}{2}, \omega_l + \frac{\Delta\omega}{2})$ , where  $\Delta\omega = \omega_l - \omega_{l-1}$ . This generates Equation 2.28.

$$T_s(\omega_l, b) = \frac{1}{\Delta\omega} \sum_{ak: |\omega(a_k, b) - \omega_l| \leq \Delta\omega/2} W_s(a_k, b) a_k^{-\frac{3}{2}} (\Delta a)_k$$

**Equation 2.28**

As can be observed in Equation 2.28, the output signal will only be synchrosqueezed along the frequency axis. This does not have an impact on the time shift [150]. MATLAB offers the synchrosqueezed wavelet transform functionality.

### 2.7.3 Phase study

Performing a phase study on flame signals can facilitate efforts to understand the pressure amplification trends that are seen in combustion resonance [151]–[155]. Before a phase study can be conducted, there is a requirement to extract and compute the phase of combustion-related time-series signals as a means of delineating their phase difference. Rayleigh describes how the combustion can be amplified if the pressure and heat release are in phase; as such, the most effective means of identifying this relation is by calculating the phase variation between the pressure signal and the heat release.

The Hilbert transform is mathematically defined using an integral to transform a time domain function into a complex function, as follows [156]:

$$U(s) = \int_{-\infty}^{\infty} \left[ \frac{1}{\pi(s - 1)} \right] u(t) dt$$

**Equation 2.29**

Whereby the time domain data  $u(t)$  is multiplied by the Hilbert transform kernel, given in square brackets, and then integrate it regarding time,  $t$ . The output is obtained in terms of  $s$ , which is a time-dependent variable. According to Hahn [156], the theory behind the Hilbert transform links closely to the Fourier transform in that both use integrals, albeit with dissimilar kernels. Using an integral, the Hilbert transform's output can be reverted to its original form,  $u(t)$ , as follows [156]:

$$u(t) = \int_{-\infty}^{\infty} \left[ \frac{1}{\pi(t-s)} \right] U(s) ds$$

**Equation 2.30**

Whereby the original transform from Equation 2.29,  $U(s)$ , is multiplied by the conjugate Hilbert transform kernel, given in square brackets, and integrate it regarding the time-dependent variable,  $s$ . For further details on the Hilbert transform, the reader is referred to Hahn [156], who extensively covered its working principle. Regarding the Hilbert transform, in this work the Hilbert function in MATLAB is applied to the time domain data, however, it emerges that the function's output is not solely an imaginary signal that is delineated by Equation 2.29, but, rather, represents both a real component (the original signal) and an imaginary component (the Hilbert transform data) [157]. Thus, the imaginary component is extracted from the output, thereby demonstrating the signal phase, which is derived by creating and adding the phase quadrature component to the real-value signal. In other words, the parts of the complex Fourier spectrum of the real-value signal are rotated [158].

Before Hilbert transform can be applied to a signal, there is a requirement to use a bandpass filter to attain the phase of the desired frequency. While the Hilbert transform can be applied directly to an unfiltered signal to access phase information, the data provided would represent a summation of the phase data from other frequencies. As such, it would be difficult to comprehend.

Lee et al. [159] studied the coupling of combustion instability methods in a lean premixed gas turbine combustor. As can be observed in Figure 2.30, the clearest amplification was observed in the  $-90^\circ$  to  $90^\circ$  phase difference range. This indicates that the erratic heat addition boosts the system energy when in phase, and vice versa. It is important to note that, even though they were in phase, some of the plotted points were of low intensity. This is indicative of greater acoustic damping in comparison to gain.

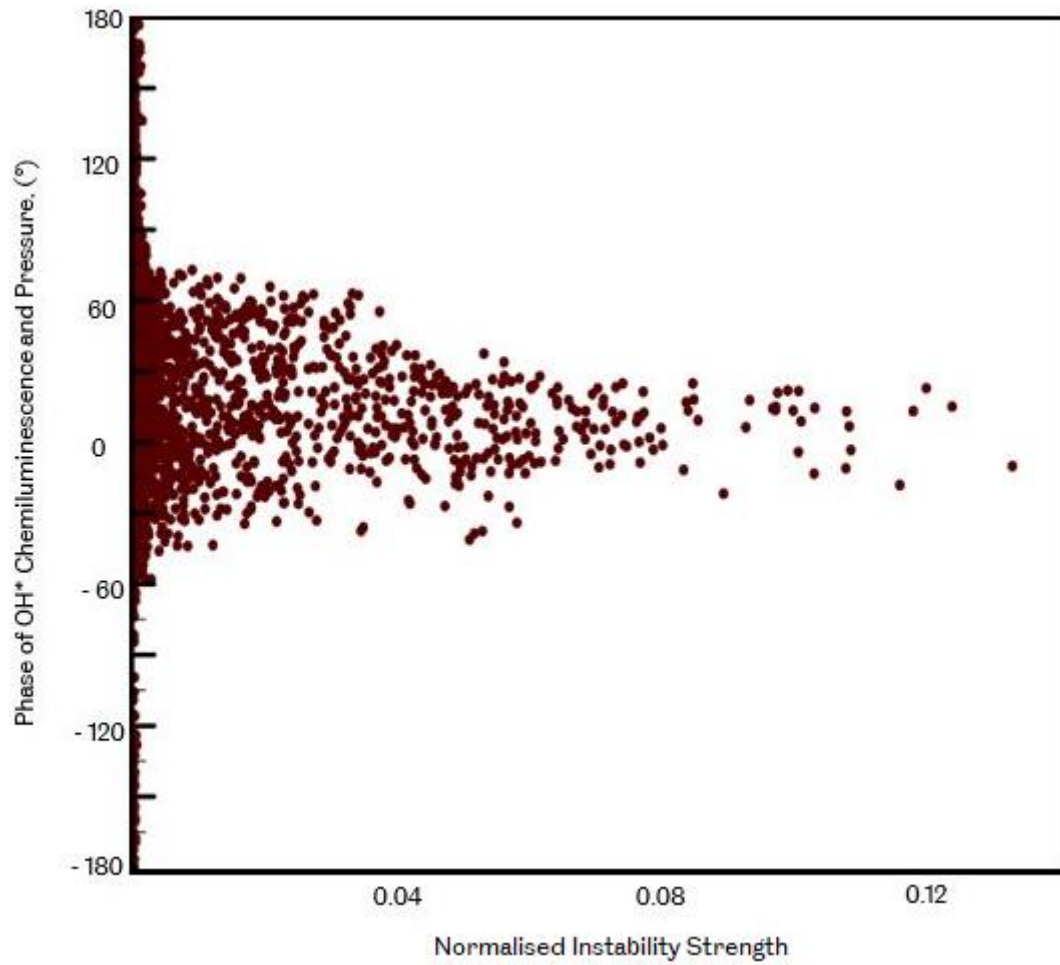


**Figure 2.30: Phase of the OH\* chemiluminescence against normalised instability strength for all operating conditions. Reproduced from [159]**

## 3 EXPERIMENTAL METHODOLOGIES

### 3.1 Rig setup

The experimental apparatus used in this experiment consists of two major parts, as shown in Figure 3.1 and Figure 3.2; the first part is the flame tube rig and the second one is the data acquisition tools. First, the flame tube rig consists of copper tubes connected by brass compression fittings of the same diameter and contains several connected cylindrical tubes that form a loop. Pennington [160] designed and built the rig set-up and it was subsequently developed by postgraduate students Mossa [161] and Ebieto [36]. The initial purpose of this rig was to study the flame propagation speed of different fuels, but now the rig is used to investigate thermoacoustic phenomenon. These tubes are fitted with ports that allow gases fuel to be injected using a syringe. The main combustion tube has an inner diameter of 20 mm and is 1200 mm in length. This tube is also fitted with a 650 mm quartz tube in order to provide optical access. Studies have revealed that flame propagation in tubes varies considerably depending on the source of ignition. Studies by Mossa and Woolley [71] and Wu et al. [162] showed that, the use of spark ignition not only increased the speed of flame propagation but also strengthened the flame oscillation onset. Since the spark ignition can enhance instabilities in the flame that have an impact on the flame speed and propagation, pilot flame ignition from a gas lighter was used in this experiment [163]. The rig has two fans that premix the fuels and air before ignition and produce a homogeneous mixture.

The pressure transducer PDCR 810, which has a pressure reading range of -1 to 1 bar, was used only to measure the rig pressure during mixing. On the injection port, a self-sealing mechanism called septum was utilised to prevent mixture leakage once the fuel was injected into the rig. The data acquisition tools consist of two components, a high-speed camera and a pressure transducer. The Schematics are interconnected to allow syncing of the flame recording and pressure logging, as shown in Figure 3.3. For both devices, the sampling rate was set to 2000 samples/second (or frames/second for the case of the camera) to capture the vibrating movements of the flames in the tube during propagation.

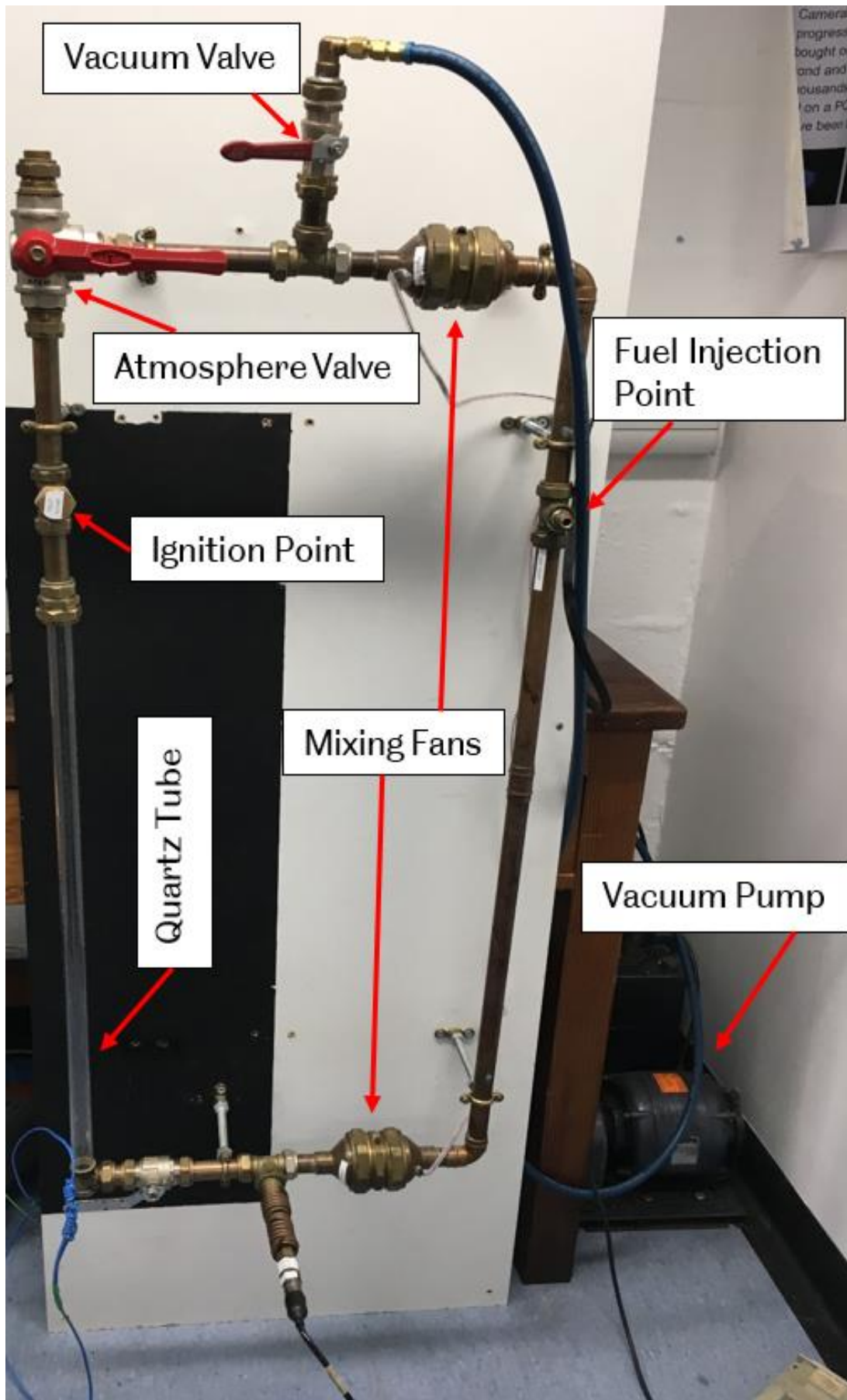


Figure 3.1: Experimental combustion rig setup

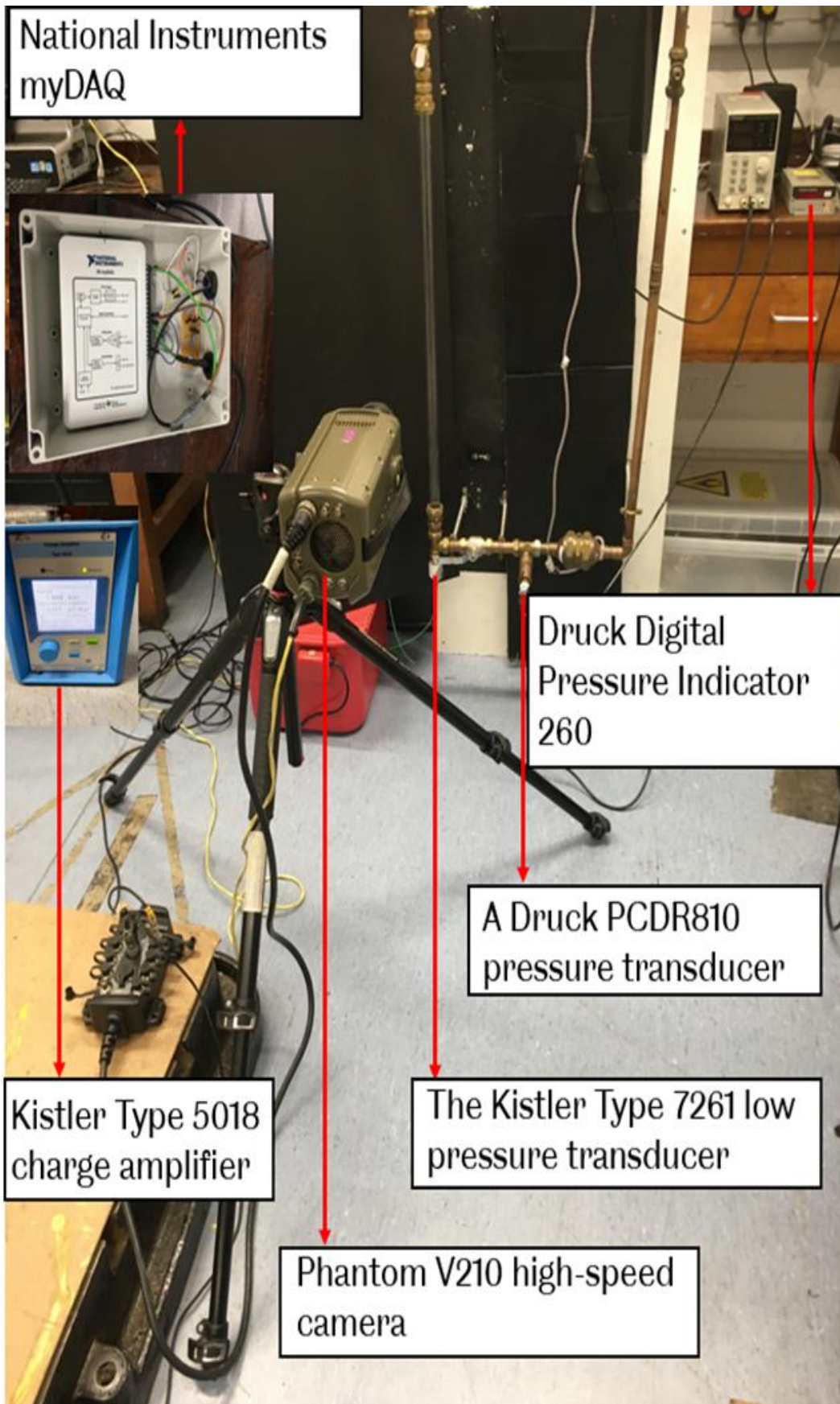
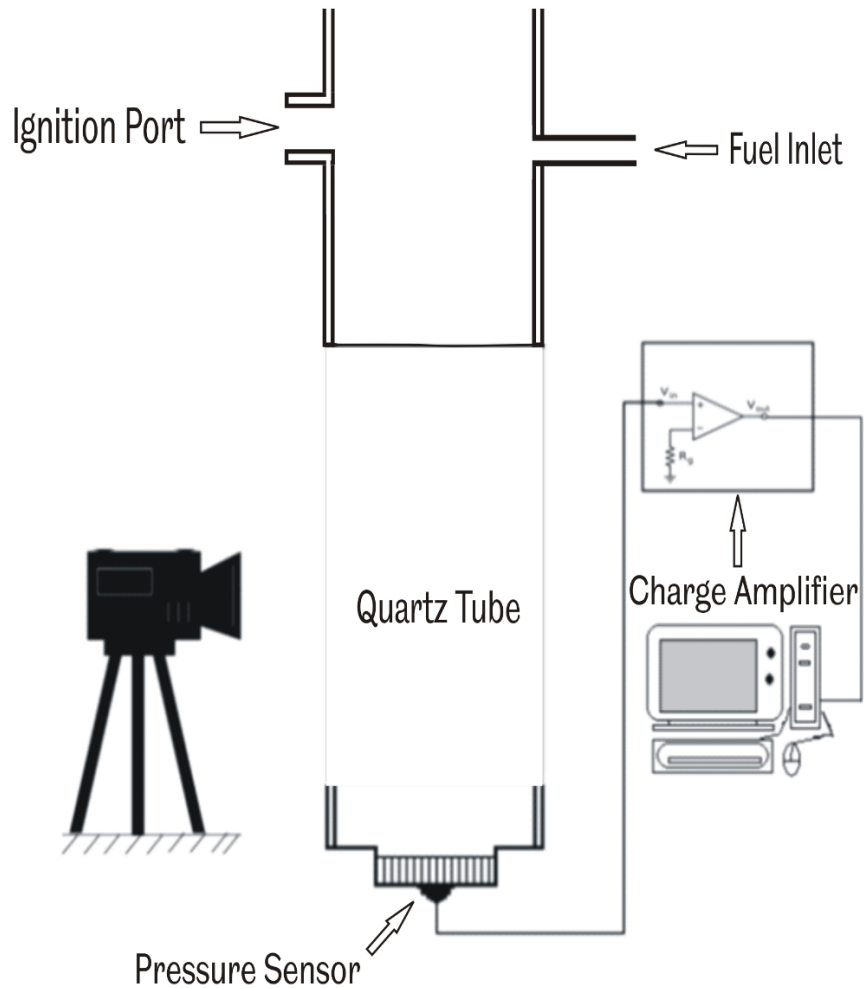


Figure 3.2: Data acquisition tools



**Figure 3.3: Schematics of downwardly propagating experiment**

A whole pressure signal (i.e. from the ignition point to the tube end) is exemplified in Figure 3.4(a), here produced from a methane flame with  $\phi = 1.0$ ,  $R_H = 0.3$ . The experimental setup uses two flames that propagate from the ignition point, and thus a zoom in is provided of the ignition point's pressure signal and of that prior to the region of flame observation as seen in Figure 3.4(b). Based on this figure, upward flame propagation has no effect on the behaviour during downward flame propagation.

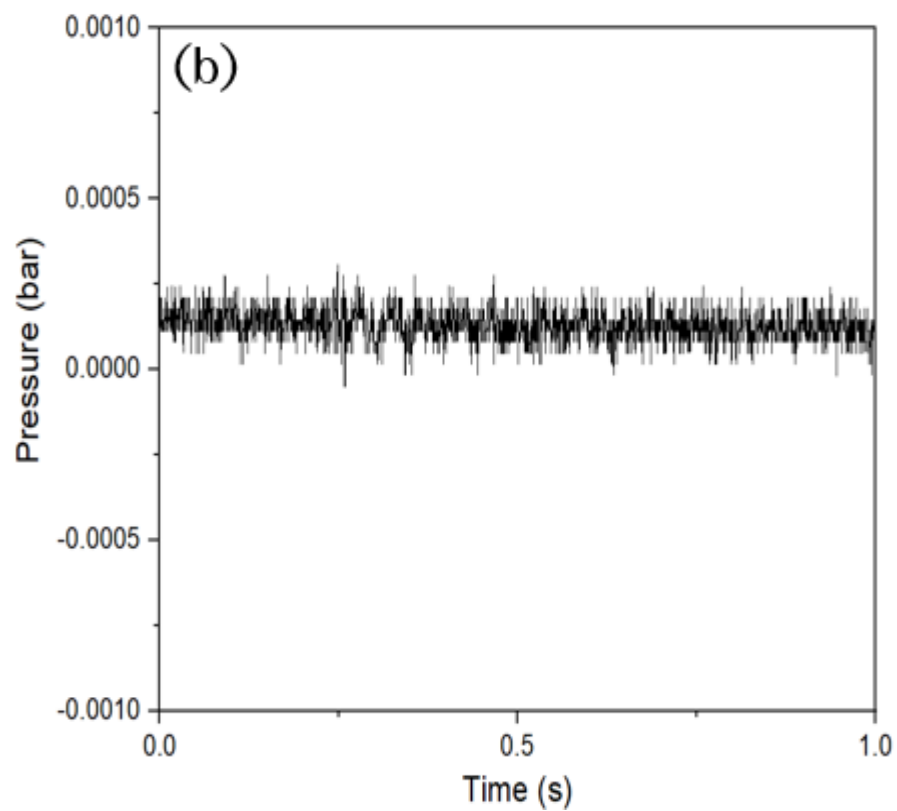
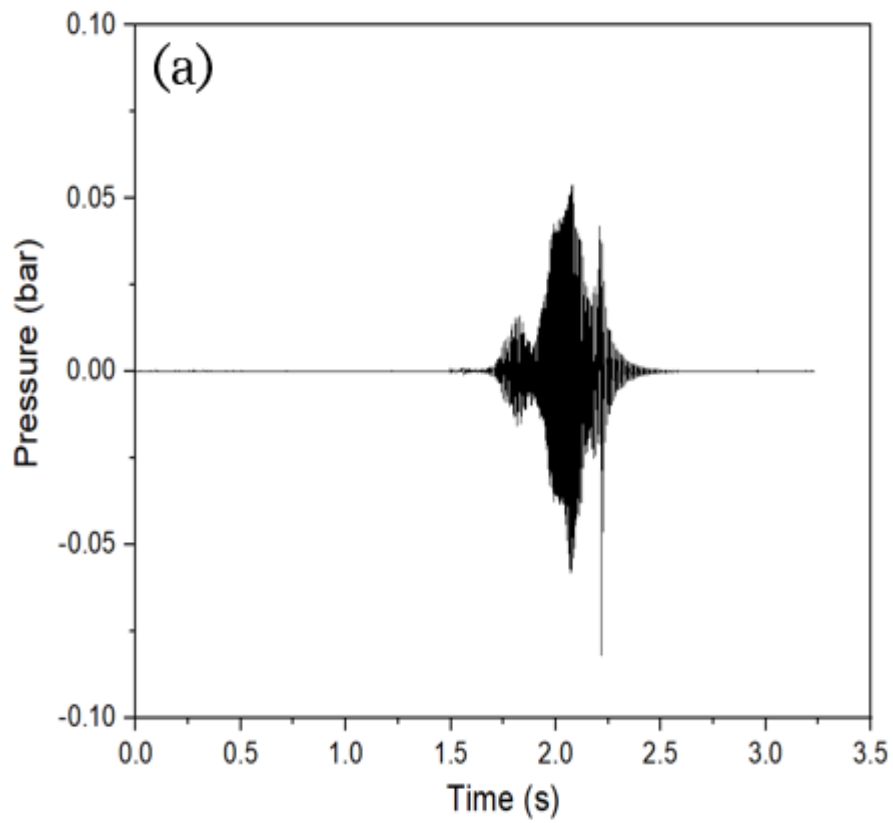


Figure 3.4: Methane flame at  $\phi = 1.0$ ,  $R_H = 0.3$  a) the whole pressure signal, b) zoomed in pressure signal from the ignition point and prior to flame observation region, both before cropping

## **3.2 Data acquisition**

### **3.2.1 High-speed camera**

All experiments in this study were performed using a Phantom V210 high-speed camera equipped with a monochrome CMOS sensor and recorded at a 1280 x 800 pixel resolution at 2,000 fps [164]. The resolution and framing rate were adjusted using Phantom Camera Control (PCC), which was also employed to trigger the camera. A Nikon AF Zoom NIKKOR 24-85mm f/2.8-4D IF lens was additionally used for the natural light experiments. Although the high framing rate illustrated the flames' details, there was some signal loss in the recording of the flames due to the difficulty in observing the images under low light intensity. The following steps were taken to mitigate this: the lens aperture of the camera was maintained at f/2.8, the quantity of light that enters the lens was maximised by situating the camera close to the quartz tube, and all experiments were conducted in a dark room to preclude extraneous sources of light. A limiting factor in these experiments was the light intensity as it restricted what could be recorded of lean mixtures. In Schmidt et al. [46], this issue was mitigated by the use of Schlieren photography. For propane flames, they were capable of achieving an equivalence ratio of  $\phi = 0.6$ . The PCC software was used to implement the post-trigger method of data capture. In this method, after being triggered by the trigger button, the camera continuously records the event, thereby capturing the images. This method proved to be very effective in capturing the event. Appendix A describes the detailed procedures for the optical calibration.

### **3.2.2 Pressure measurement**

Two pressure transducers were used, a Kistler Type 7261 and a Druck PCDR810. The Kistler Type 7261 transducer, with the ability to read a pressure range of 0-1 bar, was used to log the pressure fluctuations at the end of the tube during flame propagation. The sensitivity of the transducer was set to -2321 pC/bar for a pressure range of 0-1 bar. The transducer generates a charge when pressure is applied which is then amplified using a Kistler Type 5018 charge amplifier, which is linked to a computer, and the outcomes are logged using the LabView program. A Druck PCDR810 transducer was used to track rig pressure during fuel mixing and calculate the rig volume. The output

pressure was displayed in bar using a pressure transducer that was connected to a Druck Digital Pressure Indicator 260. The Druck pressure transducer, which is equipped with a silicon diaphragm and a titanium module, calculates the strain gauge deformation due to pressure and translates this into a signal that can be measured. As the transducer was used solely to monitor the overall pressure of the rig during vacuuming and the injection of the fuel, the pressure was not logged. Appendix B describes the pressure measurement settings.

### **3.2.3 The synchronisation of optical and pressure data**

In order to analyse the data, the pressure and optical data must be synchronised. This aim was realised using a National Instruments myDAQ (Part number 781326-01) data acquisition instrument with 16 bit ADC and DAC resolution [165]. On pressing the trigger button the box sent a transistor-transistor logic signal (0 to ~5V); this signal fell on release of the button. Pressure readings from the charge amplifier alongside the trigger signal were logged using the LabVIEW program. Figure 3.5(a) illustrates the trigger signal/pressure signal found during experimentation with a significant variation in voltage which makes it hard to identify the pressure signal. Figure 3.5(b) zooms in on the pressure signal, offering a superior view. To implement synchronisation, firstly, the pressure signal had to be cropped. At the start a trigger signal rises to 5 V and towards the end it is dropping back towards 0 V. The pressure signal was cropped, with the trigger signal's rise being regarded as the start and its drop being the end. The cropped pressure signal needs to be converted from Voltage to bar, stated as 0.1 bar / V on the Kistler Type 5018 charge amplifier screen. Once the conversion was done, the flame propagation in the video recording needs to be tracked.

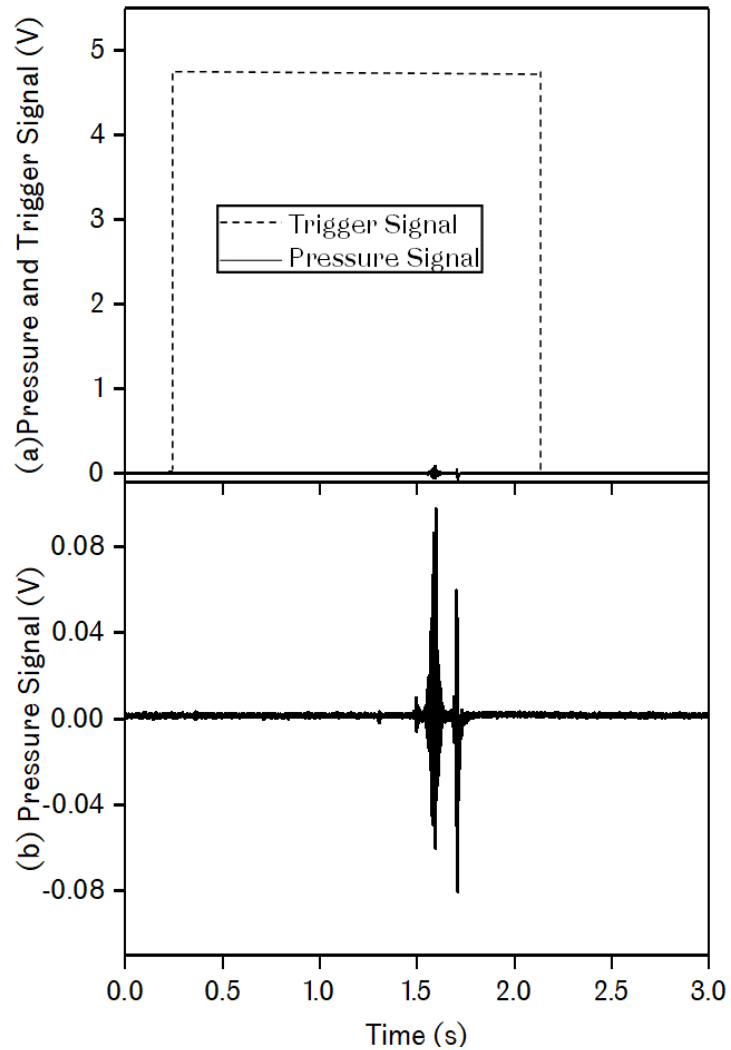


**Figure 3.5: a) Both trigger and pressure synchronisation signals, b) pressure signal magnified, both signals prior to cropping**

Having tracked the propagation of the flame through the video and, therefore, obtaining the flame positional signal, it has to undergo synchronisation with the pressure signal. Because the Phantom camera works using a post-trigger system, it makes a continuous recording until the release of the trigger, meaning that the end of the video synchronises with the trigger signal ending, and this is also effectively the ending of the cropped pressure signal (see Figure 3.6).

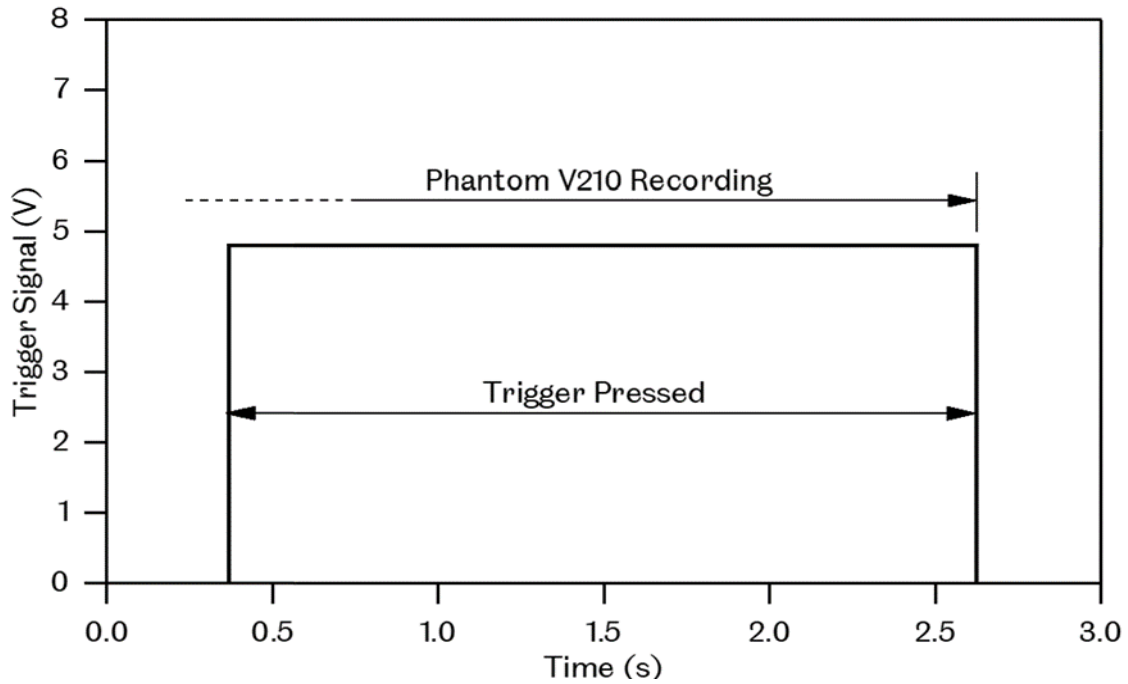


**Figure 3.6: Video recording to trigger signal synchronisation**

Before synchronisation, testing of the synchronisation process was undertaken relating recordings of a metal plate tapping a specific area of the flame tube for the production of sound captured with the pressure transducer. Tracking of the plate movement was accomplished in a similar fashion to the tracking of the flame. Figure 3.7 shows that, as the metal plate touched the tube, its tracking motion was generally reversed. The time of plate reversal compared with the time of pressure increase was recorded and illustrated in Table 3.1. With all 10 tests a maximum deviation of  $6.00 \times 10^{-4}$  seconds was observed. This compares with a typical combustion event that may take 0.5 seconds as seen in Figure 3.8.

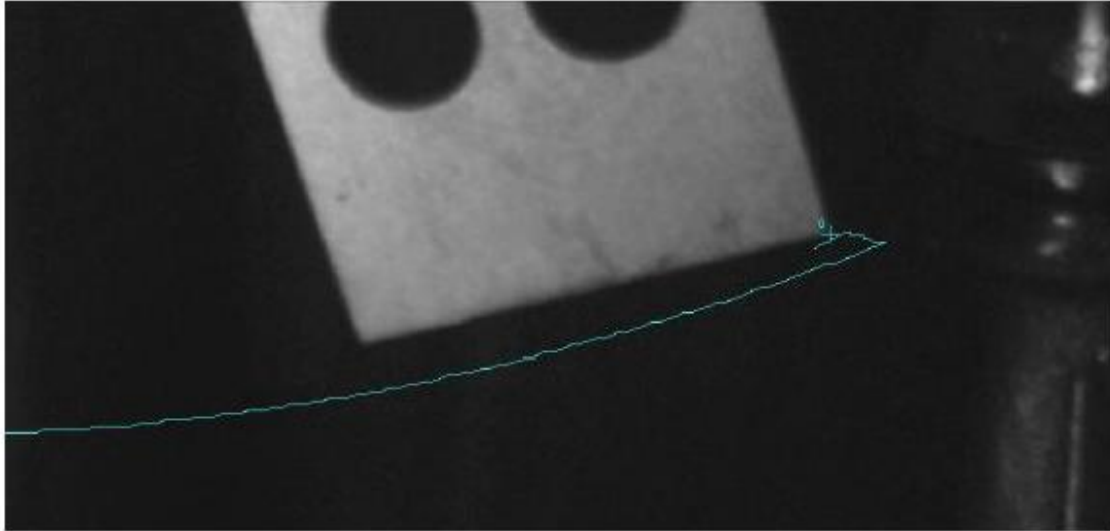


Figure 3.7: The tracked metal plate edge (green line) reverses after coming into contact with the tube

Table 3.1: Synchronisation test results

Run no.	Time of pressure increase (sec)	Time of plate reversal (sec)	Time difference (sec)	Maximum time difference (sec)
1	2.3616	2.3616	0	6.00E-04
2	1.3076	1.3073	3.00E-04	
3	1.4566	1.4560	6.00E-04	
4	1.5973	1.5970	3.00E-04	
5	1.5193	1.5190	3.00E-04	
6	1.7236	1.7233	3.00E-04	
7	1.6196	1.6193	3.00E-04	
8	1.4196	1.4193	3.00E-04	
9	1.9246	1.9246	0	
10	1.9850	1.9846	4.00E-04	

The flame position signal was tracked in accordance with the trigger signal, aligning the pressure signal, as illustrated in Figure 3.5. Comparison of the raw data shown in Figure 3.5 with Searby's work [11], shows a similar quality of pressure signal, but superior flame recordings as regards the capture of oscillatory motion. Referring back to Figure 2.17 from Searby's work [11], there seems to be a smooth flame front position which removes any opportunities for extended examination of flame front oscillatory behaviours that this research is undertaking.

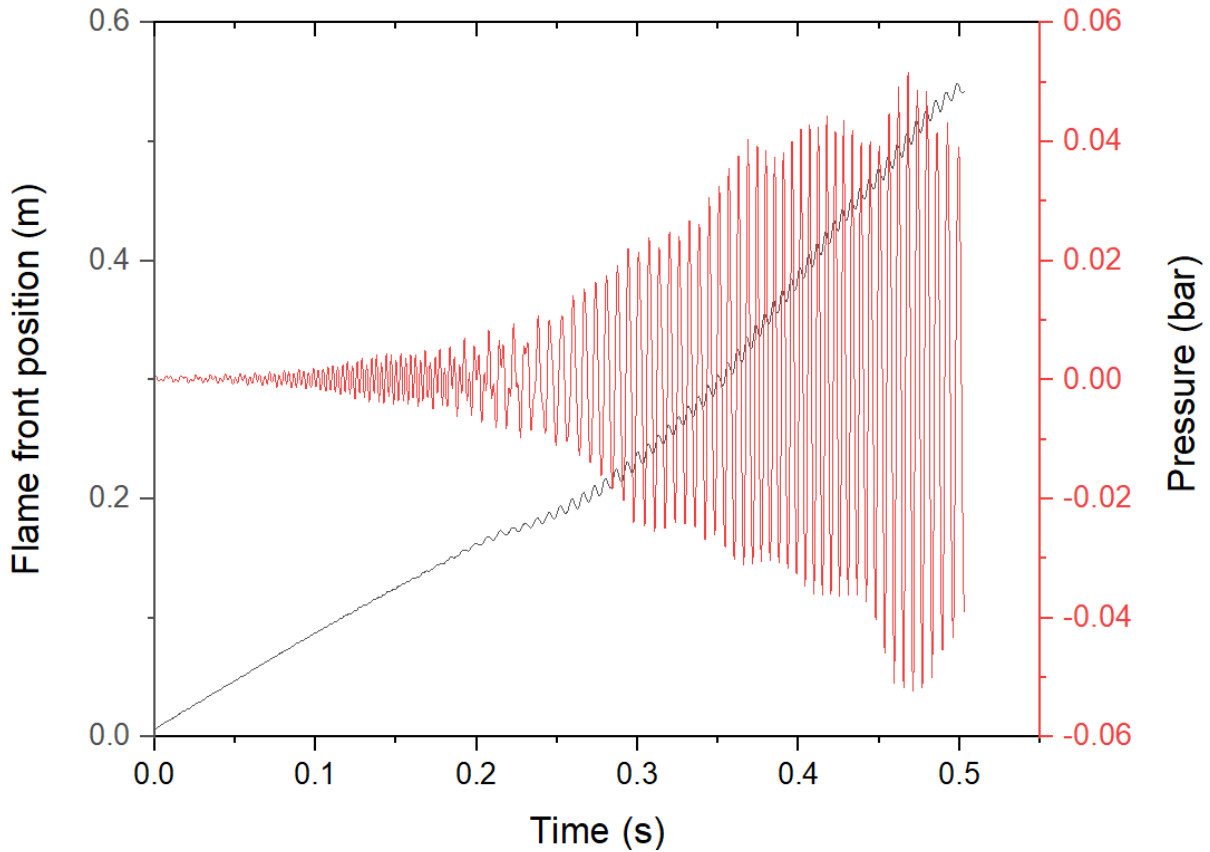


Figure 3.8: Example of a synchronised flame front position and pressure signals for methane flame at  $\phi = 1.0$ ,  $R_H = 0.2$

### 3.3 Fuel

#### 3.3.1 Fuel type

This research used propane, methane, and hydrogen fuels. All storage cylinders were stored outside the laboratory. The necessary gas for each experiment was collected using Kynar gas sampling bags which have an on/off valve to facilitate filling and self-sealing septum valves which allow collection of the fuel with a syringe [36], which stops air from being able to enter the bag. The procedure of fuel collection is given in Appendix C, whereas the complete experimental procedure is available in Appendix D.

#### 3.3.2 Calculation of rig volume

Some problems were encountered with the methods used to estimate the rig volume, namely geometric calculation and water displacement [95]. The geometrical calculation method proved to be unsuitable due to the substantial uncertainty arising from the internal structural features of the mixing fans, compression fittings, three-way valves and other components with similarly complex shapes. Consequently, the

water displacement method was employed, i.e. filling the entire rig with water and then estimating the volume by dividing the weight of this water by its density. Although this resulted in a higher degree of accuracy, it was unsuitable due to the frequent changes in the rig geometry.

The current study made use of a rig volume calculation technique [36] that was based on Boyle's law to calculate the rig volume. Boyle's law says that the pressure of an ideal gas at a constant temperature is inversely proportional to the volume of the gas at a given mass. Assuming that the gas within the rig maintains a constant temperature and acts like an ideal gas, the rig volume was determined prior to beginning a batch of experiments utilising the Druck PDCR810 pressure transducer, a syringe of known volume. At the beginning of the experiment, the total volume rig should be calculated and, to do this, a number of steps must be followed. Firstly, a vacuum is created inside the rig by expelling the air from the rig and turning off the pump. The next step is to inject 50 ml of air into the rig using a syringe. Once 50 ml of air has been injected, the syringe is removed from the injection port. Finally, it is necessary to allow 60 seconds for the pressure to stabilise. The pressure is recorded after the completion of each step, so that the volume of the rig can be calculated using the following equations [166].

$$V_1 = \frac{P_2 V_2}{P_1}$$

**Equation 3.1**

$$V_2 = \frac{50 P_3}{P_2 - P_3}$$

**Equation 3.2**

$$V_3 = 50 + V_2$$

**Equation 3.3**

$$V_4 = \frac{P_3 V_4}{P_4}$$

**Equation 3.4**

The volume of the rig can be found by taking  $V_4$  and subtracting the 50 ml of added air. The average volume of the rig is obtained once this process has been completed three times. The purpose of finding the rig volume is to determine the amount of each fuel that is added to the rig; this is dependent on the equivalence ratio and blend composition. Furthermore, a justification for why this method should be carried out before each experiment is that the rig is occasionally used by other faculty members in different configurations. Since the tubes in the rig are often dismantled, the total rig volume would be affected. As shown in Table 3.2, the total volume of the rig produces an average rig volume of 1163 ml. The different volume subscripts correspond to Table 3.2.

**Table 3.2: The readings of pressure and volume**

S/N	Pressure (atm)			Time (secs)			Volume (ml)		
	1	2	3	1	2	3	1	2	3
1	0.9593	0.9591	0.9592	0	0	0	1159.5	1157.0	1156.6
2	0.9574	0.9575	0.9574	20	20	20	1161.8	1158.9	1158.8
3	0.9179	0.9179	0.9178	35.58	35.18	35.13	1211.8	1208.9	1208.8
4	0.9157	0.9157	0.9155	60	60	60	1214.8	1211.8	1211.8
<b>Total Volume of Rig</b>							1164.8	1161.8	1161.8

### 3.3.3 Calculation of fuel volume

Fuel volume was calculated on the basis of the equivalence ratio Equation 2.8 detailed in the last chapter. This type of equivalence ratio works well with single air-fuel mixtures, but it cannot be employed for the mixture of two fuels or more. This research employed the  $R_H$  method for the systematic adding of hydrogen to the fuel mixture. This method was suggested by Yu et al. [12] using Equation 2.11 ( $\phi$ , equivalence ratio) and Equation 2.12 ( $R_H$ , hydrogen addition). The chief virtue of this methodology is that the quantity of hydrogen addition has no dependence on the primary fuel/equivalence ratio. Table 3.3 shows an example of the mixtures used for testing in this research with the mole fraction (employing Equation 2.10–2.12) and calculated laminar burning velocity (employing CHEMKIN [167]) and showing volumes of hydrogen and methane for every equivalence ratio at varying hydrogen addition levels. In total,

122 mixtures were tested, with burning and recording being done three times for each mixture, making 336 runs in total. The standard deviation of the three maximum pressure values for every mixture was calculated (see Table 3.3), with a range from  $9.96 \times 10^{-05}$  –  $6.04 \times 10^{-02}$  bar. Since each mixture was performed three times, the procedure for selection of one representative, run of the three repeat runs, is available in Appendix E.

Table 3.3: Tabulated laminar burning velocity, mole fraction, volume for methane – air mixtures with hydrogen addition,  $R_H$  and the standard deviation

$R_H$	Equivalence Ratio, $\phi$	Burning Velocity, $U_L$ (m/s)	Mole Fraction		Volume, mL		Standard Deviation (bar)
			Methane	Hydrogen	Methane	Hydrogen	
<b>0</b>	0.8	0.280	0.078	0	90.18	0	8.51E-03
	0.9	0.350	0.086	0	100.48	0	2.28E-03
	1.0	0.389	0.095	0	110.58	0	4.22E-02
	1.1	0.392	0.104	0	120.49	0	4.49E-03
	1.2	0.340	0.112	0	130.22	0	1.82E-02
	1.3	0.240	0.120	0	139.77	0	2.03E-02
	1.4	0.130	0.128	0	149.14	0	6.04E-02
	1.5	0.090	0.136	0	158.34	0	1.17E-02
<b>0.1</b>	0.8	0.357	0.070	0.027	81.98	31.29	3.52E-02
	0.9	0.435	0.079	0.027	91.34	31.29	4.22E-03
	1.0	0.469	0.086	0.027	100.53	31.29	2.84E-03
	1.1	0.470	0.094	0.027	109.54	31.29	5.62E-03
	1.2	0.422	0.102	0.027	118.38	31.29	5.23E-04
	1.3	0.324	0.109	0.027	127.06	31.29	2.13E-02
	1.4	0.210	0.117	0.027	135.58	31.29	5.94E-03
	1.5	0.128	0.124	0.027	143.95	31.29	1.15E-02
<b>0.2</b>	0.8	0.436	0.065	0.049	75.15	57.36	2.25E-03
	0.9	0.507	0.072	0.049	83.73	57.36	4.87E-03
	1.0	0.546	0.079	0.049	92.15	57.36	4.61E-03
	1.1	0.550	0.086	0.049	100.41	57.36	3.11E-02
	1.2	0.510	0.093	0.049	108.51	57.36	2.18E-03
	1.3	0.420	0.100	0.049	116.47	57.36	4.62E-04
	1.4	0.290	0.107	0.049	124.28	57.36	3.50E-03
	1.5	0.170	0.113	0.049	131.95	57.36	1.61E-02
<b>0.3</b>	0.8	0.520	0.060	0.068	69.37	79.42	5.60E-03
	0.9	0.590	0.066	0.068	77.29	79.42	6.43E-03
	1.0	0.620	0.073	0.068	85.06	79.42	1.26E-03
	1.1	0.630	0.080	0.068	92.68	79.42	1.88E-03
	1.2	0.590	0.086	0.068	100.17	79.42	3.28E-04
	1.3	0.500	0.092	0.068	107.51	79.42	1.05E-03
	1.4	0.380	0.099	0.068	114.72	79.42	3.18E-03
	1.5	0.260	0.105	0.068	121.80	79.42	3.32E-02
<b>0.4</b>	0.8	0.590	0.055	0.085	64.41	98.33	9.15E-03
	0.9	0.660	0.062	0.085	71.77	98.33	6.03E-03
	1.0	0.690	0.068	0.085	78.98	98.33	5.28E-03
	1.1	0.700	0.074	0.085	86.06	98.33	2.83E-02
	1.2	0.670	0.080	0.085	93.01	98.33	9.96E-05
	1.3	0.590	0.086	0.085	99.83	98.33	9.36E-04
	1.4	0.470	0.092	0.085	106.53	98.33	8.52E-04
	1.5	0.340	0.097	0.085	113.10	98.33	2.32E-02

### **3.4 Experimental errors**

Any experimental scenario inevitably contains errors. Errors can be classified into two categories: systematic errors and random errors. Systematic errors are those that occur generally, though not always, due to errors in the way the data is acquired. Random errors do not occur in every set of experimental data. A number of precautions were taken to mitigate any errors that might be present.

#### **3.4.1 Systematic errors**

It was crucial that the data acquisition system was properly calibrated to prevent systematic errors. With the optical data acquisition system, the smallest error in angle of the camera lens and the tube could create a systematic error which would appear in every recording if it were not corrected. Such errors were eliminated through the alignment of the tube with the camera software's horizontal grid display, with realignment taking place following a number of experimental runs. It was also noted that the high-speed camera, after prolonged use, would begin producing high frequency noises that would cause systematic errors when recording the flame. To stop this occurring, after every 10 experiments current session referencing (CSR) was undertaken.

In order to prevent systematic errors in the pressure acquisition system it was crucial to select the right settings using the charge amplifier interface. It was shown that if the settings were not correct then the pressure signal was not correct either. It was also important to ensure that the pressure transducer was not disconnected from the charge amplifier whilst still turned on, as it was shown that this would overload the charge amplifier. If the charge amplifier is overloaded, one cannot just restart the unit; it must be left for a number of hours of recovery. When the charge amplifier experiences overload then the "overload" button will flash red and, even at ambient pressure, will display negative pressure readings.

### **3.4.2 Random errors**

Table 3.1 shows a synchronisation error caused by the pressure-flame position synchronisation; it would appear that this is a random error. This is a small error and may, therefore, be disregarded. A major source of random errors in this research was gas cross-contamination. This happens when different types of gas were collected using syringes and sampling bags that have already been used for others. All syringes and sampling bags should have clear labels to ensure they are only used for a single type of gas.

Random errors were also caused by gas dilution. The gas bags employed in this experiment have septum valves for gas collection, similar to those employed in the rig's injection port. In time, the septum will experience wear and be unable to self-seal, initiating leaks which mean the gas will be undiluted. This was a cause of error that frequently went unnoticed and was potentially serious. If it was clear that wear had occurred, the septum on the gas sampling bags and on the rig was immediately replaced. One important requirement of this research is that the fuel-air mixture should be homogeneous. Random errors may be present if under-mixing or over-mixing occurs. Fuel mixtures should undergo mixing for exactly three minutes every time to ensure that all experiments were using the same consistent mixture.

Errors can occur with pilot flame ignition if there is a lack of consistency in the time between opening the ignition port and ignition itself. Certain fuel mixtures may ignite more swiftly than others, which also contributes to mixture dilution. The angle at which the pilot flame was held at the ignition port can also cause random errors. To minimise this problem, it was ensured that the pilot flame was consistently orientated in the same position. Gas related random errors listed above contributes to the calculated standard deviation of the maximum pressure listed in Table 3.3.

### **3.4.3 Measurement errors**

- i. To remove the air and combustion product from previous experiments the rig was vacuumed to a pressure of almost -0.9 bar each time, that means the first time 10% of residuals were left inside the rig. By doing this three times, the maximum residuals that can exist inside the rig is 0.001% which wouldn't cause

any change in the flame behaviour. When the vacuum pressure reading is around -0.8 bar, which is the worst case, the inaccuracy is about 1%.

- ii. To calculate the recording distance, the number in point B (597 mm) was subtracted from the number in point A (30 mm) as seen in Figure 3.9. The inaccuracy encountered at these two points is  $\pm 1$  mm which equate 0.5%.

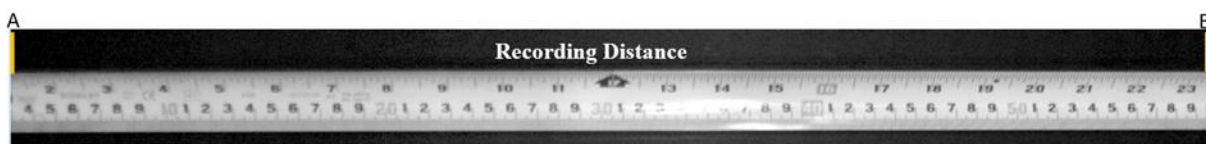


**Figure 3.9: Measuring the recorded distance of the tube**

- iii. The inaccuracies were caused by the syringe ranges between  $\pm 0.5$  ml, which equated to 1%. This, however, has no effect on the accuracy of the equivalency ratio calculation.
- iv. The overall inaccuracy in experimental procedure was about 2% to 3%.

## 4 POST-PROCESSING

### 4.1 Introduction

In this chapter the methodology employed for the conversion of raw data (pressure signals/flame imagery) into usable data to compare different flame. Flame propagation was effectively captured using high-speed imagery, but the experiments overall generated many frames which required analysis. Manually analysing this number of frames would take considerable time and labour, so it was clear that the workflow had to be automated.

The three primary software programs employed for the analysis were Phantom Camera Control [168], VirtualDub [169], and MATLAB [170]. Phantom Camera Control was employed for preparing raw video files which were then processed using MATLAB. Flame positions as a function of time were found by processing the flame recordings with automated tracking through MATLAB. The flame front and flame tail were both tracked, which allowed for the flame length and flame mean position to be calculated. In addition, flame pixel size was tracked to attempt to create a representation of the area over which the flame was projected.

Having undertaken tracking, MATLAB was additionally employed in processing raw data so that the flame velocity and distance amplitude could be calculated. The calculation of these parameters was undertaken so that the influence on flame propagation of thermoacoustic oscillations could be quantified. The most significant aspects of velocity and distance amplitude have been tabulated in order to compare them, and this comparison is subject to a detailed discussion in this chapter. To simplify matters, analysis was only undertaken of the flame front.

To undertake further analysis of thermoacoustic oscillations, velocity and distance amplitude were both subjected to frequency analysis to determine temporal frequencies that resulted in oscillations. Phase and frequency analysis was also undertaken on the pressure signals registered at the end of the tube in order to find the correlation between pressure and the flame's thermoacoustic oscillations.

## **4.2 Classification of flames**

The images of flames obtained by this research are similar to the findings of Coward and Hartwell [69], Guenouche [6], and Searby [11]. At the start, the flame showed steady propagation through the tube, but after it had crossed the halfway point a period of oscillation occurred in which the shape of the flame underwent dramatic transformation, subsequently continuing to high oscillation. Post experiment processing had various aims, including the tracking of the progress of the flame through the tube and providing detailed measurements of the changes in the shape of the flame.

## **4.3 Preparation of raw video**

### **4.3.1 Cropping and conversion of video**

For all the high-speed films, only around 20% of the total number of frames showed flame propagation. This was as a result of the triggering system, which was reliant on a technician seeing that a flame was propagating down the tube and activating the trigger. Because of this, far more data than the desired event was gathered because the human reaction times varied between experiments and between operators. Phantom Camera Control (PCC) [168] software was employed to remove extraneous material by undertaking a manual search for images in which a flame was present. These files were then extracted and saved as .AVI files capable of being read by MATLAB [170]. An additional cut raw version was saved in .cin, the proprietary camera format, saving pertinent information, e.g., exposure time and time since trigger was activated.

This research also employed VirtualDub [169] in order to crop video image sizes prior to them being processed further by MATLAB. The width and height of the video was cropped so that only the area in which the flame could be seen remained, thereby reducing the necessary amount of time required for computation. Once the videos were edited they were imported into MATLAB as Bitmaps, with VirtualDub numbering them in sequence.

#### 4.4 Flame front, tail, thickness and area tracking

Recording of flame progression was generally achieved through the identification of the flame's leading-edge, with this being used as the point for the determination of flame velocity and for analysing frequencies. The advantage of the leading edge is that it is easy to find in natural light. Nevertheless, it should be noted that flames are 3-D shapes and it would have been possible to select alternative reference points. When flame shapes remain consistent as they travel through the tube then velocities will be identical at all reference points. Nevertheless, if flames start to oscillate due to the acoustic field's influence, the shape will change and, thus, calculated velocities for specific reference points will vary. It has been demonstrated that this may cause problems in determining data for turbulent premixed velocities in which various reference positions were selected dependent on the specific experimental methodology [171]. A graphical illustration of determination of flame front position, tail and thickness from the filmed image seen in Figure 4.1.

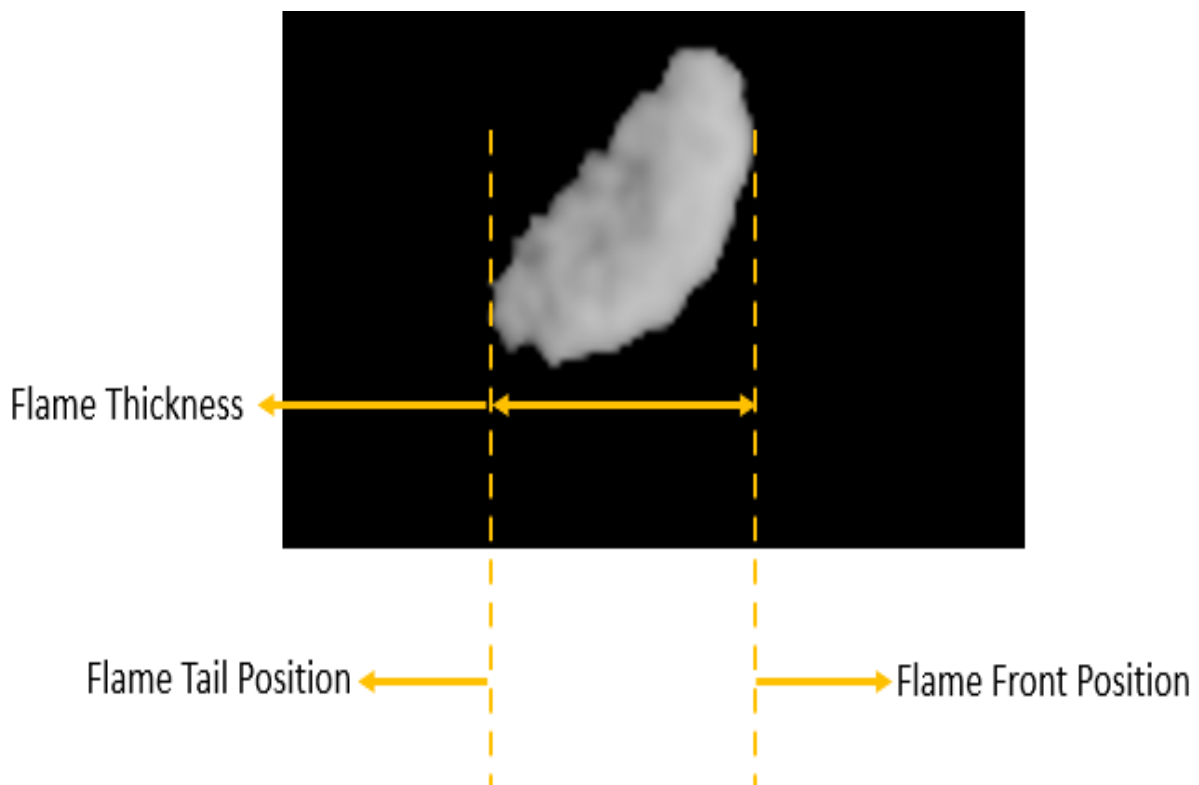


Figure 4.1: Flame front, tail, and thickness from the filmed images

I) The flame's leading-edge. It was easy to find this, being the initial point at which light appeared within unburned gas in natural light images. There was usually sharp definition at the edge of the flame, making the value easy to ascertain. This reference position is the one chosen by past researchers [161], [36].

II) Flame tail, at the back edge of the flame. This represents the point furthest back in the burned gas that the visible flame can be found. It could be problematic identifying this because the flame's light levels were frequently low as burned gas surrounds the flame making the edge diffuse. This is the reference position with the greatest sensitivity to threshold values chosen in the course of image processing.

The area of the flame was calculated as the number of white pixels existing in each frame covering the area of the projected flame. Whilst this figure is not an accurate measure of the actual area of the flame, it is useful for relative measurements of flame area and is easy to find. The area of the flame was not converted into metric units so that it would not become confused with the actual flame area.

The next step involves investigating how the flame area is affected by different thresholding. Hereby, a level between 0 and 1 is defined to transform the image into a binary picture comprising only black and white pixels, i.e. all grey pixels are eliminated. Figure 4.2 (b to c) shows the impact of the different thresholding levels, namely at 0, 0.5, and 0.9 respectively on the flame image. The corresponding flame area at 0, 0.5, and 0.9 levels of thresholding is shown in Figure 4.3. This figure shows no clear differences in the flame area at the different thresholding levels.



Figure 4.2: Image thresholding. (a) Grayscale image. (b) zero threshold. (c) 0.5 threshold. (d) 0.9 threshold

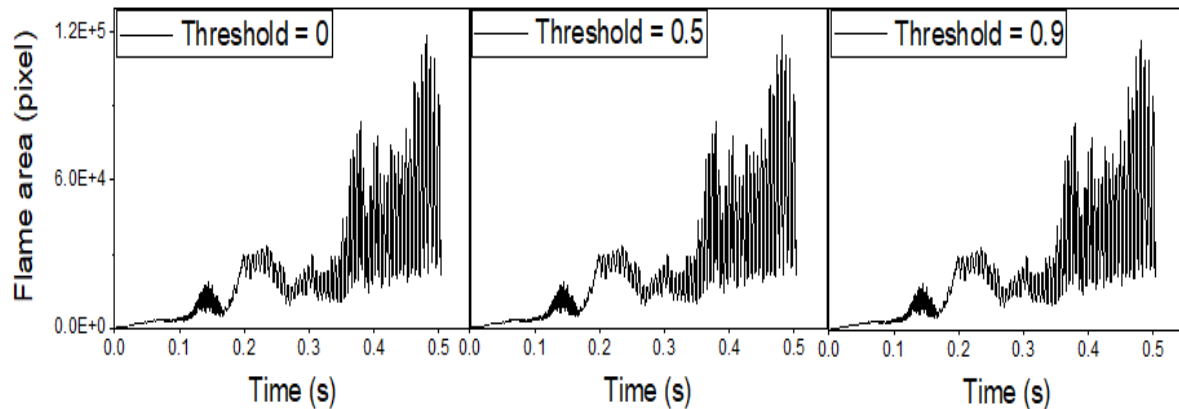


**Figure 4.3: The corresponding flame area at 0, 0.5, and 0.9 levels of thresholding**

The pixel-distance conversion rate was used to multiply the tracked values; for example, after calibration a conversion rate of  $4.4 \times 10^{-4}$  m/pixel was used. In the event that the imaging equipment was moved, this value might have changed and an additional calibration would be necessary. The process of tracking every part was undertaken for every flame within the flame recording. Tracking was only undertaken when the flame tail became visible, eliminating errors regarding flame area and thickness. Tracking ended when the flame front comes to the last pixel in the recorded flame.

#### **4.4.1 Analysis of flame front**

The tracked flame front was employed to quantify flame oscillation magnitude. Nevertheless, it was problematic to undertake quantification of these oscillations on the sole basis of flame front position. In Figure 4.4(a), it appears that the flame front position comprises low-frequency components (steadily increasing) and high-frequency components (oscillating), making it appear logical to separate the flame into oscillating/small oscillating components. In this analysis, a  $\phi = 1.0$  flame with  $R_H = 0.4$  hydrogen was used as our example.

Filtering of flame positions was achieved employing a low-pass Finite Impulse Response (FIR) filter for the removal of high-frequency components. FIR filters are frequently used as they have a finite length of impulse response time. FIR filters were selected because they have greater stability than Infinite Impulse Response (IIR) filters [172]. The variations found when using 26 Hz and 100 Hz low-pass filters are shown in

Figure 4.4. Figure 4.4(a) shows that the 100 Hz filter offered a filtered flame position with significant deviation from the original flame position. This produced a distance amplitude that contained low-frequency components, as illustrated in Figure 4.4(b), which is shown by the fact that the underlying value (red line) steadily increases in comparison with the 26 Hz filter, which fluctuates close to the zero-axis.

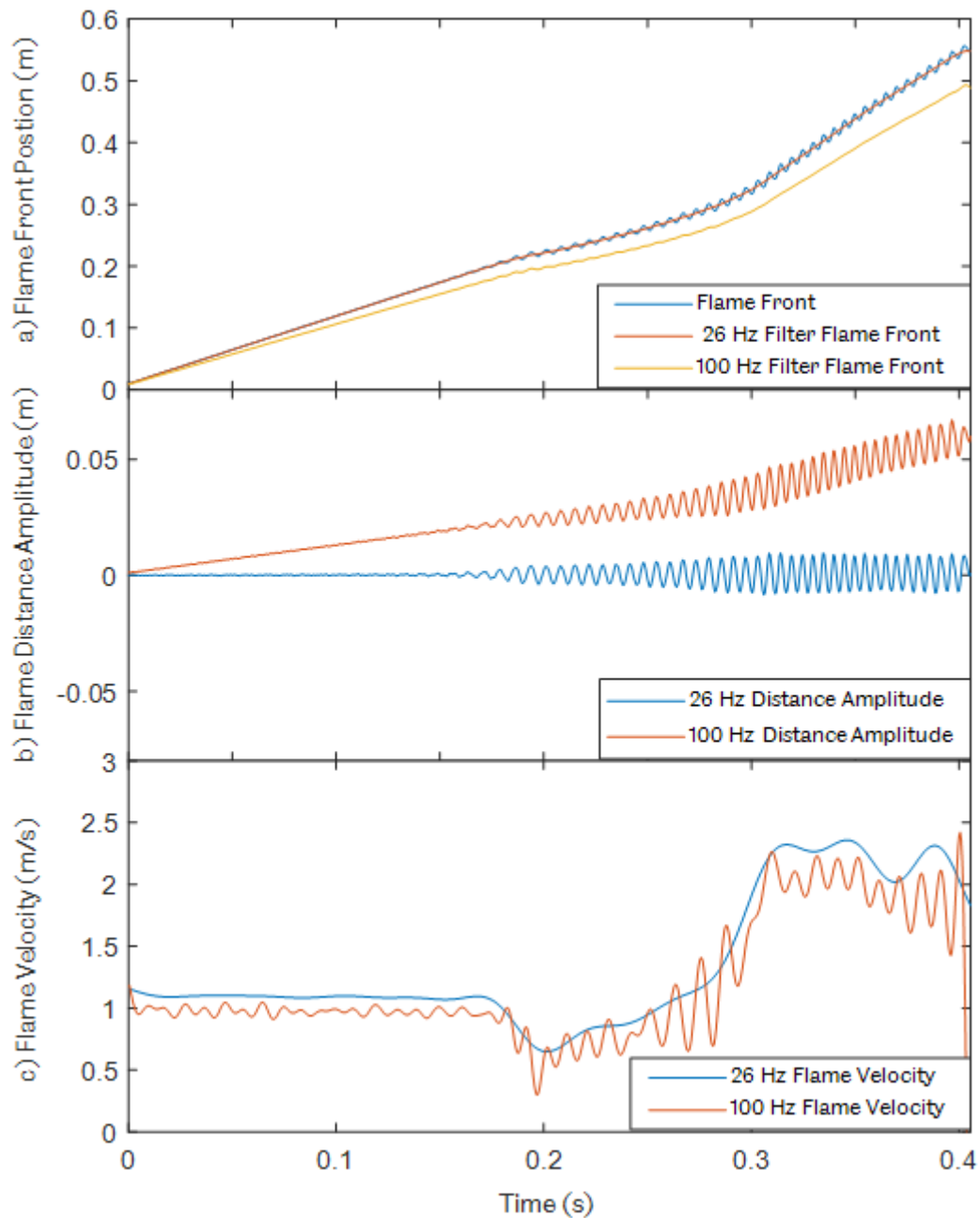


**Figure 4.4: The influence of different passband frequencies on a) flame position and b) flame distance amplitude and c) underlying flame velocity**

Having been filtered, differentiation was then applied to the underlying flame front in order to find the underlying flame velocity (low-pass velocity) as seen in Figure 4.4(c). The underlying velocity may be imagined as being the velocity of the flame with no high-frequency oscillations, i.e., the overall speed of the flame. The interpretation of the flame's velocity change when no high-frequency oscillations are present facilitates analysis. The equation below was employed for the calculation of velocity, with  $ds$  representing the displacement differential and  $dt$  representing the time interval, in this instance 1/2000 seconds, a calculation made on the basis of the camera's frame rate:

$$v = \frac{ds}{dt}$$

**Equation 4.1**

The underlying velocity found with both the 26 Hz filter and the 100 Hz filter is shown in Figure 4.4(c). Such speed changes are helpful in subsequent analysis where the high pass velocity is calculated by applying differentiation to the flame distance amplitude. The properties of the filter are listed in Table 4.1. To maintain the frequency of components beneath 80 Hz and eliminate higher frequencies, the passband frequency to 26 Hz, with a 1 dB passband ripple; meanwhile, a stopband frequency of 204 Hz and a 40 dB attenuation was used. The stopband frequency was set at 204 Hz for the creation of a short filter for the accommodation of short length data. If the stopband frequency is reduced a long filter is produced, which can cause filtering errors in certain instances [173].

**Table 4.1: The properties of the low-pass finite impulse response filter**

<b>Filter Property</b>	<b>Value</b>
<b>Passband Frequency</b>	26 Hz
<b>Stopband Frequency</b>	204 Hz
<b>Passband Ripple</b>	1 dB
<b>Stopband Attenuation</b>	40 dB
<b>Sampling Rate</b>	2000 Hz

Following filtering, the flame distance amplitude ( Figure 4.5(e)) was found by subtracting the low-pass flame front ( Figure 4.5(c)) from the original flame front position ( Figure 4.5(a)); this is effectively the flame front's high-pass component. Equation 4.1 is used to compute Figure 4.5(b), (d), and (f) as respective derivatives of (a), (c) and (e).

Having separated raw velocity and flame front into separate parts, essential parameters underwent tabulation in order to compare them with other flames, these being the underlying start velocity (i), the maximum underlying velocity as a result of oscillation (ii), the maximum amplitude of the high-pass flame front (iii), and the maximum velocity of the high-pass (iv). Figure 4.5 shows an oscillating flame with an obvious underlying velocity peak (see Figure 4.5(d)).

It became obvious why the flame front position should be separated into low- and high-pass components. It is problematic to interpret the raw flame velocity of Figure 4.5(b) because high-frequency oscillations overshadow it. On the basis of the low-pass velocity shown in Figure 4.5(d), It appears that the flame decelerates and accelerates as a result of the high-pass velocity components that can be seen in Figure 4.5(f).

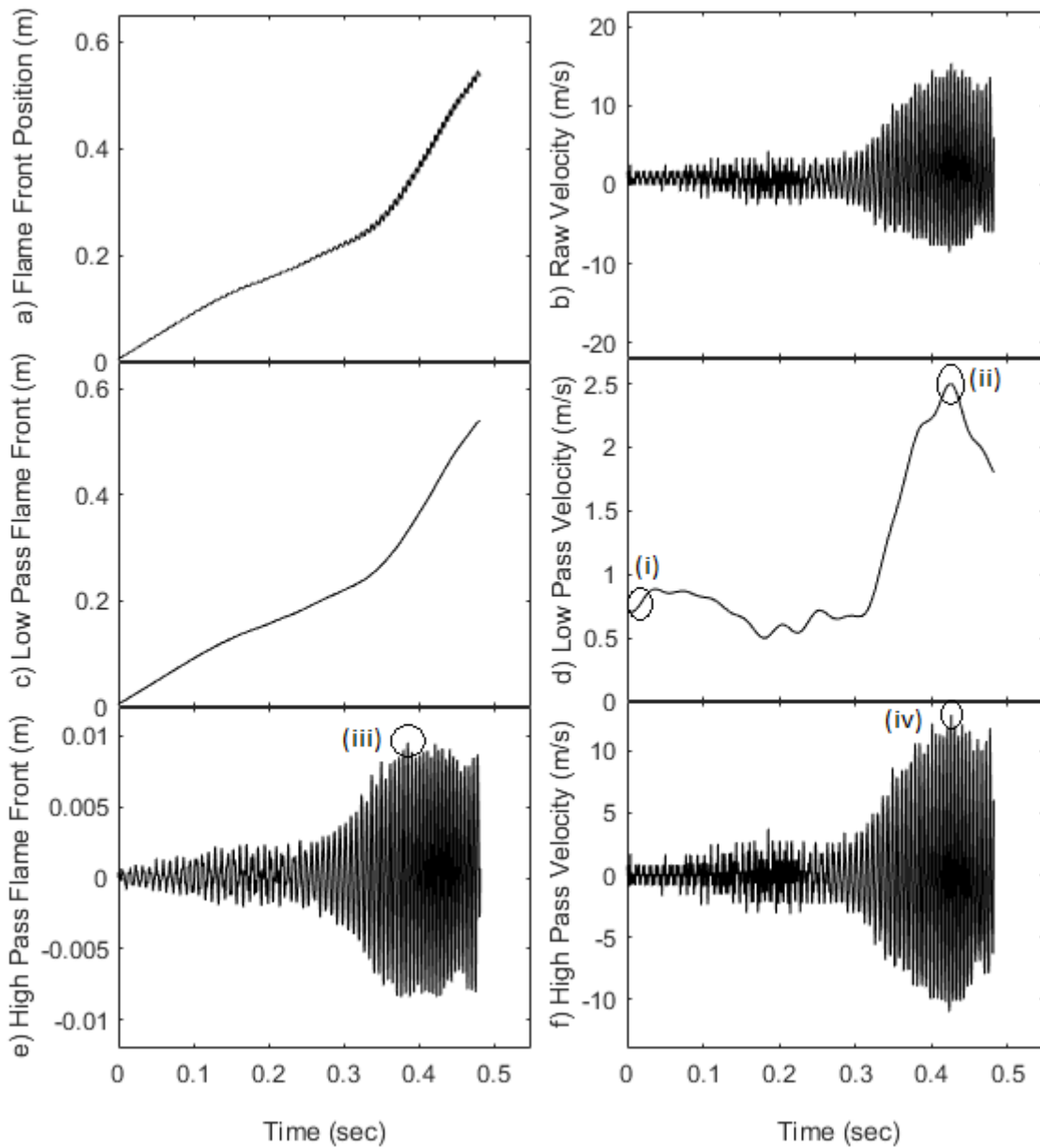


Figure 4.5: The position of the flame front and their derivatives

## 4.5 MATLAB analysis of frequency

The analysis of the frequency played a central part in this research. For understanding the thermoacoustic reactions inside the tube, an algorithm was employed for analysis of the pressure signal's spectral contents and the flame's distance amplitude, this being synchrosqueezed wavelet transform (SST).

#### 4.5.1 Synchrosqueezed wavelet transform (SST)

A significant problem with FFT analysis is that the components can be subject to spectral broadening. With standard experimental pressure signals, oscillatory components move around their specific harmonics in time, creating spectral broadening. Observing the raw data made it clear that flame propagation created a variety of resonance modes at various points through the tube, so at a specific flame position a flame might be influenced by one, two, or no acoustically driven oscillations of varying frequencies and amplitudes. Additionally, with the flame propagating through the tube, there were variations in temperature distribution which caused the excitation frequencies to change. With increases in the proportions of burned gas it can be seen that each mode's frequency should rise [7]. This problem could have been solved by cutting the signal into distinct sections and undertaking FFT individually for each one. The synchrosqueezed wavelet transform (SST) tool is a type of empirical mode decomposition tool [144], [69]. It can assist in analysis of a signal's spectral contents within the time-frequency domain, employing a combined wavelet analysis/reallocation methodology [144]. MATLAB can provide a workflow based on SST, created from the extraction of a signal's oscillatory modes.

The synchrosqueezed wavelet transform is available for use in MATLAB [84] along with a simple explanation of the execution of the wavelet synchrosqueezing algorithm in [80]. Implementing the Synchrosqueezed Transform on  $X_{total}$  produced Figure 4.6, which was able to detect the 30 Hz frequency that lasted for the whole 0.2 seconds, and also the 50 Hz frequency.

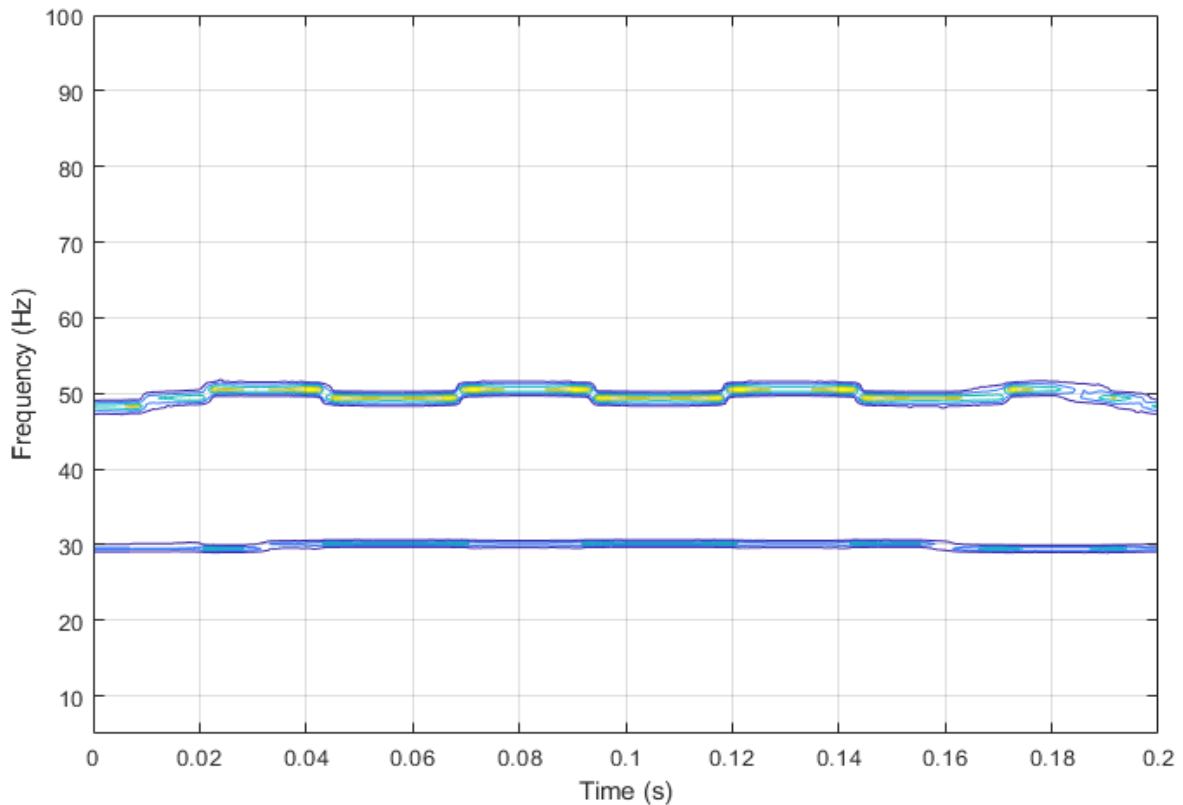


**Figure 4.6: Synchrosqueezed transform plot for  $X_{total}$ , clearly showing the existence of 2 different dominant frequencies**

The extraction process consists of four important steps. Firstly, the SST algorithm must be run for the raw signal, so that time-domain information becomes transformed into time-frequency domain information, creating the contour plot illustrated in Figure 4.7. On the basis of this contour plot, two modes were observed, one of approximately 200 Hz and one of approximately 400 Hz; these appear and decay at various points. It should be noted that the contours that can be seen signify the highest energy region in the time-frequency plane; the fact that they appeared between approximately 0.12 and 0.4 seconds demonstrates that this was the period at which the oscillations have the greatest strength.

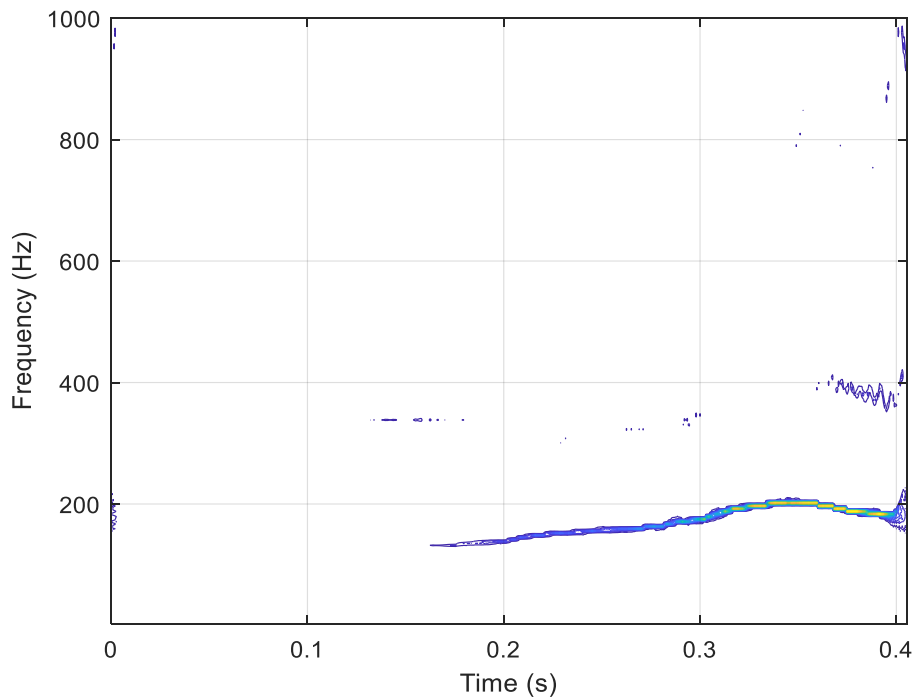


**Figure 4.7: Synchrosqueezed transform contour plot of raw signal**

The next step in this process is to apply the right penalty term, followed by the third step which is to extract the time-frequency ridges, those areas in the time frequency plane that have the greatest energy as shown by the contours illustrated in Figure 4.7. Penalty terms must be employed for performing ridge extraction if there is more than a single oscillating component contained in a time-domain signal.

In this instance, the penalty term was defined as “frequency bins scaling penalty”, which is a nonnegative scalar value in which “frequency bins” represent the intervals between the frequency domain’s samples. Frequency intervals are generally found from the MATLAB data. Effectively, penalties are introduced for frequency shifts when detecting the highest energy regions (contours) by multiplying the square of the distance between frequency bins (interval) by the penalty value [147]. An example would be a frequency bin having a 3 Hz interval with a penalty value 10, creating a penalty equivalent to 90 Hz, which prevents a time frequency ridge jumping to any other ridge less than 90 Hz away.

Figure 4.8 illustrates what happens when the penalty term was applied to the contours of Figure 4.7. Figure 4.8 illustrates the three plots with a variety of penalties applied. For each plot, the three dashed lines are referred to as “time-frequency ridges”,

representing the instantaneous frequencies of our three oscillatory components against time.

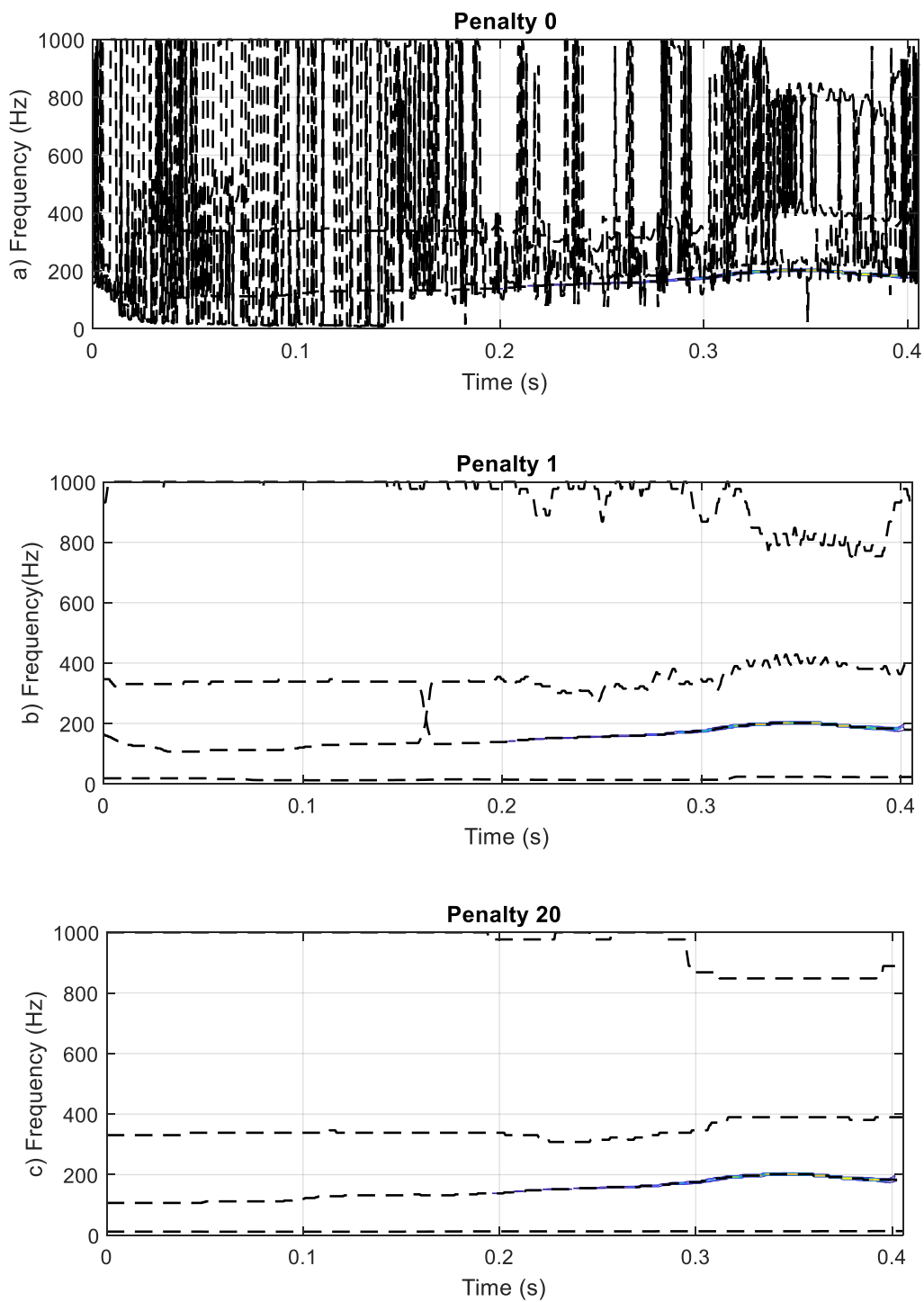


**Figure 4.8: Penalty levels' effect on the frequency ridges formation formed from a) no penalty, b) penalty = 1, and c) penalty = 20**

MATLAB's frequency ridge detection algorithm found these time-frequency ridges, representing the trio of oscillatory components comprising the raw signal. This detection algorithm was employed for finding the region containing the highest energy within the time-frequency plane [174] created by the SST, as shown in Figure 4.7. If no penalty is imposed, time-frequency ridges can leap across modes, meaning that the modes will be incorrectly reconstructed, as shown in Figure 4.8(a). The algorithm permits frequency jumping, allowing frequent intersection of ridges; on reconstruction this would lead to the production of wideband frequency signals, which would completely destroy the validity of the process. The influence of employing a penalty of 1 is illustrated in Figure 4.8(b), with the time-frequency ridges showing significant differences from those that have no penalty applied. The ~1000 Hz mode was separated from other modes, but the ~200 and ~400 Hz modes were close together. A penalty of 20 creates time-frequency ridges with distinct separations, as illustrated in Figure 4.8(c). Having discovered the most appropriate penalty, the time-frequency ridges were extracted as part of step three; step four was to reconstruct these extracted ridges.

An  $R_H = 0.3$ ,  $\phi = 1.0$  methane flame pressure signal was used for the SST workflow; the pressure signal SST contour plot is illustrated in Figure 4.9. If only considering the contour plot, two distinct modes were identified, namely one each in the 100-200 Hz and 300-400 Hz regions. As presented in Figure 4.10, time-frequency ridges were produced to enable an analysis of the signal. While the algorithm identified a third mode; this was clipped at the level of the Nyquist frequency, i.e. half the pressure signal's sampling rate. Since it is not capable of accurately representing the third mode, the clipped mode was not analysed. The time-frequency ridges indicate that each mode's frequency increased or decreased at various time points, in line with Markstein's assertion [7]. Subsequently, as presented in Figure 4.11, the Inverse Synchrosqueezed wavelet transform (ISST) was used to convert the time-frequency ridges back to the previous domain, whereby each respectively possessed mode frequencies of ~200 Hz and ~400 Hz. The SST and ISST codes are available in Appendix G.

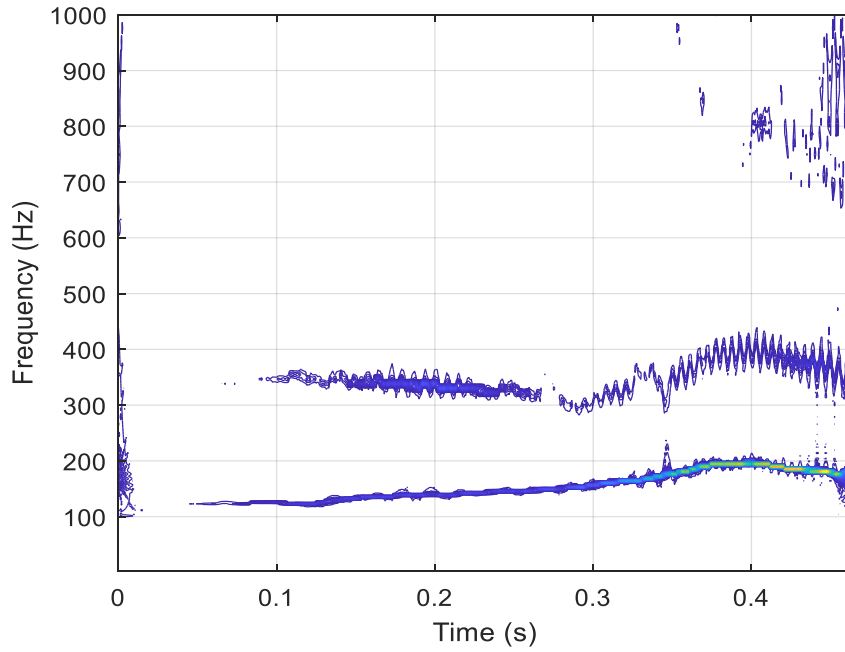


Figure 4.9: SST contour plot of a pressure signal of a  $\phi = 1.0$ ,  $R_H = 0.3$  methane flame

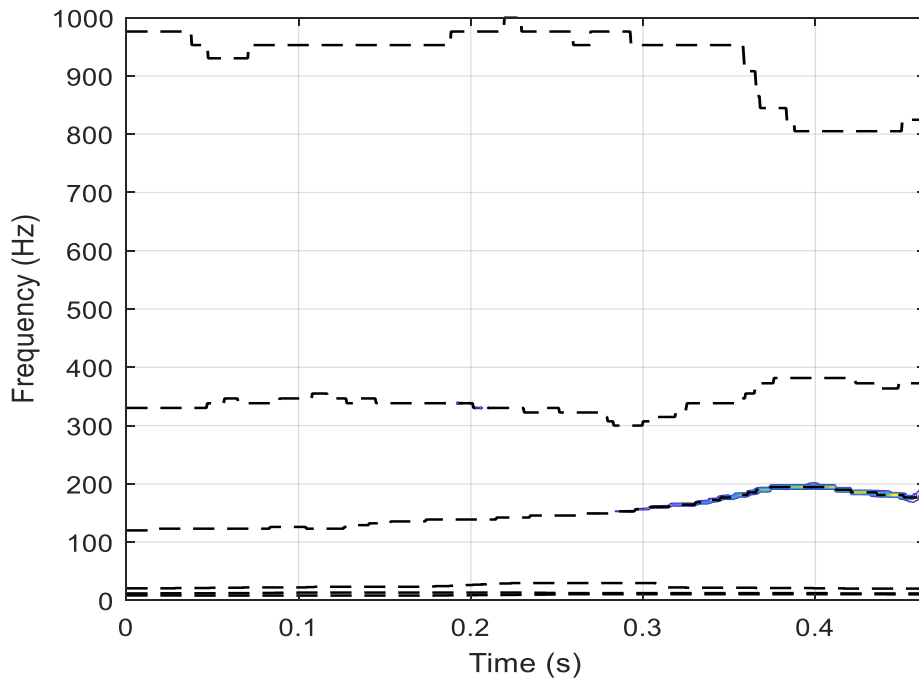


Figure 4.10: SST frequency ridges at penalty of 20 of a pressure signal of a  $\phi = 1.0$ ,  $R_H = 0.3$  methane flame

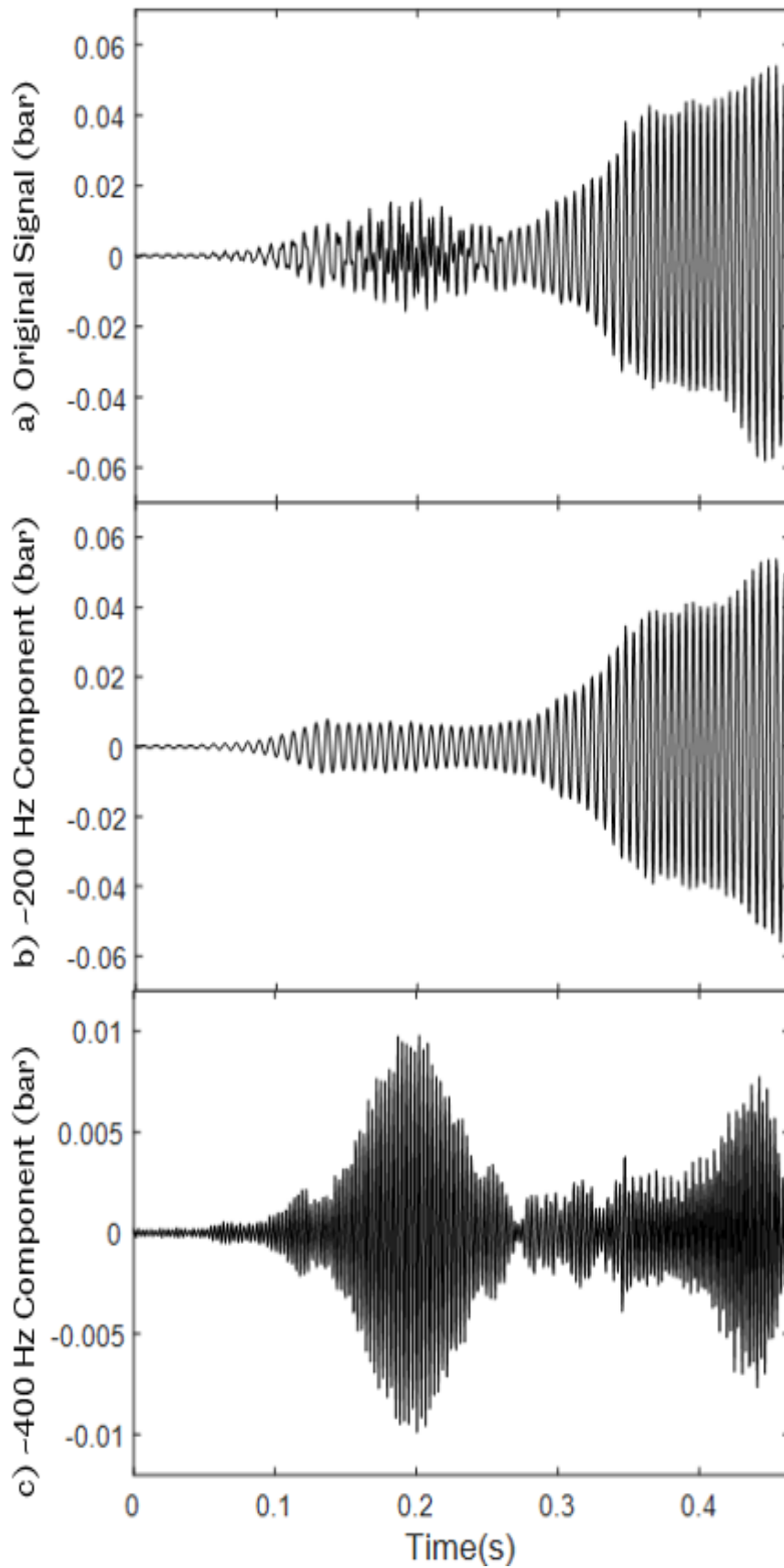


Figure 4.11: Reconstruction of a) the original pressure signal into b) -200 Hz pressure component, and c) -400 Hz pressure component of a  $\phi = 1.0$ ,  $R_H = 0.3$  methane flame

#### 4.5.2 Phase study

Thermoacoustic influences often have associations with rapid acceleration for confined premixed flames [174]. A phase study was undertaken of pressure signal/flame area in order to find the correlation between pressure signal and heat release. As mentioned previously, flame front length represents the flame's projection in 2D and is employed as a representation of the heat release of the flame. The instantaneous phase of time domain pressure and flame area signals was obtained using a Hilbert transform (define relationships between real and imaginary parts of complex signals) [175]. Having obtained the instantaneous phase, the phase difference was calculated for the signals and plotted with the pressure signal to ascertain the correlation. A signal's phase comes from its imaginary section. It found this problematic with the experimental data because pressure and flame front position only comprise actual components. By imposing a quarter-cycle time shift onto the signal, the Hilbert transform can generate imaginary components (see Smith [158]). Before the Hilbert transform was performed, it was crucial that the signal should be filtered using a bandpass filter to effect the removal of undesired frequency bands (see Cohen [142]).

The function was tested on wave  $X_2$  and  $X_3$  to obtain their phase. Based on their information in Table 2.3, both waves were similar in frequency and amplitude, but with a different phase, where  $X_3$  leads  $X_2$  by  $90^\circ$ . Figure 4.12(a) shows the plot for their instantaneous phase, where it could be clearly seen that wave  $X_3$  started with an instantaneous phase of  $90^\circ$  whereas  $X_2$  started with  $0^\circ$ . The phase difference was calculated by subtracting the instantaneous phase of  $X_2$  with  $X_3$  for the whole duration in Figure 4.12(b), and it was found to be constant at  $-90^\circ$ .

In order to use the Hilbert Transform on a signal, it is important to apply a bandpass filter to obtain the phase of the desired frequency. Applying the Hilbert transform directly to an unfiltered signal would still give the phase information, but it would be the summation of phase information from other frequencies, making it difficult to understand. Similar to the example in Figure 4.12, wave  $X_2$  and  $X_3$  were used since they contain a similar single frequency of 50 Hz, but with a different phase. If  $X_1$  was used for this example, the phase difference would not be constant at  $-90^\circ$ .

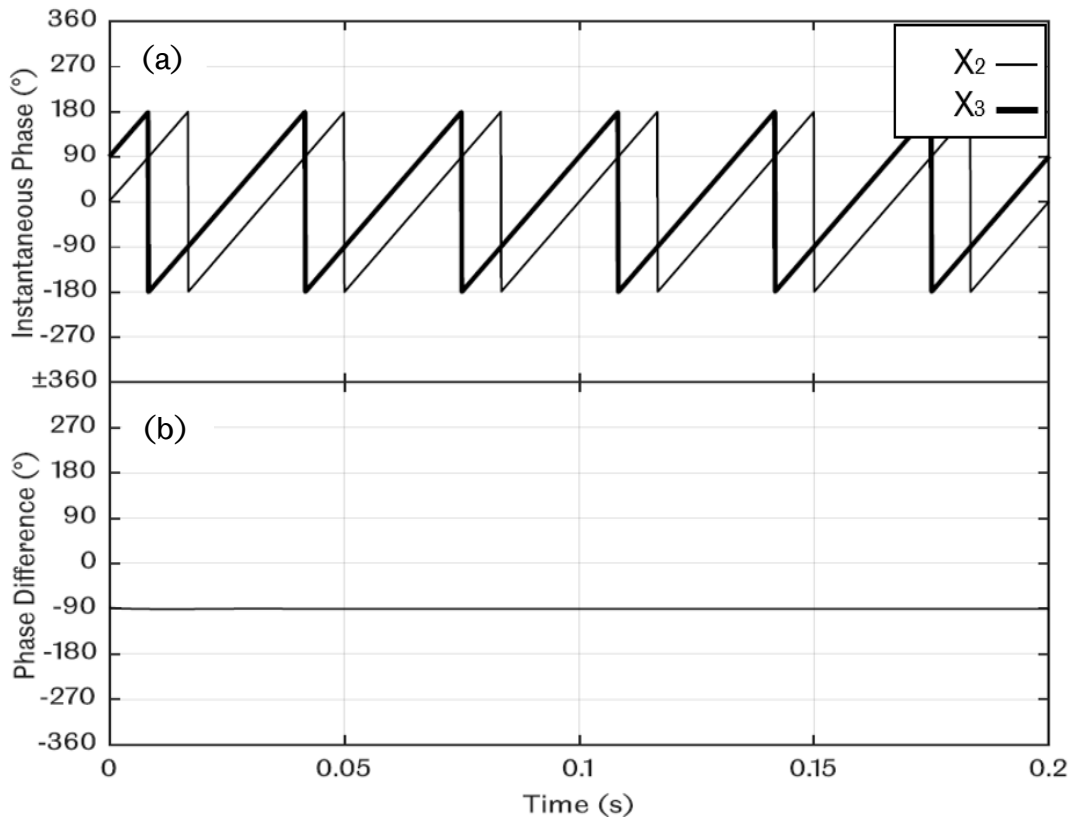


**Figure 4.12: Plots of a) instantaneous phase of  $X_2$  and  $X_3$ , followed by b) phase difference between both signals**

In the present research, because of the components of  $\sim 200$  Hz and  $\sim 400$  Hz were observed, the bandpass filter was used to separate the signal into a pair of components. Figure 4.13 illustrates the quartet of phase plots that were constructed, of  $\sim 200$  Hz and  $\sim 400$  Hz for both flame area and pressure. All four plots displayed the predicted sawtooth wave shape, signifying the phase angle of a sinusoid against time.

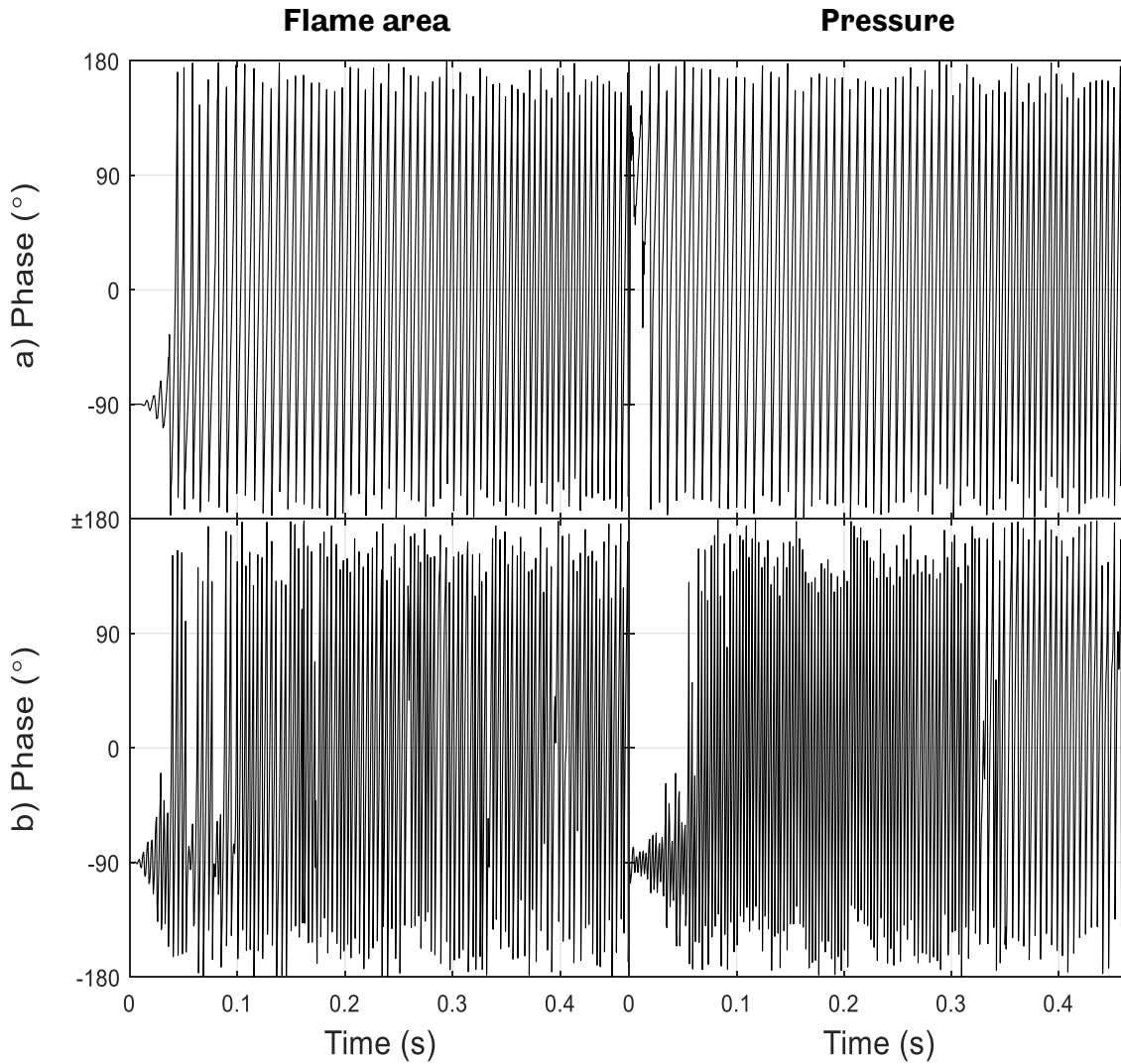


**Figure 4.13: Phase plots for a) ~200 Hz components, b) ~400 Hz components of a  $\phi = 1.0$ ,  $R_H = 0.3$  methane flame**

Direct subtraction among the oscillatory modes was used to estimate the phase difference between the respective oscillatory components: the phase of the ~200 Hz flame area was subtracted from the phase of the ~200 Hz pressure; this was also done for the components at ~400 Hz. The phase differences between the flame area signal and the pressure signal for the components at both ~200 Hz and ~400 Hz are depicted in Figure 4.14.

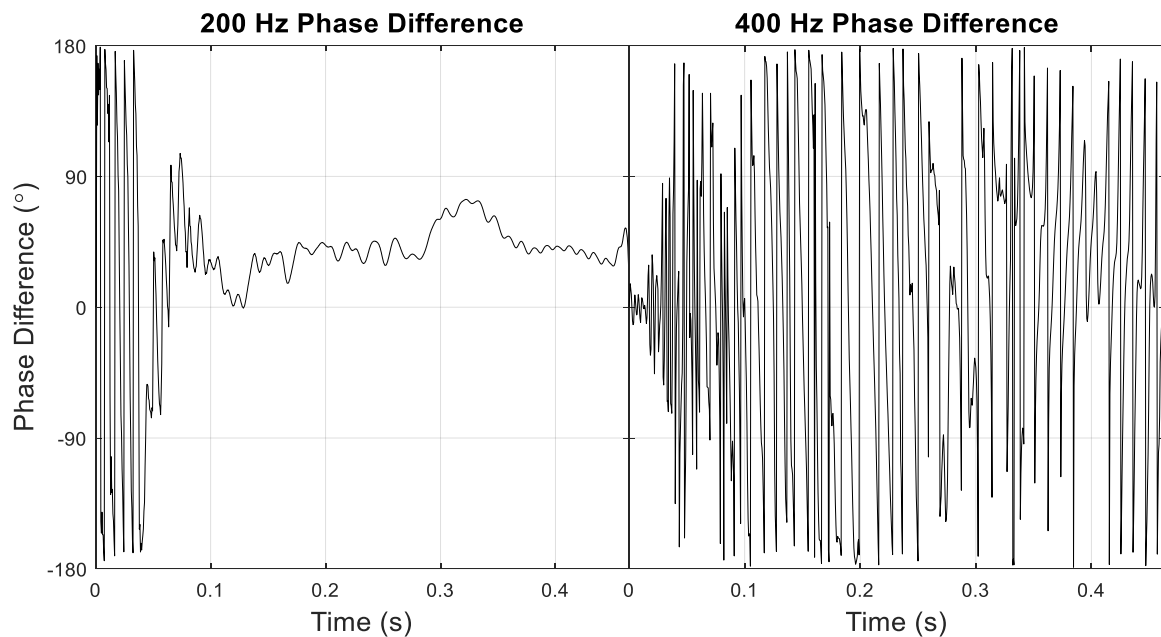


**Figure 4.14: Phase difference plots against time for a) ~200 Hz components, b) ~400 Hz components of a  $\phi = 1.0$ ,  $R_H = 0.3$  methane flame**

Based on these observations, the ~200 Hz components contain a phase-locking period in which the phase difference holds at  $\sim 0^\circ$ ; this suggests that the investigated signals oscillated during the same phase. However, in Figure 4.13(b) the phase difference plot fluctuated throughout, suggesting that the ~400 Hz components did not experience phase locking. When two signals experience phase locking, this tends to imply that a feedback loop has formed, which increases the system's vibration [176]. Rayleigh [61] stated that vibration is promoted when heat is either introduced into compressed air or removed from rarefied air; in the opposite case, the vibration decays. It seems reasonable to assume that this theory can be tested by plotting the phase difference versus the oscillation pressure. The relationship between the pressure and the phase difference for both the ~200 Hz and ~400 Hz components is presented in Figure 4.15 (a) and Figure 4.15(b), respectively. It emerged that the pressure amplification was within  $0^\circ - \pm 90^\circ$  phase difference range, as shown in Figure 4.15(a), which supports Rayleigh's [61] assertion on phase locking. The behaviour shown in Figure 4.15 (b) is as expected of the non-phase locking interaction shown in Figure 4.14(b).

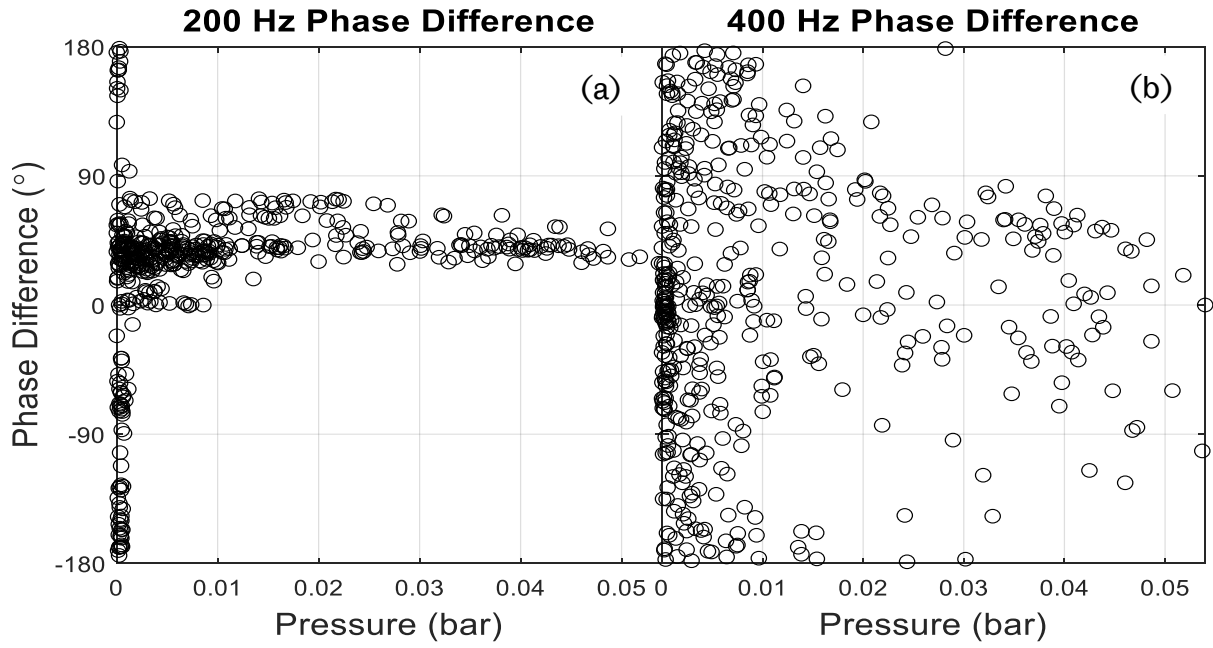


Figure 4.15: Phase difference plots against pressure for a) -200 Hz components, b) -400 Hz components of a  $\phi = 1.0$ ,  $R_H = 0.3$  methane flame

## 5 EXPERIMENTAL RESULTS

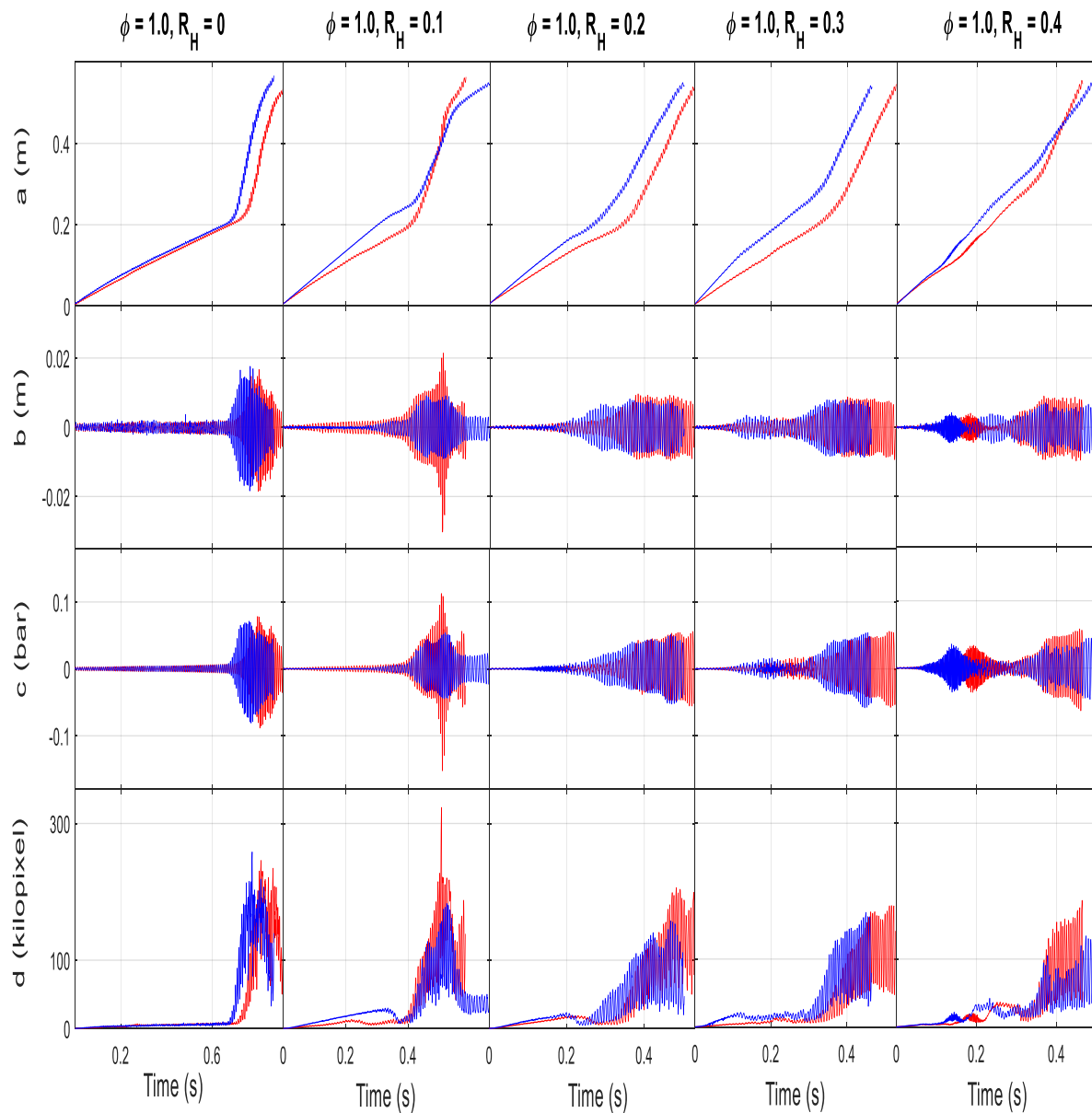
This section presents the results from the experiments involving methane-air and propane-air flames, mixed with hydrogen via the  $R_H$  and volumetric methods, propagating downward towards the closed end of a tube. The primary aim of the experiment was to examine how flame propagation behaviour changes as hydrogen content is increased. This section first discusses the effects of adding different amounts of hydrogen at fixed equivalence ratios, and then studies the effects of equivalence ratio changes under a constant hydrogen addition amount.

### 5.1 $R_H$ method

#### 5.1.1 The effect of hydrogen addition

The following examines how the addition of hydrogen impacts flame propagation, specifically in terms of the increased laminar burning velocity, which prior research [3] has shown to relate to the magnitude of the oscillations. For  $\phi = 1.0$ , the hydrogen will be changed from  $R_H = 0 - 0.4$ . Generally, the behaviour of methane and propane is similar, thus methane flames were used to present the data. Differences between propane flame and methane flame will be discussed later in this section. The flame front position was plotted against time in Figure 5.1 (a). For  $R_H = 0$  it was observed that there was a change in gradient at around 0.2 m; this was the result of a change in the flame speed. As the hydrogen concentration was increased, the change in gradient became less apparent until at  $R_H = 0.4$  the flame propagated down the tube at a fairly constant rate. The flame front position amplitudes obtained using high pass filtering the flame front positions are plotted against time as shown in Figure 5.1(b). Here you can see that the flame oscillated up to  $\pm 0.018$  m. The largest oscillation was observed for the  $R_H = 0$  flame in the latter part of the tube. Adding hydrogen caused the oscillations to decrease, however, they were observed much earlier in the flame propagation. The tube end pressure is plotted against time in Figure 5.1(c). These figures appear to be similar to those for the flame front position amplitudes. The flame position oscillations are the consequence of induced pressure waves which are in turn a consequence of flame acceleration. The pure methane flame showed the highest pressure oscillation of  $\pm 0.07$  bar. Figure 5.1(d) plots the flame area against time. The

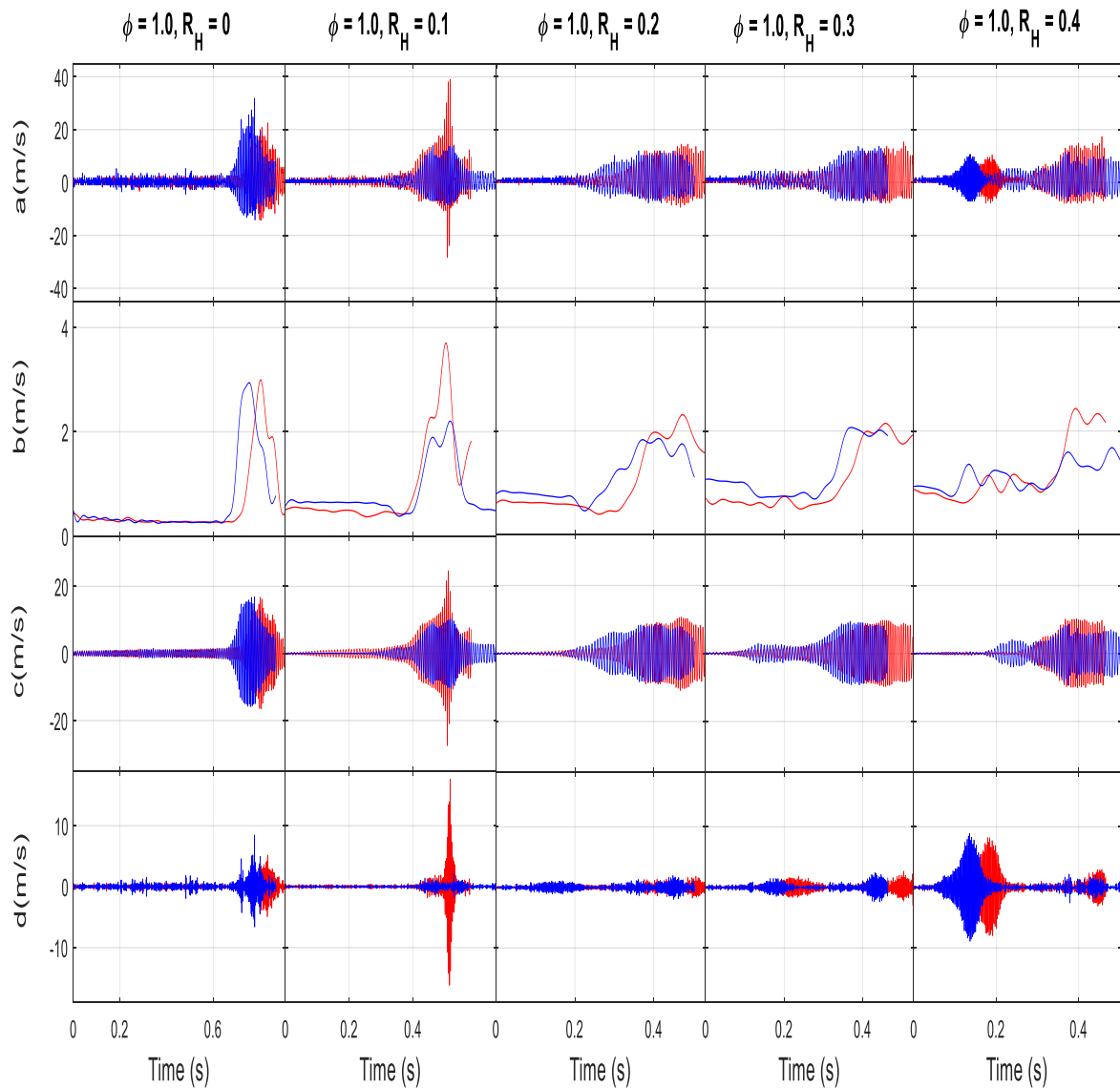
flame area steadily increased in all cases. In addition, with the exception of the  $R_H = 0$  flame, the flame areas first decreased when they passed through the primary acoustic field and then increased. In contrast, upon reaching the secondary acoustic field, the flames demonstrated an immediate increase in flame area. Meanwhile, the  $R_H = 0.4$  flame demonstrated a different behaviour in that a slight flame area occurred in the initial propagation stages.



**Figure 5.1: Effect of hydrogen addition on methane (blue), propane (red) on  $\phi = 1.0$ ,  $R_H = 0 - 0.4$  flames, on a) flame front position, b) flame front position amplitude, c) tube end pressure, and d) flame area**

Differentiating the flame front position in Figure 5.1(a) enabled the raw flame front speed to be obtained, as shown in Figure 5.2(a). What is noteworthy is that flame speeds of up to ~32 m/s were observed; these are much larger than typical laminar burning velocities of ~0.4 m/s. Figure 5.2(b) presents the underlying flame speed plotted against time. There was an initial period where the flame propagated steadily up to 0.2 m. This period became shorter when hydrogen was increased. As expected, the increasing hydrogen content caused an increase in the initial underlying flame speed. The initial underlying speed of  $R_H = 0$  flame was approximately ~0.3 m/s. This is of the same order as the laminar burning velocity. For the  $R_H = 0.1 - 0.3$  methane flames, the underlying speed reduction is likely to have directly linked to the ~200 Hz speed component oscillation, while the initial increase in the underlying speed of the  $R_H = 0.4$  methane flame is believed to be as a direct result of the ~400 Hz speed component oscillation.

The ~200 Hz speed component, which is presented in Figure 5.2(c), was generally considered to have caused the observed increase/decrease in the underlying flame speed, since the increase in the former was accompanied by an increase/decrease in the latter. Figure 5.2(d) plots the ~400 Hz speed component against time. As can be seen in the figure, the increase in the ~400 Hz speed component in the latter section of the tube coincides with the peak magnitude of the ~200 Hz speed component, indicating that the ~400 Hz component increase results from that of the ~200 Hz speed component. However, it was also observed that the increase in the ~400 Hz speed component occurred before any significant increase in the ~200 Hz speed component, for example with the  $R_H = 0.4$  flame. In addition, the ~400 Hz speed oscillation instigated significant changes to the initial underlying flame speed.



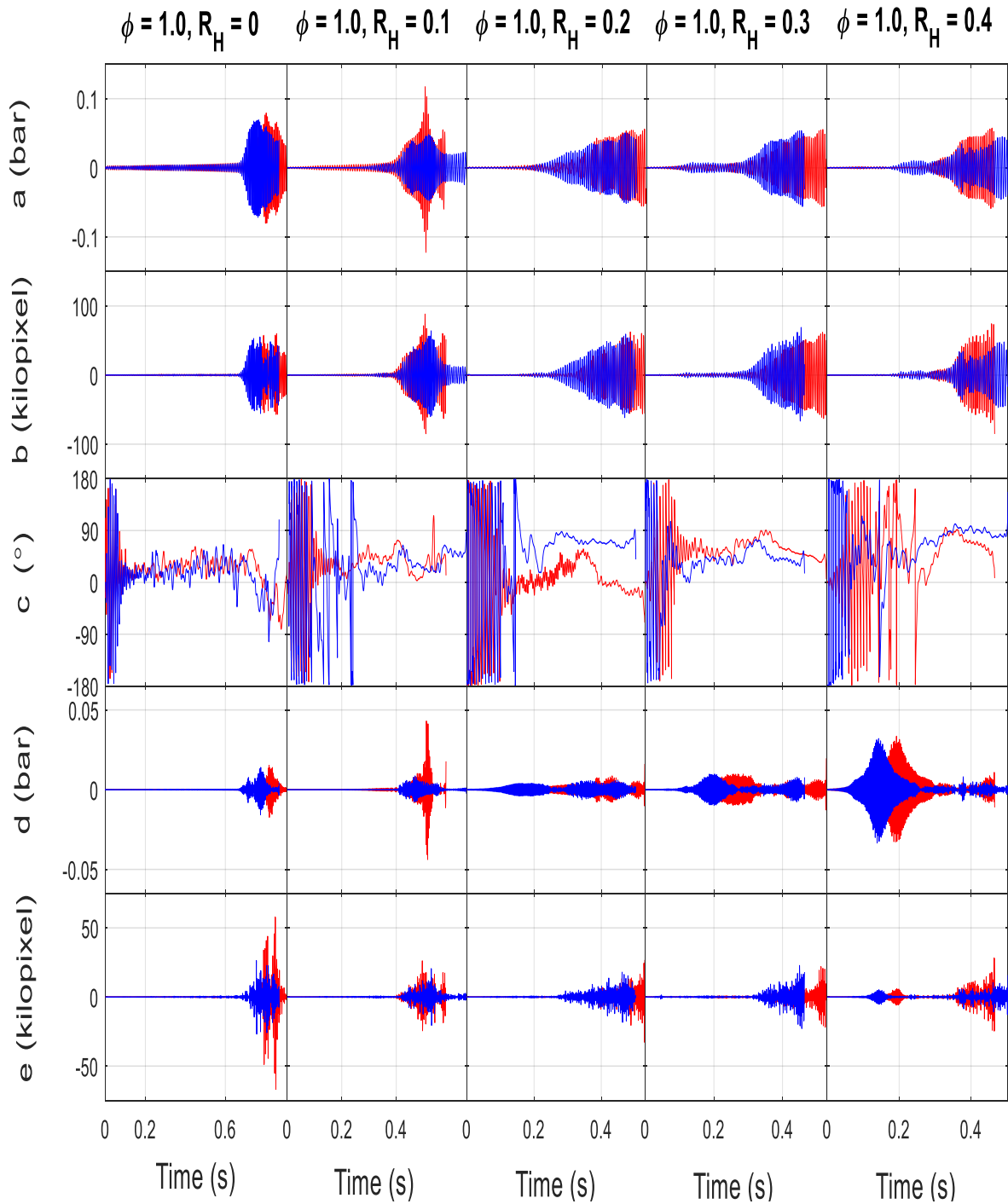
**Figure 5.2: Effect of hydrogen addition on methane (blue), propane (red) on  $\phi = 1.0$ ,  $R_H = 0 - 0.4$  flames, on a) raw flame speed, broken down into b) underlying flame speed, c)  $\sim 200$  Hz speed component, and d)  $\sim 400$  Hz speed component.**

Figure 5.3(a) and Figure 5.3(b), respectively, present the  $\sim 200$  Hz components of the tube end pressure and flame area, both plotted against time. It emerges that all flames'  $\sim 200$  Hz pressure component behaviours are reflected in their flame area. Furthermore, based on the observation that the pressure oscillations built up before the flame area increased, the flame area oscillations may have been driven by pressure.

A phase study was conducted between tube end pressure and flame area, wherein the raw signals were broken down into their ~200 Hz components and the phase differences were calculated. The primary focus was on the phase difference between tube end pressure and flame area to determine their relationship. A 0° phase difference indicates that there was phase matching between the flame pressure signal and the flame area, which would have amplified the pressure.

Figure 5.3(c) plots the phase difference between the ~200 Hz components against time, illustrating that all flames generally had a phase-matching period that caused the pressure and flame area oscillations to build up – a phenomenon that evidences the relationship between the ~200 Hz components of tube end pressure and the flame area. Notably, the abrupt flame area reduction was not linked to tube end pressure, which showed a more gradual decay. Given that the increases in flame area and pressure were gradual in most cases, this is unexpected behaviour. Moreover, during the period of phase matching, following the abrupt decline in the flame area, a sudden increase occurred for the phase difference, as found for the  $R_H = 0$  flame.

The ~400 Hz components of tube end pressure and flame area are plotted against time in Figure 5.3(d) and Figure 5.3(e), respectively. As demonstrated in the figures, the ~400 Hz pressure components of the  $R_H = 0.2$  and  $R_H = 0.4$  flames exhibited a different behaviour compared to other flames, building up to a significant level prior to the increase of the ~200 Hz pressure component. This increase was similarly reflected in the ~400 Hz speed component. This behaviour demonstrates that the ~400 Hz pressure component can build up despite there being no increase in the ~200 Hz pressure component.



**Figure 5.3: Effect of hydrogen addition on methane (blue), propane (red) on  $\phi = 1.0$ ,  $R_H = 0 - 0.4$  flames, on a)  $\sim 200$  Hz pressure component, b)  $\sim 200$  Hz area component, c) phase difference between a) and b), d)  $\sim 400$  Hz pressure component, e)  $\sim 400$  Hz flame area component**

The comparison between the flame behaviour for methane and propane flames is shown here. Both flames showed similar behaviour at different levels of hydrogen addition. The initial flame propagation of methane flames was noticeably higher than the propane flames, as evidenced by the distance achieved by these flames observed in Figure 5.1(a). In comparison to the other propane flames, the  $R_H = 0$  pure methane

flame showed the highest oscillations, reaching a flame front amplitude of  $\sim\pm 0.018$  m, while the  $R_H = 0.1$  propane flame achieved an amplitude of  $\sim\pm 0.025$  m. The observed decrease in the flame front amplitude following the addition of hydrogen was unexpected since an increased flame front amplitude was expected to result from the steady increase in the laminar burning velocity. All propane flames had an initial underlying speed that was lower than that of the methane flames. This behaviour was also unexpected, as propane's laminar burning velocity is higher than that of methane. Moreover, the maximum underlying speed achieved by propane flames is shown in Figure 5.2(b). This behaviour was also reflected in the  $\sim 200$  Hz and  $\sim 400$  Hz velocity components, as presented respectively in Figure 5.2(c) and Figure 5.2(d).

#### 5.1.1.1 Flame shape analysis

The methane flame shapes were analysed and compared between the mixtures with different amounts of hydrogen to determine any key differences during propagation. Figure 5.4 shows the flame position and the tube end pressure against time at  $\phi = 1.0$ ,  $R_H = 0$  flame. The flame initially propagated as a vibrating curve as seen in Figure 5.6(a) with a small-amplitude oscillation, reaching  $\sim\pm 0.0016$  bar, as shown in Figure 5.4(a). As the flame flattened as seen in Figure 5.6(b), it experienced a decreased velocity due to a reduced surface area, as shown in Figure 5.5(b). The flame's transition from vibrating curved to vibrating flat occurred within several acoustic cycles during the period of primary acoustic instability, until  $\sim 0.07$  seconds. Finally, the occurrence of a turbulent flame as seen in Figure 5.6(c) led to the secondary oscillation stage during the high-level acoustic oscillations, as shown in Figure 5.4(c). The violent flame oscillation was mirrored in the underlying velocity in Figure 5.5(c), where it reached a maximum oscillating amplitude of  $\sim 3.0$  m/s.

The flame front position and the tube end pressure signal as a function of time at  $\phi = 1.0$ ,  $R_H = 0.1$  flame is shown in Figure 5.7 where the curved flame as seen in Figure 5.9(a) was found to correspond to very low acoustic pressure. When the pressure started building up, at  $\sim 0.25$  seconds, the curved flame experienced a slight distortion, as shown in Figure 5.9(b). Meanwhile, the saturation of the primary instability to  $\sim\pm 0.006$  bar at  $\sim 0.35$  seconds caused a cellular flame shape to emerge. At the onset of secondary instability, at  $\sim 0.4$  seconds, tulip structures as seen in Figure 5.9(c)

underwent oscillations towards a high amplitude, which began to decay upon reaching a maximum acoustic pressure of  $\sim\pm 0.05$  bar at  $\sim 0.52$  seconds. Drawing on Figure 5.8, three regions are proposed based on the flame's underlying speed, namely a) a steady underlying speed b) a decreased underlying speed, and c) an increased underlying speed.

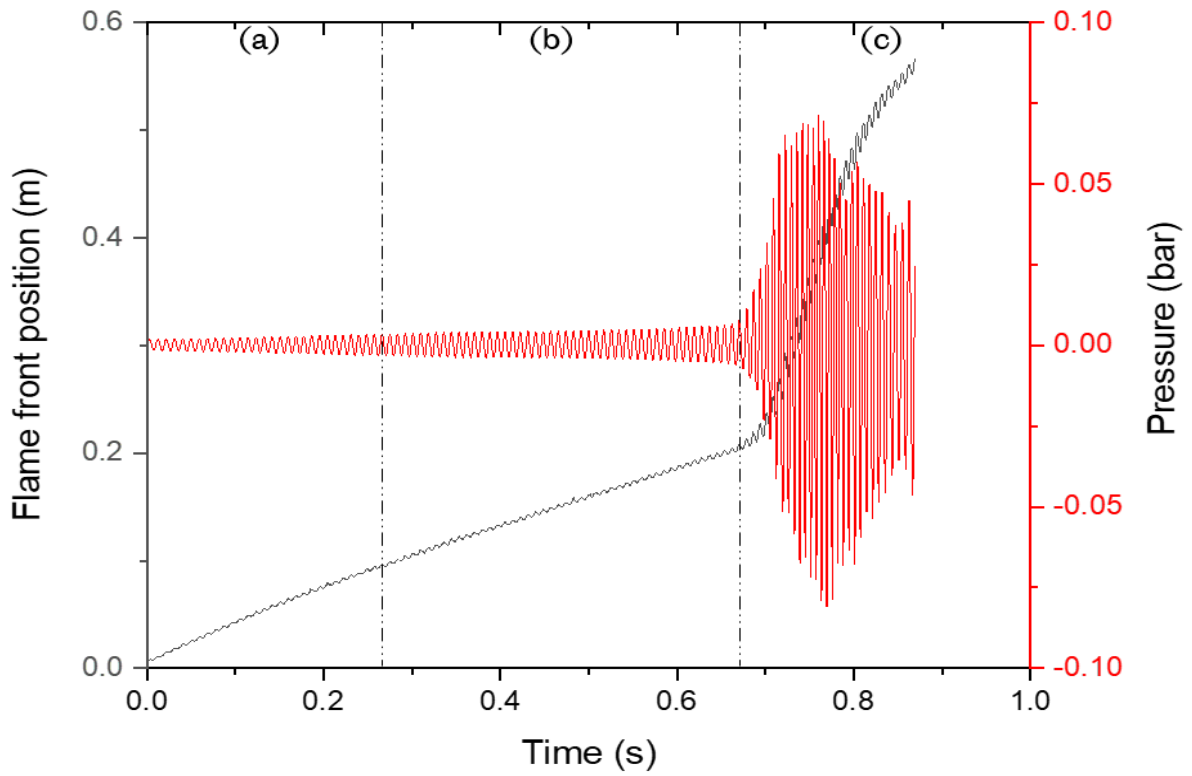


Figure 5.4: Flame front position and tube end pressure against time of methane on  $\phi = 1.0$ ,  $R_H = 0$  flame

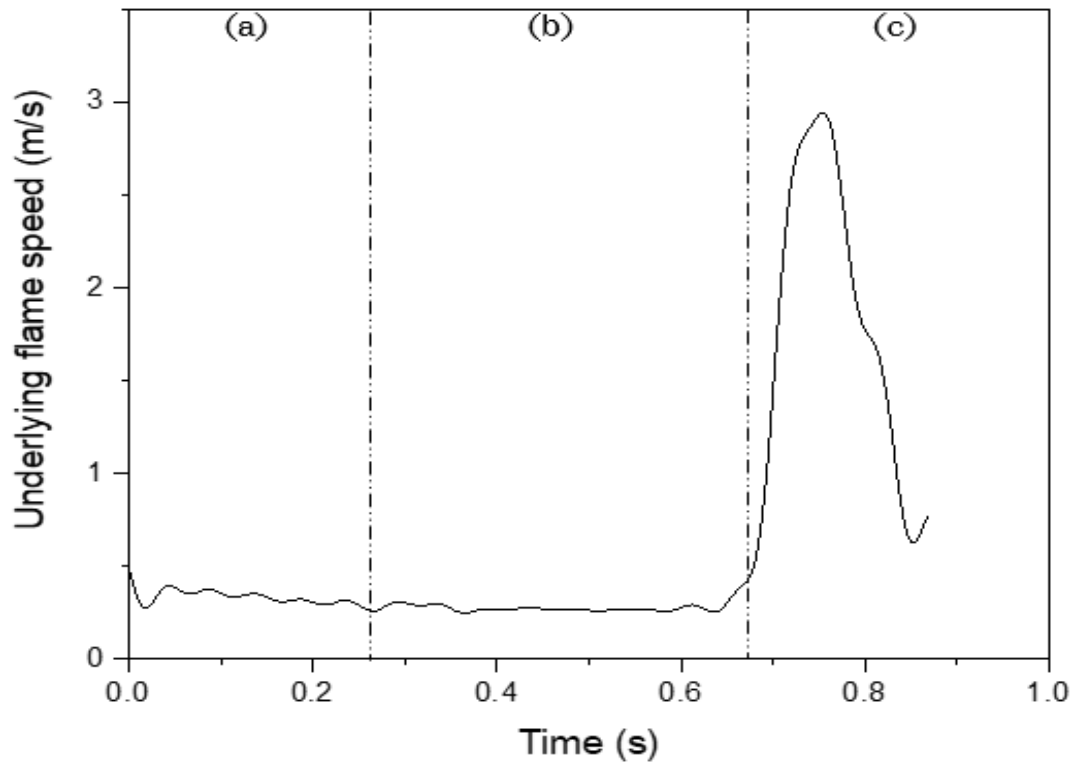


Figure 5.5: Underlying flame speed against time of methane on  $\phi = 1.0$ ,  $R_H = 0$  flame

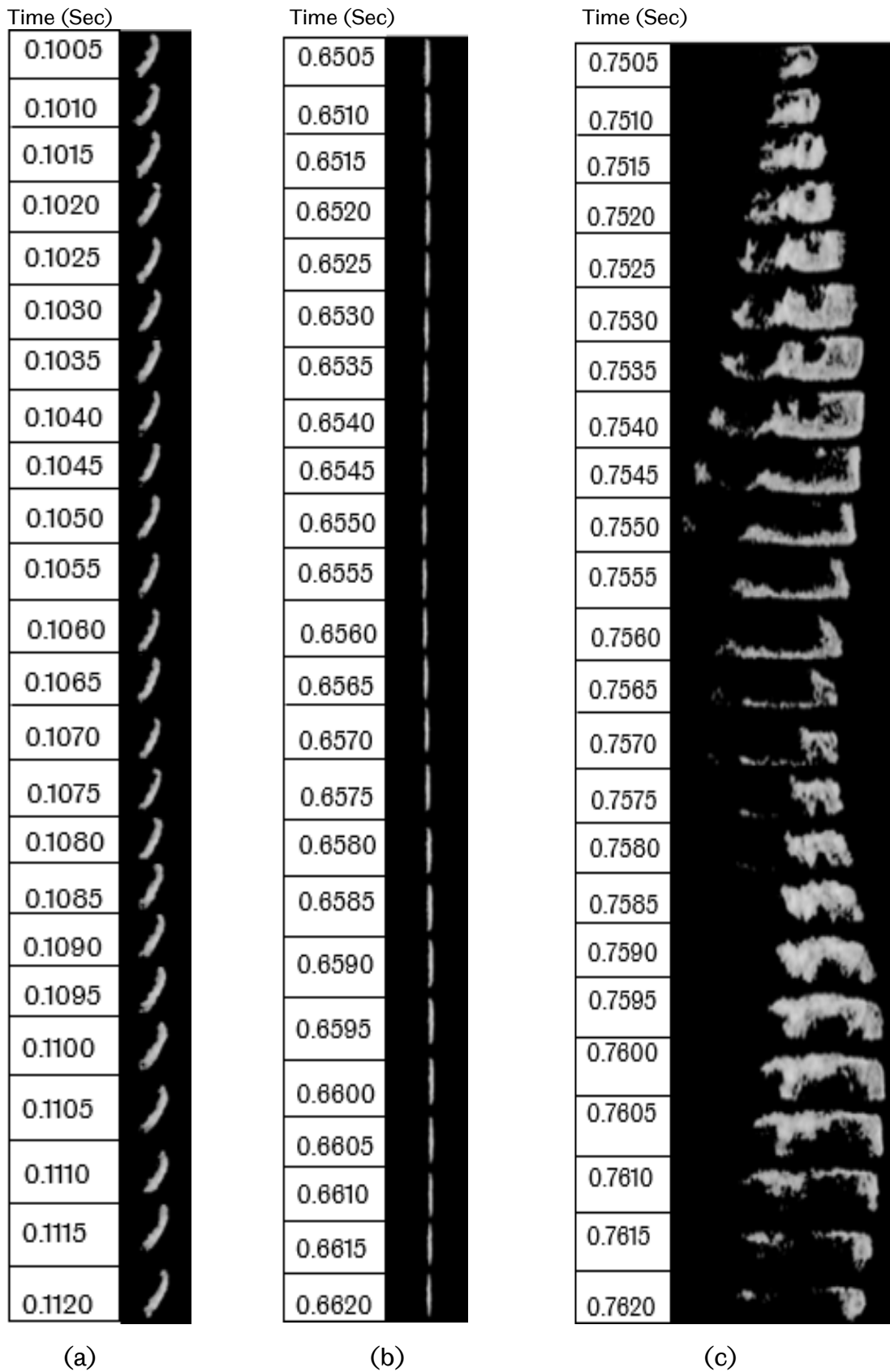


Figure 5.6: Representative images for flame behaviour in different regimes of methane on  $\phi = 1.0$ ,  $R_H = 0$  flame. Interval of 1/2000 second increments for each frame downwards

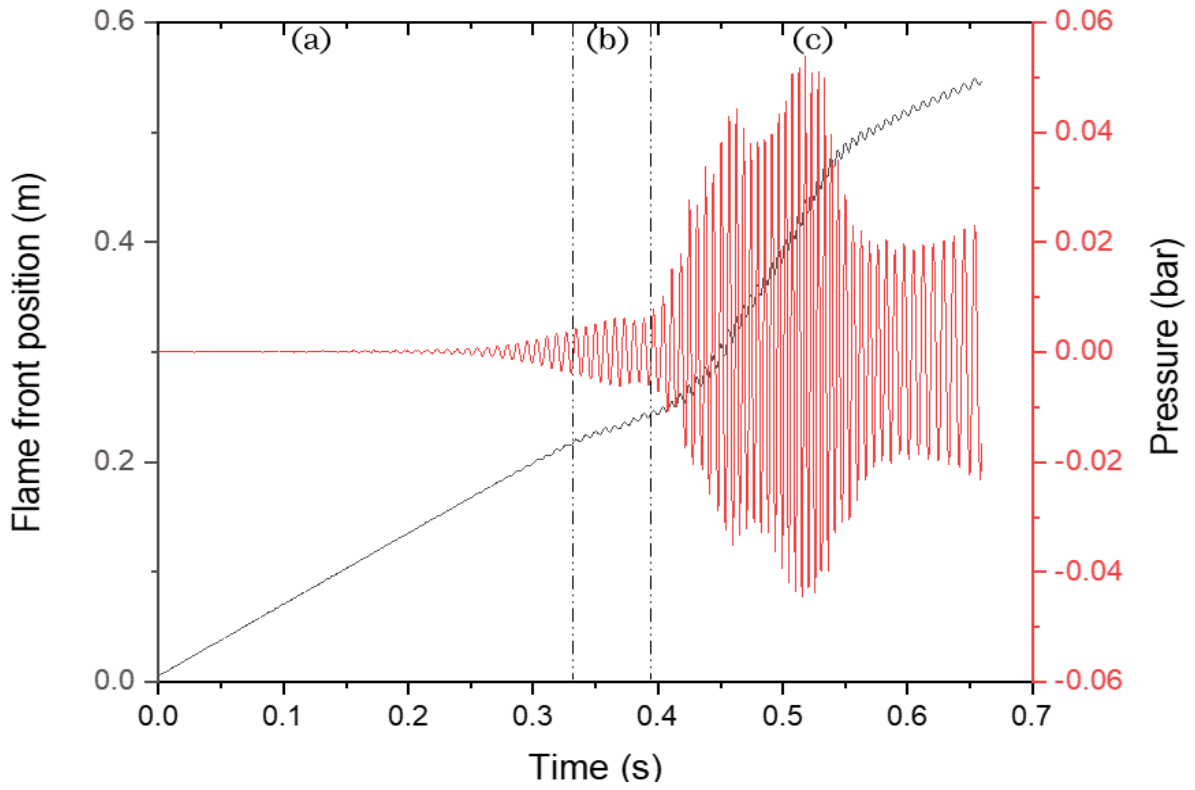


Figure 5.7: Flame front position and tube end pressure against time of methane on  $\phi = 1.0$ ,  $R_H = 0.1$  flame

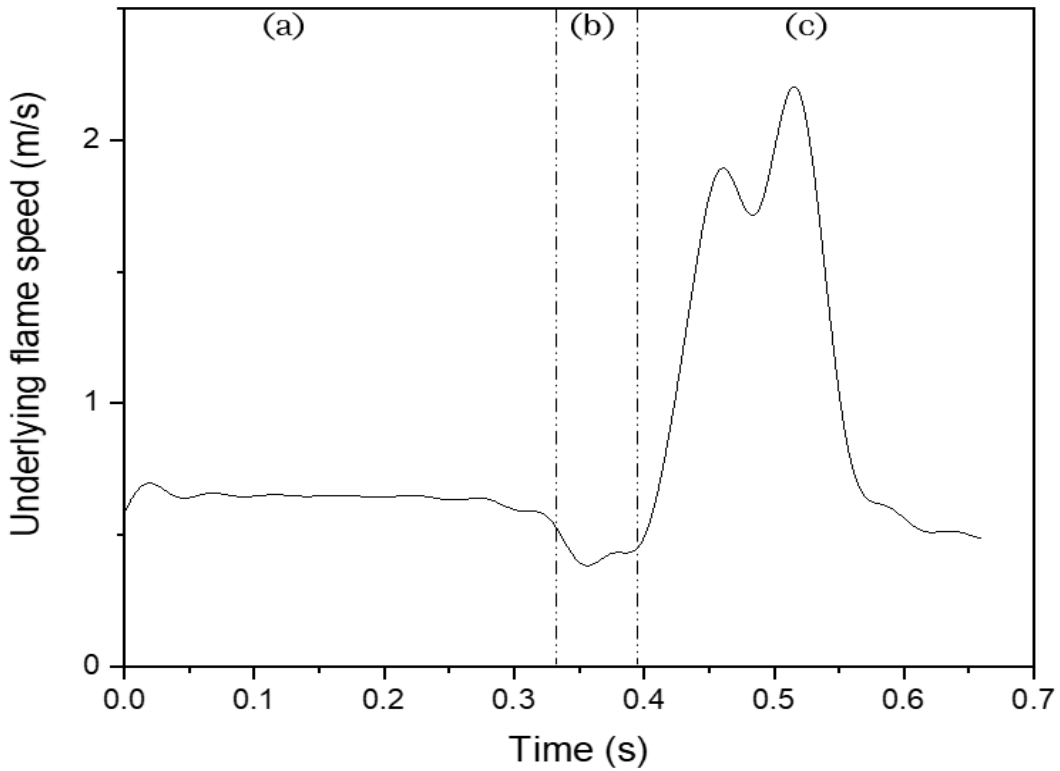


Figure 5.8: Underlying flame speed against time of methane on  $\phi = 1.0$ ,  $R_H = 0.1$  flame

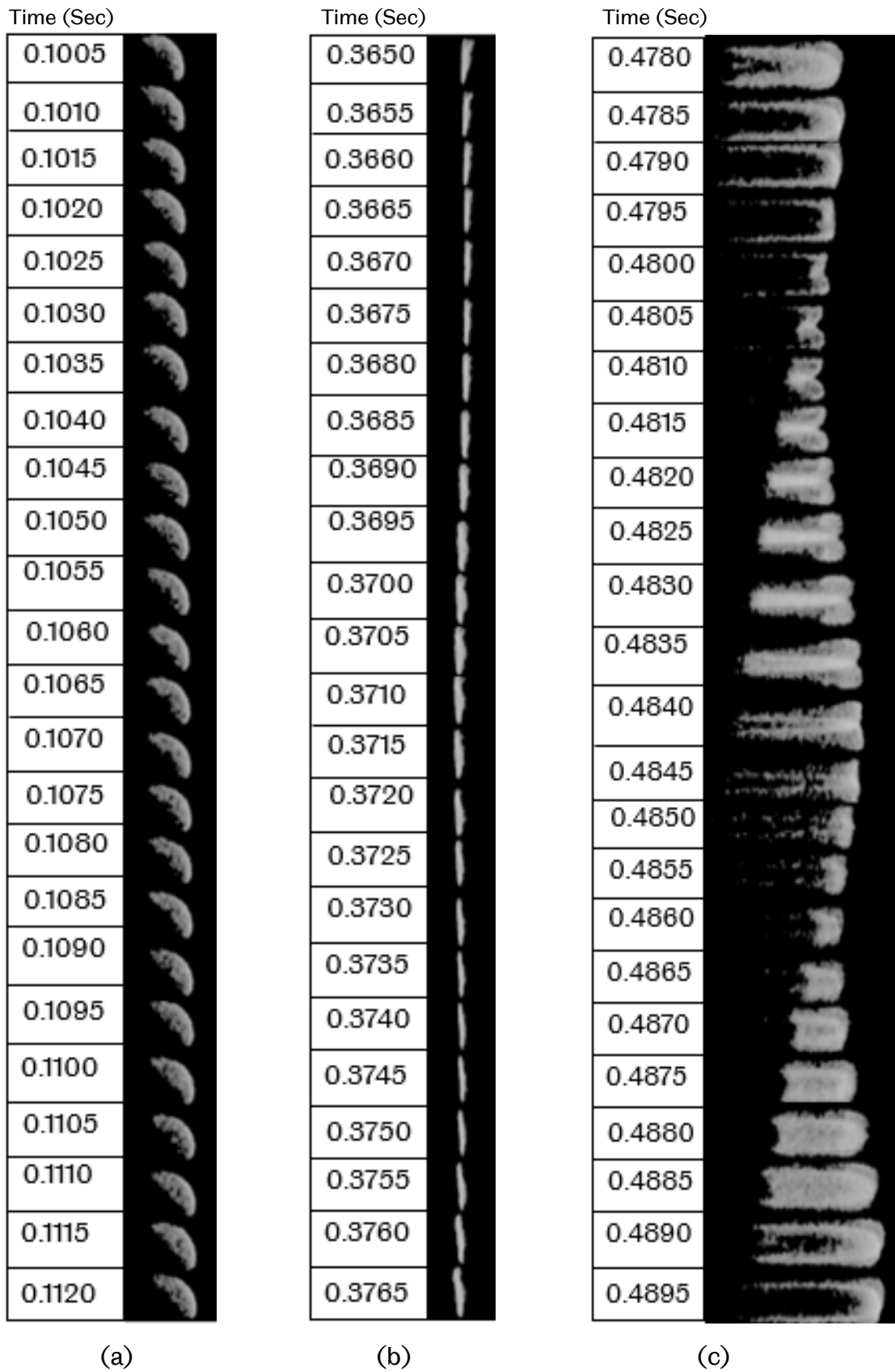


Figure 5.9: Representative images for flame behaviour in different regimes of methane on  $\phi = 1.0$ ,  $R_H = 0.1$  flame. Interval of 1/2000 second increments for each frame downwards

Figure 5.10 shows the flame position and the tube end pressure against time at  $\phi = 1.0$ ,  $R_H = 0.2$  flame. A regime of non-vibrating flame in which the curved flame propagated was identified as shown in Figure 5.12(a). After propagating over a certain distance, acoustic pressure was generated and the initial curved flame began to vibrate. During primary acoustic instability, whereby the pressure amplitudes were observed to increase with further downward flame propagation as observed in Figure 5.10(b) and Figure 5.12(b). During this downward propagation, the cellular structure disappeared and the flame took on a tulip shape, leading to a secondary oscillation stage characterised by high-level acoustic oscillation, as seen in Figure 5.10(c) and Figure 5.12(c). It was found that the underlying velocity of the curved flame before transition to the vibrating curved flame was higher and started to decrease gradually until  $\sim 0.15$  seconds, as shown in Figure 5.11(a). Hereby, the surface area of the flame reduced, leading to a rapid flame deceleration and exhibiting flame surface inversion, which previous researchers have termed tulip flames, as observed in Figure 5.11(b). This significantly increased the flame's underlying speed, as shown in Figure 5.11(c).

The flame front position and the tube end pressure signal as a function of time at  $\phi = 1.0$ ,  $R_H = 0.3$  flame is shown in Figure 5.13. In Figure 5.14, three regions were proposed based on the underlying speed of the flame, which are a) steady underlying speed b) decrease of underlying speed, and finally, c) increase of underlying speed. Similar behaviour to that of  $R_H = 0.2$  flame, where there were three regimes of propagation, is observed in Figure 5.15, however, there was a distinct difference in the growth of the magnitude of the acoustic pressure, with highly cellular structures forming on the flame, as shown in Figure 5.13(b) and Figure 5.15(b). Figure 5.16 shows the flame position and the flame acoustic pressure against time at  $\phi = 1.0$ ,  $R_H = 0.4$  flame. Acoustic pressure corresponding to the first harmonic mode was observed in the early flame propagation stage after the flame had moved downward following ignition, as illustrated in Figure 5.16(b). Plotting the underlying flame speed against time in Figure 5.17 revealed a behavioural dissimilarity with other flames, highlighting an increase in the initial underlying speed as shown in Figure 5.17(b). The corresponding flame images of three regimes of propagation are shown in Figure 5.18.

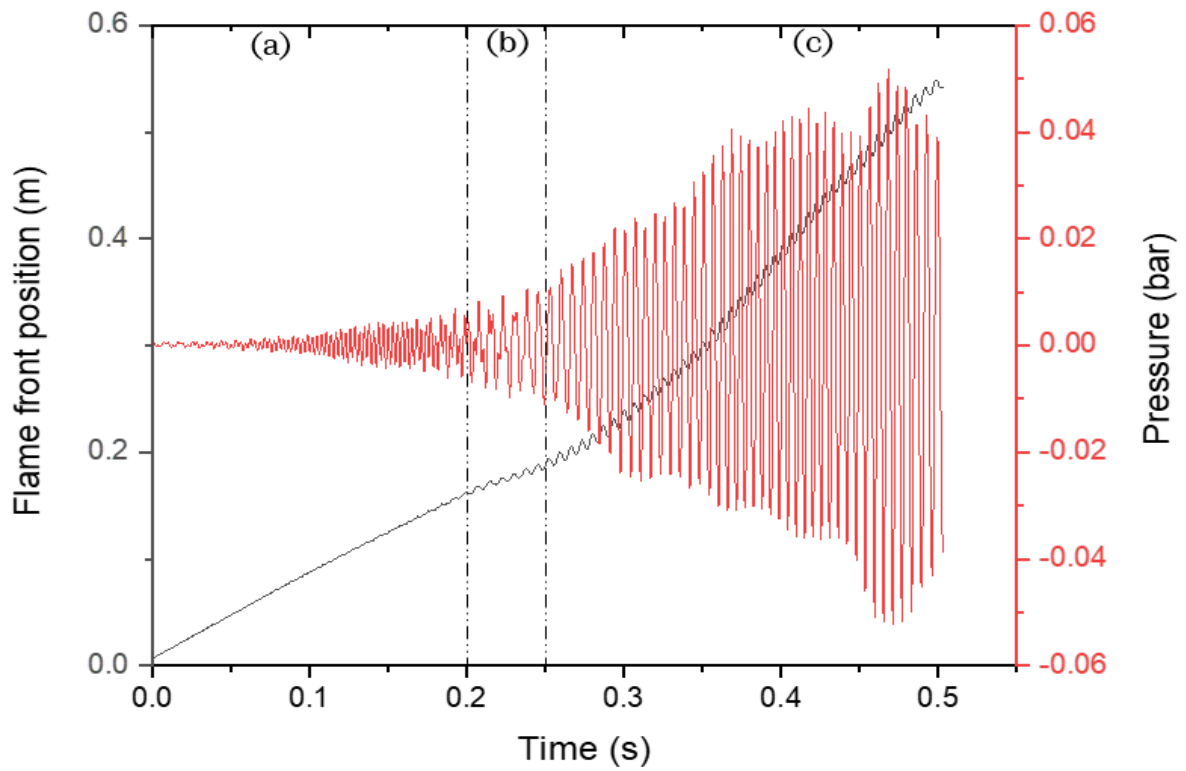


Figure 5.10: Flame front position and tube end pressure against time of methane on  $\phi = 1.0$ ,  $R_H = 0.2$  flame

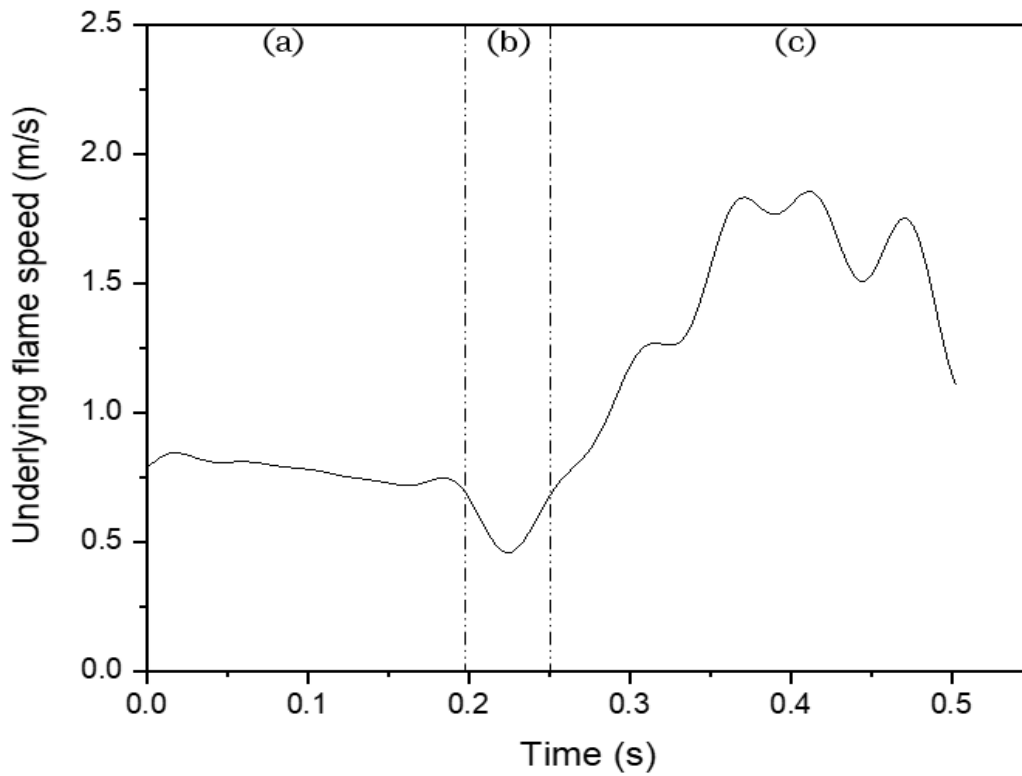


Figure 5.11: Underlying flame speed against time of methane on  $\phi = 1.0$ ,  $R_H = 0.2$  flame

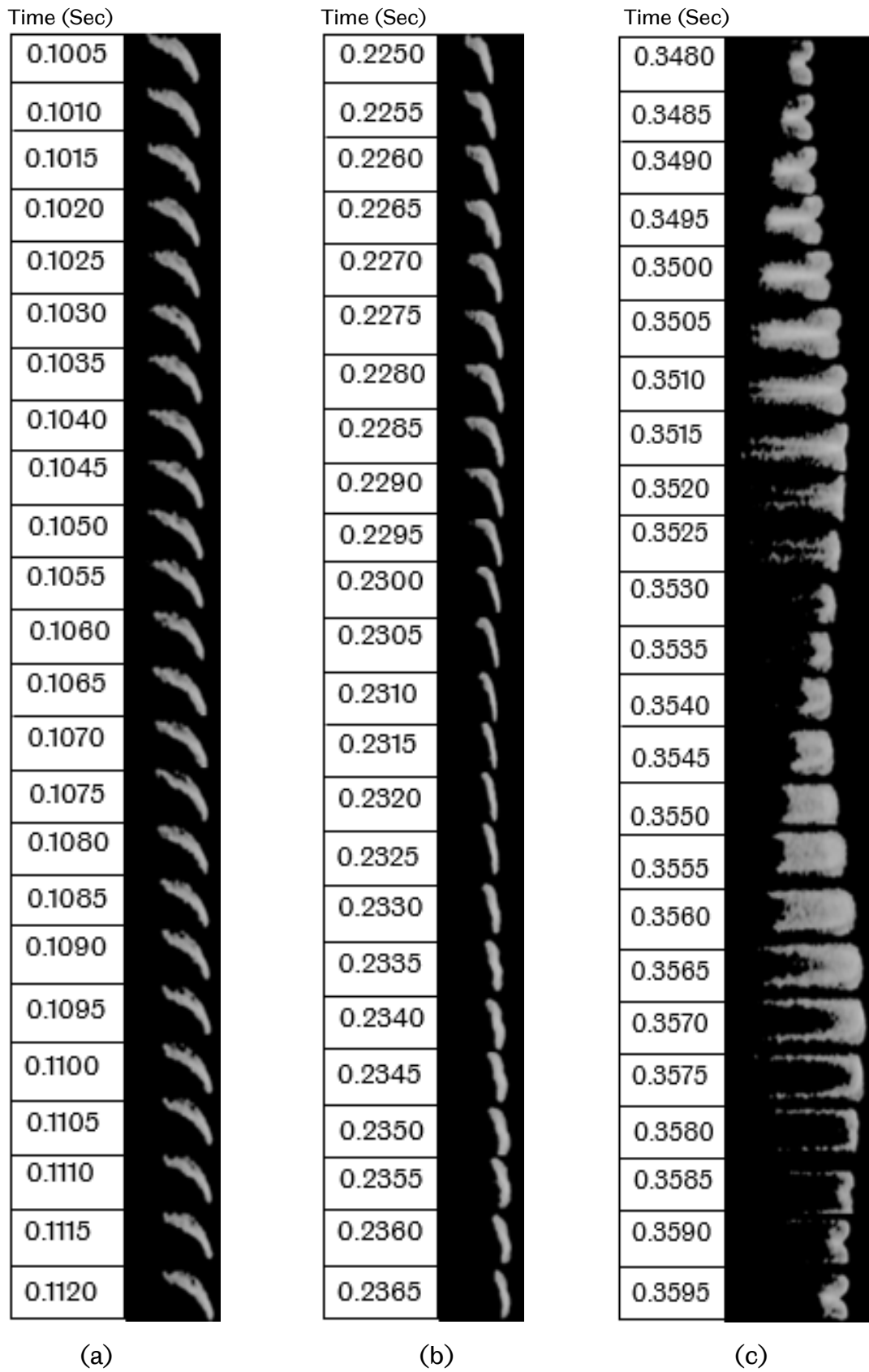


Figure 5.12: Representative images for flame behaviour in different regimes of methane on  $\phi = 1.0$ ,  $R_H = 0.2$  flame. Interval of 1/2000 second increments for each frame downwards

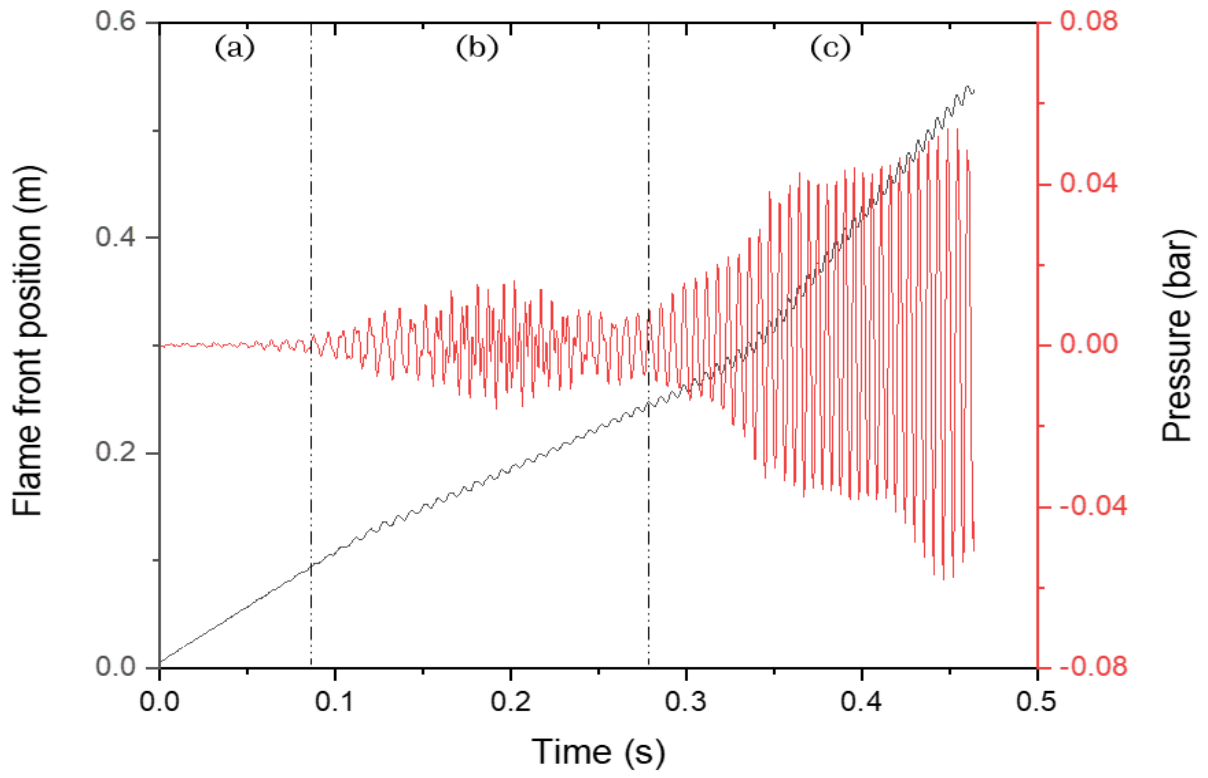


Figure 5.13: Flame front position and tube end pressure against time of methane on  $\phi = 1.0$ ,  $R_H = 0.3$  flame

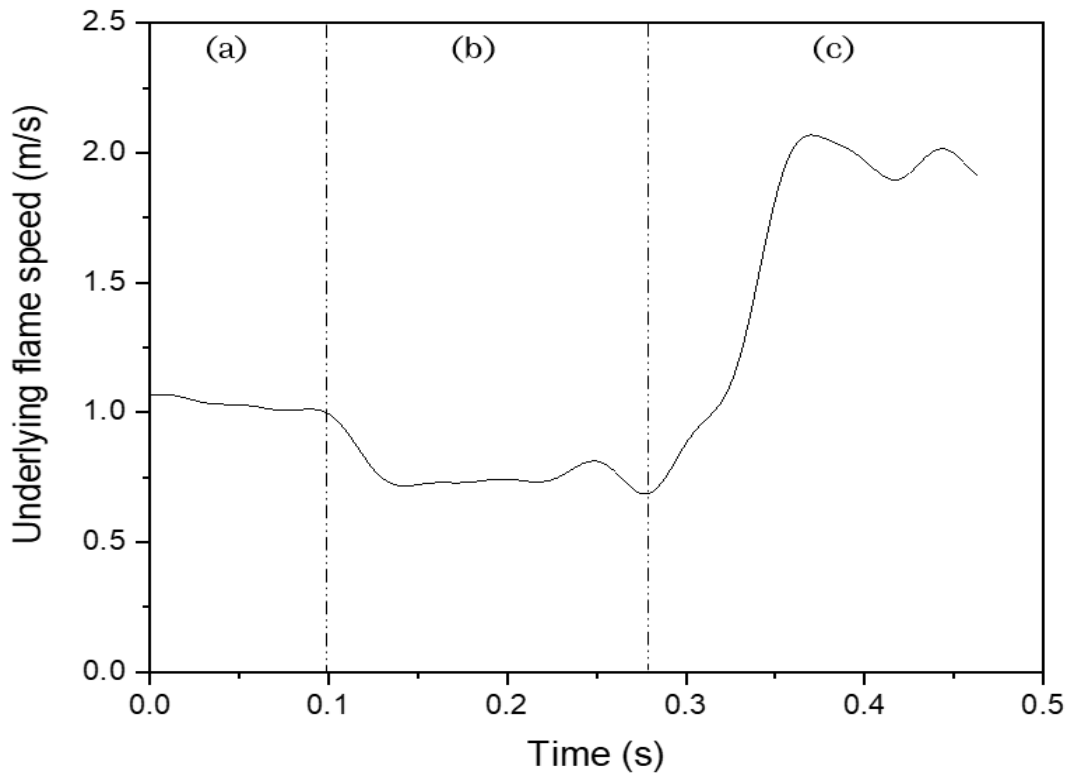
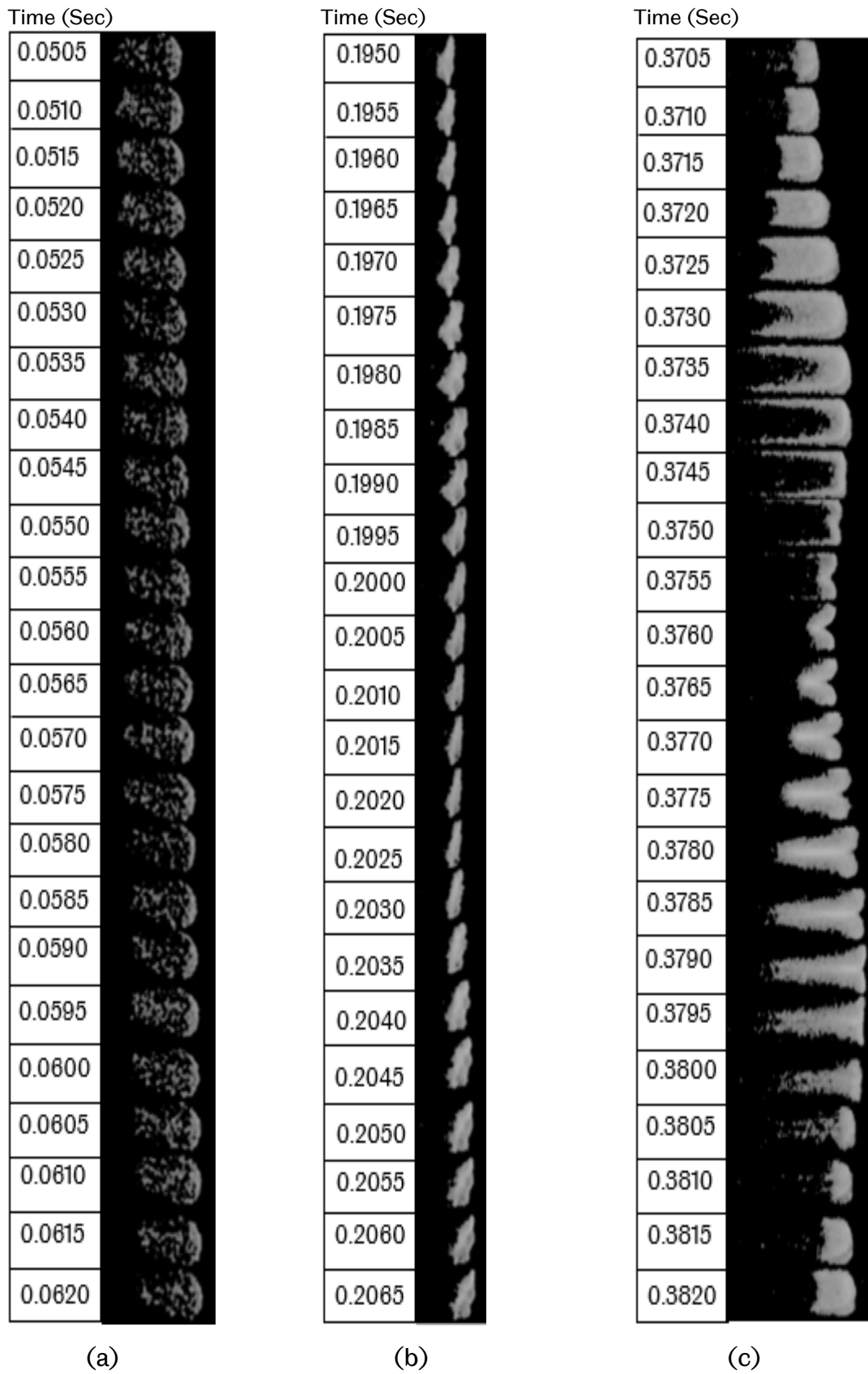


Figure 5.14: Underlying flame speed against time of methane on  $\phi = 1.0$ ,  $R_H = 0.3$  flame



**Figure 5.15: Representative images for flame behaviour in different regimes of methane on  $\phi = 1.0$ ,  $R_H = 0.3$  flame. Interval of 1/2000 second increments for each frame downwards**

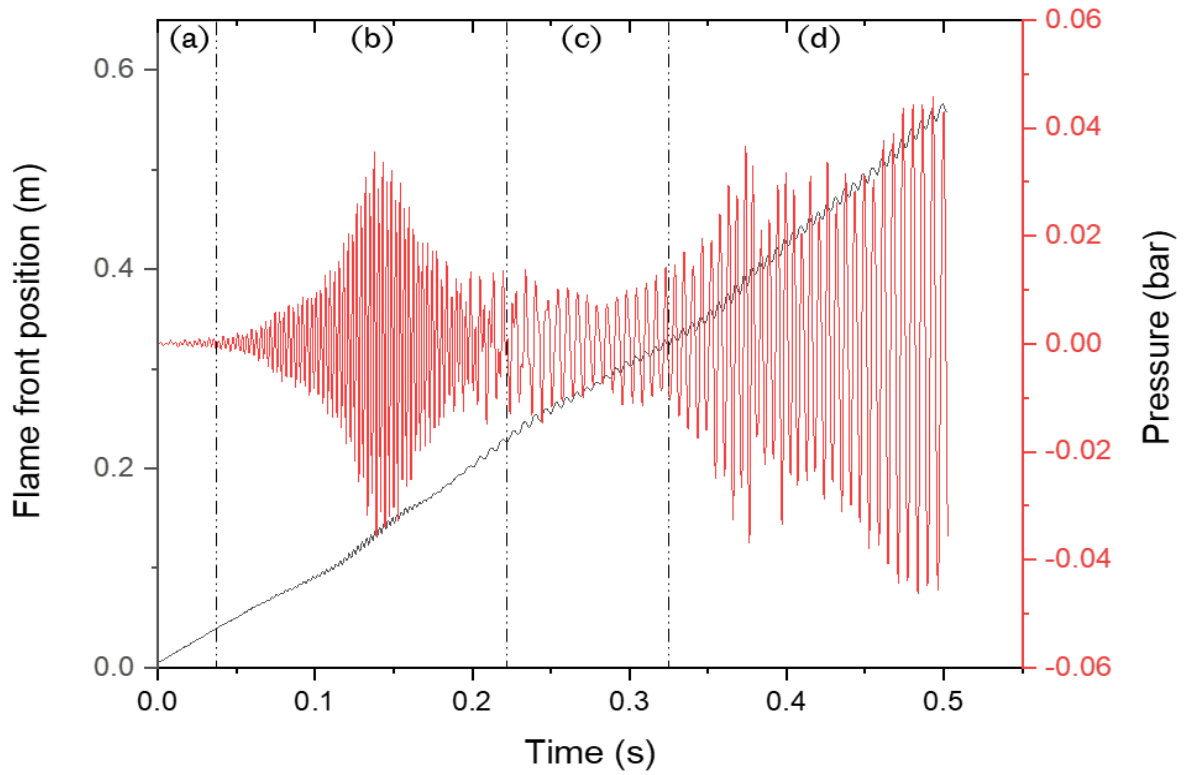


Figure 5.16: Flame front position and tube end pressure against time of methane on  $\phi = 1.0$ ,  $R_H = 0.4$  flame

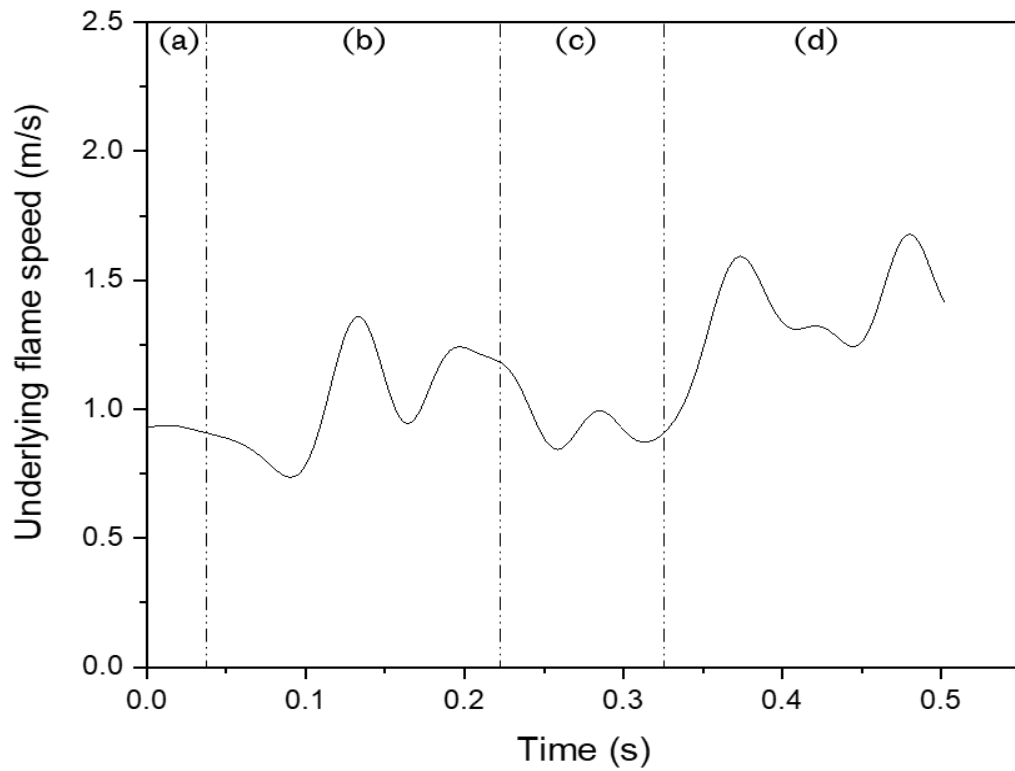


Figure 5.17: Underlying flame speed against time of methane on  $\phi = 1.0$ ,  $R_H = 0.4$  flame

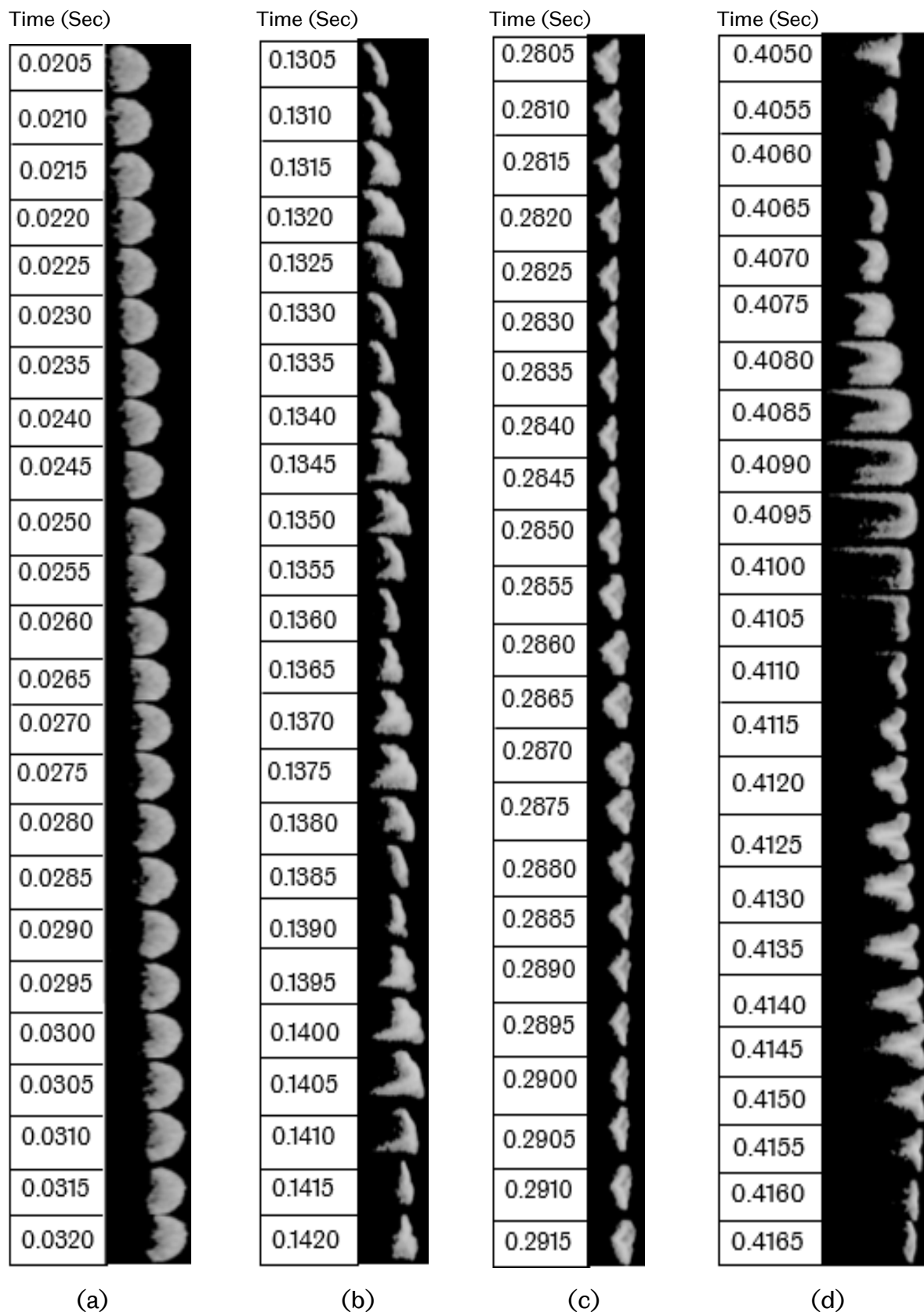


Figure 5.18: Representative images for flame behaviour in different regimes of methane on  $\phi = 1.0$ ,  $R_H = 0.4$  flame. Interval of  $1/2000$  second increments for each frame downwards

A comparison of flame characteristics for methane and propane flames at selected regions where both flames showed an obvious difference is presented here. All of the methane flames from  $R_H = 0 - 0.4$  were curved and steady at the start of propagation. This regime was only observed in methane flames, however, while propane flames propagate with a vibrating curved flame, showing an obviously higher acoustic sound based on their pressure fluctuations in the early stage of propagation, as shown in region (a) in Figure 5.19, Figure 5.22, Figure 5.25, and Figure 5.28. Similarly, this behaviour emerged in their initial underlying speed, which increased significantly, unlike with the propane flame as shown in region (a) in Figure 5.20, Figure 5.23, Figure 5.26, and Figure 5.29. The corresponding flame images of methane and propane flame are shown in Figure 5.21(a), Figure 5.24(a), Figure 5.27(a), and Figure 5.30(a).

In the case of region (b), both  $R_H = 0.1$  and  $0.2$  flames showed similar behaviour where the methane flame had a lower pressure oscillation compared to the propane flame, as shown in Figure 5.19(b), but roughly the same in Figure 5.22(b). While the methane flames apparently oscillated with minimal elongation, the propane flames were significantly different in terms of both shape and speed. Comparing their underlying velocity in Figure 5.20(b) and Figure 5.23(b), the maximum underlying velocity of the methane flames was  $\sim 2.2$  m/s and  $\sim 1.7$  m/s respectively, whereas that of the propane flames was  $\sim 3.7$  m/s and  $\sim 2.3$  m/s, respectively.

Looking at Figure 5.28(b), in the case of the  $R_H = 0.4$ , both flames demonstrated signs of instability that corresponded to the first harmonic which was linked to their cellular structure as shown in Figure 5.30(b), and the first harmonic oscillation was mirrored in their initial underlying speed in Figure 5.29(b). Similar to region (b) of  $R_H = 0.1$  and  $0.2$  flames, a relationship between the increase in the pressure oscillations and the flames' elongation was also observed on the flame propagation imagery in Figure 5.30(c), and in terms of the underlying velocity, Figure 5.29(c), the methane flames achieved  $\sim 1.6$  m/s, while the propane flames reached  $\sim 2.4$  m/s.

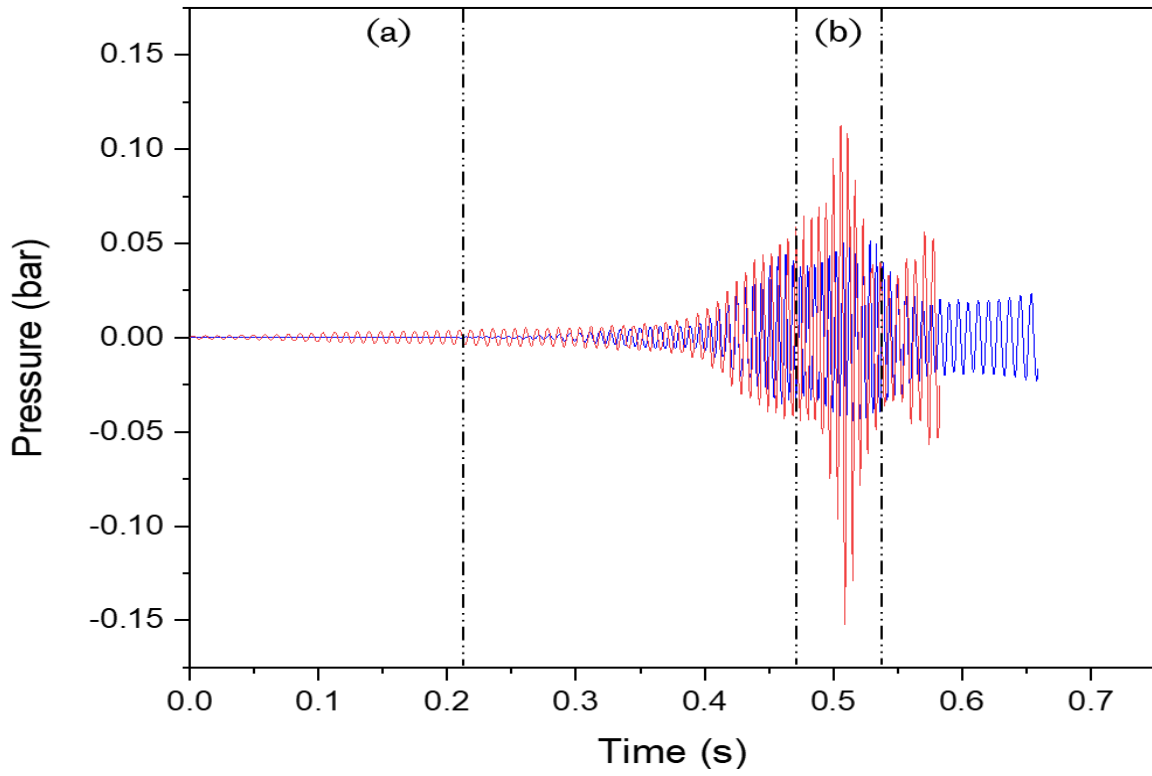


Figure 5.19: Tube end pressure against time of methane (blue), and propane (red) on  $\phi = 1.0$ ,  $R_H = 0.1$  flames

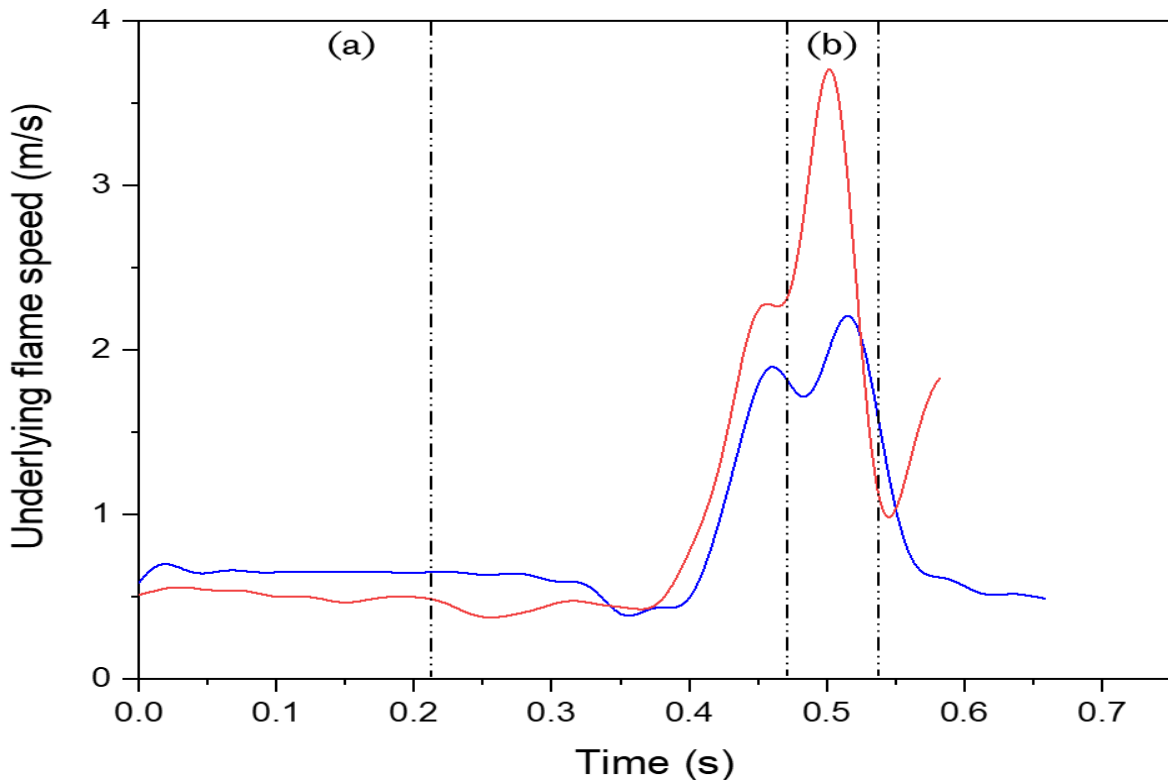


Figure 5.20: Underlying flame speed against time of methane (blue), and propane (red) on  $\phi = 1.0$ ,  $R_H = 0.1$  flames

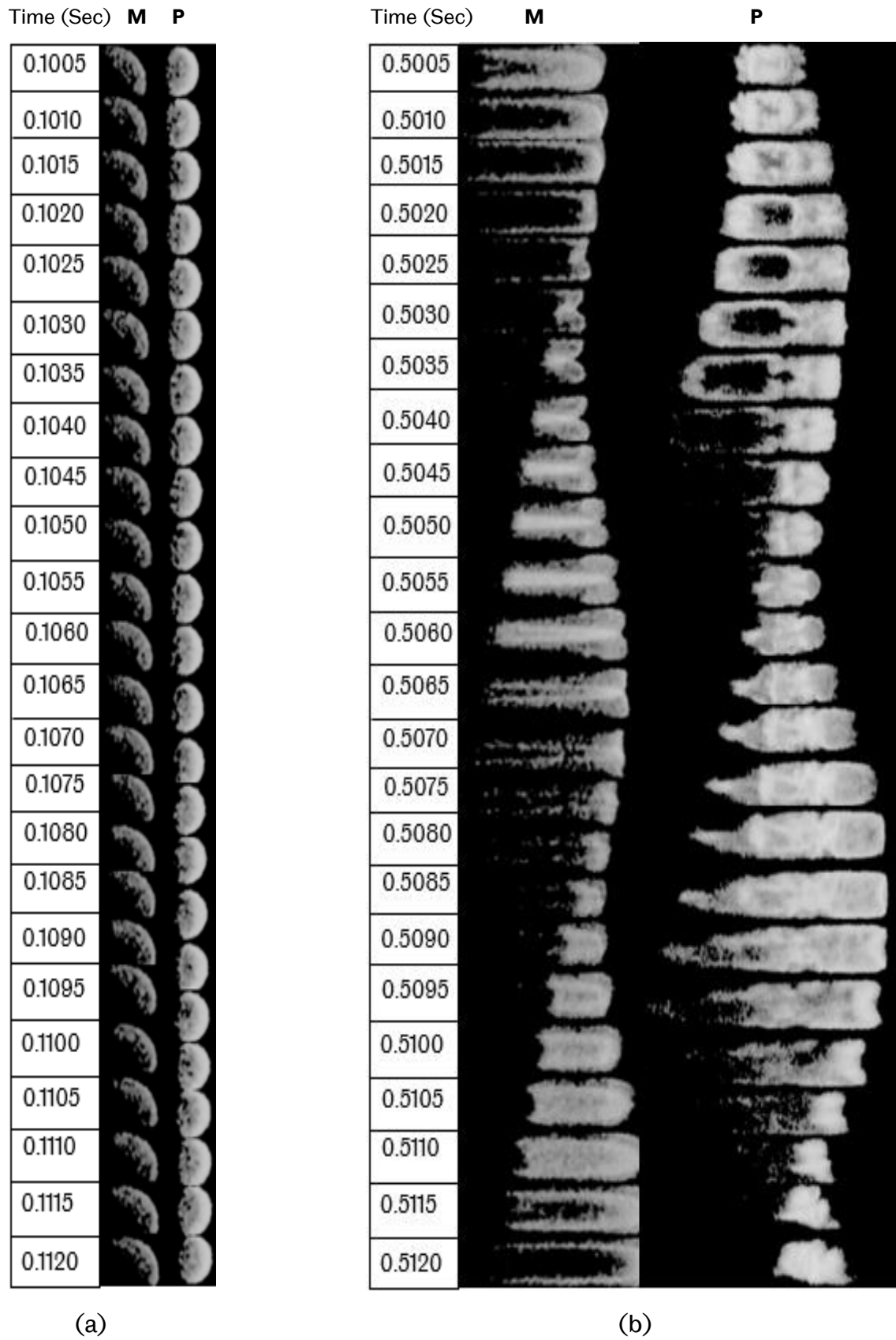


Figure 5.21: Representative images for flame behaviour in different regimes of methane (M) and propane (P) on  $\phi = 1.0$ ,  $R_H = 0.1$  flames. Interval of 1/2000 second increments for each frame downwards

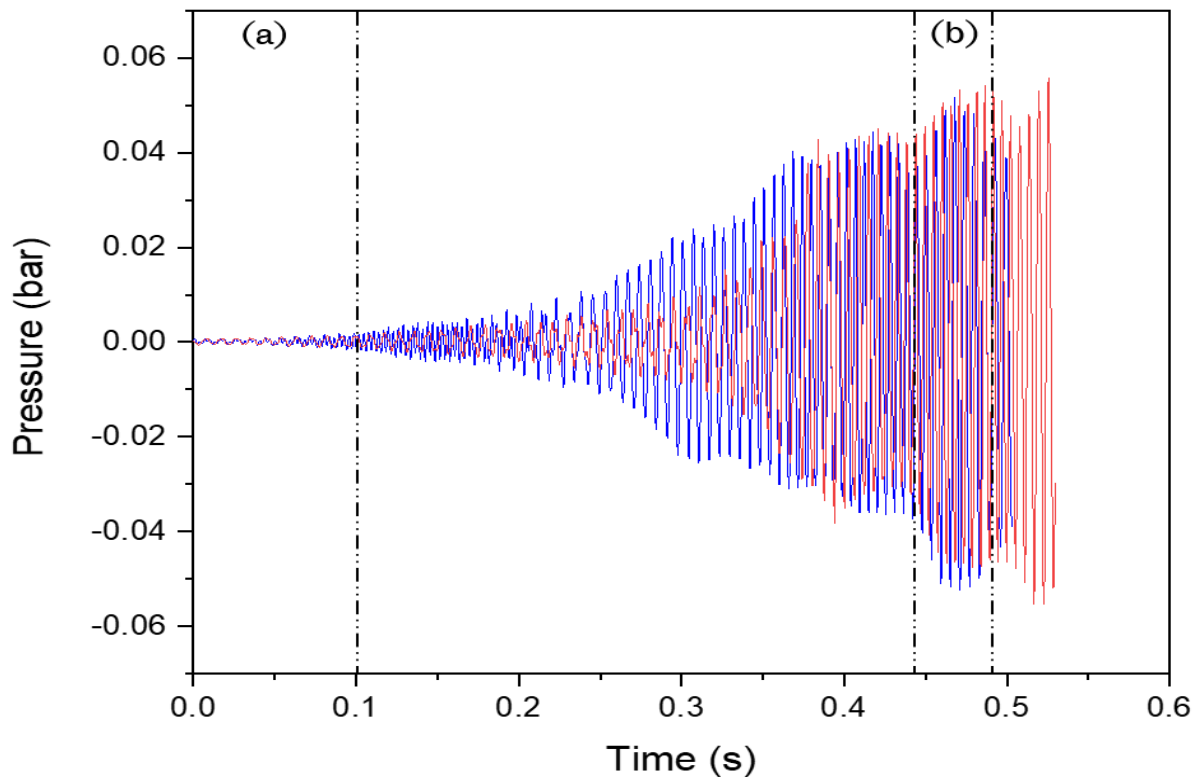


Figure 5.22: Tube end pressure against time of methane (blue), and propane (red) on  $\phi = 1.0$ ,  $R_H = 0.2$  flames

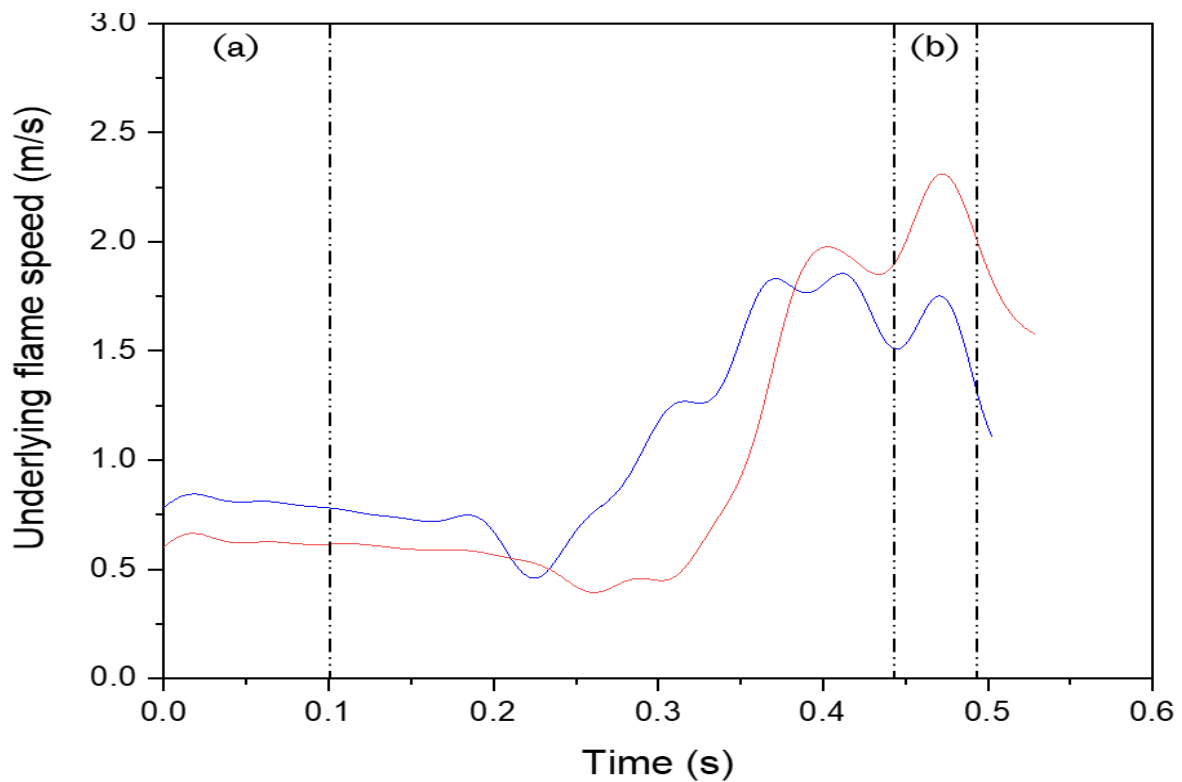
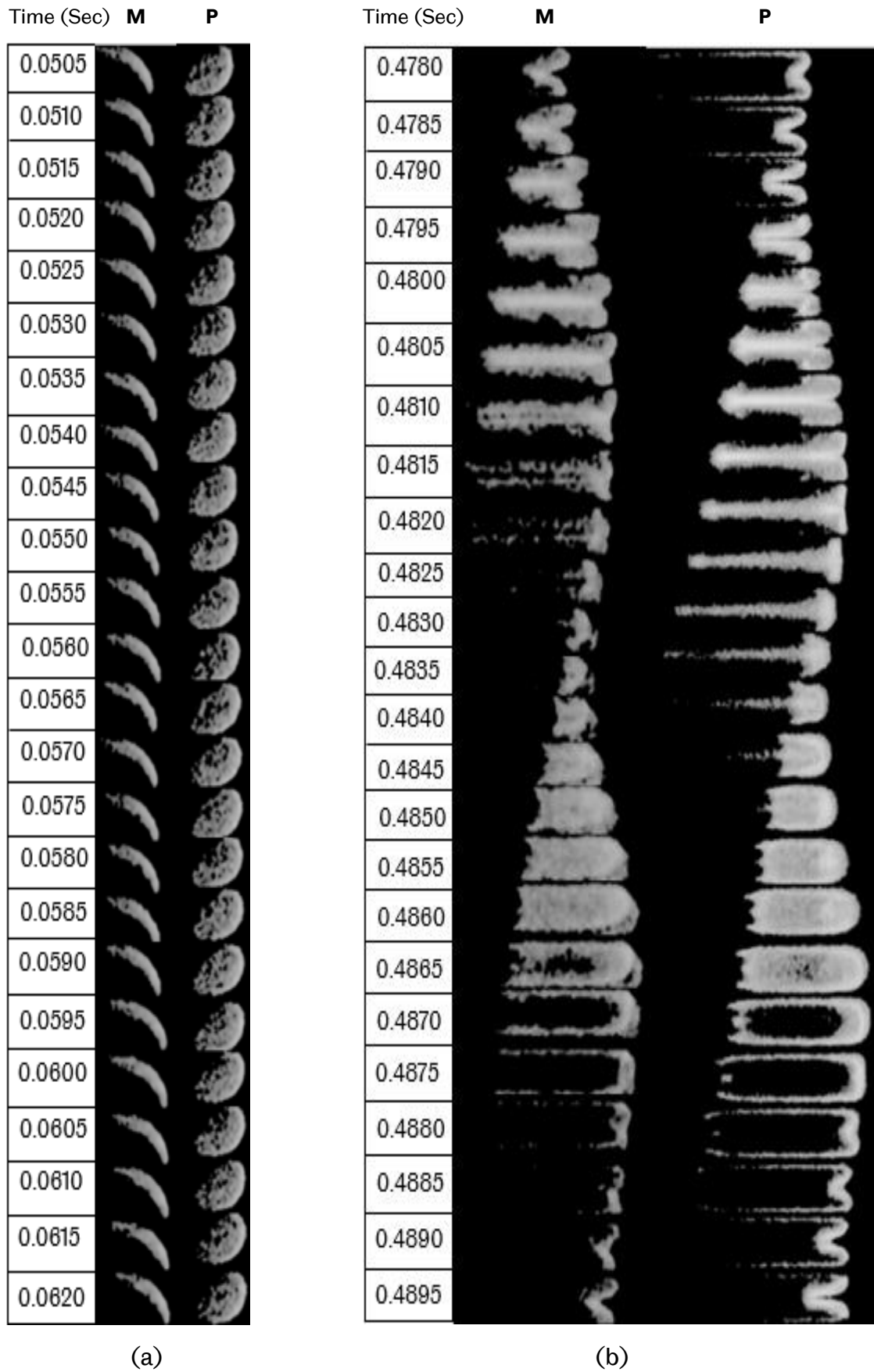


Figure 5.23: Underlying flame speed against time of methane (blue), and propane (red) on  $\phi = 1.0$ ,  $R_H = 0.2$  flames



**Figure 5.24: Representative images for flame behaviour in different regimes of methane (M) and propane (P) on  $\phi = 1.0$ ,  $R_H = 0.2$  flames. Interval of 1/2000 second increments for each frame downwards**

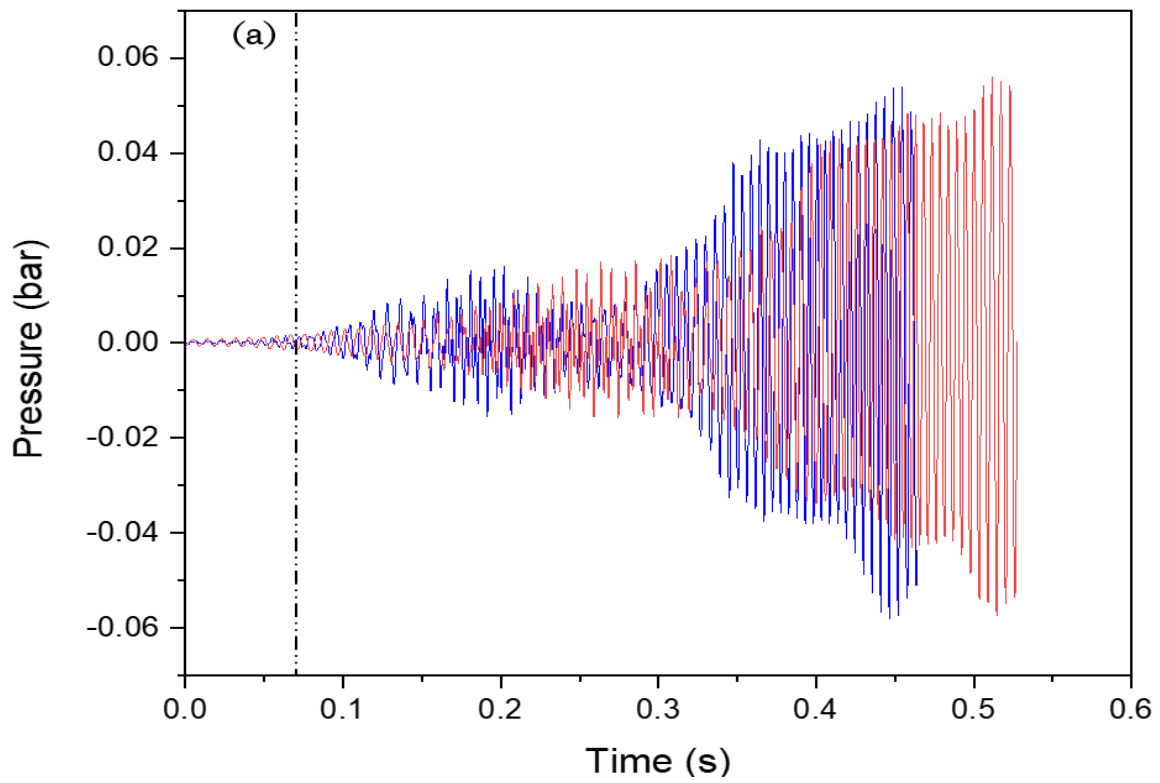


Figure 5.25: Tube end pressure against time of methane (blue), and propane (red) on  $\phi = 1.0$ ,  $R_H = 0.3$  flames

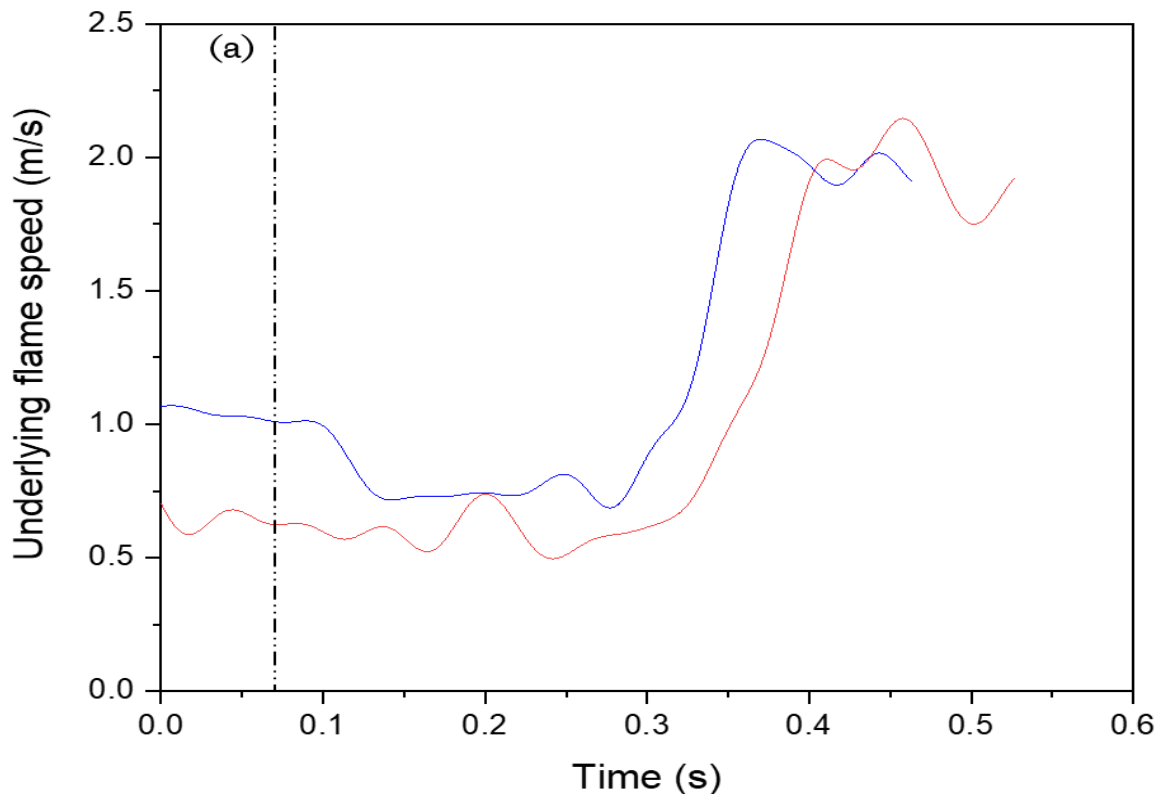
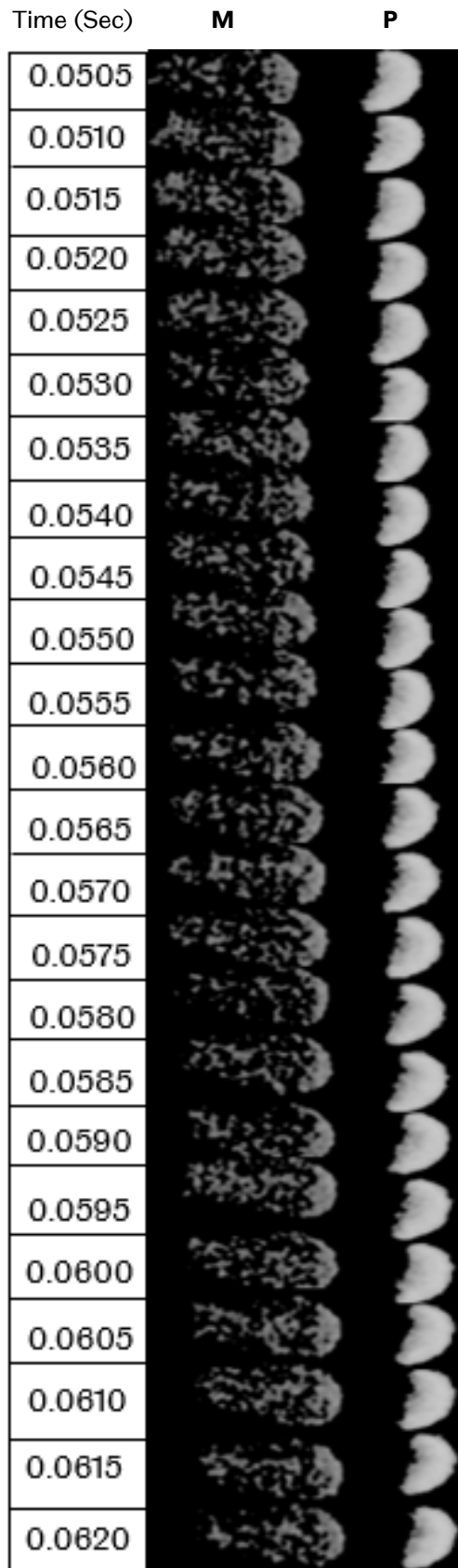


Figure 5.26: Underlying flame speed against time of methane (blue), and propane (red) on  $\phi = 1.0$ ,  $R_H = 0.3$  flames



(a)

Figure 5.27: Representative images for flame behaviour in different regimes of methane (M) and propane (P) on  $\phi = 1.0$ ,  $R_H = 0.3$  flames. Interval of 1/2000 second increments for each frame downwards

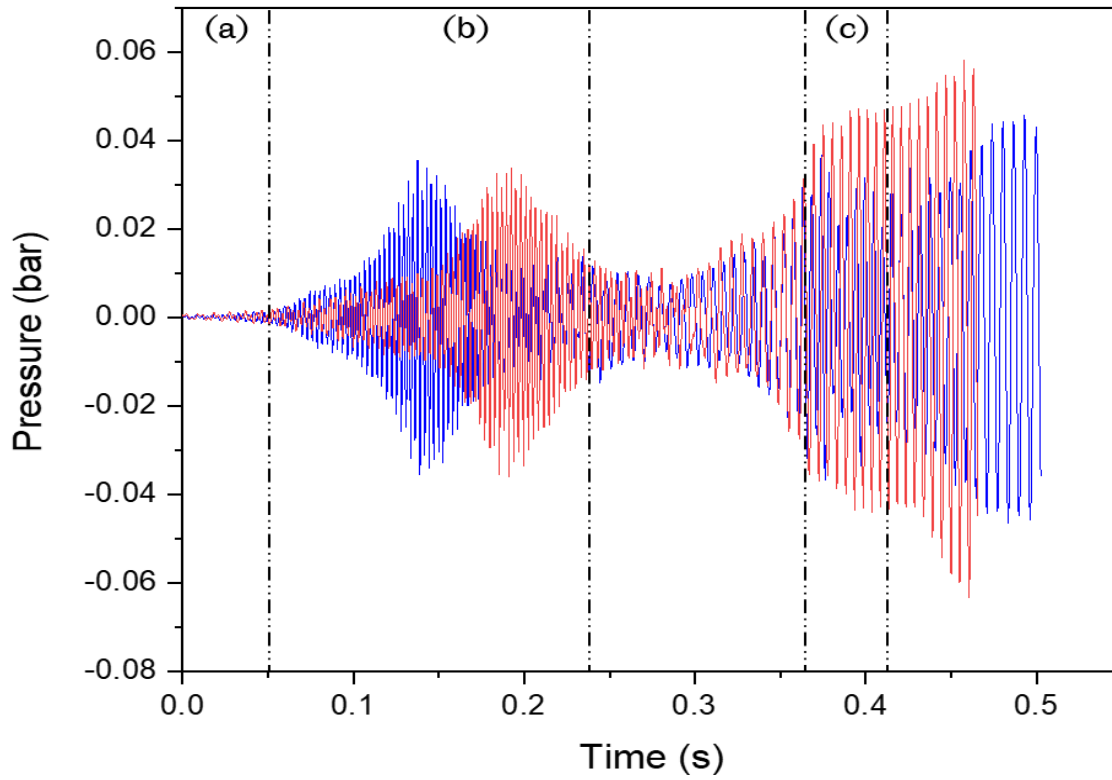


Figure 5.28: Tube end pressure against time of methane (blue), and propane (red) on  $\phi = 1.0$ ,  $R_H = 0.4$  flames

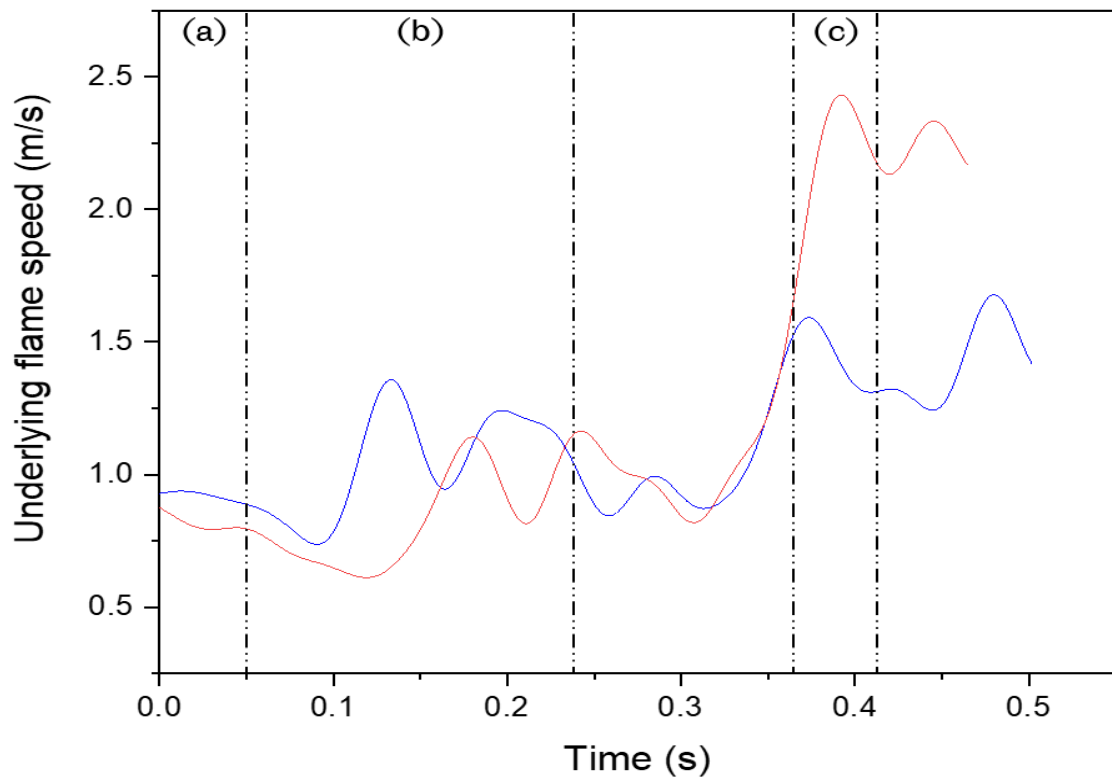


Figure 5.29: Underlying flame speed against time of methane (blue), and propane (red) on  $\phi = 1.0$ ,  $R_H = 0.4$  flames

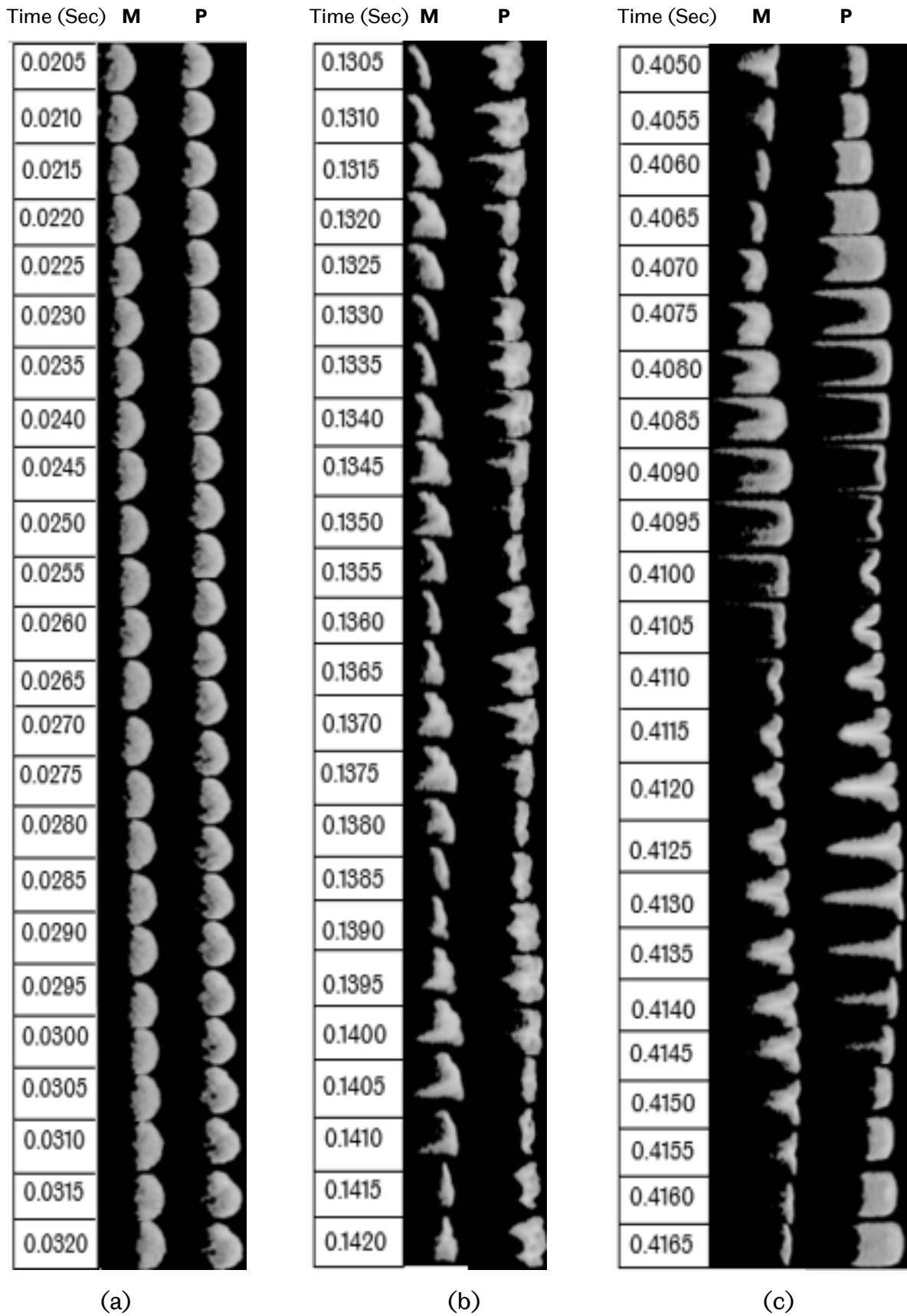


Figure 5.30: Representative images for flame behaviour in different regimes of methane (M) and propane (P) on  $\phi = 1.0$ ,  $R_H = 0.4$  flames. Interval of 1/2000 second increments for each frame downwards

### 5.1.2 The effect of equivalence ratio

Figure 5.31 presents the results of the analysis of the flame images and pressure recordings for flames to which hydrogen had been added, i.e.  $R_H = 0.1$ , and with equivalence ratios,  $\phi$ , ranging from 0.9 to 1.2. The flame front positions were plotted against time in Figure 5.31(a). With the methane flames, the oscillations began to affect the  $\phi = 0.9$  and 1.2 flames at a distance of  $\sim 0.1$  m, while the  $\phi = 1.0$  and 1.1 flames were affected at  $\sim 0.2$  m and  $\sim 0.15$  m, respectively. All of the flames oscillated with approximately the same magnitude. Figure 5.31(b) plots the flame front position amplitudes against time, revealing that all flames experienced a similar increase in distance amplitude.

The tube end pressure signals were plotted against time in Figure 5.31(c), showing that the oscillating flames reached a maximum pressure of around  $\sim 0.06$  bar for all flames. The plot of flame area against time is given in Figure 5.31(d), whereby all flames showed a steady increase in the initial flame area, beginning at  $\sim 0.1$  kilopixels and finishing within  $\sim 50$  to 120 kilopixels. This flame area increase was similarly reflected in the raw flame front speed.

The flame area of all flames fluctuated during their oscillatory periods. The flame area response to the pressure increase was unlike the previously tracked parameters. Specifically, the flame area first decreased and then increased with larger amplitude oscillations, while the other parameters increased proportionally with the increase in pressure. The flame areas of all oscillating flames decreased prior to their increase during the oscillation, each with different magnitudes that were possibly linked to flame pressure. Notably, the flame area for the  $\phi = 1.2$  flame demonstrated unexpected behaviour, growing to  $\sim 225$  kilopixels despite a low laminar burning velocity. The richer flames exhibited an overall brighter appearance than the leaner flames.

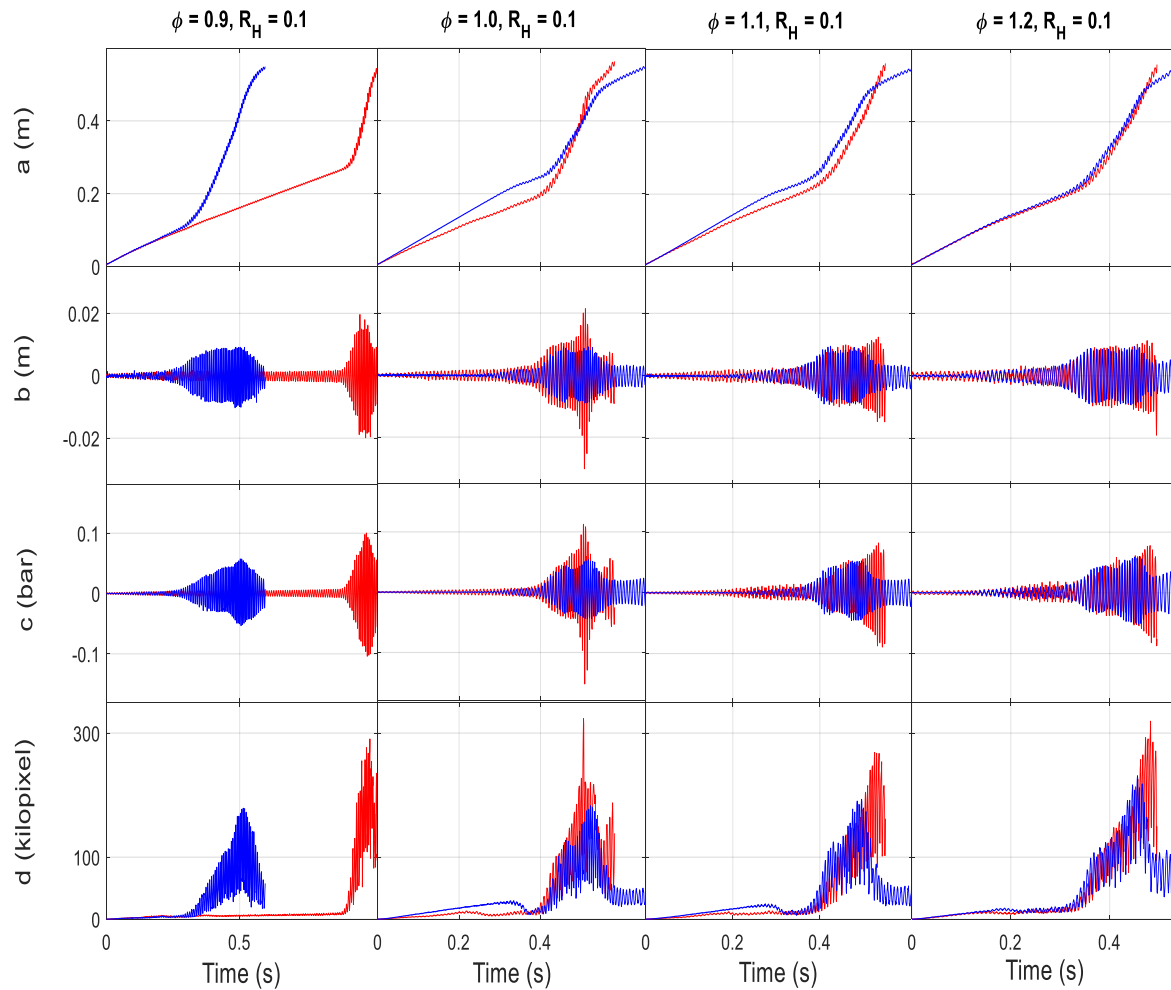


**Figure 5.31: Effect of equivalence ratio on methane (blue), propane (red) on  $\phi = 0.9$ - $1.2$ ,  $R_H = 0.1$  flames, on a) flame front position, b) flame front position amplitude, c) tube end pressure, and d) flame area**

The maximum raw speed correlated with the magnitude of the flame front displacement, with all flames achieving approximately  $\sim 14$  m/s. Figure 5.32(a) shows the raw flame speed plot against time. For the methane flames, no significant increase or decrease was found in the maximum raw speed with increasing or decreasing equivalence ratio. Returning to Figure 5.32(b), it showed that, as expected, the flames' initial underlying speed increased with their laminar burning velocity; however, further increases in the equivalence ratio beyond 1.1 led to increases in the initial underlying speed. This was unexpected as the laminar burning velocity declines with increases in the equivalence ratio beyond 1.1. The  $\phi = 1.2$  flame reached the highest peak speed, at  $\sim 2.5$  m/s, the  $\phi = 0.9$  and 1.1 flames both reached a maximum speed of  $\sim 2.3$  m/s, and the  $\phi = 1.0$  flame peaked at  $\sim 2.1$  m/s.

Figure 5.32(c) plots the 200 Hz component speed against time. The  $\sim 200$  Hz components are reasonably symmetrical along the x-axis. The underlying speed fluctuations found in Figure 5.32(b) were due to the  $\sim 200$  Hz speed component, while its higher magnitude fluctuation induced a higher peak in the underlying flame speed. The  $\phi = 0.9, 1.0, 1.1$  and  $1.2$  flames achieved maximum peak amplitudes of  $\sim \pm 11$  m/s,  $\sim \pm 10$  m/s,  $\sim \pm 11$  m/s and  $\sim \pm 12$  m/s, respectively, suggesting that the  $\sim 200$  Hz speed component was responsible for the underlying speed fluctuations.

Figure 5.32(d) plots the third speed component, i.e. the  $\sim 400$  Hz, against time. In general, its fluctuation appears to relate to that of the 200 Hz speed component, with the decay in the  $\sim 200$  Hz component causing decay in the 400 Hz speed component. The  $\phi = 0.9$  and  $1.2$  flames had a higher 400 Hz pressure component, with a maximum of  $\sim \pm 0.010$  bar, compared to the  $\sim \pm 0.008$  bar attained by the  $\phi = 1.0$  and  $1.1$  flames. The  $\phi = 1.2$  flame also presented a different appearance compared to the other flames, with a higher-order frequency clearly emerging during the initial propagation stage.

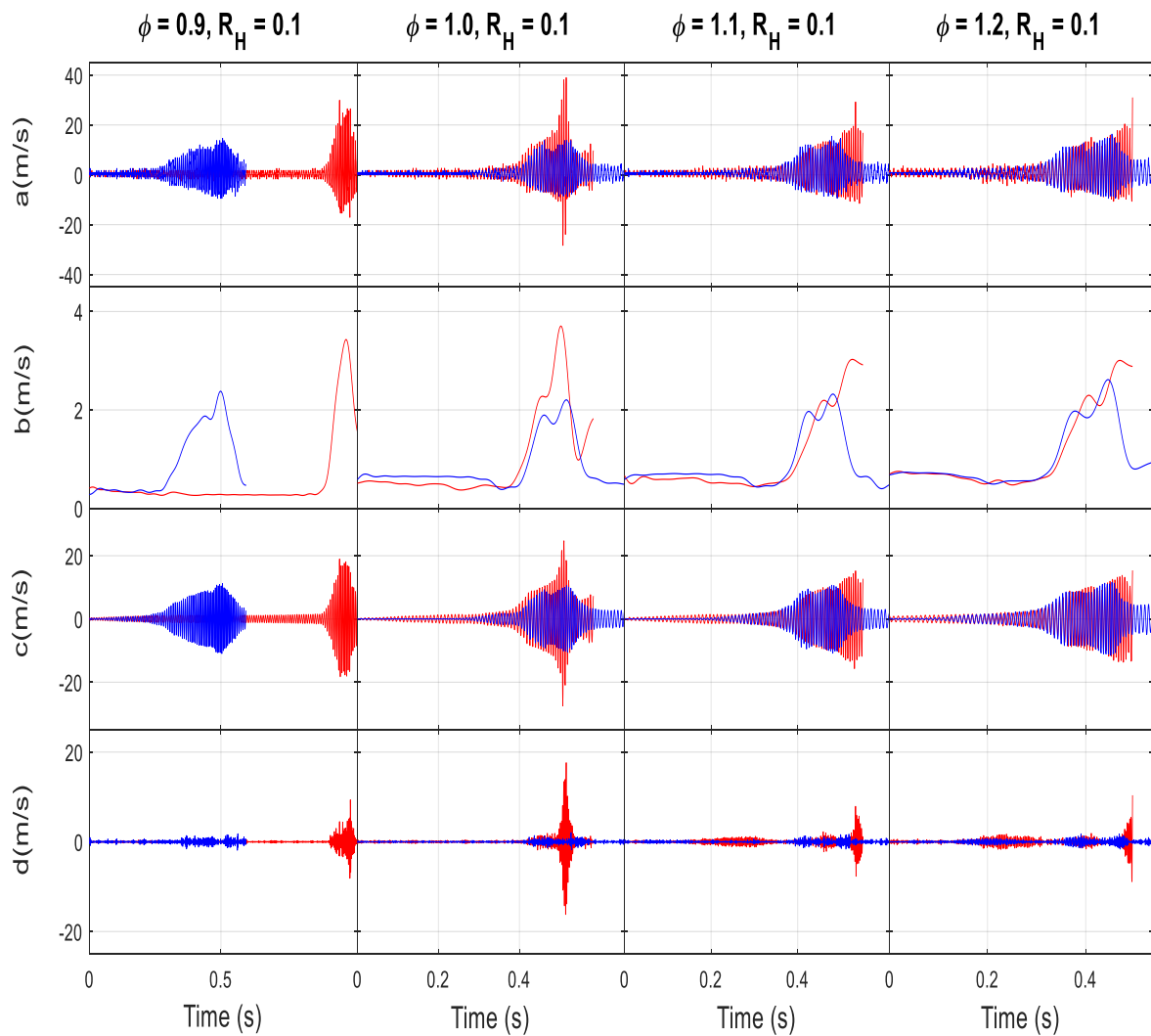


**Figure 5.32: Effect of equivalence ratio on methane (blue), propane (red) on  $\phi = 0.9-1.2$ ,  $R_H = 0.1$  flames, on a) raw flame speed, broken down into b) underlying flame speed, c) 200 Hz speed component, and d) 400 Hz speed component**

The tube end pressure signals presented in Figure 5.31(c) are disassembled into their  $\sim 200$  Hz and  $\sim 400$  Hz components in Figure 5.33(a) and Figure 5.33(d), respectively. Regarding amplitude, the  $\sim 200$  Hz pressure component fluctuations were similar to those of the  $\sim 200$  Hz speed component. The  $\phi = 0.9$  flame's  $\sim 200$  Hz pressure component achieved a maximum magnitude of  $\sim \pm 0.01$  bar, inducing the excitement of its  $\sim 400$  Hz component, which reached  $\sim \pm 0.02$  bar. For the  $\phi = 1.0, 1.1$  and  $1.2$  flames, the excitement of the  $\sim 200$  Hz pressure component reached maximum magnitudes of  $\sim \pm 0.12$  bar,  $\sim \pm 0.08$  bar and  $\sim \pm 0.07$  bar, respectively. The higher magnitude of fluctuation seen for the  $\sim 200$  Hz component of the  $\phi = 1.0$  flame caused a higher  $\sim 400$  Hz pressure fluctuation magnitude of  $\sim \pm 0.04$  bar, compared to the  $\sim \pm 0.017$  bar seen for the  $\phi = 1.1$  flame and the  $\pm 0.013$  bar for the  $\phi = 1.2$  flame.

The  $\phi = 1.1$  and  $1.2$  flames demonstrated a distinct behavioural pattern, whereby the  $\sim 400$  Hz component rose significantly before a significant increase in the  $\sim 200$  Hz component. This increase was mirrored by the speed component, as discussed above. This behaviour evidences that the  $\sim 400$  Hz pressure component can build up despite there being no increase in the  $\sim 200$  Hz pressure component. Figure 5.33(c), which plots the phase difference between the  $\sim 200$  Hz components against time, shows that, in general, all methane and propane flames experienced a period of phase matching that prompted enhanced pressure and flame area fluctuations.

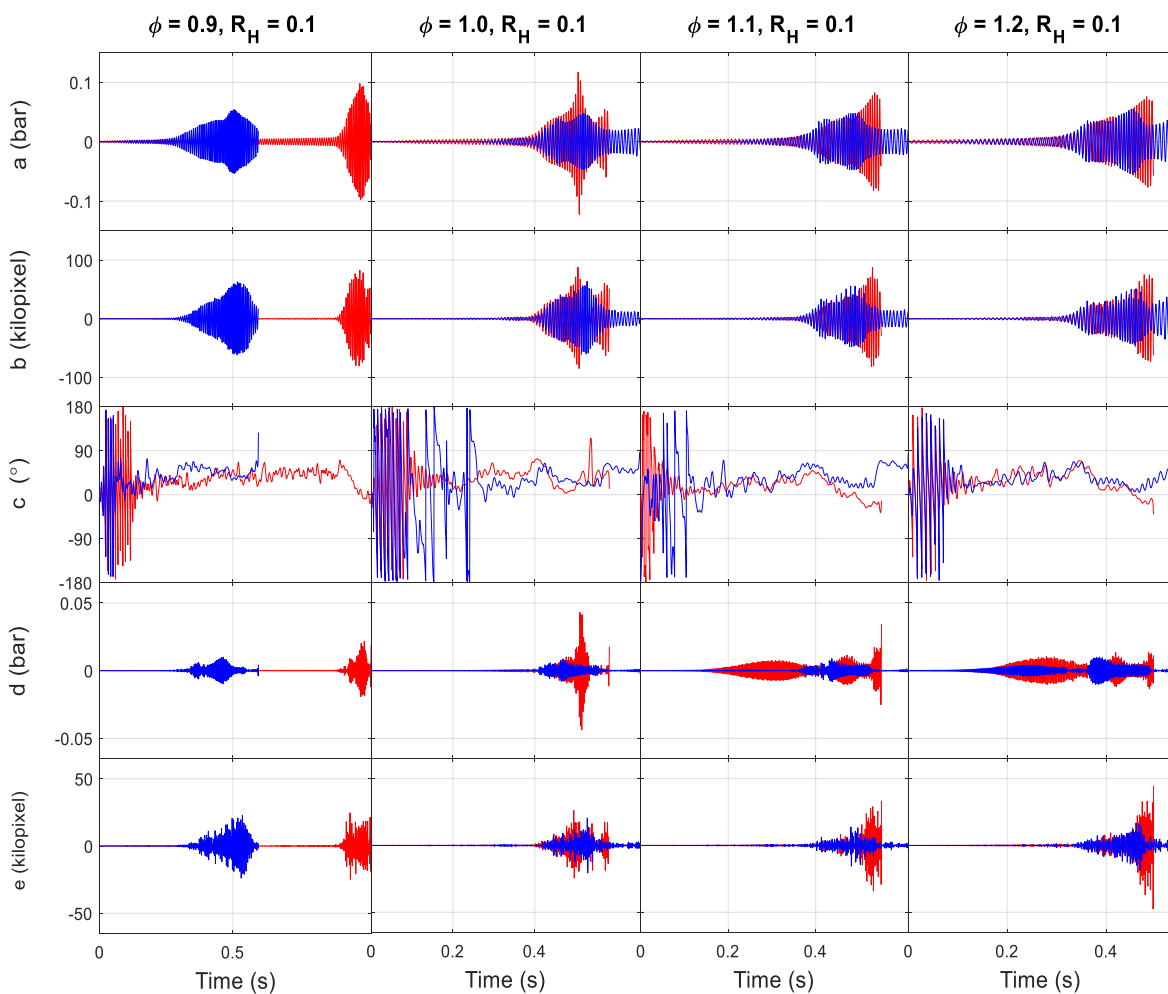


**Figure 5.33: Effect of equivalence ratio on methane (blue), propane (red) on  $\phi = 0.9-1.2$ ,  $R_H = 0.1$  flames, on a)  $\sim 200$  Hz pressure component, b)  $\sim 200$  Hz area component, c) phase difference between a) and b), d)  $\sim 400$  Hz pressure component, e)  $\sim 400$  Hz flame area component**

The comparison of the flame behaviour for methane and propane flame is shown below. The flame front positions were plotted against time in Figure 5.31(a). For the  $\phi = 0.9$  flames, the propane flame showed relatively steady propagation along the tube, with an amplitude increase towards its end, while the methane flame showed a shorter period of steady propagation. In the case of  $\phi = 1.0$  and 1.1 flames, the initial flame propagation of methane flames was noticeably faster than the propane flames as evidenced by the distance travelled by these flames, as observed in Figure 5.31(a). The  $\phi = 1.0$  propane flame exhibited high amplitude oscillation in both flame front amplitude and pressure. Figure 5.31(d) shows that the flame area of the propane flames were, again, the highest compared to methane flames. Similarly, this behaviour was found concerning their raw and underlying speeds, as found in Figure 5.32(a) and Figure 5.32(b), respectively. The  $\phi = 1.1$  and 1.2 flames have a distinct pattern of behaviour, wherein the  $\sim 400$  Hz pressure component rose significantly prior to the significant increase in the  $\sim 200$  Hz pressure component, as shown in Figure 5.33(d). This increase was also evidenced in its speed component as observed in Figure 5.32(d). Thus, it may be concluded that the build-up of the  $\sim 400$  Hz pressure component is possible even when the  $\sim 200$  Hz pressure component has not experienced an increase.

#### 5.1.2.1 Flame shape analysis

The flame shapes of methane were studied under different equivalence ratios to find out the key differences between them in their propagation. Flame position and tube end pressure are shown over time in Figure 5.34 for  $\phi = 0.9$  flame. Figure 5.34(a) shows that the flame initially propagated as a vibrating curve with a small-amplitude oscillation, reaching  $\sim \pm 0.0006$  bar. As a result, a tulip flame develops, generating the secondary oscillation stage among the high-level acoustic waves, as illustrated in Figure 5.34(b). When the flame oscillated violently, the underlying velocity in Figure 5.35(b) was mirrored in the oscillating amplitude of the flame, which was about  $\sim 2.4$  m/s at its peak.

The corresponding flame images of two regimes and the transition period (i.e. flame shapes transition from a to b) of propagation are shown in Figure 5.36. The behaviour of the  $\phi = 1.0$  was shown in section 5.1.1. In the case of the  $\phi = 1.1$  and 1.2 flames, Figure 5.37 and Figure 5.40 illustrate the position of the flame front and the tube end pressure signal as a function of time respectively. According to Figure 5.37(a) and Figure 5.40(a), the curved flame in Figure 5.37(a) and Figure 5.40(a) is linked to the very low acoustic pressure. When pressure builds, the curving flame becomes somewhat distorted, as seen in Figure 5.37(b) and Figure 5.40(b). The saturation of the primary instability resulted in the formation of the cellular flame seen in Figure 5.39(b) and Figure 5.42(b). At the initiation of the secondary instability, the tulip structures in Figure 5.39(c) and Figure 5.42(c) begin oscillating with a large amplitude reaching a maximum acoustic pressure as shown in Figure 5.37(c) and Figure 5.40(c). Three zones were recommended in Figure 5.38 and Figure 5.41 depending on the flame's underlying speed: a) constant underlying speed, b) decreasing underlying speed, and c) increasing underlying speed.

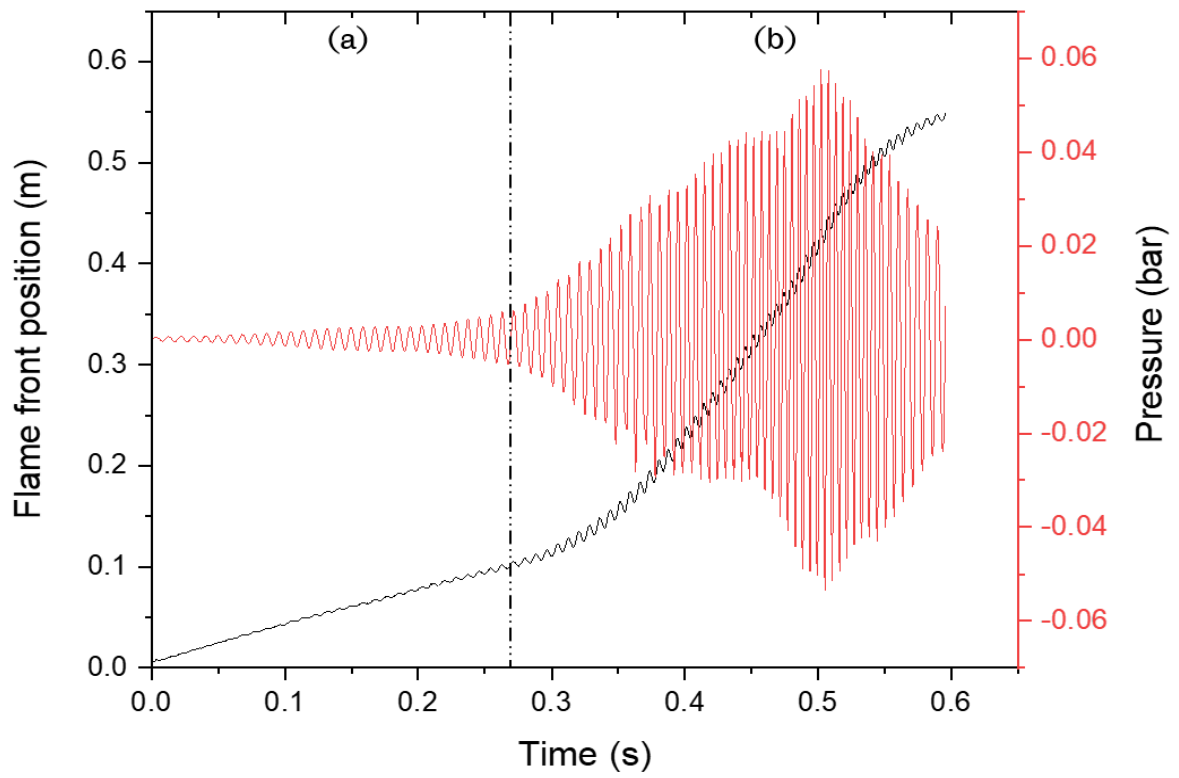


Figure 5.34: Flame front position and tube end pressure against time of methane on  $\phi = 0.9$ ,  $R_H = 0.1$  flame

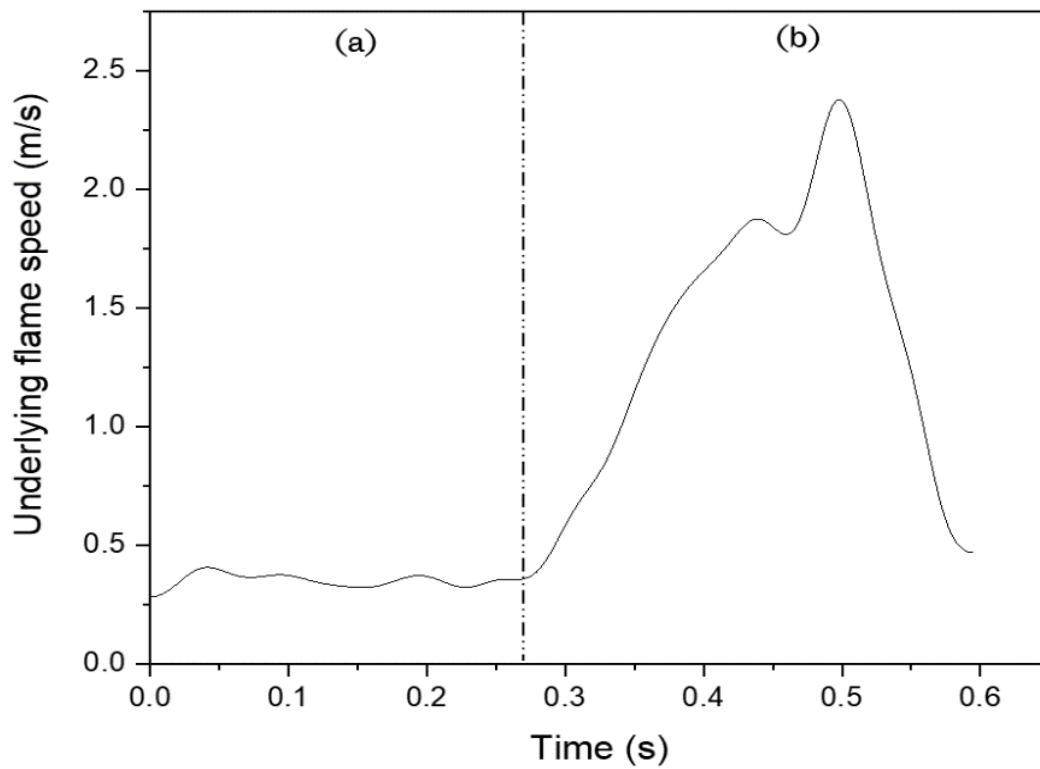


Figure 5.35: Underlying flame speed against time of methane on  $\phi = 0.9$ ,  $R_H = 0.1$  flame

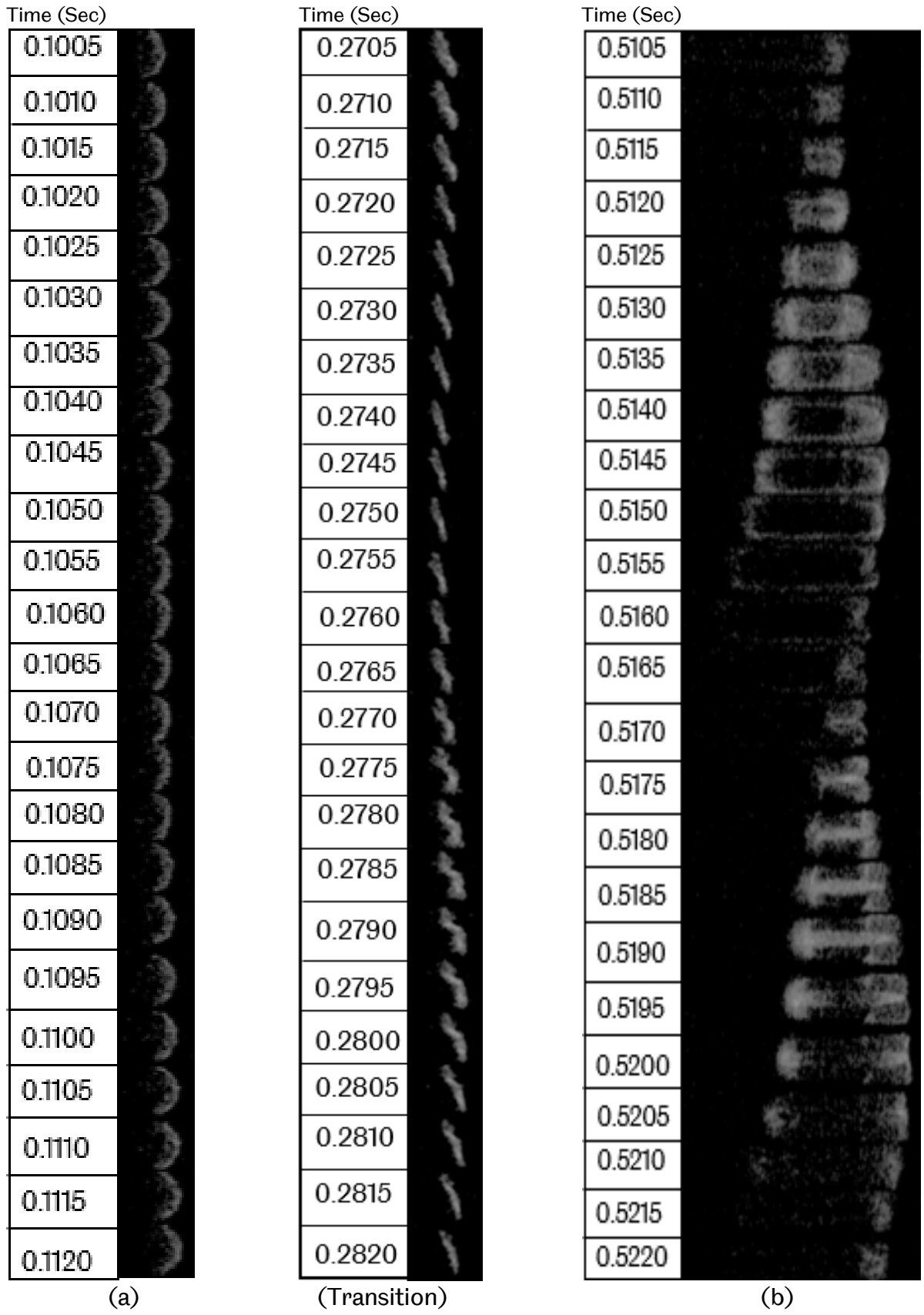


Figure 5.36: Representative images for flame behaviour in different regimes of methane on  $\phi = 0.9$ ,  $R_H = 0.1$  flame. Interval of 1/2000 second increments for each frame downwards

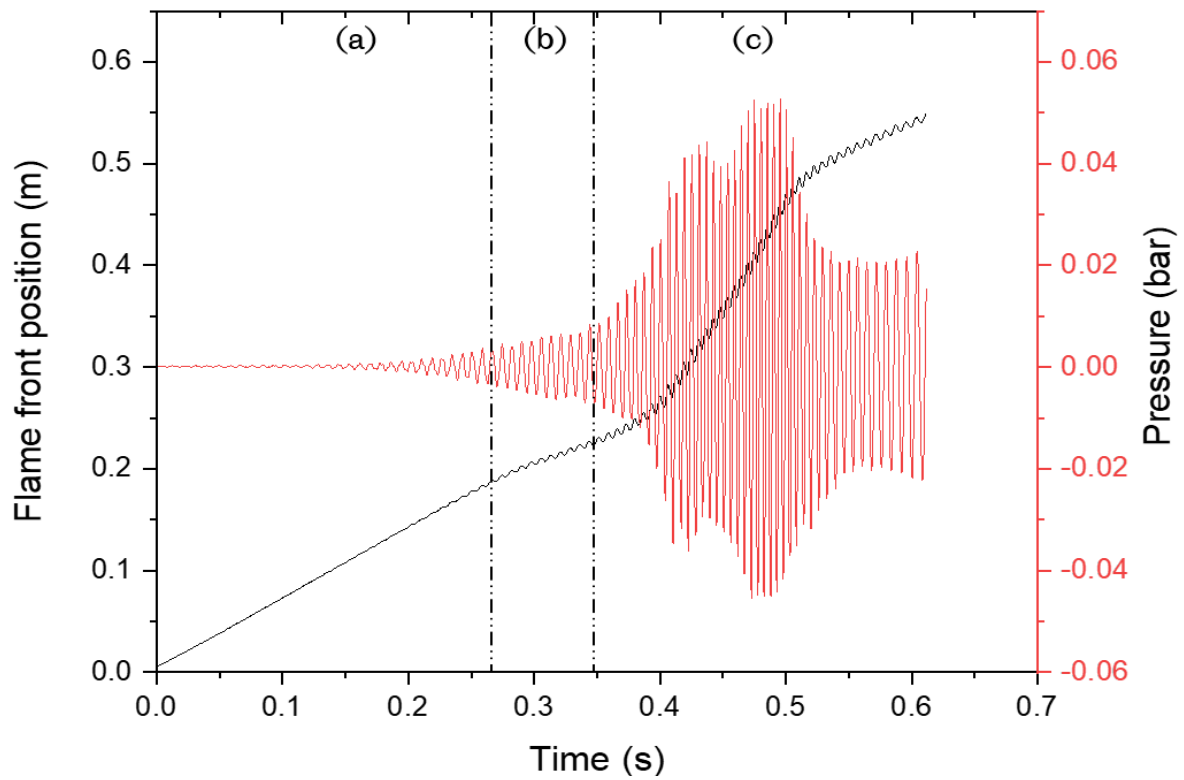


Figure 5.37: Flame front position and tube end pressure against time of methane on  $\phi = 1.1$ ,  $R_H = 0.1$  flame

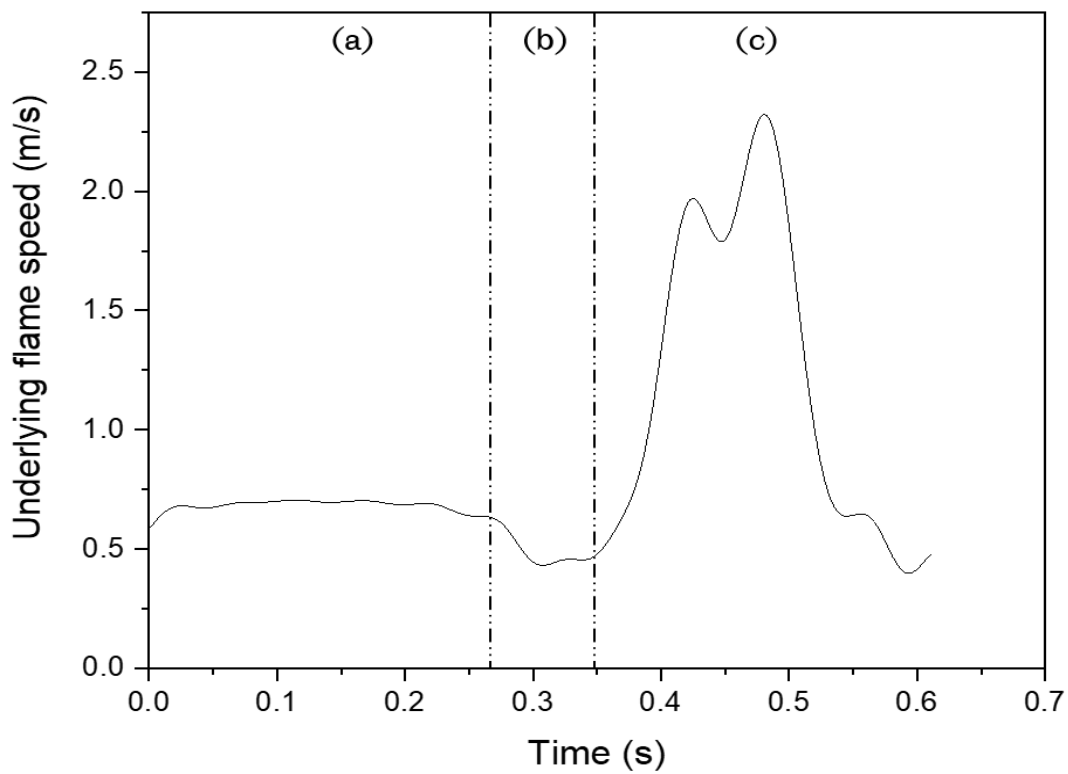
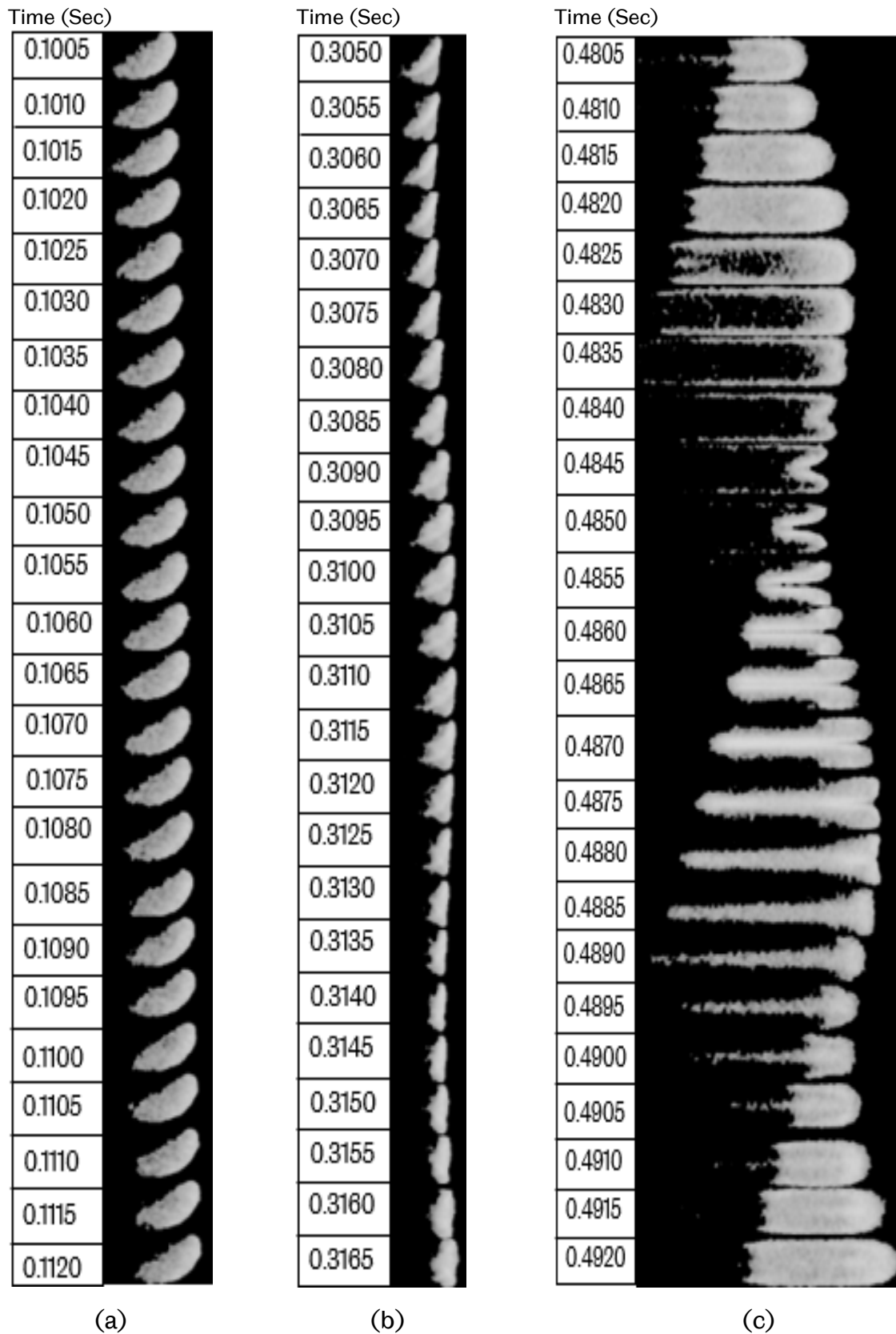


Figure 5.38: Underlying flame speed against time of methane on  $\phi = 1.1$ ,  $R_H = 0.1$  flame



**Figure 5.39: Representative images for flame behaviour in different regimes of methane on  $\phi = 1.1$ ,  $R_H = 0.1$  flame. Interval of 1/2000 second increments for each frame downwards**

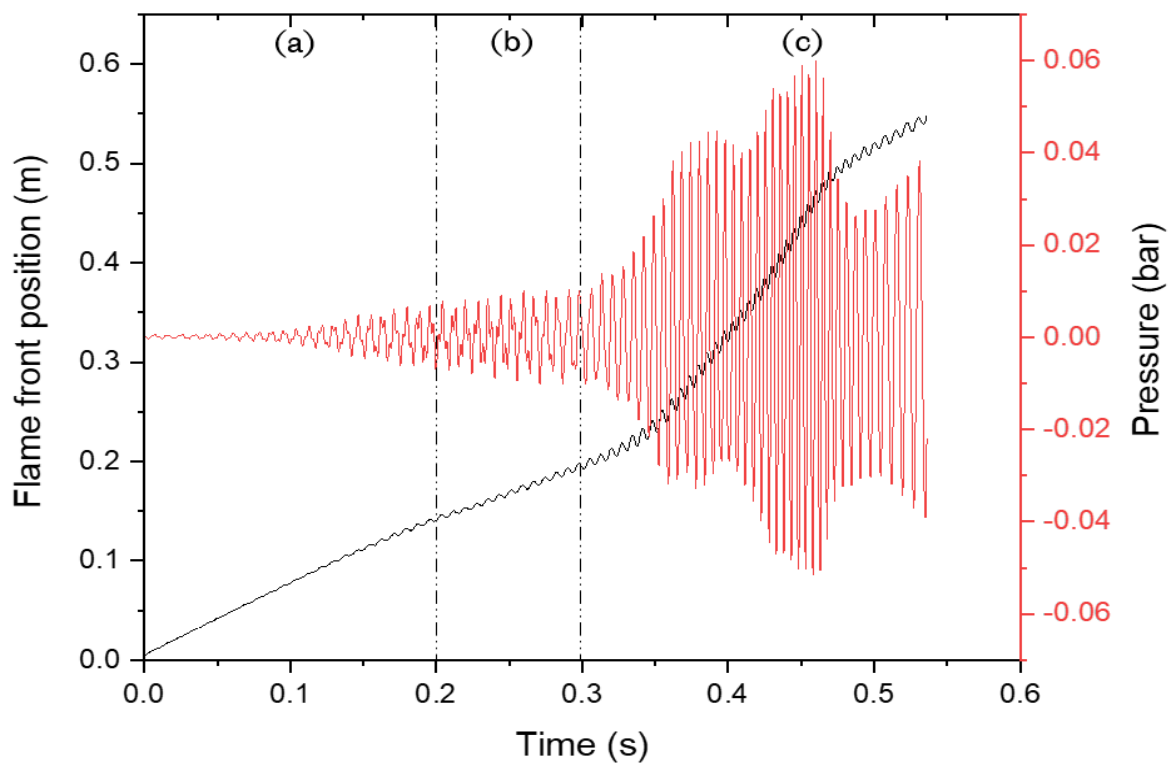


Figure 5.40: Flame front position and tube end pressure against time of methane on  $\phi = 1.2$ ,  $R_H = 0.1$  flame

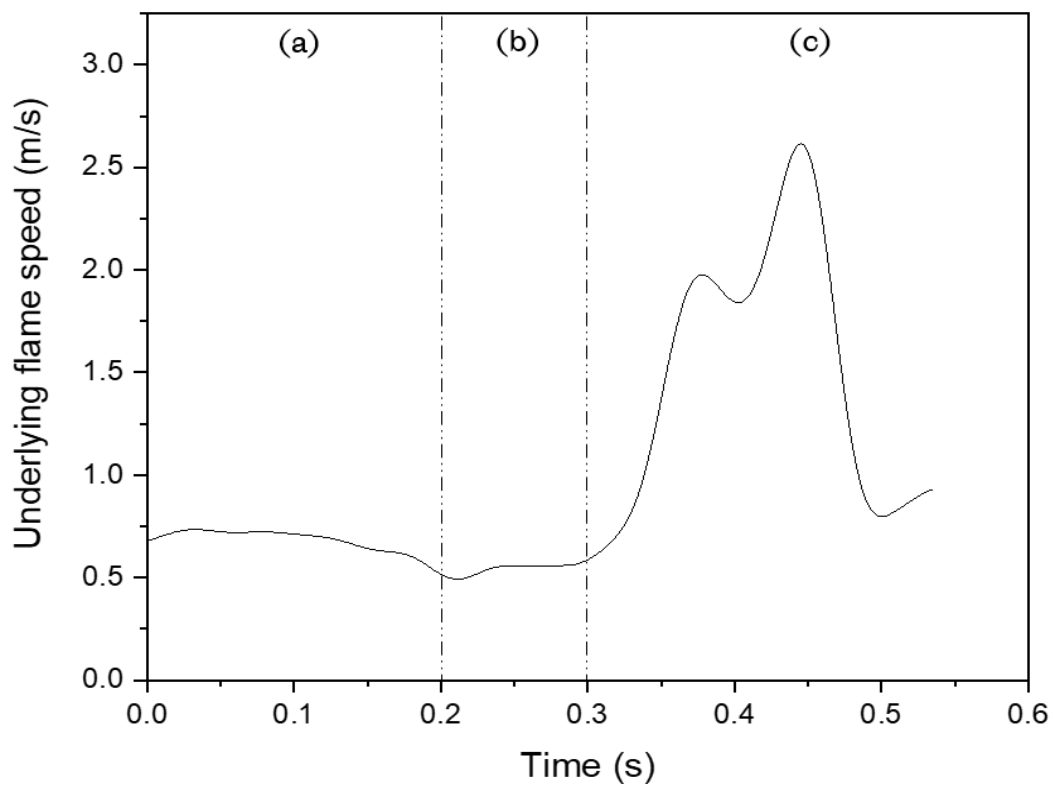
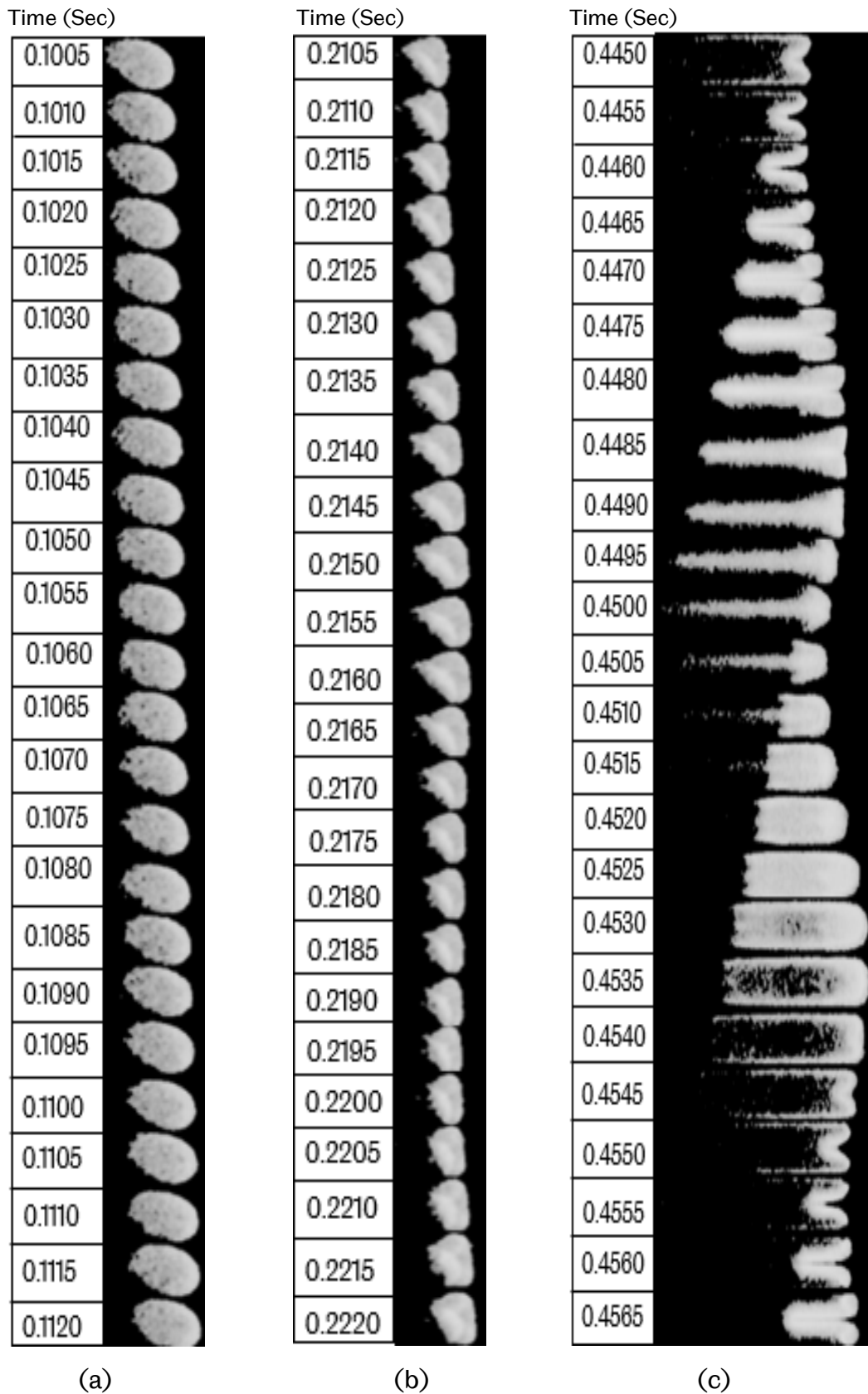


Figure 5.41: Underlying flame speed against time of methane on  $\phi = 1.2$ ,  $R_H = 0.1$  flame



**Figure 5.42: Representative images for flame behaviour in different regimes of methane on  $\phi = 1.2$ ,  $R_H = 0.1$  flame. Interval of 1/2000 second increments for each frame downwards**

It is shown here that a comparison between the flame characteristics of methane and propane flames is made at specified areas where both flames exhibited a clear variation in their characteristics. From  $\phi = 0.9$  to 1.2, all of the methane flames begin propagating with a curved and constant flame except for the  $\phi = 0.9$  flame. As demonstrated in region (a) in Figure 5.46, and Figure 5.49, this regime was only observed in methane flames; on the other hand, propane flames travel with a vibrating curved flame, producing more acoustic sound, which was evident based on their flame pressure variations in the early stage of propagation. According to Figure 5.47(a) and Figure 5.50(a), the methane flames grew in speed more than the propane flames, indicating that their flame behaviour was mirrored in their initial underlying speed. Figure 5.48(a) and Figure 5.51(a) depict the matching flame pictures of the methane and propane flames, respectively.

In the case of the  $\phi = 0.9$  flame, when compared to the propane flame, the methane flame showed a reduced pressure oscillation, as shown in Figure 5.43(b). In Figure 5.45(b), although it seems that the methane flame oscillates with elongation, the propane flame undergoes a significant elongation which was reflected in a considerable change in the speed of the flame. In Figure 5.44(b), the methane flame attained a maximum underlying velocity of  $\sim 2.4$  m/s, whereas propane obtained a maximum underlying velocity of  $\sim 3.4$  m/s.

In the case of the  $\phi = 1.1$  and 1.2 flames, based on Figure 5.46(b) and Figure 5.49(b), both flames showed signs of instability associated with the cellular structure, as shown in Figure 5.48(b) and Figure 5.51(b). The methane flames produced a lower acoustic pressure compared to the propane flames, which was evident from their flame pressure variations in the middle stages of propagation as shown in Figure 5.46(b) and Figure 5.49(b). According to Figure 5.48(c) and Figure 5.51(c), they exhibited comparable behaviour to that found in the  $\phi = 0.9$  flame, where the methane flame seems to oscillate with less elongation than the propane flame.

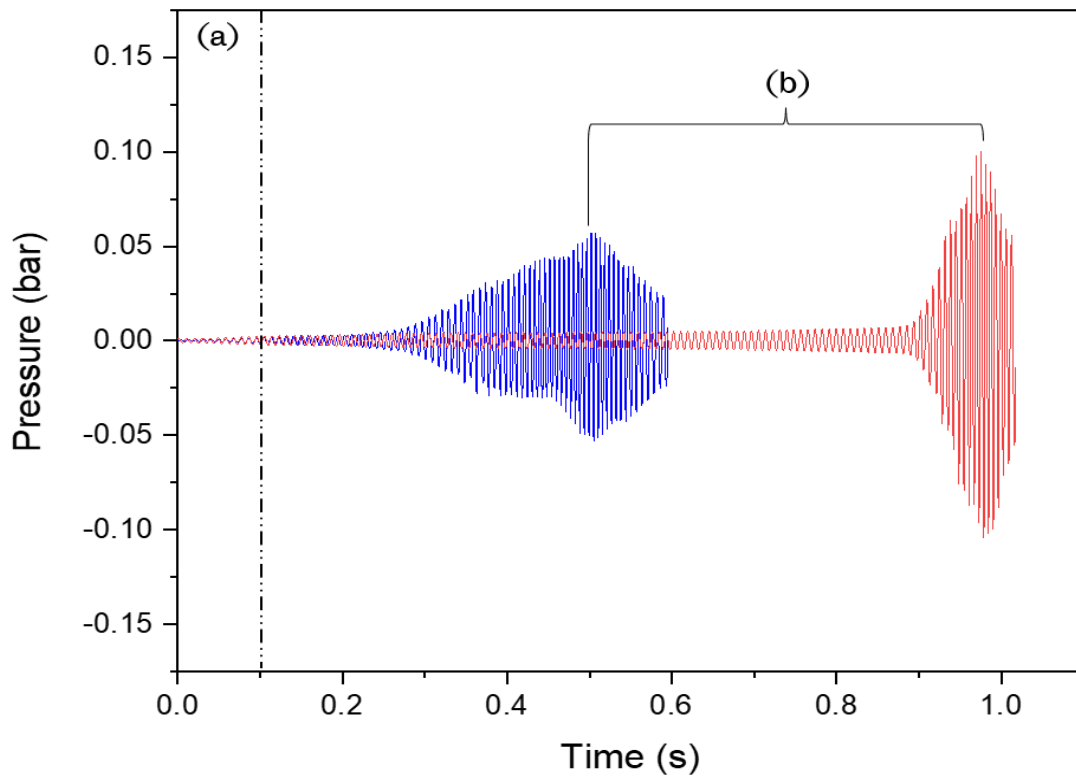


Figure 5.43: Tube end pressure against time of methane (blue), and propane (red) on  $\phi = 0.9$ ,  $R_H = 0.1$  flames

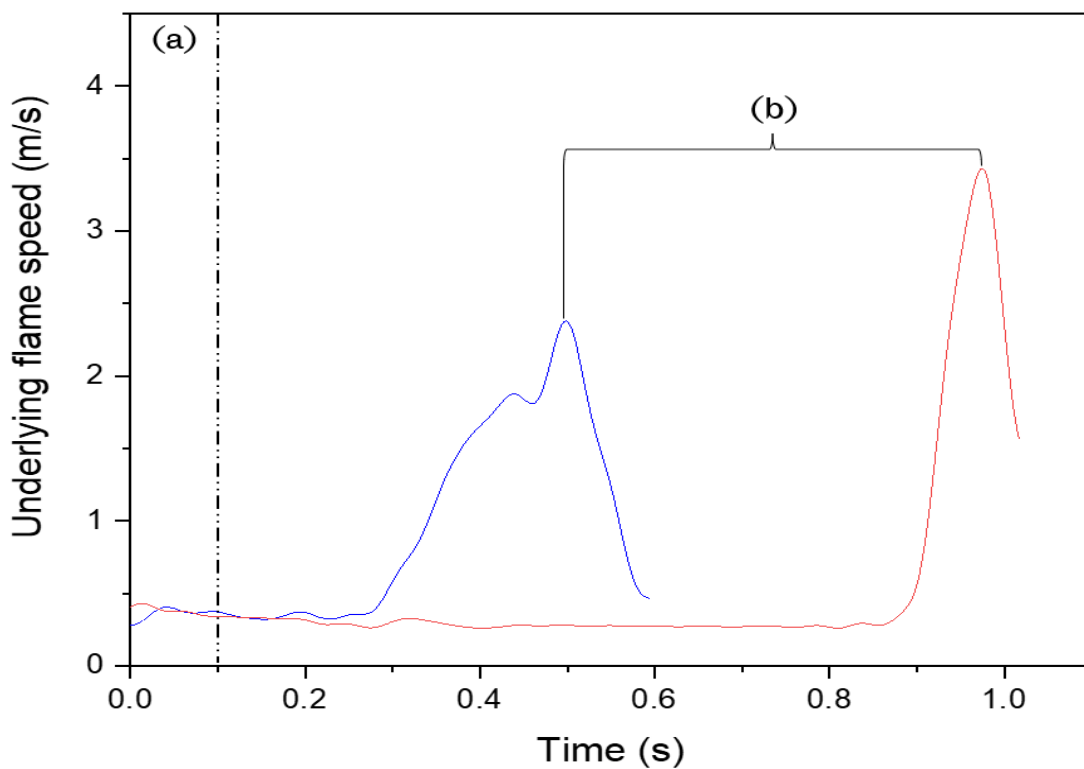


Figure 5.44: Underlying flame speed against time of methane (blue), and propane (red) on  $\phi = 0.9$ ,  $R_H = 0.1$  flames

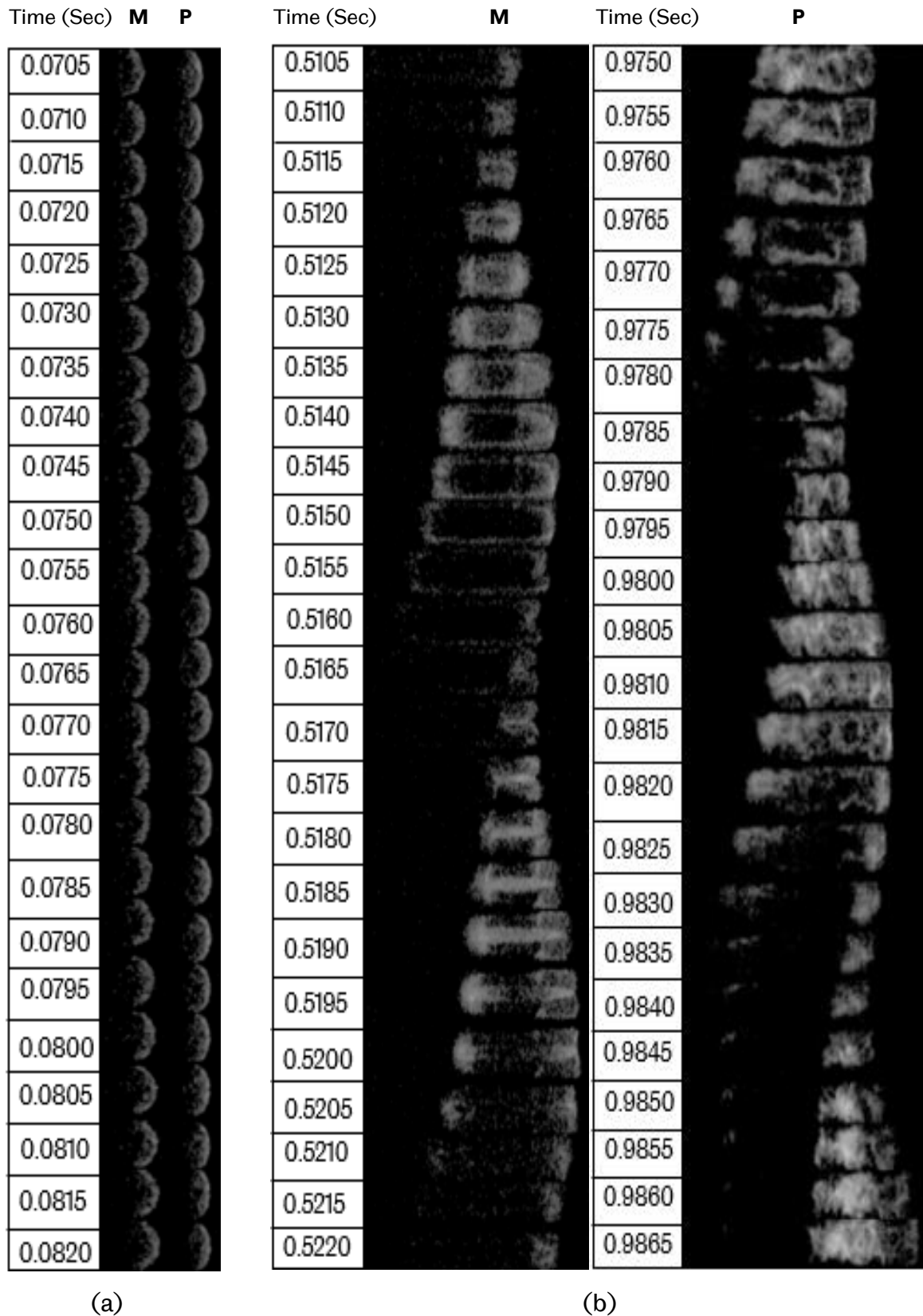


Figure 5.45: Representative images for flame behaviour in different regimes of methane (M) and propane (P) on  $\phi = 0.9$ ,  $R_H = 0.1$  flames. Interval of 1/2000 second increments for each frame downwards

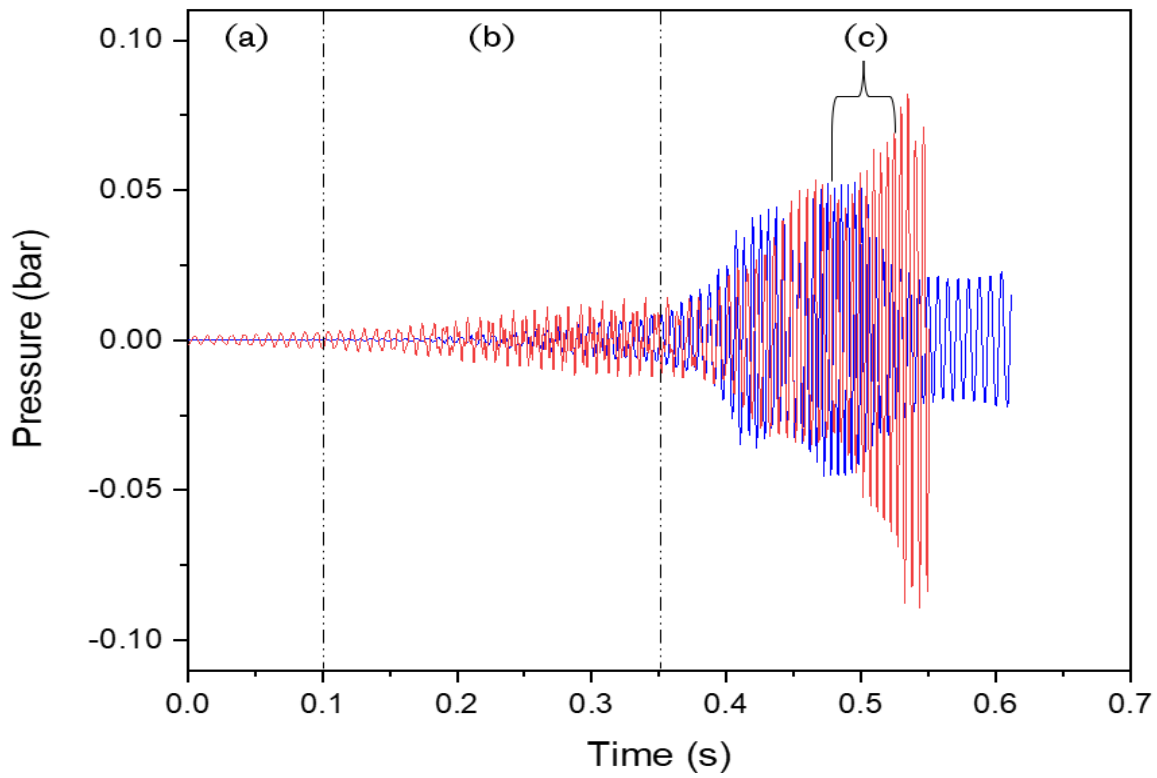


Figure 5.46: Tube end pressure against time of methane (blue), and propane (red) on  $\phi = 1.1$ ,  $R_H = 0.1$  flames

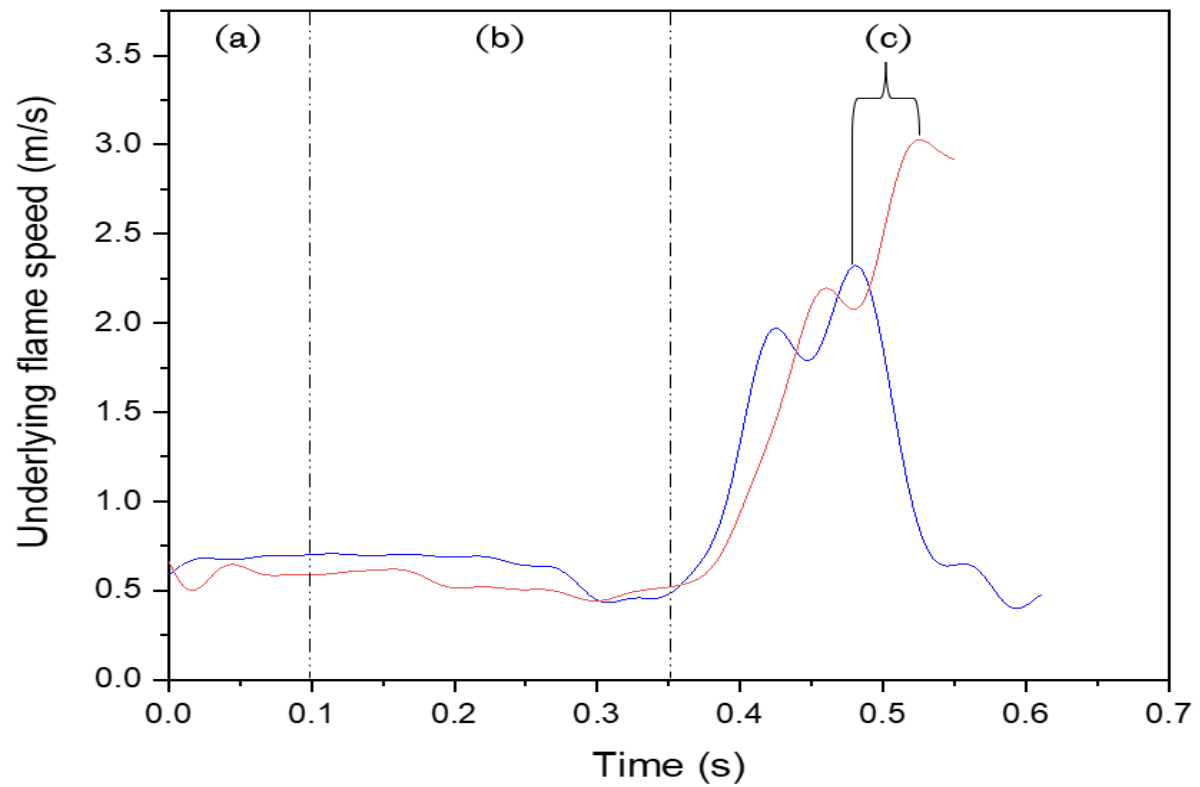


Figure 5.47: Underlying flame speed against time of methane (blue), and propane (red) on  $\phi = 1.1$ ,  $R_H = 0.1$  flame

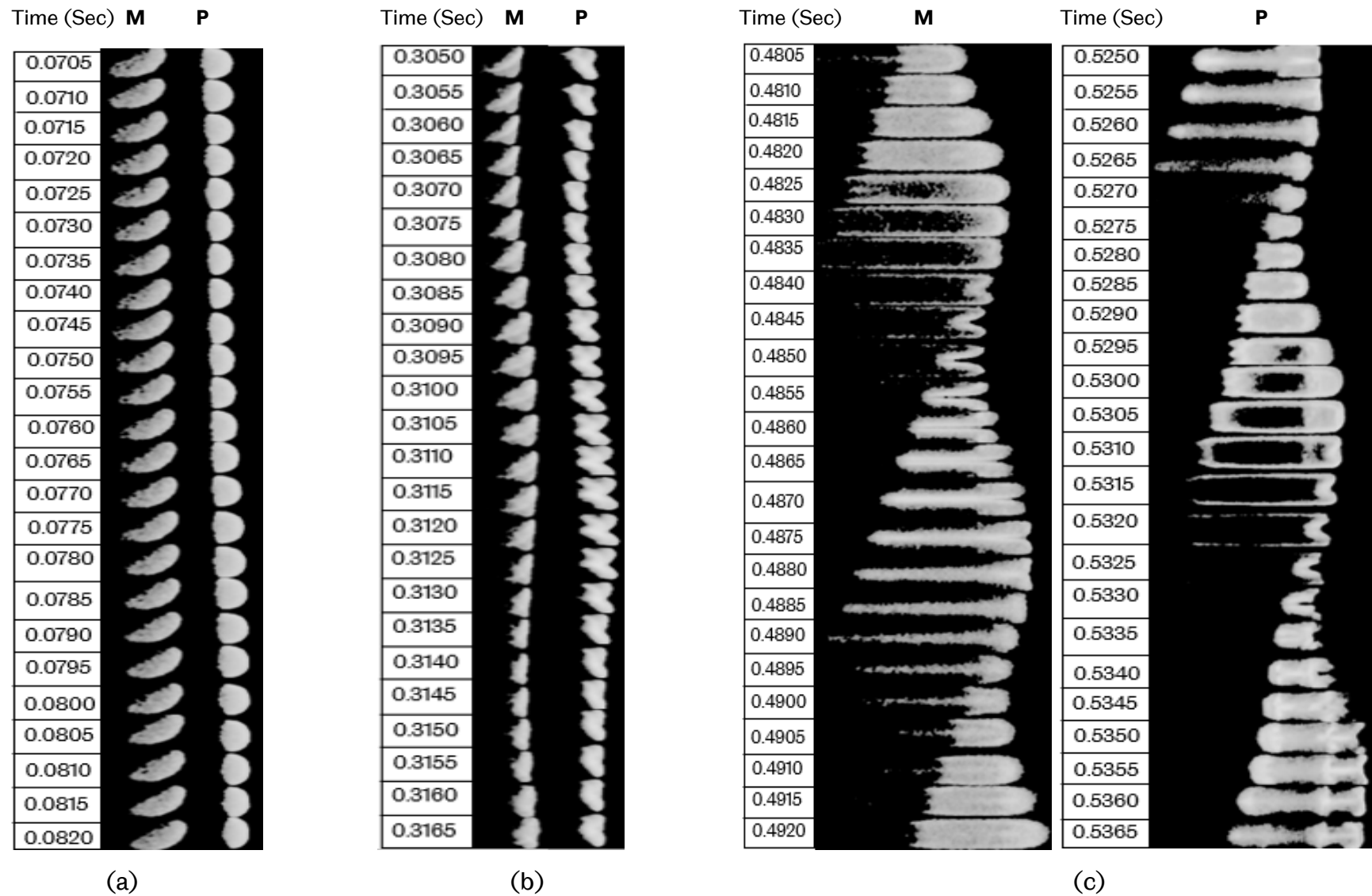


Figure 5.48: Representative images for flame behaviour in different regimes of methane and propane on  $\phi = 1.1$ ,  $R_H = 0.1$  flames. Interval of 1/2000 second increments for each frame downwards

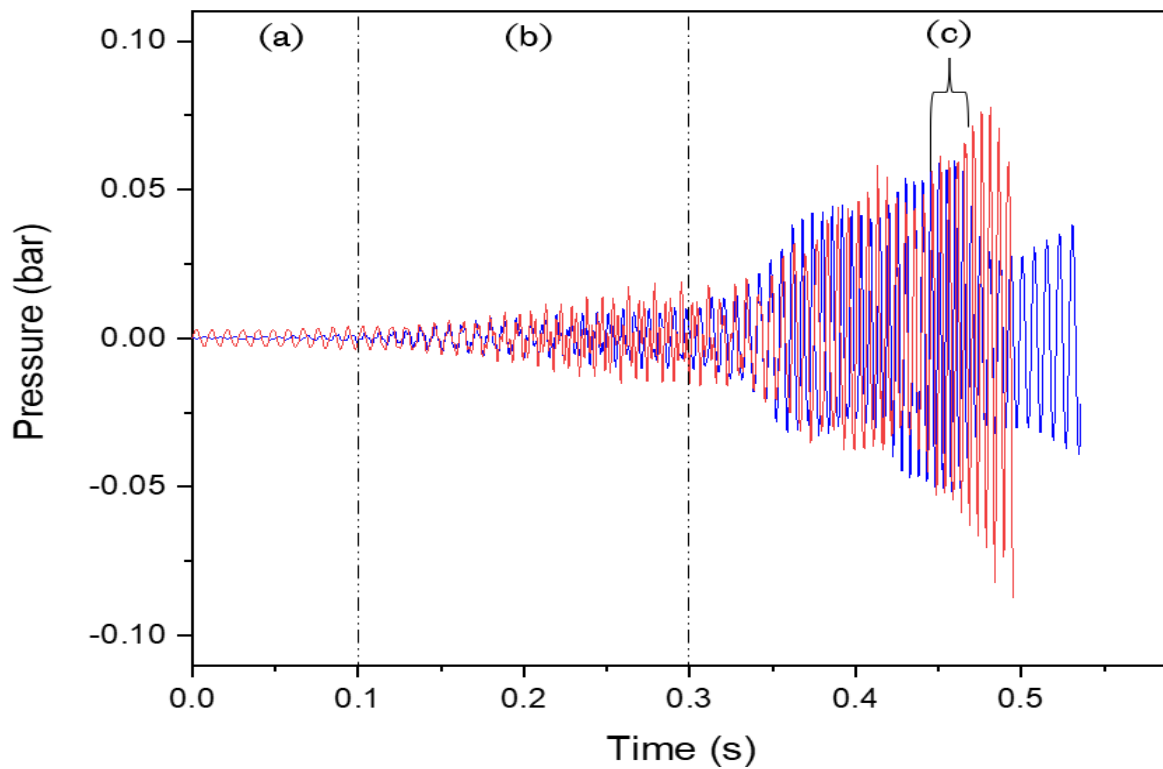


Figure 5.49: Tube end pressure against time of methane (blue), and propane (red) on  $\phi = 1.2$ ,  $R_H = 0.1$  flames

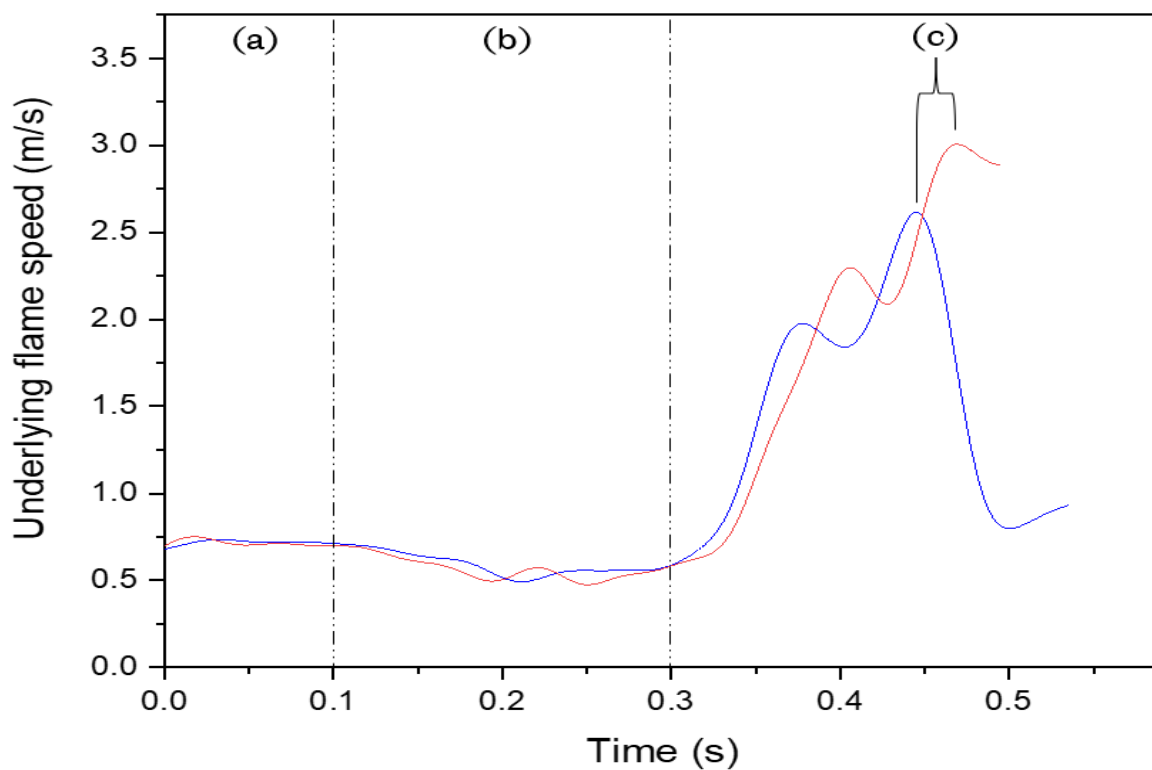


Figure 5.50: Underlying flame speed against time of methane (blue), and propane (red) on  $\phi = 1.2$ ,  $R_H = 0.1$  flames

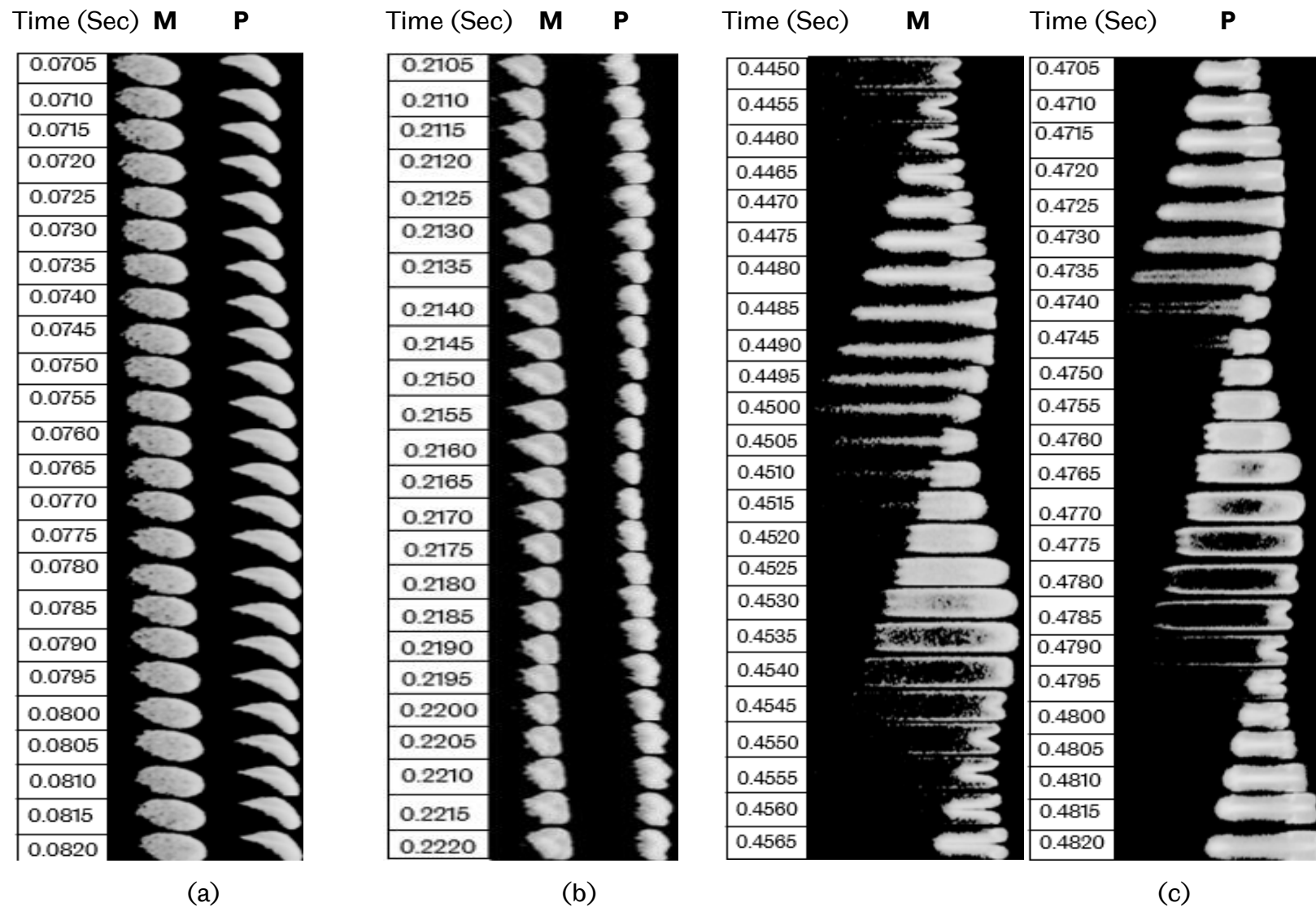


Figure 5.51: Representative images for flame behaviour in different regimes of methane and propane on  $\phi = 1.2$ ,  $R_H = 0.1$  flames. Interval of 1/2000 second increments for each frame downwards

### 5.1.3 Lean flame with hydrogen addition

More analysis has been performed on the flame front position of the flames at  $\phi = 0.8$  and hydrogen addition,  $R_H = 0.4$  flame. The flame front position, flame front position amplitudes, underlying speed, tube end pressure are plotted against time and labelled in Figure 5.52 as (a), (b), (c), and (d) respectively.

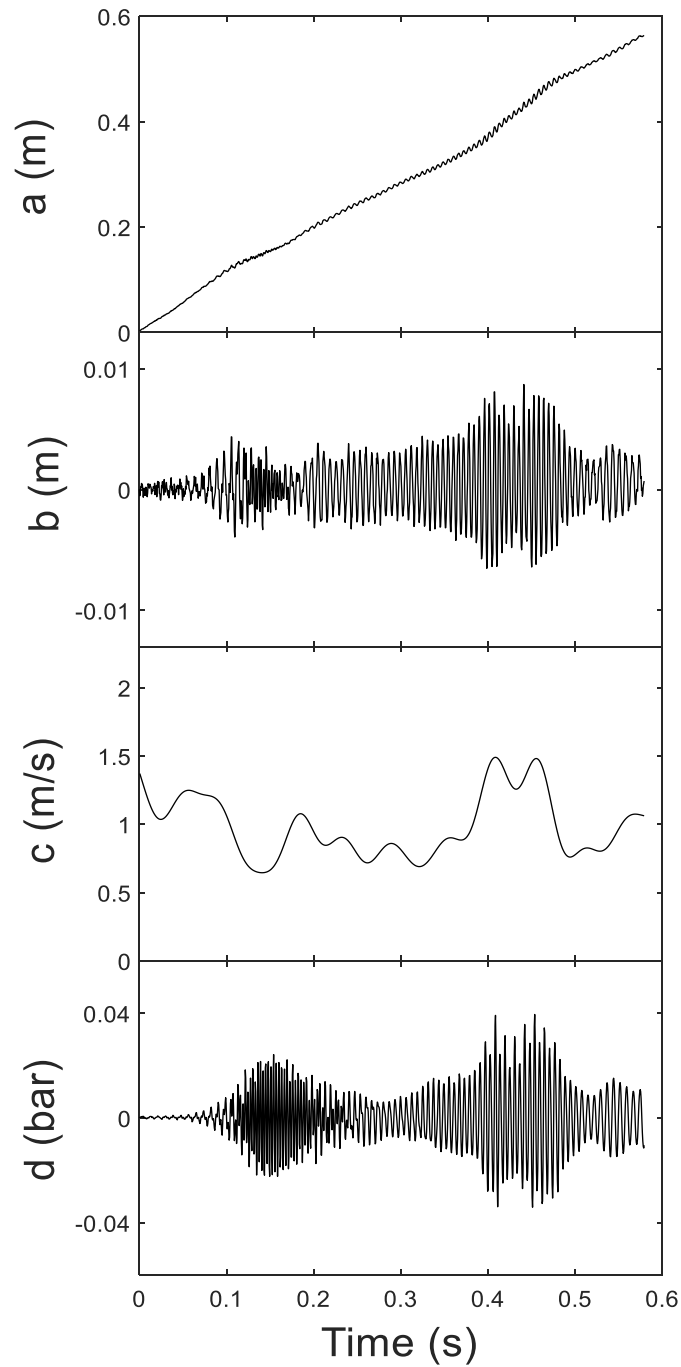


Figure 5.52: Effect of equivalence ratio on methane on  $\phi = 0.8$ ,  $R_H = 0.4$  flames, on a) flame front position, b) flame front position amplitude, c) Underlying flame speed and d) tube end pressure

The flame front position was plotted against time in Figure 5.52(a). It was observed that the flame propagated down the tube at a fairly constant rate. The flame front position amplitude is plotted against time as shown in Figure 5.52(b). Here you can see that the flame oscillated up to  $\pm 0.008$  m. Figure 5.52(c) presents the underlying flame speed plotted against time. The maximum underlying flame speed was approximately  $\sim 1.4$  m/s. The tube end pressure signal was plotted against time in Figure 5.52(d), showing that the oscillating flame reached a maximum pressure of around  $\sim 0.04$  bar.

The initial underlying speed reduction is likely to have directly linked to the  $\sim 200$  Hz speed component oscillation as seen in Figure 5.52. The  $\sim 200$  Hz speed component, which is presented in Figure 5.53(a), was generally considered to have caused the observed increase/decrease in the underlying flame speed, since the increase in the former was accompanied by an increase/decrease in the latter. Figure 5.53(b) plots the  $\sim 400$  Hz speed component against time. As can be seen in the figure, the increase in the  $\sim 400$  Hz speed component in the latter section of the tube coincides with the peak magnitude of the  $\sim 200$  Hz speed component, indicating that the  $\sim 400$  Hz component increase results from that of the  $\sim 200$  Hz speed component. Figure 5.53(c) and Figure 5.53(d), respectively, present the  $\sim 200$  Hz and  $\sim 400$  Hz components of the tube end pressure. Regarding amplitude, the  $\sim 200$  Hz pressure component fluctuations were similar to those of the  $\sim 200$  Hz speed component. It is also worth noting that the growth of the  $200$  Hz pressure component started after the growth of the  $200$  Hz speed component, suggesting that the pressure was driven by the change in flame speed. The  $\sim 400$  Hz pressure component exhibited a behaviour where the pressure builds up to a significant level. This increase was similarly reflected in the  $\sim 400$  Hz speed component. This behaviour demonstrates that the  $\sim 400$  Hz pressure component cannot build up without there being increase in the  $\sim 200$  Hz pressure component.

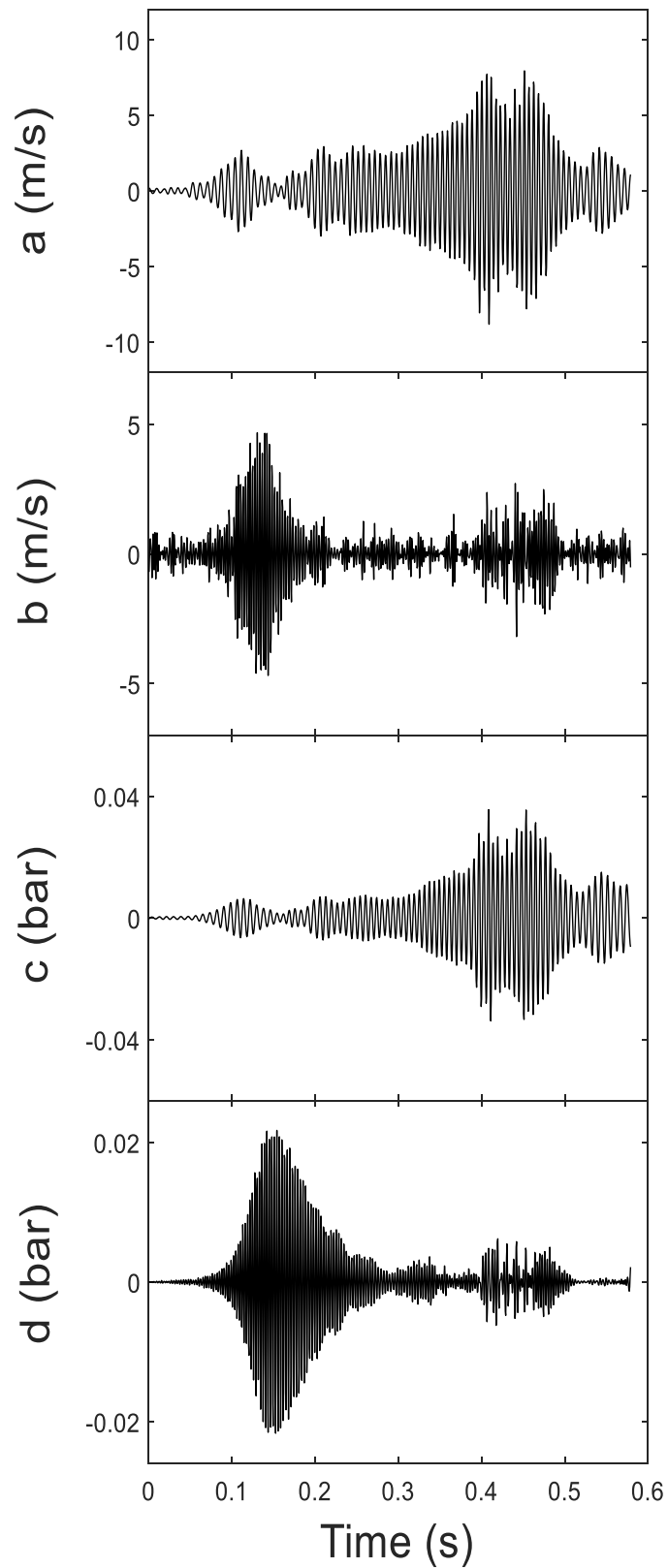
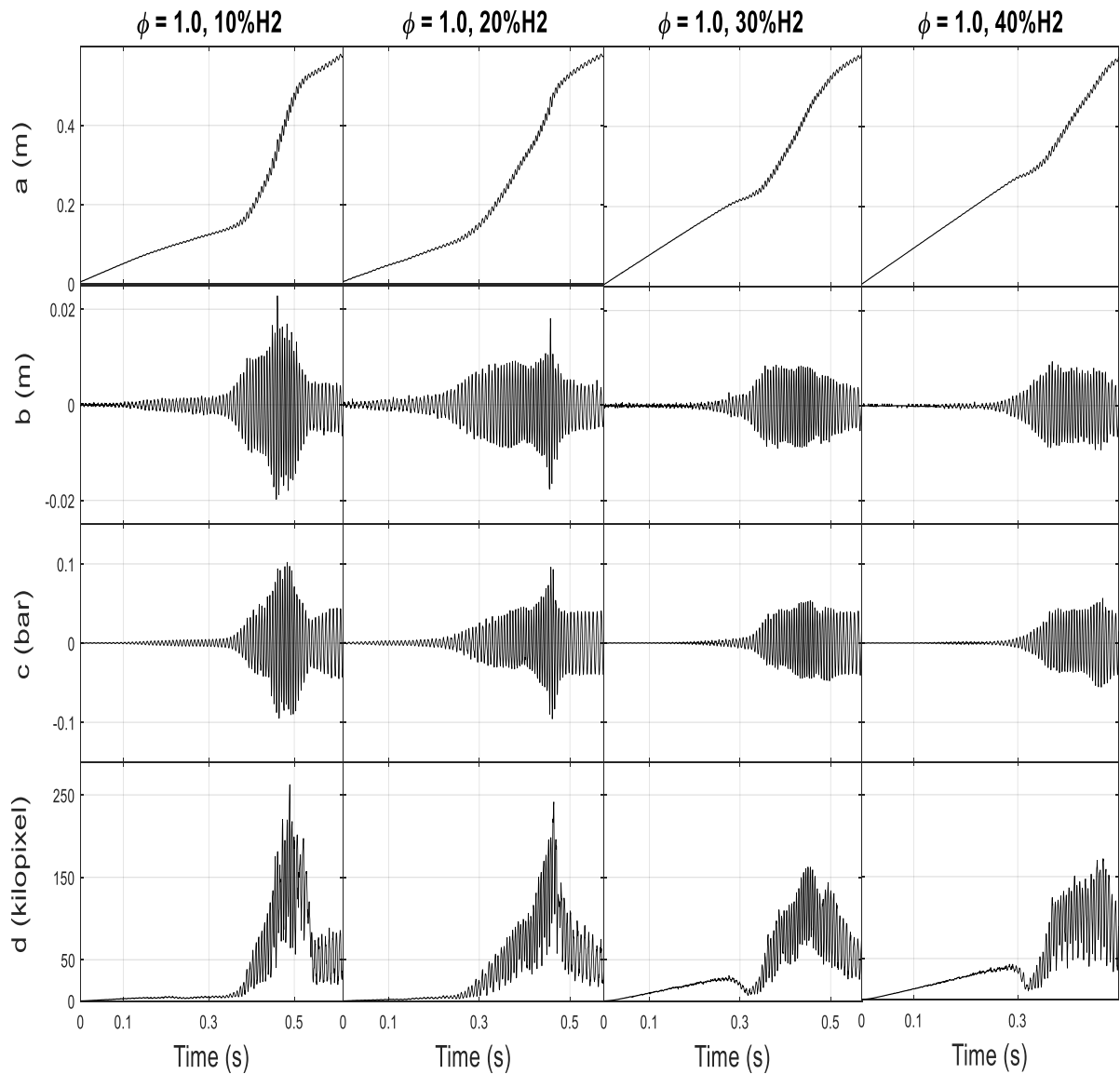


Figure 5.53: Effect of equivalence ratio on methane on  $\phi = 0.8$ ,  $R_H = 0.4$  flames, on a)  $\sim 200$  Hz speed component, b)  $\sim 400$  Hz speed component, c)  $\sim 200$  Hz pressure component and d)  $\sim 400$  Hz pressure component

## 5.2 Volumetric method

### 5.2.1 The effect of hydrogen addition

This section examines how hydrogen addition affects flame propagation, maintaining  $\phi = 1.0$  while changing the hydrogen from 10% $H_2$  to 40% $H_2$ . Figure 5.54(a), which plots the flame front position versus time, demonstrates that all flames oscillated and that the flame oscillations began to decline with the increased addition of hydrogen. Based on Figure 5.54(b), the methane flame with 10% $H_2$  oscillated the most, achieving a  $\sim\pm 0.02$  m flame front amplitude. The addition of hydrogen led to decreased oscillations, reaching  $\sim\pm 0.018$  m,  $\sim\pm 0.008$  m, and  $\sim\pm 0.008$  m for 20% $H_2$ , 30% $H_2$ , and 40% $H_2$ , respectively. This reduction in oscillations with hydrogen addition beyond 10% $H_2$  is remarkable as it was previously thought that the increased laminar burning velocity would instigate a monotonic increase in the flame front amplitude. With increasing hydrogen, the propagation time declined, resulting in few oscillation cycles impacting the flame, as observed for the 30% $H_2$  and 40% $H_2$  flames. The tube end pressures of the 10% $H_2$  and 20% $H_2$  flames, which are plotted in Figure 5.54(c), appear to have a similar magnitude, while those of the 30% $H_2$  and 40% $H_2$  flames had a lower magnitude. Figure 5.54(d) reveals a steady flame area increase for the 30% $H_2$  and 40% $H_2$  flames. During their oscillation, the area of the flames first decreased and then increased. The 10% $H_2$  and 20% $H_2$  flames increased substantially to  $\sim 250$  kilopixels, while the 30% $H_2$  and 40% $H_2$  flames increased more moderately, reaching just  $\sim 150$  kilopixels. This was similarly observed for their raw speed, where the 10% $H_2$  and 20% $H_2$  flames accelerated significantly while the other two flame types did not.



**Figure 5.54: Effect of hydrogen addition on methane on  $\phi = 1.0$ , 10% $H_2$  - 40% $H_2$  flames, on a) flame front position, b) flame front position amplitude, c) tube end pressure, and d) flame area**

The raw flame speed was plotted against time in Figure 5.55(a), whereby the fluctuations are asymmetrical in relation to the x-axis and do not fall below -16 m/s. On the positive side of the raw speed plots, the 10% $H_2$  flame attained the highest peak speed of ~43 m/s, while the 20% $H_2$  flame followed with ~31 m/s. Increasing hydrogen beyond 20% $H_2$  resulted in a decrease in the maximum raw speed, clearly indicating that the increased laminar burning velocity influenced the raw flame speed, causing it to scarcely reach a negative value compared to the flames with lower hydrogen addition. In plotting the underlying flame speed against time, it emerged that, in general, there was a steady increase in the initial underlying speed, as expected, due to the increased hydrogen content. Furthermore, all flames accelerated beyond their

initial speed. Finally, a reduction in the maximum underlying speed was found for increased hydrogen content in that all flames exhibited a slight deceleration during their propagation through the tube, as evidenced by the dips in their underlying speeds. This observed deceleration of all flames is likely to have been due to the ~200 Hz speed component oscillation revealed here. Specifically, the ~200 Hz speed component was found to be responsible for the fluctuations in the underlying speed. It was also noticed that greater fluctuations in the ~200 Hz speed component resulted in a higher peak in the underlying flame speed. Meanwhile, the ~400 Hz speed component, presented in Figure 5.55(d), only increased when the ~200 Hz speed component was seen to increase. Towards the tube's end, this ~400 Hz speed component increase coincided with the ~200 Hz speed component's peak magnitude, indicating that the latter's increase was due to the increase in the former.

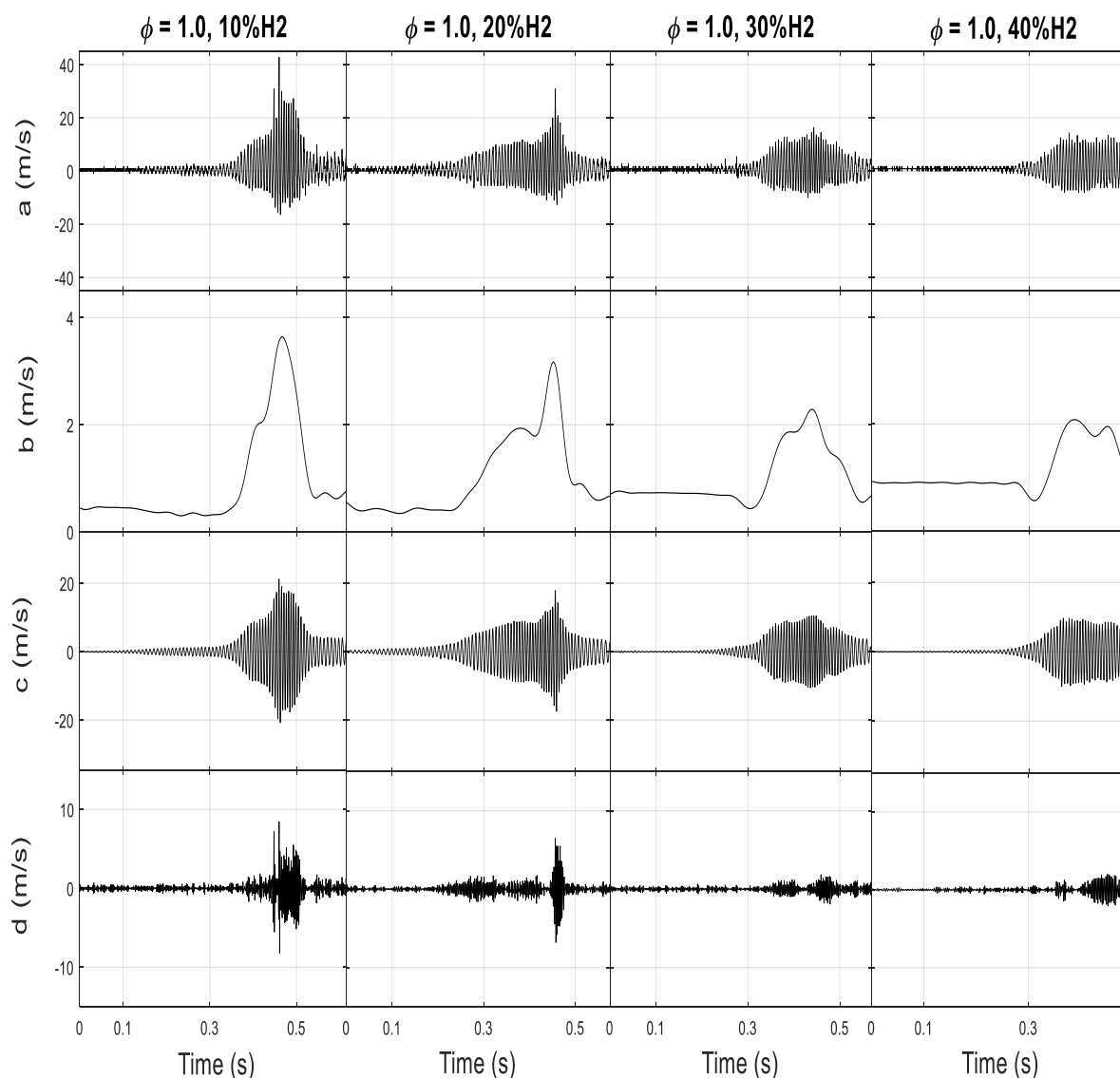


**Figure 5.55: Effect of hydrogen addition on methane on  $\phi = 1.0$ , 10% $H_2$  - 40% $H_2$  flames, on a) raw flame speed, broken down into b) underlying flame speed, c) 200 Hz speed component, and d) 400 Hz speed component**

The tube end pressure signals were dismantled into their  $\sim 200$  Hz and  $\sim 400$  Hz components and are plotted in Figure 5.56(a) and Figure 5.56(d), respectively. For the 10% $H_2$  and 20% $H_2$  flames, the oscillatory  $\sim 200$  Hz components of the tube end pressure signals had a similar magnitude, while those of the 30% $H_2$  and 40% $H_2$  flames were smaller. The higher fluctuation magnitude seen in the 10% $H_2$  and 20% $H_2$  flames'  $\sim 200$  Hz components induced a higher  $\sim 400$  Hz pressure fluctuation. For the flames with a low hydrogen content, the  $\sim 400$  Hz pressure component only increased with a corresponding increase in the  $\sim 200$  Hz pressure component. The 30% $H_2$  and 40% $H_2$  flames presented a different behaviour, showing a slight increase in the  $\sim 400$  Hz component prior to a significant increase in the  $\sim 200$  Hz component.

Figure 5.56(a) and Figure 5.56(b), respectively, plot the  $\sim 200$  Hz component of the tube end pressure and flame area against time, while Figure 5.56(c) plots the phase difference between the  $\sim 200$  Hz components against time. In general, there was a period of phase matching for all flames, which subsequently caused a build-up in the pressure and flame area oscillations; this was followed by an increased phase difference once the flame area had reduced abruptly for the 10% $H_2$  and 20% $H_2$  flames.

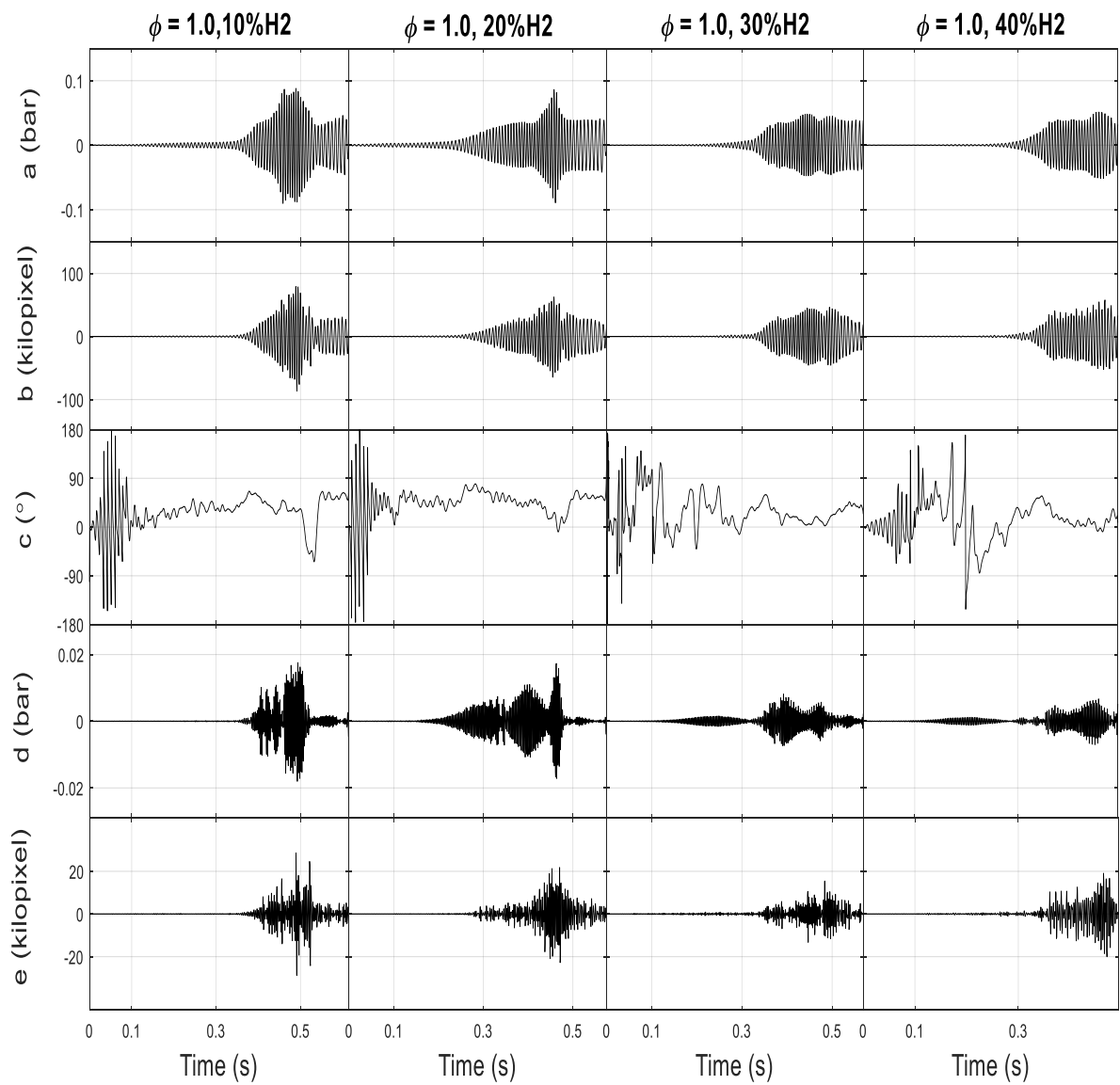


**Figure 5.56: Effect of hydrogen addition on methane on  $\phi = 1.0$ , 10% $H_2$  - 40% $H_2$  flames, on a) -200 Hz pressure component, b) -200 Hz area component, c) phase difference between a) and b), d) -400 Hz pressure component, e) -400 Hz flame area component**

## 6 DISCUSSION

### 6.1. Overall flame behaviour

The study investigated the propagation of premixed methane and propane flames in a vertical tube under the increasing addition of hydrogen ( $R_H = 0 - 0.4$ ) at a constant equivalence ratio ( $\phi = 1.0$ ). Further consideration was given to the effect of increasing the equivalence ratio ( $\phi = 0.9 - 1.2$ ) under constant hydrogen addition ( $R_H = 0.1$ ).

Mandilas et al. [104] noted that laminar flame instabilities showed an earlier onset following the addition of hydrogen for  $R_H = 0 - 0.4$ . In the current study, the instabilities began before the flame propagation distance had reached 0.2 m, as shown in the comparison presented in Figure 5.1(a) and Figure 5.1(b). A significantly more substantial flame oscillatory behaviour due to increased laminar burning velocity was predicted, as revealed by Searby [11]. Furthermore, primary instability has been seen in moderately strong mixtures, while it precedes secondary instability in mixtures that are stronger, with the strength being calculated according to the laminar burning velocity of the mixture [3], [85], [177]. However, while the slower flames' oscillatory behaviour was unexpected as their lower laminar burning velocity was very low, it was found that they achieved maximum pressure and high underlying flame speeds compared to faster flames. Markstein and Somers [60] made similar observations and suggested that slower burning flames could produce greater oscillations as they spend more time in areas that are susceptible to vibration.

Dubey et al. [82], who experimentally examined downward flame propagation in closed-end tubes, found an increase in flame instability that was in line with the increase in burning velocity. This work's findings contradict their observations; found here is a greater instability among flames that had a slower burning velocity. Dubey et al. [82] revealed that secondary instability displays a greater sensitivity to modifications to the tube length, instigating secondary or parametric instability suppression at certain burning velocities.

The authors attributed this to the influence of acoustic velocity (i.e. the flow velocity produced from acoustic fluctuations), which is highly sensitive to changes in burning velocity. Thus, in their study, they satisfactorily proved that the dominant mechanism for acoustic instability in downward propagating flames is velocity coupling, which correlates with flame area changes that modulate the heat release, impacting thermoacoustic stability.

These results are in line with those of the current work. Nonetheless, when there are no changes in the flame area during flame propagation, pressure coupling may be similarly crucial [83]. Dubey et al. [3], found that higher acoustic modes showed parametric instability, and flames stemming from various acoustic modes were observed with increasing laminar burning velocity. In the current study, an increase in laminar burning velocity led to the emergence of instabilities associated with the first harmonic.

## **6.2. Comparison between methane and propane flames using $R_H$ method**

Figure 6.1 presents a scatter plot showing peak tube end pressure (the average of 10 maximum pressure values) versus laminar burning velocity for methane flames. For the propane flames, the complexity in the calculation of the laminar burning velocity meant that the reference velocity was the minimum underlying speed rather than the laminar burning velocity. Hence, Figure 6.2 portrays the scatter plot of the peak tube end pressure versus the minimum underlying speed for propane flames. The procedure to select the minimum underlying speed as a reference velocity is found in Appendix F.

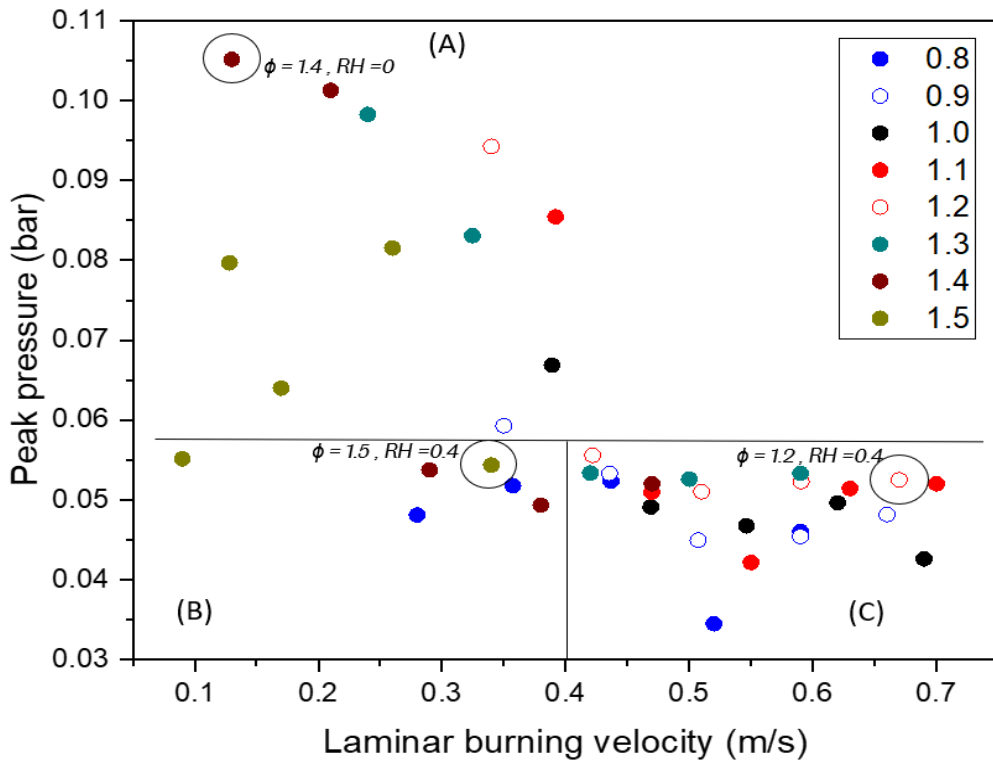


Figure 6.1: Peak pressure against laminar burning velocity scatter plot for methane flames at  $\phi = 0.8-1.5$  and  $R_H = 0-0.4$

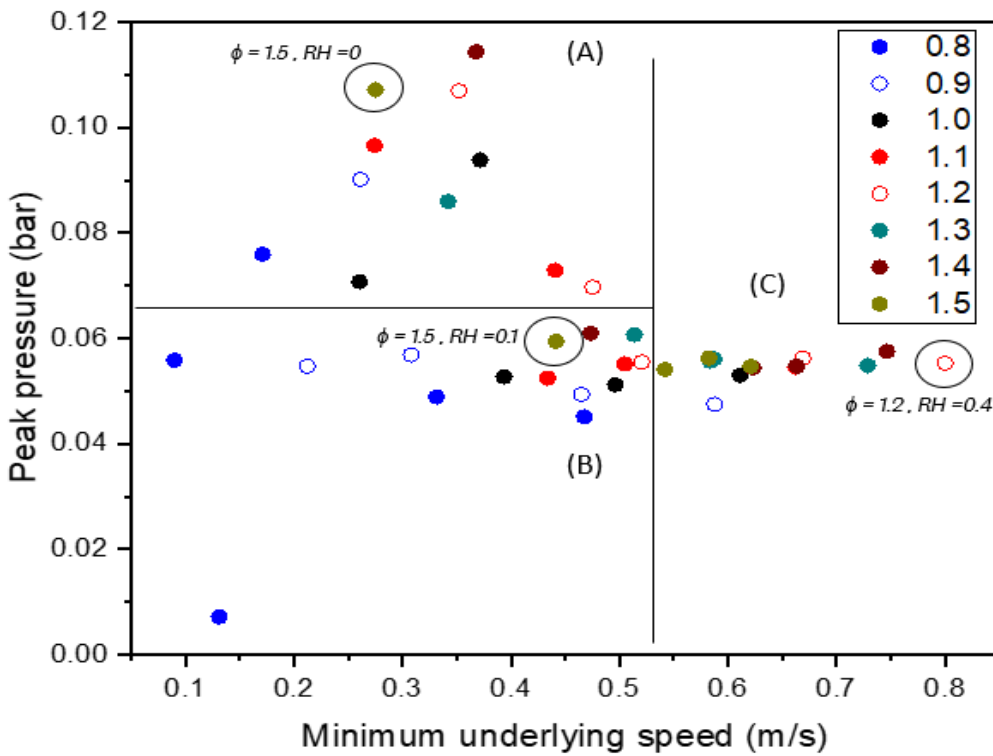


Figure 6.2: Peak pressure against minimum underlying speed scatter plot for propane flames at  $\phi = 0.8-1.5$  and  $R_H = 0-0.4$

The scatter plots contain three regions, namely (A), (B), and (C), according to the magnitude of their peak pressure. All high peak pressure methane flames were within a laminar burning velocity range of 0.13 to 0.39 m/s, while the propane flames were within the minimum underlying speed range of 0.1-0.52 m/s. Region (A) in Figure 6.1 and Figure 6.2 show that the methane and propane flames, respectively, had the highest peak pressures (above the 0.06 bar threshold, reaching at least 0.11 bar). Despite their low burning velocities, the flames in region (B) demonstrated no high pressure. The methane flames in region (C) achieved only a peak pressure of ~0.055 bar at a laminar burning velocity range of 0.42-0.70 m/s, while the propane flames achieved ~0.057 bar within a minimum underlying speed range of 0.52-0.80 m/s. While there was an increase in the laminar burning velocity, reaching almost double the magnitude, the peak pressures remained constant. In addition, there was no high pressure amplitude in region (C) even though it had a higher laminar burning velocity than region (A).

As expected, the methane flames in Figure 6.3 displayed a behaviour that is similar to that in Figure 6.1, implying a more substantial increase in the peak underlying speed of ~3 to 4.5 m/s in region (A) for rich mixtures. Even though regions (A) and (B) had similar laminar burning velocity ranges, only eight of the 17 experimental runs conducted in both regions had a peak underlying speed magnitude above ~3 m/s. Meanwhile, in region (C), there was only a peak underlying speed magnitude of ~2.7 m/s, suggesting that, unlike in region (A), increasing the laminar burning velocity beyond ~0.4 m/s does not produce a high peak underlying speed.

The behaviour of the propane flames in Figure 6.4 was, as expected, similar to that in Figure 6.2. Generally, all flames that had a high peak underlying speed were in the minimum underlying speed range of 0.1-0.52 m/s. Irrespective of the similar minimum underlying speed ranges of region (A) and region (B), out of the 26 experiments performed in both regions, only 13 presented a peak underlying speed magnitude above ~2.8 m/s. As per region (C), the peak underlying speed magnitude was only ~2.7 m/s. This indicates that if the minimum underlying speed is increased beyond ~0.54 m/s, this does not lead to high peak underlying speed, in contrast to region (A).

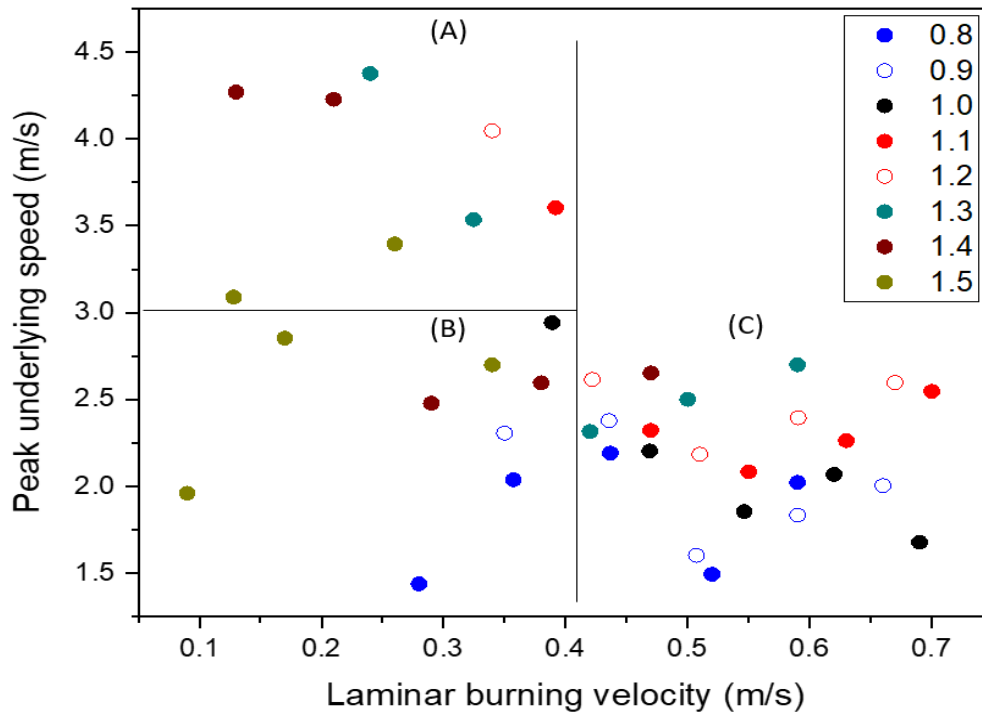


Figure 6.3: Peak underlying flame speed against laminar burning velocity scatter plot for methane flames at  $\phi = 0.8-1.5$  and  $R_H = 0-0.4$

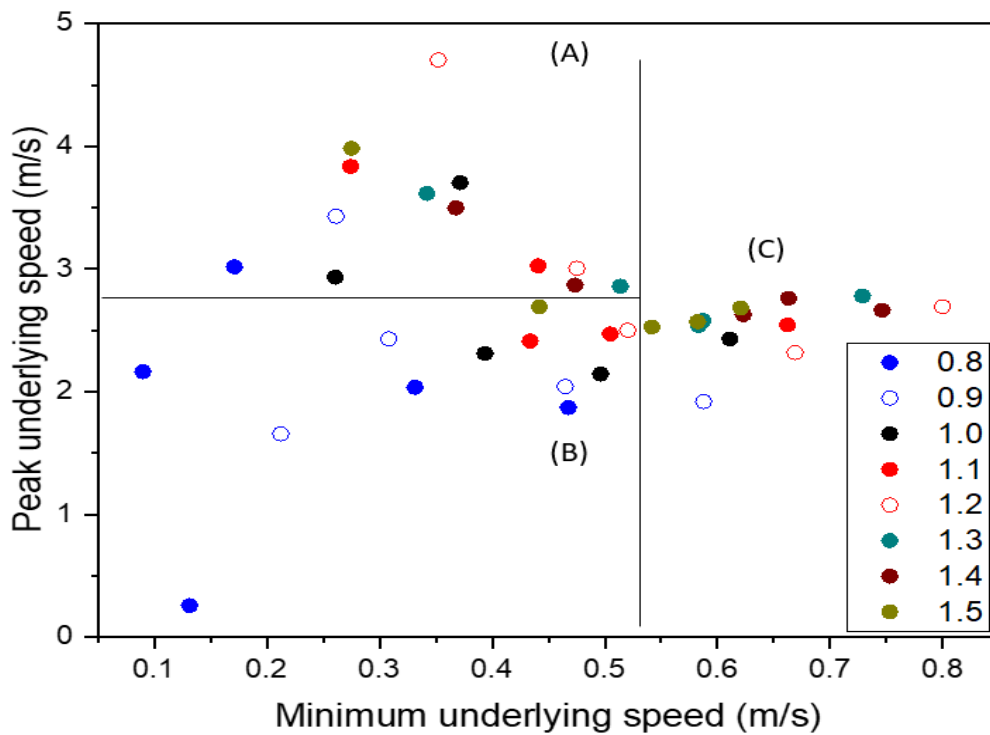


Figure 6.4: Peak underlying flame speed against minimum underlying speed scatter plot for propane flames at  $\phi = 0.8-1.5$  and  $R_H = 0-0.4$

With the methane flames, as presented in Figure 6.5, the peak underlying speed tended to show an increase that correlated with increasing peak pressure. Forty experiments were performed, of which only 10 displayed peak underlying speed magnitudes above  $\sim 2.7$  m/s; these are depicted in region (a) in Figure 6.5. There was no evidence of lean mixtures in this region. The flames in region (B) achieved a maximum peak pressure of  $\sim 0.06$  bar, which is almost half that in region (A), namely  $\sim 0.1$  bar. Finally, in region (B) the flames achieved a  $\sim 2.7$  m/s highest peak underlying speed, while those in region (A) reached  $\sim 4.4$  m/s.

As shown in Figure 6.6, the peak underlying speed of the propane flames generally rose with increasing peak pressure. Only seven of the 40 experimental runs, as plotted in Figure 6.6, region (a), presented a peak underlying speed magnitude that went above  $\sim 3$  m/s. This region further indicated the presence of lean, stoichiometric, and rich mixtures. While a maximum peak pressure of  $\sim 0.11$  bar was achieved in region (A), the flames in region (B) reached  $\sim 0.08$  bar. Meanwhile, the flames in region (B) reached a highest peak underlying speed of  $\sim 3$  m/s, while in region (A) they achieved  $\sim 4.7$  m/s.

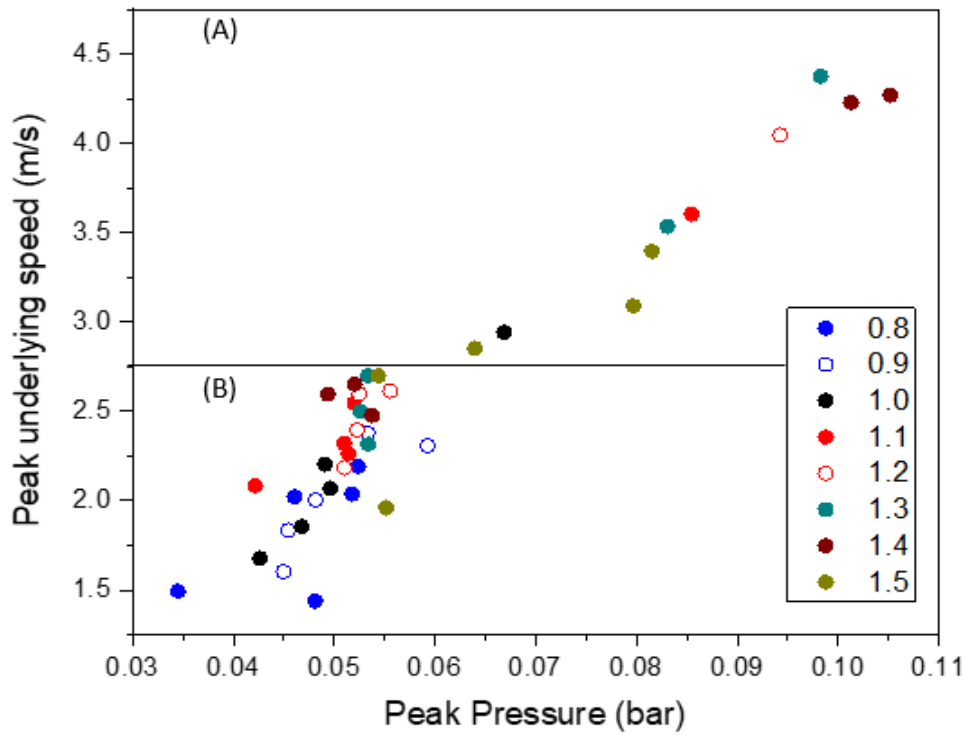


Figure 6.5: Peak underlying flame speed against peak pressure scatter plot for methane flames at  $\phi = 0.8-1.5$  and  $R_H = 0-0.4$

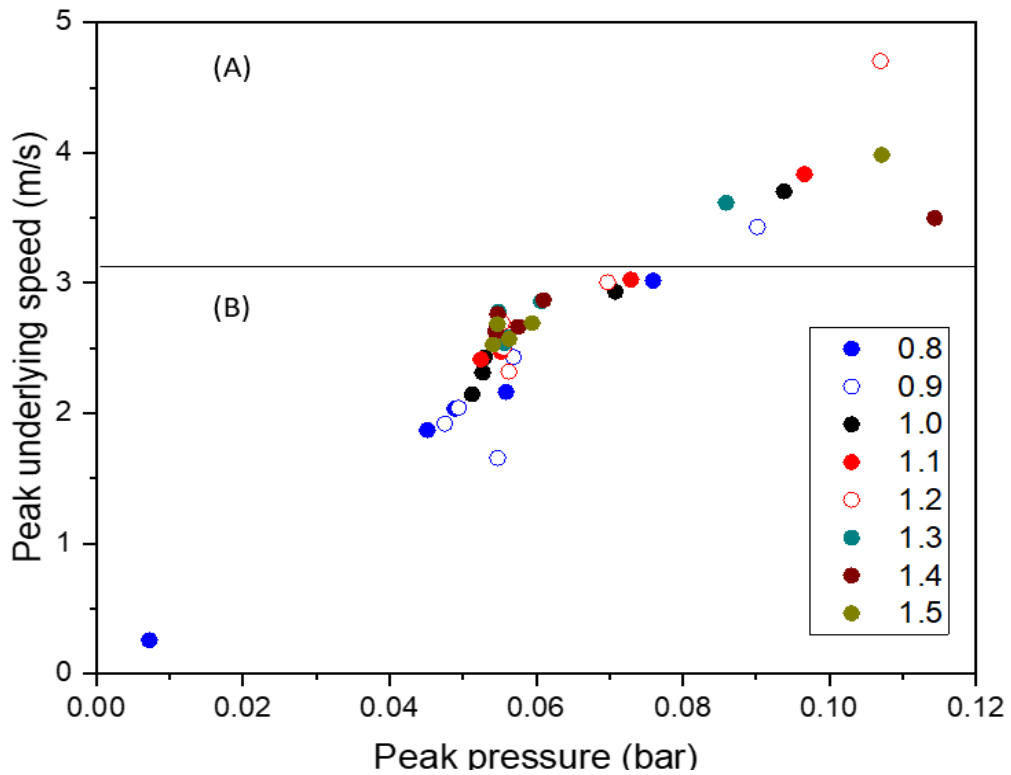


Figure 6.6: Peak underlying flame speed against peak pressure scatter plot for propane flames at  $\phi = 0.8-1.5$  and  $R_H = 0-0.4$

To perform a comparison, a flame was selected from each region. The first methane flame was  $\phi = 1.4$ ,  $R_H = 0$ , the second was  $\phi = 1.5$ ,  $R_H = 0.4$ , and the third was  $\phi = 1.2$ ,  $R_H = 0.4$ , as shown in Figure 6.1. Figure 6.7, 6.8, and 6.9, respectively, plot the tube end pressure signal and underlying flame speed against time for the  $\phi = 1.4$ ,  $R_H = 0$  flame,  $\phi = 1.5$ ,  $R_H = 0.4$  flame, and  $\phi = 1.2$ ,  $R_H = 0.4$  flame. Meanwhile, as Figure 6.7 shows, the first propane flame was  $\phi = 1.5$ ,  $R_H = 0$ , the second was  $\phi = 1.5$ ,  $R_H = 0.1$ , and the third was  $\phi = 1.2$ ,  $R_H = 0.4$ . The tube end pressure signal and underlying flame speed were plotted against time for these flames, as presented in Figure 6.10, 6.11, and 6.12, respectively. Plotting the tube end pressure signal and underlying flame speed enabled the peak pressure region (i) to be identified as the potential key parameter facilitating the comparison between flames. As the analysis and comparison of the shapes of the methane and propane flames were performed among the three mixtures to discern key differences, this section only addresses the parameter of the peak pressure region (i).

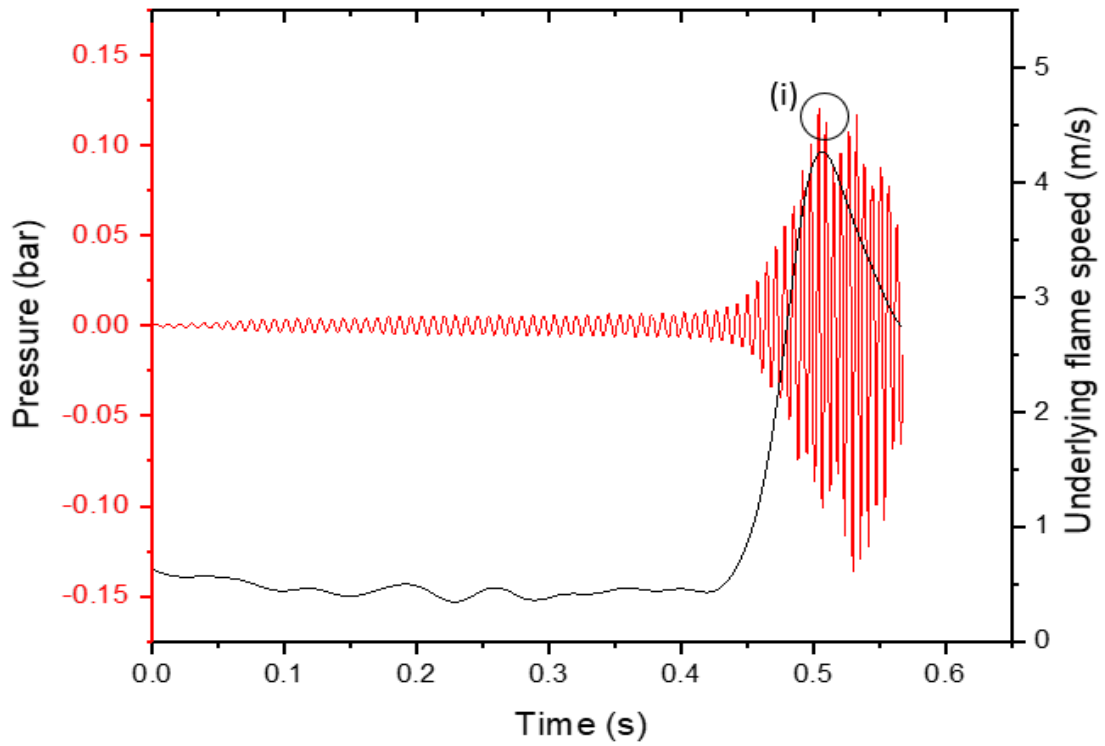


Figure 6.7: Tube end pressure and underlying flame speed against time of methane on  $\phi = 1.4$ ,  $R_H = 0$  flame

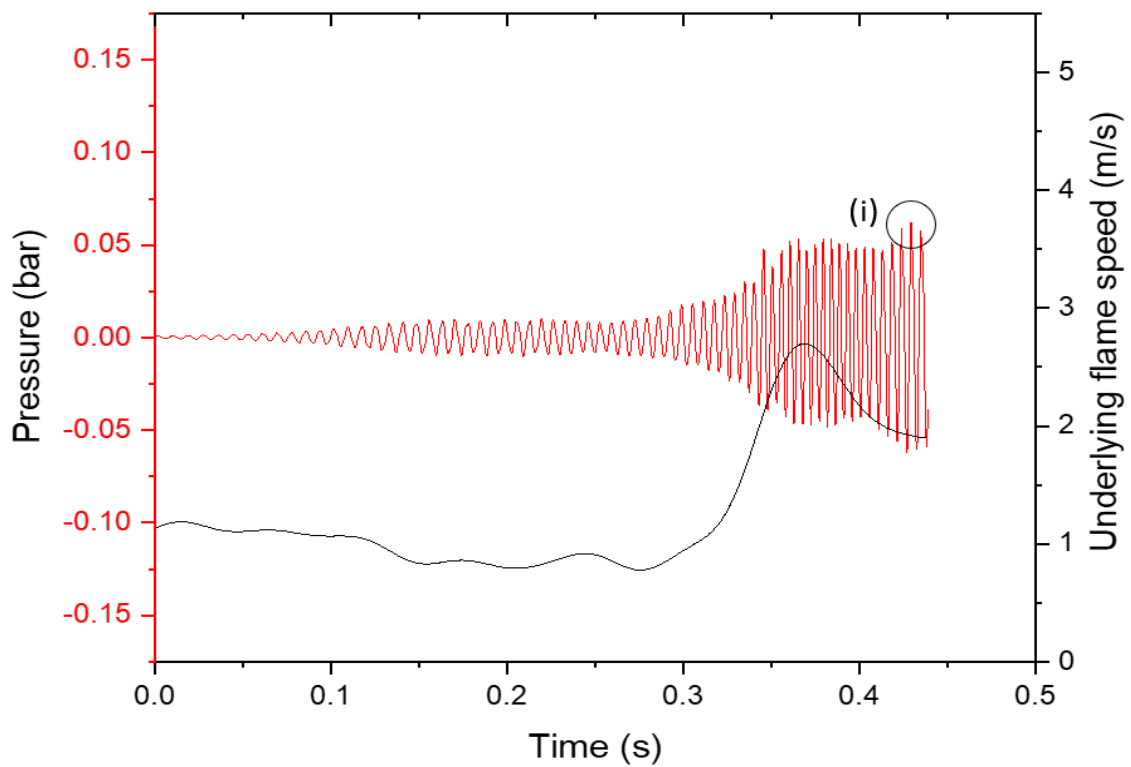


Figure 6.8: Tube end pressure and underlying flame speed against time of methane on  $\phi = 1.5$ ,  $R_H = 0.1$  flame

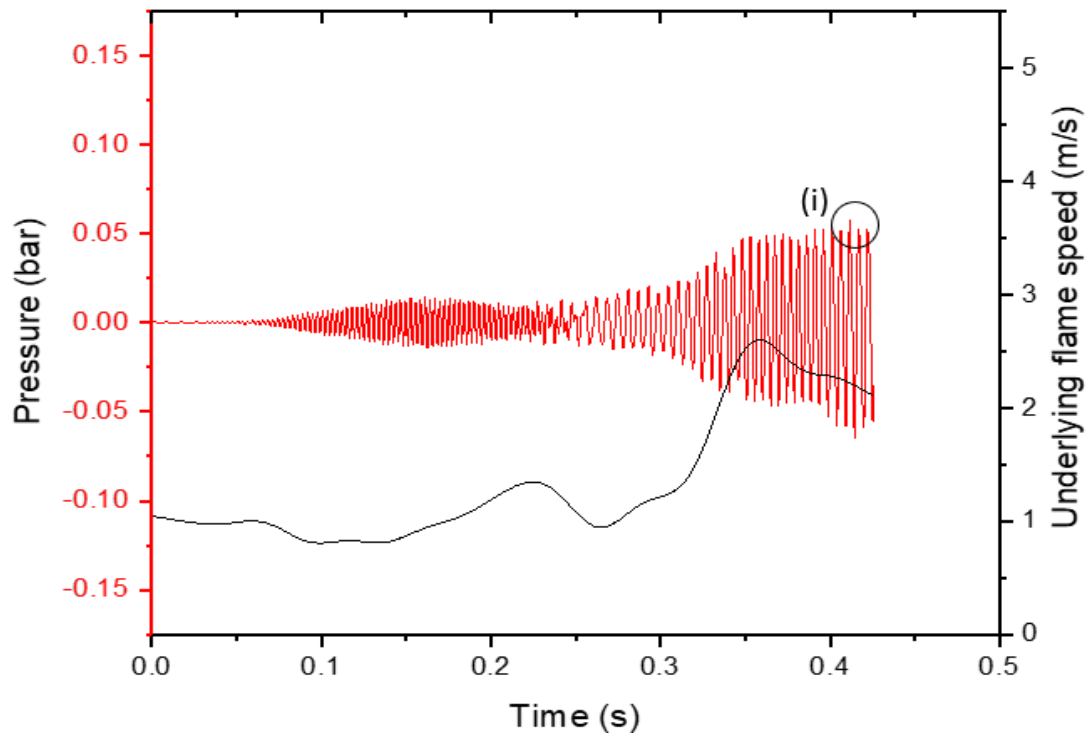


Figure 6.9: Tube end pressure and underlying flame speed against time of methane on  $\phi = 1.4$ ,  $R_H = 0$  flame

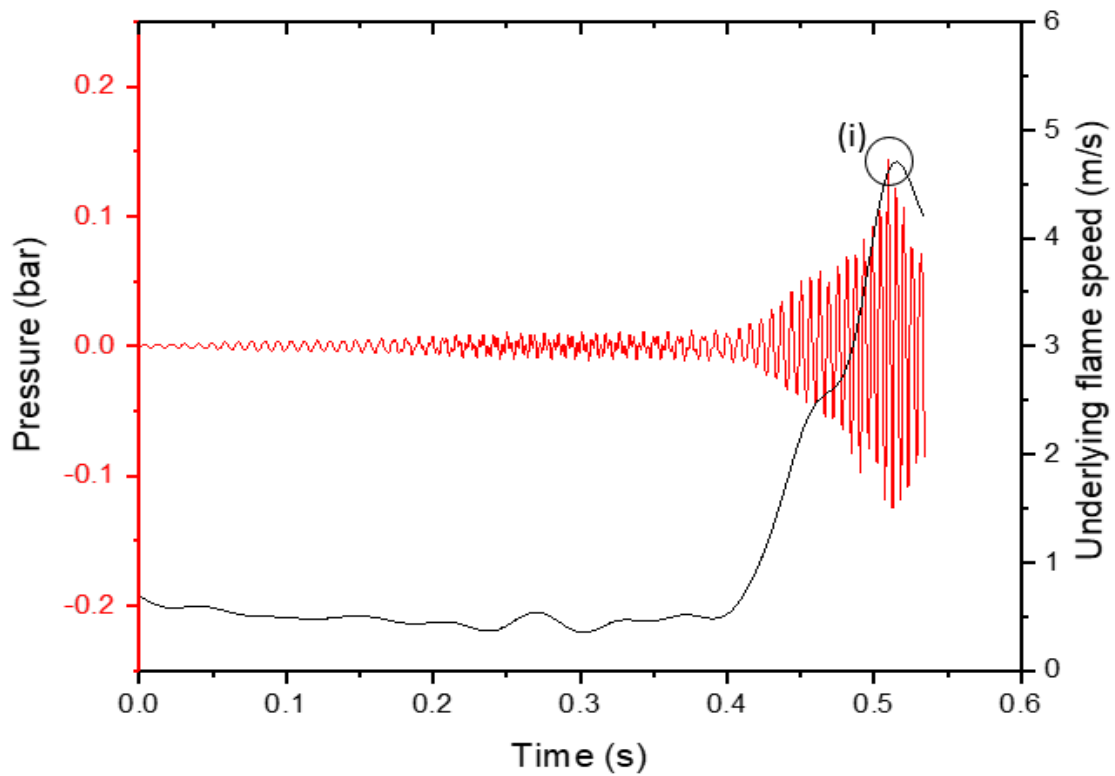


Figure 6.10: Tube end pressure and underlying flame speed against time of propane on  $\phi = 1.5$ ,  $R_H = 0$  flame

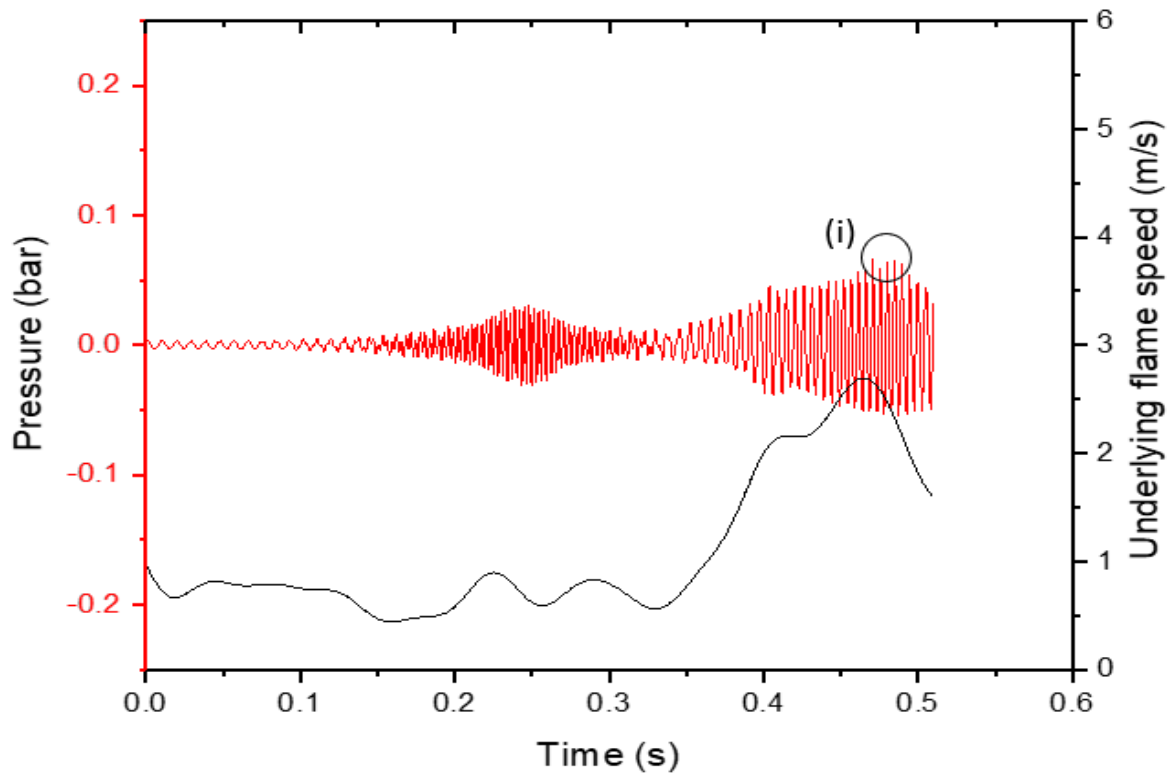


Figure 6.11: Tube end pressure and underlying flame speed against time of propane on  $\phi = 1.5$ ,  $R_H = 0.1$  flame

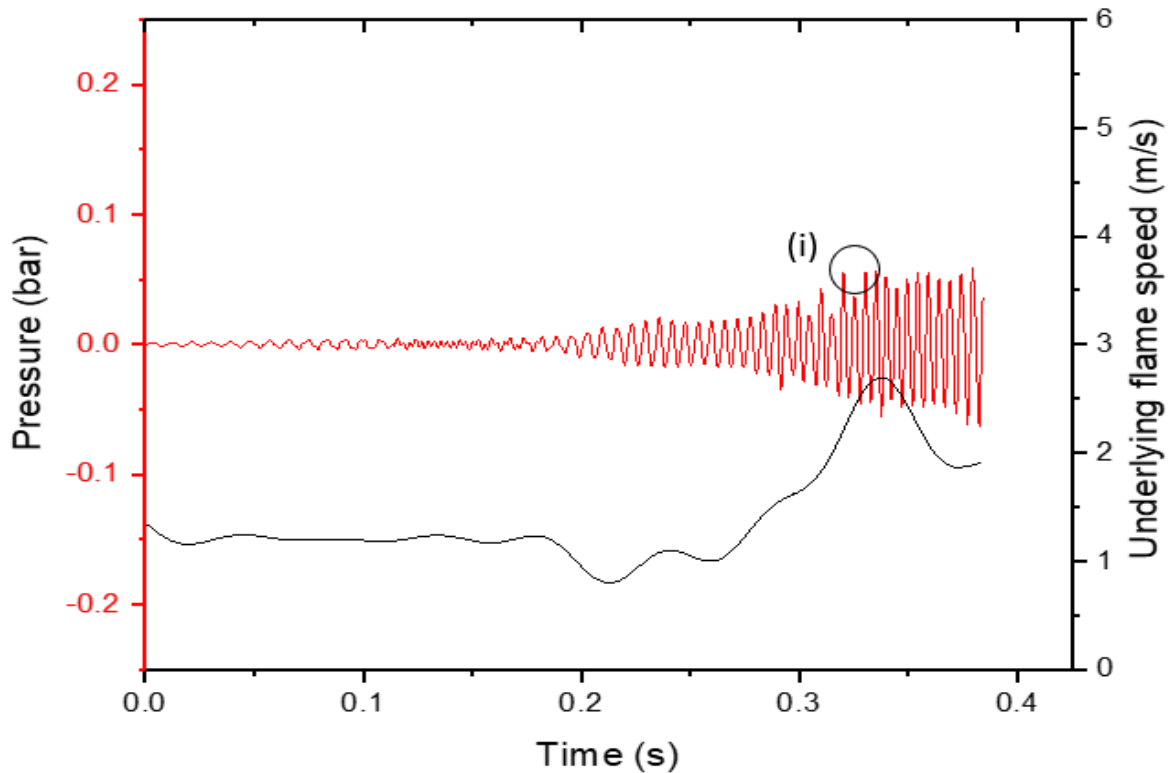
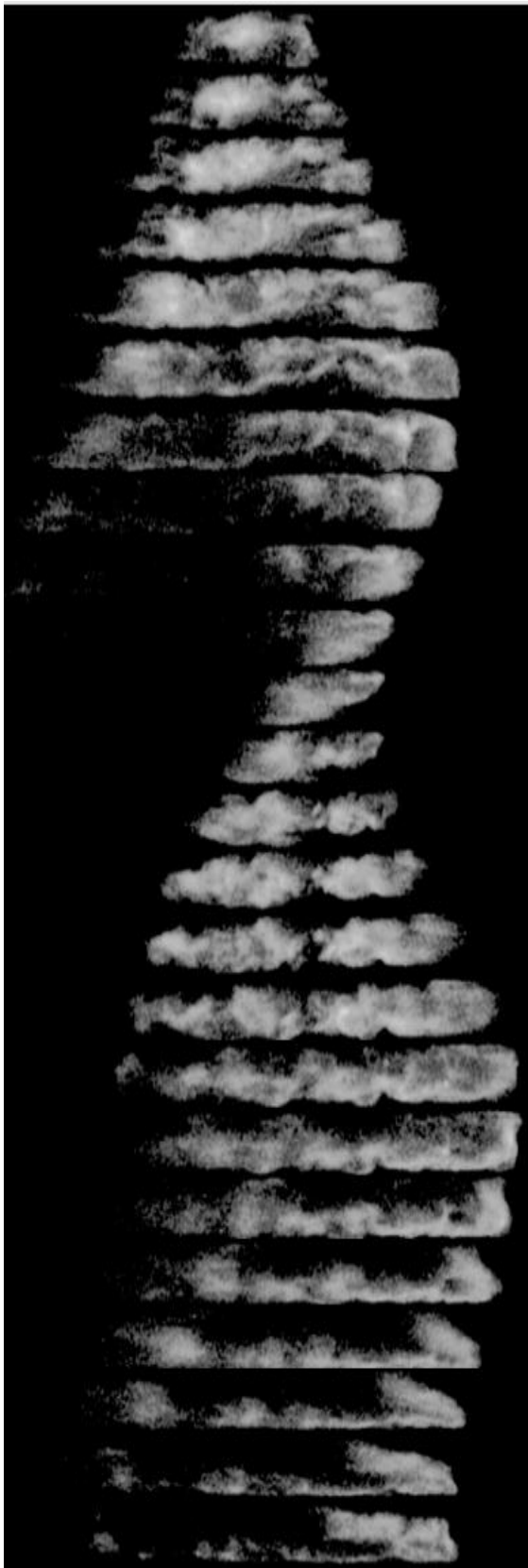


Figure 6.12: Tube end pressure and underlying flame speed against time of propane on  $\phi = 1.2$ ,  $R_H = 0.4$  flame

Figure 6.13 and Figure 6.14 present the sequences of the methane and propane flames, respectively, in region (i). Due to the similar behaviours of the methane and propane flame shapes, only methane flames were further explored here. The  $\phi = 1.4$ ,  $R_H = 0$  flame images taken in the parametric region indicated a wrinkled flame shape at peak pressure, which is believed to have increased the surface area, thereby accelerating the flame. There were no signs of a transition to parametric instability, i.e. alternating flame shapes at half the excitation frequency, as found by Markstein [7]. An interesting pattern was observed for the flame length fluctuation during propagation, which, despite the alternating flame structure, was in phase with the pressure. As depicted by the oscillating image sequence in Figure 6.13, longer flames were produced due to higher pressure.

$\phi = 1.4, R_H = 0$



$\phi = 1.5, R_H = 0.4$



$\phi = 1.2, R_H = 0.4$



Figure 6.13: Representative images for flame behaviour in different regimes of methane on  $\phi = 1.4, R_H = 0$  flame,  $\phi = 1.5, R_H = 0.4$  flame, and  $\phi = 1.2, R_H = 0.4$  flame. Interval of  $1/2000$  second increments for each frame downwards

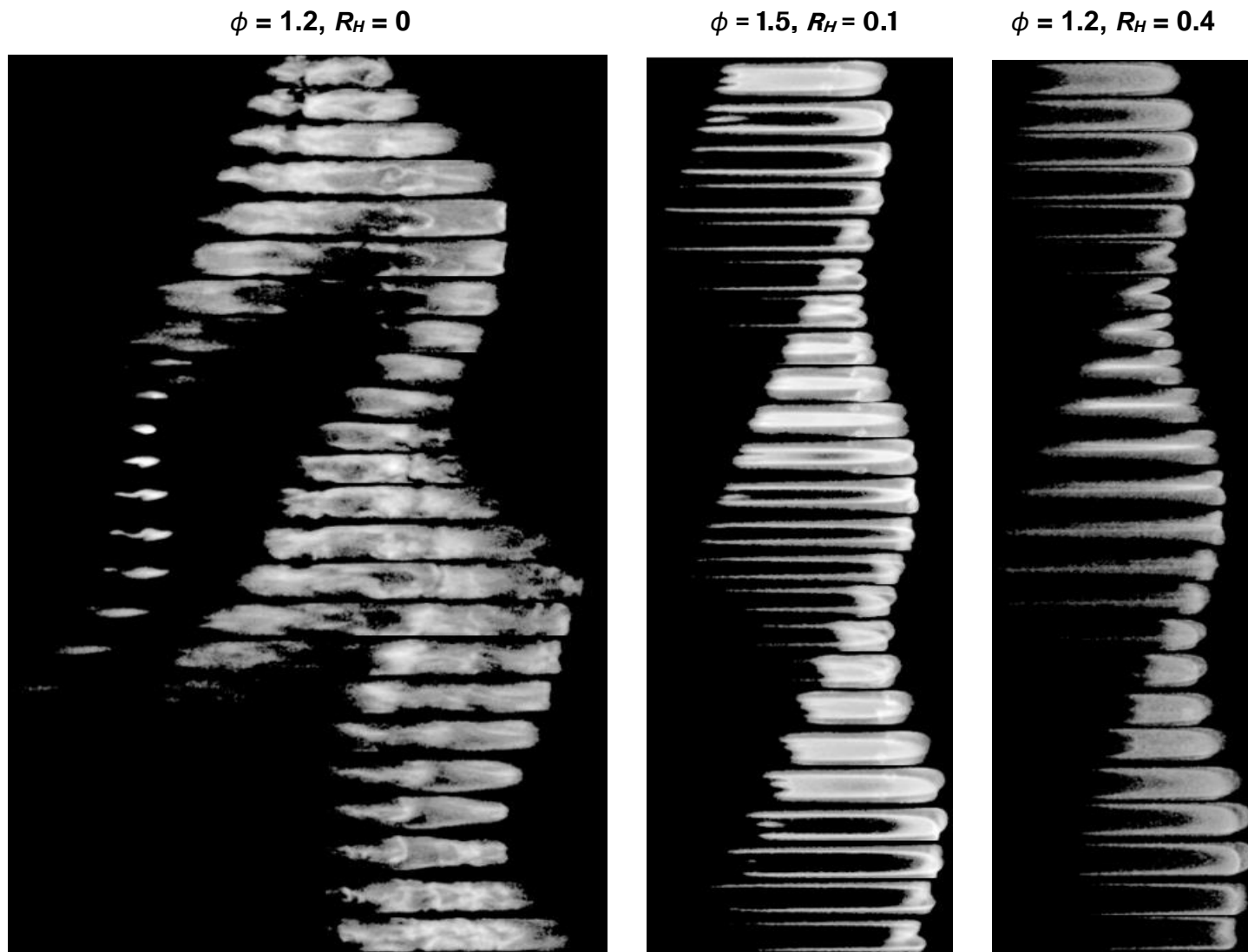


Figure 6.14: Representative images for flame behaviour in different regimes of propane on  $\phi = 1.5, R_H = 0$  flame,  $\phi = 1.5, R_H = 0.1$  flame, and  $\phi = 1.2, R_H = 0.4$  flame. Interval of 1/2000 second increments for each frame downwards

### 6.3. Overarching discussion

The following comprehensively summarises the methane and propane flame behaviours in the  $R_H$  method. Hereby, Figure 6.15-6.21 present the tube end pressure plotted against time for the methane and propane flames according to Figure 6.1 and Figure 6.2. Meanwhile, Table 6.1 and Table 6.2 summarise the behaviour of the methane and propane flames.

Region (A) revealed different tendencies for the methane and propane flames. Most of the methane flames in this were rich, while the propane flames evidenced a wider range of equivalence, tending towards lean equivalence ratios. Tentatively, this may be attributed to the effect of the Lewis number in that flames that are resistant to thermo-diffusive instability have the highest propagation pressures and rates. Only three of the 11 methane flames presented  $\sim 400$  Hz oscillation in the earlier part of the tube; for the propane flames, six out of the 11 flames showed  $\sim 400$  Hz oscillation.

In region (B), all methane flames and most of the propane flames showed no  $\sim 400$  Hz oscillation in the earlier part of the tube. Both flame types had smaller surface areas in region B than in region A.

The methane and propane flames in region (C) all had higher burning velocities, and most demonstrated a  $\sim 400$  Hz instability preceding the main parametric instability. However, the  $\sim 400$  Hz instability had a small amplitude and had little visible impact on the flame shape. Nonetheless, the emergence of the  $\sim 400$  Hz oscillation appeared to correlate with clear parametric oscillations at a later stage.

## Region - A

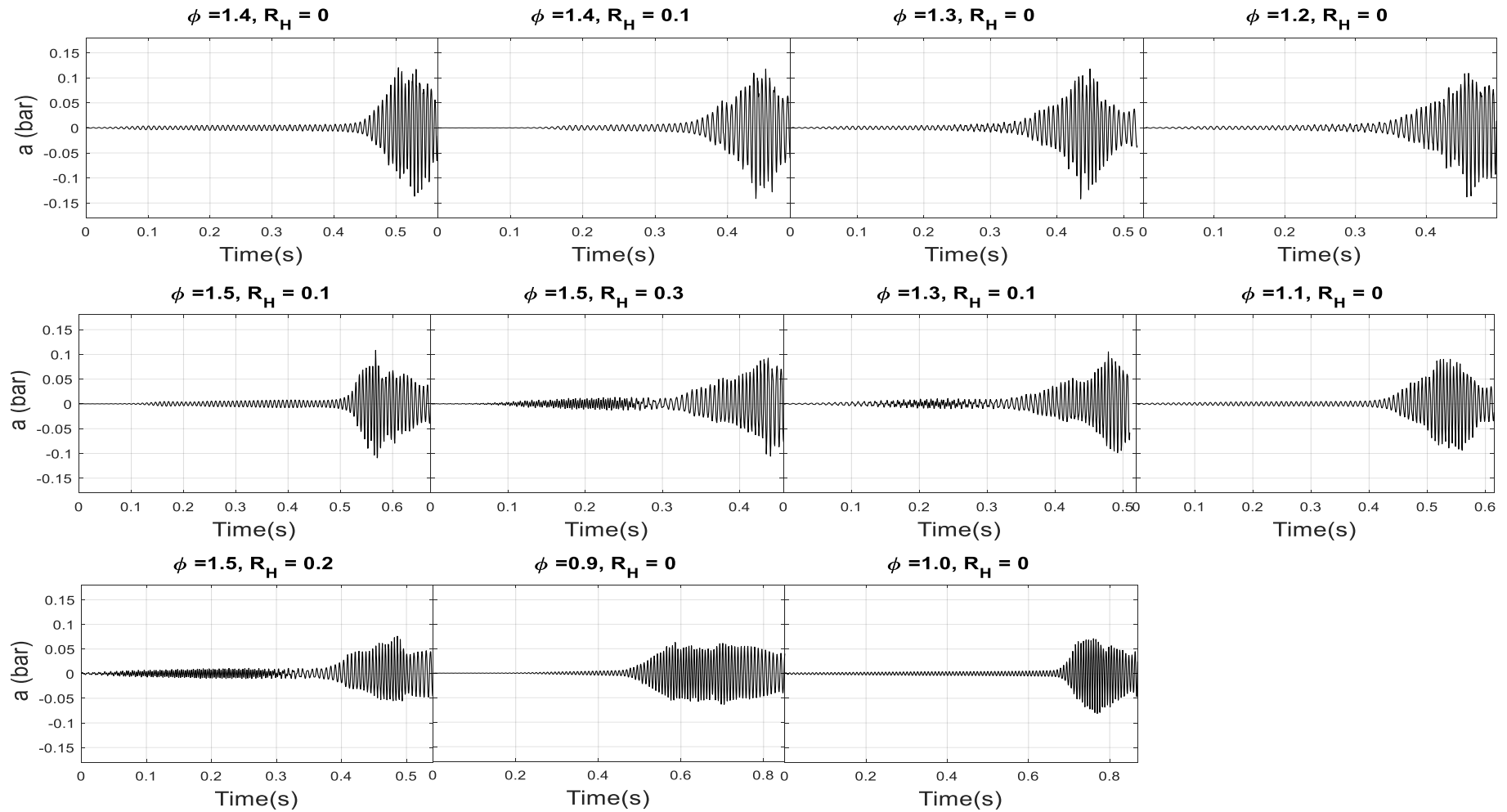
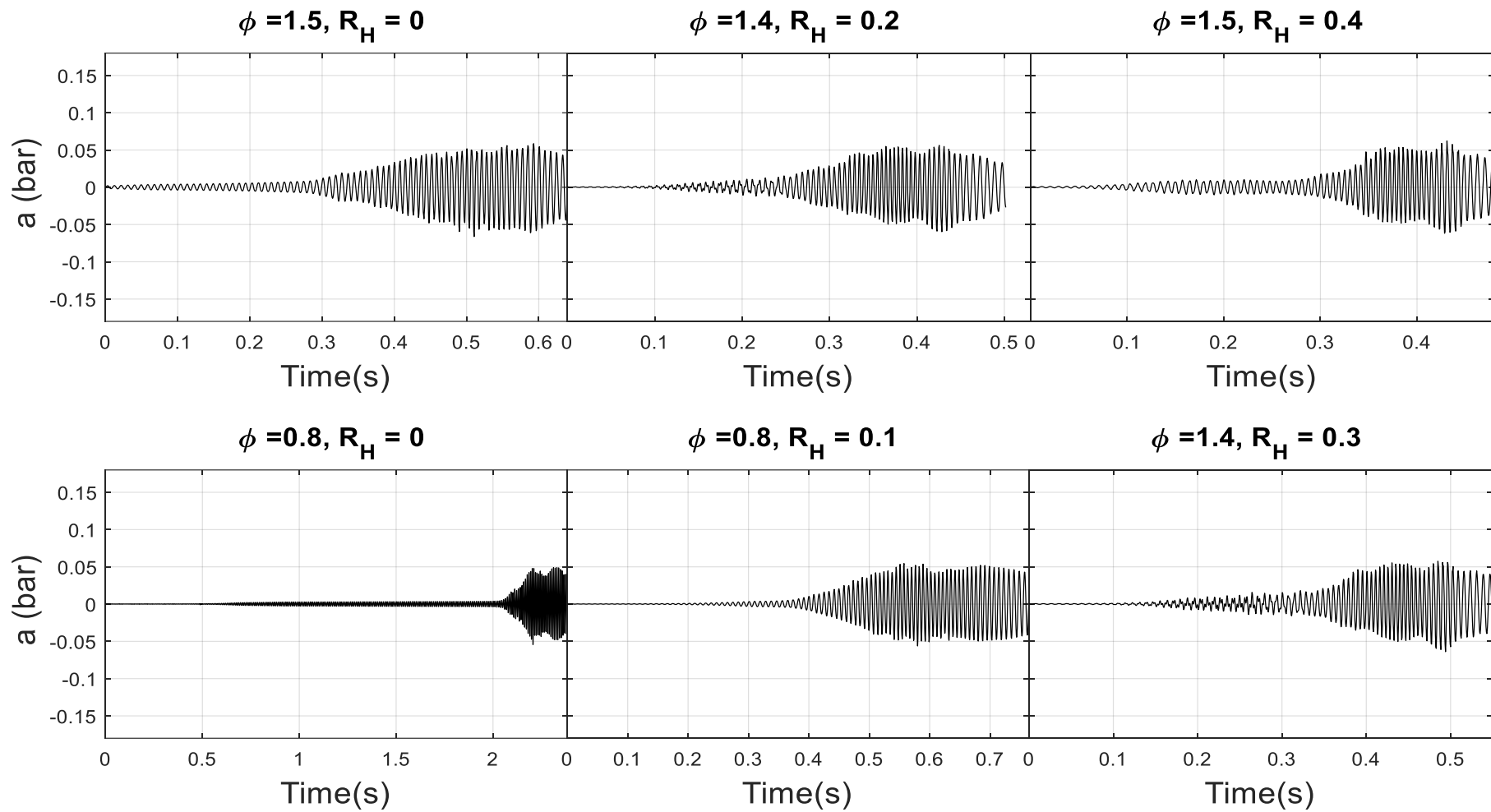


Figure 6.15: Tube end pressure against time of methane flames in region (A)

**Region – B**



**Figure 6.16: Tube end pressure against time of methane flames in region (B)**

### Region – C

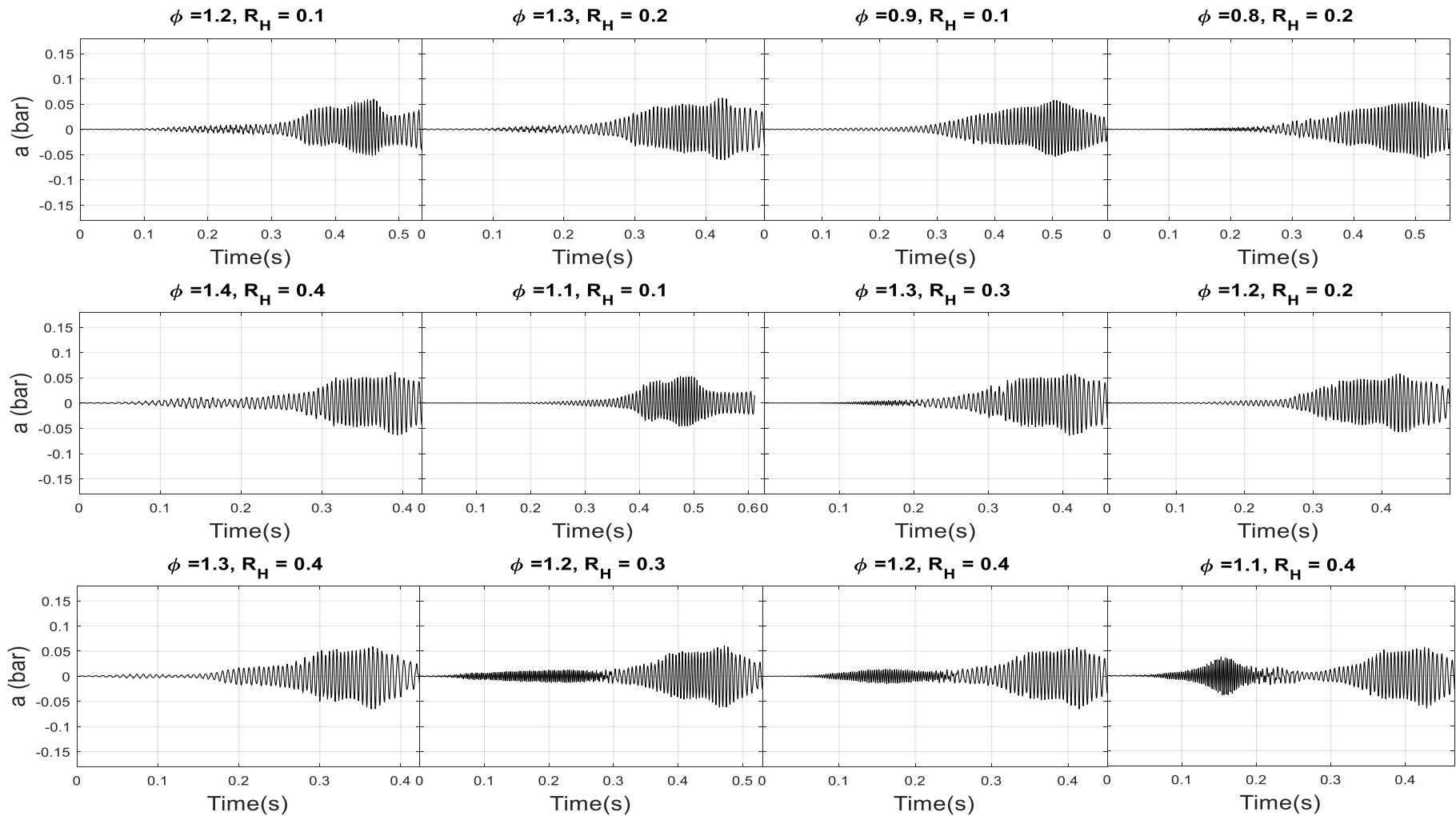


Figure 6.17: Tube end pressure against time of methane flames in region (C)

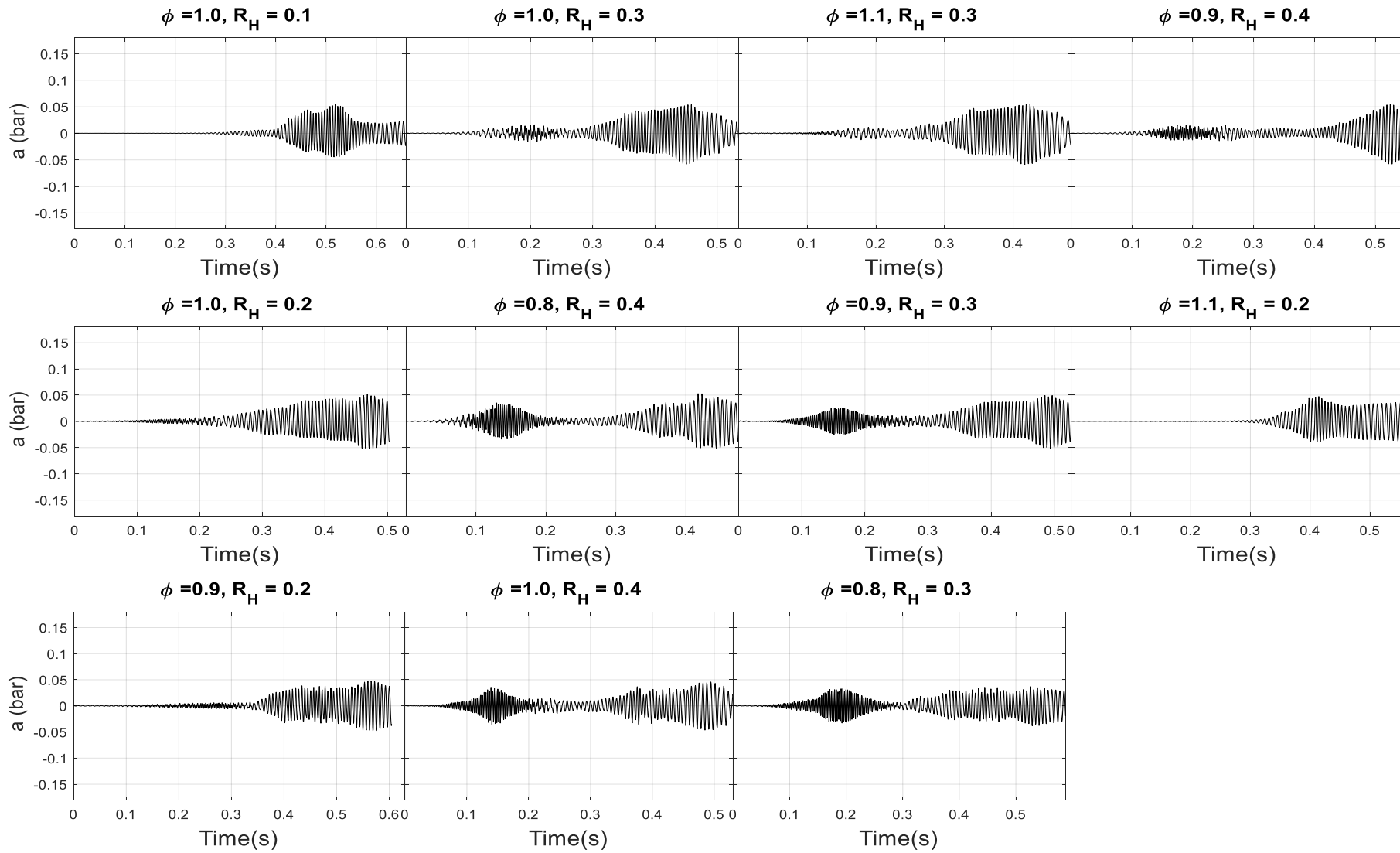


Figure 6.18: Tube end pressure against time of the rest of the methane flames in region (C)

## Region – A

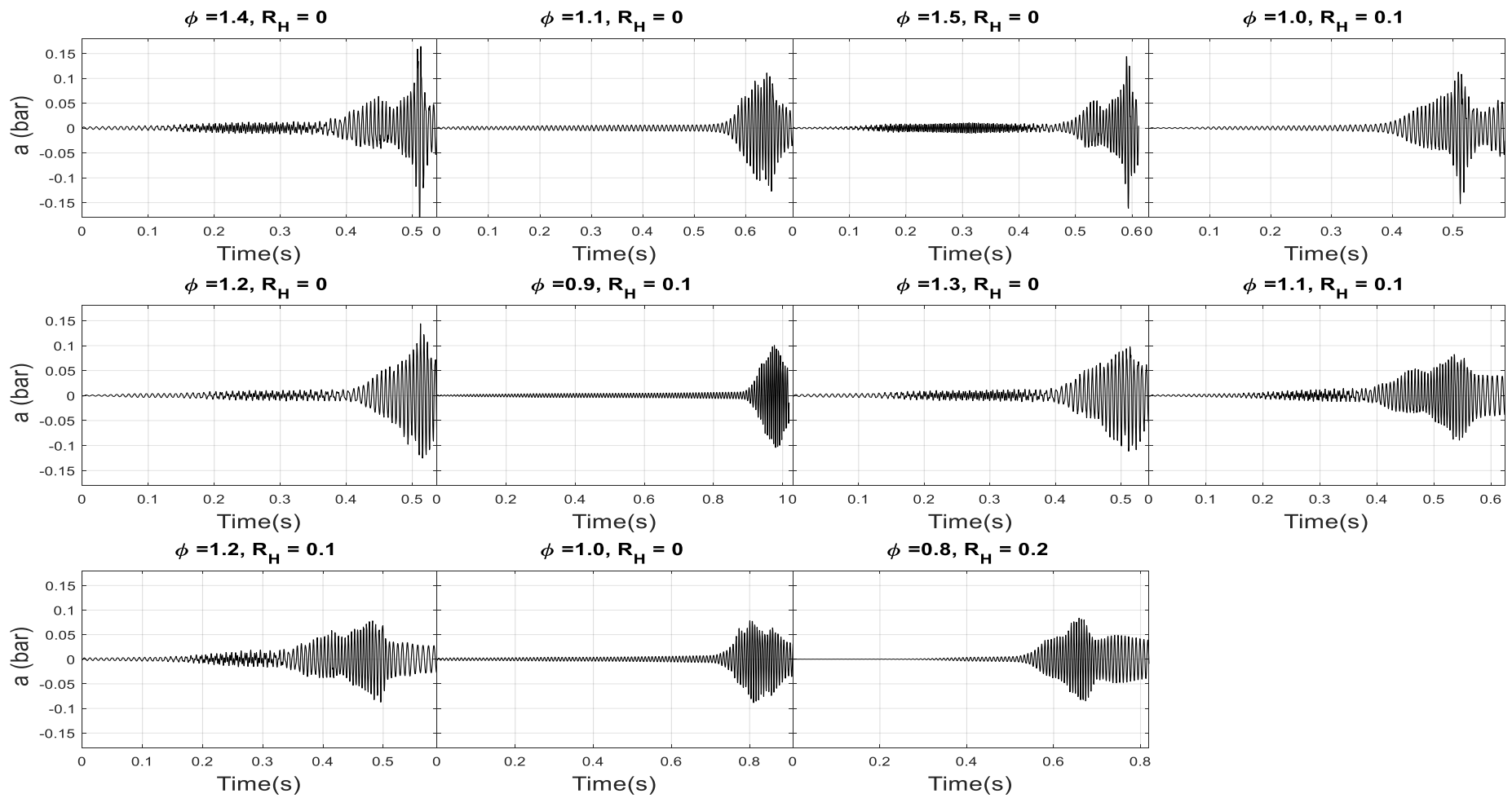


Figure 6.19: Tube end pressure against time of propane flames in region (A)

## Region – B

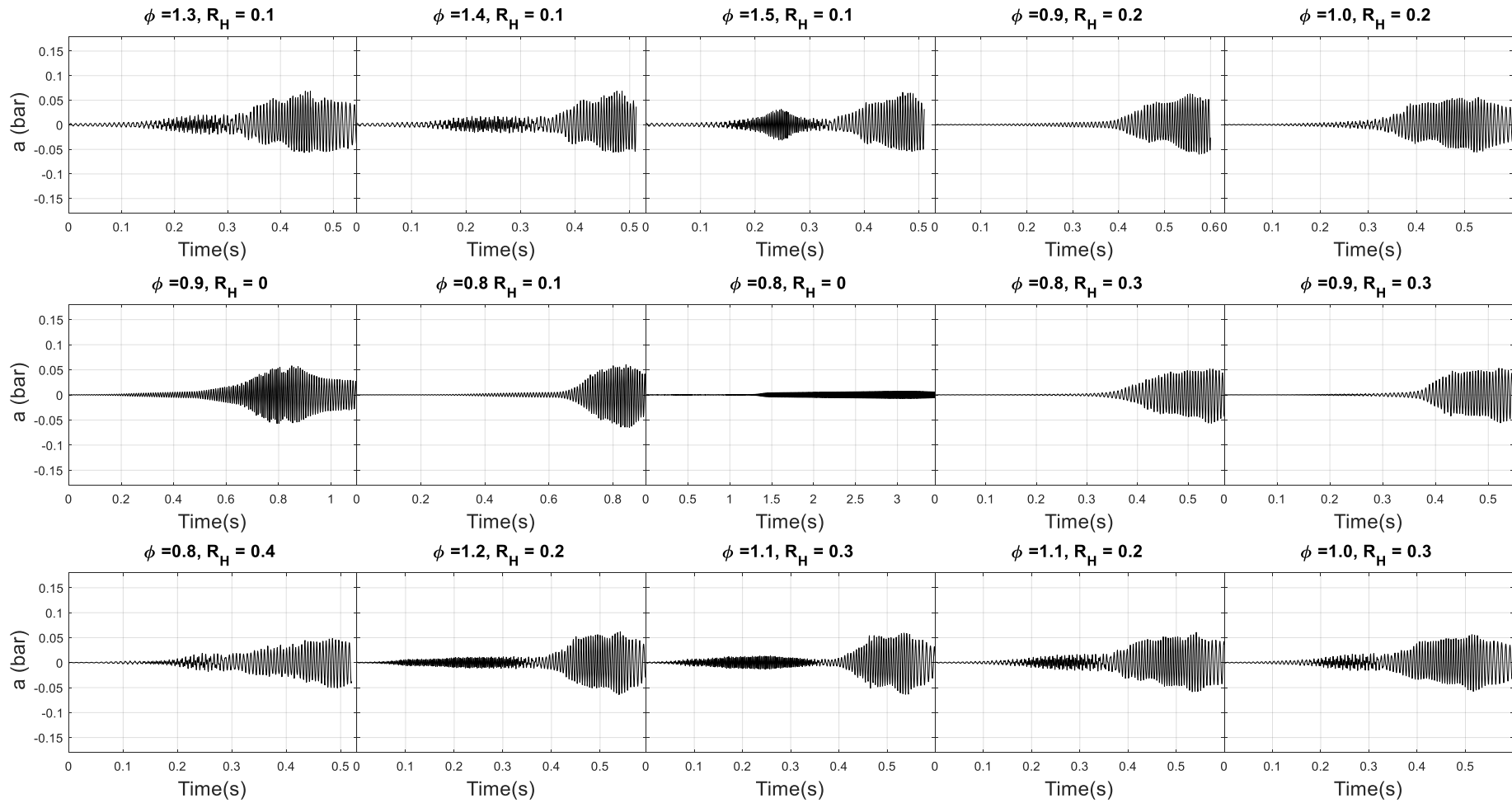


Figure 6.20: Tube end pressure against time of propane flames in region (B)

### Region – C

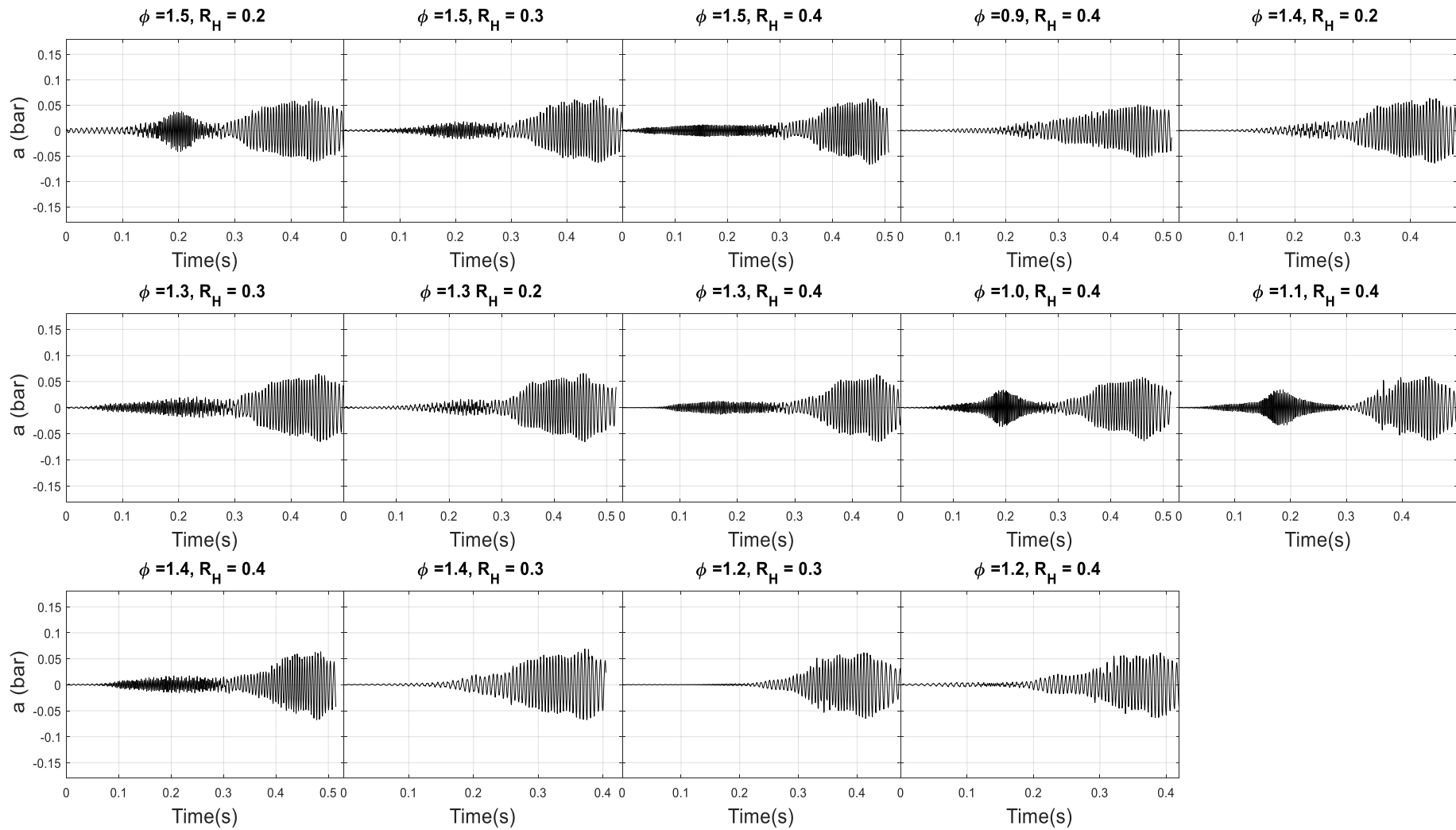


Figure 6.21: Tube end pressure against time of propane flames in region (C)

**Table 6.1: Summary of methane behaviour based on the peak pressure and laminar burning velocity**

Equivalence ratio, $\phi$	Amount of Hydrogen addition, $R_H$				
	0	0.1	0.2	0.3	0.4
0.8	B	B	C	C	C
0.9	A	C	C	C	C
1	A	C	C	C	C
1.1	A	C	C	C	C
1.2	A	C	C	C	C
1.3	A	A	C	C	C
1.4	A	A	B	B	C
1.5	B	A	A	A	B

**Table 6.2: Summary of propane behaviour based on the peak pressure and minimum underlying speed**

Equivalence ratio, $\phi$	Amount of Hydrogen addition, $R_H$				
	0	0.1	0.2	0.3	0.4
0.8	B	B	A	B	B
0.9	B	A	B	B	C
1	A	A	B	B	C
1.1	A	A	B	B	C
1.2	A	A	B	C	C
1.3	A	B	C	C	C
1.4	A	B	C	C	C
1.5	A	B	C	C	C

## 7 CONCLUSION

The current work examined the downward propagation of premixed hydrocarbon and hydrogen-air flames towards the closed end of a tube. The flames presented various interesting and unstable behaviour patterns during their propagation. Previous studies have focused more on the boundary condition effects in relation to the flame chemistry, i.e., altering the tube dimensions while utilising pure fuels with varying equivalence ratios.

For example, while Markstein and Somers [28] studied the physical and chemical factors affecting the unsteady propagation of flames in tubes, their investigation was limited to rich premixed hydrocarbon mixtures, namely methane and butane. The gap in the literature on the effects of chemical factors on unstable propagation motivated the current study to constantly maintain the physical factors while systematically altering the chemical factors.

Therefore, in the current study, the tube dimensions were kept constant at a diameter of 0.02 m and a length of 1.2 m; the tube was oriented vertically and one side was open to the ambient atmosphere. A quartz tube with a diameter of 0.02 m and a length of 0.65 m provided optical access; a high-speed camera was used to record the flame's entire period of instability across a tube length of approximately 0.5 m. Tube pressure was tracked by equipping the tube with a pressure transducer at the end that did not have the ignition. Unlike other premixed flame rigs, this configuration allowed relatively small amounts of fuel to be used, which substantially reduced the hazard involved.

This study investigated methane-hydrogen-air flames and propane-hydrogen-air flames using equivalence ratios,  $\phi = 0.8-1.5$  increasing in 0.1 increments for each level of hydrogen addition,  $R_H$ , which also increased in 0.1 increments from  $R_H = 0-0.4$ . This method facilitated the comparison between the methane and propane flames. Furthermore, the volumetric method was also employed to ensure that each equivalence ratio was systematically enriched with hydrogen,  $H_2\%$ , increasing in 10% increments up to 40% for the methane-hydrogen-air flames. The laminar burning velocity was the main flame property changed in this study, with the aim of establishing how the laminar burning velocity affects flame instabilities.

CHEMKIN [101] was used to calculate the theoretical laminar burning velocity values. As there is currently no method for  $R_H$  mixing, it was not possible to theoretically calculate the Lewis number for the methane-hydrogen fuel mixture. Finally, the oscillatory modes within the signal were extracted using synchrosqueezed wavelet transform (SST).

This study discerned a close relationship between the behaviour of the methane and propane flames based on the  $R_H$  method. The  $R_H$  and volumetric methods were further compared for the methane-hydrogen mixture, showing that both methods had similar methane behaviours, i.e., the addition of hydrogen led to lower oscillation. Meanwhile, there was an almost double magnitude increase in the laminar burning velocity, although the underlying speed and peak pressure remained constant. It is suggested that the observed pressure fluctuation increase is due to the velocity mechanism.

## 7.1. Future work

Upon reaching the end of the present work, the author became aware of the many different paths that can be taken to further explore the current data. These include examining the primary and secondary instability growth rates for different acoustic modes. As acoustic losses affect the growth rate, the author proposes estimating both concurrently. This work was subject to the limitation of light intensity, whereby the lean side of the equivalence ratio was limited to 0.8. Therefore, the author remains curious about the behaviour of lean flames in a flame tube. A lean flame (with an equivalence ratio below 0.8) could only be recorded through Schlieren imaging, which requires a flat surface that confines the flame to allow the density differences in the air to be recorded. Successful Schlieren imaging could be enabled with a square cross-sectional tube incorporating quartz windows.

Another interesting research path would be the further investigation of the chemical side, specifically the modification of the current mixture through the addition of carbon dioxide. As this would diminish the mixtures' reactivity, it would provide substantially greater breadth to the experimentally derived knowledge in this field.

## REFERENCES

- [1] T. Poinso, "Prediction and control of combustion instabilities in real engines," *Proc. Combust. Inst.*, vol. 36, no. 1, pp. 1–28, 2017.
- [2] E. Mallard and H. Le Chatelier, "Combustion of explosive gas mixtures," *Ann. Mine*, 1883.
- [3] A. K. Dubey, Y. Koyama, N. Hashimoto, and O. Fujita, "Experimental and theoretical study of secondary acoustic instability of downward propagating flames: Higher modes and growth rates," *Combust. Flame*, vol. 205, pp. 316–326, 2019.
- [4] W. Mason and R. V. Wheeler, "XCII.—The 'uniform movement' during the propagation of flame," *J. Chem. Soc. Trans.*, vol. 111, pp. 1044–1057, 1917.
- [5] H. Coward and F. Hartwell, "Studies in the mechanism of flame movement—part ii," *J. Chem. Soc.*, pp. 2676–2684, 1932.
- [6] H. Guenoche, "Flame propagation in tubes and in closed vessels," in *AGARDograph*, vol. 75, Elsevier, 1964, pp. 107–181.
- [7] G. H. (Ed. . Markstein, *Nonsteady Flame Propagation*, vol. 12, no. 1. Elsevier, 1964.
- [8] C. Clanet, G. Searby, and P. Clavin, "Primary acoustic instability of flames propagating in tubes: cases of spray and premixed gas combustion," *J. Fluid Mech.*, vol. 385, pp. 157–197, 1999.
- [9] Lord Rayleigh, "The explanation of certain acoustical phenomena," *Roy. Inst. Proc.*, vol. 8, pp. 536–542, 1878.
- [10] G. Searby and D. Rochwerger, "A parametric acoustic instability in premixed flames," *J. Fluid Mech.*, vol. 231, pp. 529–543, 1991.
- [11] G. Searby, "Acoustic instability in premixed flames," *Combust. Sci. Technol.*, vol. 81, no. 4–6, pp. 221–231, 1992.
- [12] G. Yu, C. K. Law, and C. K. Wu, "Laminar flame speeds of hydrocarbon+ air mixtures with hydrogen addition," *Combust. Flame*, vol. 63, no. 3, pp. 339–347, 1986.
- [13] M. Barrere and F. A. Williams, "Comparison of combustion instabilities found in various types of combustion chambers," in *Symposium (International) on*

- Combustion*, 1969, vol. 12, no. 1, pp. 169–181.
- [14] C. Clanet and G. Searby, “First experimental study of the Darrieus-Landau instability,” *Phys. Rev. Lett.*, vol. 80, no. 17, p. 3867, 1998.
- [15] J. Jarosinski and B. Veyssiere, *Combustion phenomena: Selected mechanisms of flame formation, propagation and extinction*. CRC press, 2009.
- [16] A. Clarke, “Calculation and consideration of the Lewis number for explosion studies,” *Process Saf. Environ. Prot.*, vol. 80, no. 3, pp. 135–140, 2002.
- [17] N. Swaminathan and K. N. C. Bray, *Turbulent premixed flames*. Cambridge University Press, 2011.
- [18] G. S. Jackson, R. Sai, J. M. Plaia, C. M. Boggs, and K. T. Kiger, “Influence of H<sub>2</sub> on the response of lean premixed CH<sub>4</sub> flames to high strained flows,” *Combust. Flame*, vol. 132, no. 3, pp. 503–511, 2003.
- [19] G. I. Taylor, “The instability of liquid surfaces when accelerated in a direction perpendicular to their planes. I,” *Proc. R. Soc. London. Ser. A. Math. Phys. Sci.*, vol. 201, no. 1065, pp. 192–196, 1950.
- [20] D. B. Newell and E. Tiesinga, “The international system of units (SI),” *NIST Spec. Publ.*, vol. 330, pp. 1–138, 2019.
- [21] A. von Philippovich, *Explosions-und Verbrennungsvorgänge in Gasen. Von W. Jost, M. 277 Abb. im Text. J. Springer, Berlin 1939. Pr. geh. RM. 46, 50, geb. RM. 49, 50*, vol. 53, no. 23-24. Berlin, Heidelberg: Springer Berlin Heidelberg, 1940.
- [22] F. A. Williams, *Combustion theory*. CRC Press, 2018.
- [23] M. S. Roberts, “Experiments and simulations on the incompressible, Rayleigh-Taylor instability with small wavelength initial perturbations,” 2012.
- [24] R. Lord, “Investigation of the character of the equilibrium of an incompressible heavy fluid of variable density,” *Sci. Pap.*, pp. 200–207, 1900.
- [25] D. J. Lewis, “The instability of liquid surfaces when accelerated in a direction perpendicular to their planes. II,” *Proc. R. Soc. London. Ser. A. Math. Phys. Sci.*, vol. 202, no. 1068, pp. 81–96, 1950.
- [26] H.-J. Kull, “Theory of the Rayleigh-Taylor instability,” *Phys. Rep.*, vol. 206, no. 5, pp. 197–325, 1991.
- [27] H. W. Emmons, C. T. Chang, and B. C. Watson, “Taylor instability of finite surface waves,” *J. Fluid Mech.*, vol. 7, no. 2, pp. 177–193, 1960.

- [28] G. R. Baker, D. I. Meiron, and S. A. Orszag, "Vortex simulations of the Rayleigh–Taylor instability," *Phys. Fluids*, vol. 23, no. 8, pp. 1485–1490, 1980.
- [29] C. L. Gardner, J. Glimm, O. McBryan, R. Menikoff, D. H. Sharp, and Q. Zhang, "The dynamics of bubble growth for Rayleigh–Taylor unstable interfaces," *Phys. fluids*, vol. 31, no. 3, pp. 447–465, 1988.
- [30] R. D. Richtmyer, "Taylor instability in shock acceleration of compressible fluids," Los Alamos Scientific Lab., N. Mex., 1954.
- [31] E. E. Meshkov, "Instability of the interface of two gases accelerated by a shock wave," *Fluid Dyn.*, vol. 4, no. 5, pp. 101–104, 1969.
- [32] C. L. Gardner, J. Glimm, J. Grove, O. McBryan, and R. Menikoff, "A Study of Chaos and Mixing in Rayleigh-Taylor and Richtmyer-Meshkov Unstable Interfaces.," NEW YORK UNIV NY COURANT INST OF MATHEMATICAL SCIENCES, 1987.
- [33] L. D. Cloutman and M. F. Wehner, "Numerical simulation of Richtmyer–Meshkov instabilities," *Phys. Fluids A Fluid Dyn.*, vol. 4, no. 8, pp. 1821–1830, 1992.
- [34] F. Liu, A. C. McIntosh, and J. Brindley, "A numerical investigation of Rayleigh-Taylor effects in pressure wave-premixed flame interactions," *Combust. Sci. Technol.*, vol. 91, no. 4–6, pp. 373–386, 1993.
- [35] T. Tsuruda, M. Harayama, and T. Hirano, "Growth of flame front turbulence," *J. Heat Transfer*, vol. 108, no. 4, pp. 877--881, 1986.
- [36] C. E. Ebieta, "Dynamics of Premixed Flames in Tube [Ph.D. Thesis]," University of Sheffield, 2017.
- [37] B. Higgins, "On the sound produced by a current of hydrogen gas passing through a tube," *J. Nat. Philos. Chem. arts*, vol. 1, no. 129–131, p. 2, 1802.
- [38] T. Lieuwen, H. Torres, C. Johnson, and B. T. Zinn, "A mechanism of combustion instability in lean premixed gas turbine combustors," *J. Eng. Gas Turbines Power*, vol. 123, no. 1, pp. 182–189, 2001.
- [39] M. Shahi, J. B. W. Kok, J. C. R. Casado, and A. K. Pozarlik, "Assessment of thermoacoustic instabilities in a partially premixed model combustor using URANS approach," *Appl. Therm. Eng.*, vol. 71, no. 1, pp. 276–290, 2014.
- [40] E. F. F. Chladni, *Treatise on Acoustics: The First Comprehensive English Translation of EFF Chladni's Traité d'Acoustique*. Springer, 2015.

- [41] P. Clavin and G. Searby, *Combustion waves and fronts in flows: flames, shocks, detonations, ablation fronts and explosion of stars*. Cambridge University Press, 2016.
- [42] R. L. Raun, M. W. Beckstead, J. C. Finlison, and K. P. Brooks, "A review of Rijke tubes, Rijke burners and related devices," *Prog. Energy Combust. Sci.*, vol. 19, no. 4, pp. 313–364, 1993.
- [43] S. Backhaus and G. W. Swift, "New varieties of thermoacoustic engines," in *Proceedings of the Ninth International Congress on Sound and Vibration*, 2002, pp. 8–11.
- [44] A. A. Putnam and W. R. Dennis, "Organ-pipe oscillations in a flame-filled tube," in *Symposium (International) on Combustion*, 1953, vol. 4, no. 1, pp. 566–575.
- [45] E. Mallard, "Recherches experimentales et theoriques sur la combustion des melanges gazeux explosifs," *Ann. mines*, vol. 8, no. 4, pp. 274–568, 1883.
- [46] E. H. W. Schmidt, H. Steinicke, and U. Neubert, "Flame and schlieren photographs of combustion waves in tubes," in *Symposium (International) on Combustion*, 1953, vol. 4, no. 1, pp. 658–666.
- [47] W. E. Kaskan, "An investigation of vibrating flames," in *Symposium (International) on Combustion*, 1953, vol. 4, no. 1, pp. 575–591.
- [48] M. N. Mikhail and M. R. El-Tantawy, "The acoustic boundary layers: a detailed analysis," *J. Comput. Appl. Math.*, vol. 51, no. 1, pp. 15–36, 1994.
- [49] S. K. DATTA, "SEVENTH US NATIONAL CONGRESS OF APPLIED MECHANICS."
- [50] A. A. Putnam and W. R. Dennis, "Survey of Organ-Pipe Oscillations in Combustion Systems," *J. Acoust. Soc. Am.*, vol. 28, no. 2, pp. 246–259, 1956.
- [51] P. L. Rijke, "Notiz über eine neue Art, die in einer an beiden Enden offenen Röhre enthaltene Luft in Schwingungen zu versetzen," *Ann. Phys.*, vol. 183, no. 6, pp. 339–343, 1859.
- [52] H. Young and R. Freedman, "University Physics with Modern Physics 12th International Edition." Pearson Education, 2007.
- [53] S. Candel, "Combustion dynamics and control: progress and challenges," *Proc. Combust. Inst.*, vol. 29, no. 1, pp. 1–28, 2002.
- [54] Y. Taniyama and O. Fujita, "Initiation and formation of the corrugated structure leading to the self-turbulization of downward propagating flames in a

- combustion tube with external laser absorption,” *Combust. Flame*, vol. 161, no. 6, pp. 1558–1565, 2014.
- [55] H. Xiao, R. W. Houim, and E. S. Oran, “Formation and evolution of distorted tulip flames,” *Combust. Flame*, vol. 162, no. 11, pp. 4084–4101, 2015.
- [56] H. Xiao, D. Makarov, J. Sun, and V. Molkov, “Experimental and numerical investigation of premixed flame propagation with distorted tulip shape in a closed duct,” *Combust. Flame*, vol. 159, no. 4, pp. 1523–1538, 2012.
- [57] B. Ponizy, A. Claverie, and B. Veyssi re, “Tulip flame—the mechanism of flame front inversion,” *Combust. Flame*, vol. 161, no. 12, pp. 3051–3062, 2014.
- [58] V. N. Kurdyumov and M. Matalon, “Self-accelerating flames in long narrow open channels,” *Proc. Combust. Inst.*, vol. 35, no. 1, pp. 921–928, 2015.
- [59] G. H. Markstein, “Interaction of flow pulsations and flame propagation,” *J. Aeronaut. Sci.*, vol. 18, no. 6, pp. 428–429, 1951.
- [60] G. H. Markstein and L. M. Somers, “Cellular flame structure and vibratory flame movement in n-butane-methane mixtures,” in *Symposium (international) on Combustion*, 1953, vol. 4, no. 1, pp. 527–535.
- [61] J. W. S. Rayleigh, J. W. S. B. Rayleigh, and R. B. Lindsay, *The Theory of Sound, Volume One*. Dover Publications, 1945.
- [62] G. H. Markstein, “Experimental and theoretical studies of flame-front stability,” *J. Aeronaut. Sci.*, vol. 18, no. 3, pp. 199–209, 1951.
- [63] G. H. Markstein, “Composition traverses in curved laminar flame fronts,” in *Symposium (International) on Combustion*, 1958, vol. 7, no. 1, pp. 289–295.
- [64] F. J. Higuera, “Acoustic response of a lean premixed flame propagating upward in a tube,” *Combust. Flame*, vol. 199, pp. 377–386, 2019.
- [65] O. C. de C. Ellis, “Flame movement in gaseous explosive mixtures,” *J. Fuel Sci.*, vol. 7, pp. 502–508, 1928.
- [66] A. Hariharan and I. S. Wichman, “Premixed flame propagation and morphology in a constant volume combustion chamber,” *Combust. Sci. Technol.*, vol. 186, no. 8, pp. 1025–1040, 2014.
- [67] C. Clanet and G. Searby, “On the ‘tulip flame’ phenomenon,” *Combust. Flame*, vol. 105, no. 1–2, pp. 225–238, 1996.
- [68] H. Behrens, “Flame instabilities and combustion mechanism,” in *Symposium*

- (*International*) on Combustion, 1953, vol. 4, no. 1, pp. 538–545.
- [69] H. F. Coward, F. J. Hartwell, and E. H. M. Georgeson, “306. Studies in the mechanism of flame movement. Part IV. The vibratory period,” *J. Chem. Soc.*, pp. 1482–1489, 1937.
- [70] P. Clavin, “Premixed combustion and gasdynamics,” *Annu. Rev. Fluid Mech.*, vol. 26, no. 1, pp. 321–352, 1994.
- [71] J. Yang, F. M. S. Mossa, H. W. Huang, Q. Wang, R. Woolley, and Y. Zhang, “Oscillating flames in open tubes,” *Proc. Combust. Inst.*, vol. 35, no. 2, pp. 2075–2082, 2015.
- [72] V. Vaezi and R. C. Aldredge, “Laminar-flame instabilities in a Taylor-Couette combustor,” *Combust. Flame*, vol. 121, no. 1–2, pp. 356–366, 2000.
- [73] R. C. Aldredge and N. J. Killingsworth, “Experimental evaluation of Markstein-number influence on thermoacoustic instability,” *Combust. Flame*, vol. 137, no. 1–2, pp. 178–197, 2004.
- [74] V. Vaezi and R. C. Aldredge, “Influences of acoustic instabilities on turbulent-flame propagation,” *Exp. Therm. fluid Sci.*, vol. 20, no. 3–4, pp. 162–169, 2000.
- [75] R. C. Aldredge, “Methane-air Markstein numbers from measurements of thermoacoustic instability,” *Combust. Sci. Technol.*, vol. 177, no. 5–6, pp. 1023–1047, 2005.
- [76] M. Tsuchimoto, O. Fujita, T. Honko, Y. Nakamura, and H. Ito, “Research on the relation of flame front curvature and oscillatory flame propagation by external laser irradiation method,” *Proc. Combust. Inst.*, vol. 32, no. 1, pp. 1003–1009, 2009.
- [77] J. S. Park, O. Fujita, Y. Nakamura, and H. Ito, “Transition of flat flames to turbulent motion induced by external laser irradiation,” *Proc. Combust. Inst.*, vol. 33, no. 1, pp. 1105–1112, 2011.
- [78] S. H. Yoon, T. J. Noh, and O. Fujita, “Onset mechanism of primary acoustic instability in downward-propagating flames,” *Combust. Flame*, vol. 170, pp. 1–11, 2016.
- [79] Y. Chung, O. Fujita, and N. Hashimoto, “Effect of Le on criteria of transition to secondary acoustic instability of downward-propagating flame in a tube with controlled curvature induced by external laser,” *Proc. Combust. Inst.*, vol. 37,

- no. 2, pp. 1887–1894, 2019.
- [80] S. H. Yoon, L. Hu, and O. Fujita, “Experimental observation of pulsating instability under acoustic field in downward-propagating flames at large Lewis number,” *Combust. Flame*, vol. 188, pp. 1–4, 2018.
- [81] S. H. Yoon, T. J. Noh, and O. Fujita, “Effects of Lewis number on generation of primary acoustic instability in downward-propagating flames,” *Proc. Combust. Inst.*, vol. 36, no. 1, pp. 1603–1611, 2017.
- [82] A. K. Dubey, Y. Koyama, N. Hashimoto, and O. Fujita, “Effect of geometrical parameters on thermo-acoustic instability of downward propagating flames in tubes,” *Proc. Combust. Inst.*, vol. 37, no. 2, pp. 1869–1877, 2019.
- [83] A. K. Dubey, Y. Koyama, N. Hashimoto, and O. Fujita, “Exploring a critical diameter for thermo-acoustic instability of downward propagating flames in tubes,” *Proc. Combust. Inst.*, vol. 38, no. 2, pp. 1945–1954, 2021.
- [84] A. K. Dubey, Y. Koyama, N. Hashimoto, and O. Fujita, “Acoustic parametric instability, its suppression and a beating instability in a mesoscale combustion tube,” *Combust. Flame*, vol. 228, pp. 277–291, 2021.
- [85] A. K. Dubey, Y. Koyama, S. H. Yoon, N. Hashimoto, and O. Fujita, “Range of ‘complete’ instability of flat flames propagating downward in the acoustic field in combustion tube: Lewis number effect,” *Combust. Flame*, vol. 216, pp. 326–337, 2020.
- [86] P. Clavin, P. Pelcé, and L. He, “One-dimensional vibratory instability of planar flames propagating in tubes,” *J. Fluid Mech.*, vol. 216, pp. 299–322, 1990.
- [87] A. C. McIntosh, “Pressure disturbances of different length scales interacting with conventional flames,” *Combust. Sci. Technol.*, vol. 75, no. 4–6, pp. 287–309, 1991.
- [88] P. Clavin and G. Searby, “Unsteady response of chain-branching premixed-flames to pressure waves,” *Combust. Theory Model.*, vol. 12, no. 3, pp. 545–567, 2008.
- [89] O. J. Teerling, A. C. McIntosh, J. Brindley, and V. H. Y. Tam, “Premixed flame response to oscillatory pressure waves,” *Proc. Combust. Inst.*, vol. 30, no. 2, pp. 1733–1740, 2005.
- [90] A. Wangher, G. Searby, and J. Quinard, “Experimental investigation of the

- unsteady response of premixed flame fronts to acoustic pressure waves,” *Combust. Flame*, vol. 154, no. 1–2, pp. 310–318, 2008.
- [91] G. Beardsell and G. Blanquart, “Impact of pressure fluctuations on the dynamics of laminar premixed flames,” *Proc. Combust. Inst.*, vol. 37, no. 2, pp. 1895–1902, 2019.
- [92] C. Jiménez, J. Quinard, J. Graña-Otero, H. Schmidt, and G. Searby, “Unsteady response of hydrogen and methane flames to pressure waves,” *Combust. Flame*, vol. 159, no. 5, pp. 1894–1908, 2012.
- [93] V. Bychkov, “Analytical scalings for flame interaction with sound waves,” *Phys. Fluids*, vol. 11, no. 10, pp. 3168–3173, 1999.
- [94] J. Yanez, M. Kuznetsov, and J. Grune, “Flame instability of lean hydrogen–air mixtures in a smooth open-ended vertical channel,” *Combust. Flame*, vol. 162, no. 7, pp. 2830–2839, 2015.
- [95] J. Yáñez, M. Kuznetsov, and R. Redlinger, “The acoustic–parametric instability for hydrogen–air mixtures,” *Combust. Flame*, vol. 160, no. 10, pp. 2009–2016, 2013.
- [96] Y. Ju and K. Maruta, “Microscale combustion: Technology development and fundamental research,” *Prog. energy Combust. Sci.*, vol. 37, no. 6, pp. 669–715, 2011.
- [97] K. Maruta, “Micro and mesoscale combustion,” *Proc. Combust. Inst.*, vol. 33, no. 1, pp. 125–150, 2011.
- [98] F. Veiga-López, M. Kuznetsov, D. Martínez-Ruiz, E. Fernández-Tarrazo, J. Grune, and M. Sánchez-Sanz, “Unexpected propagation of ultra-lean hydrogen flames in narrow gaps,” *Phys. Rev. Lett.*, vol. 124, no. 17, p. 174501, 2020.
- [99] G. Joulin and P. Clavin, “Linear stability analysis of nonadiabatic flames: diffusional-thermal model,” *Combust. Flame*, vol. 35, pp. 139–153, 1979.
- [100] H. Pearlman, “Excitability in high-Lewis number premixed gas combustion,” *Combust. Flame*, vol. 109, no. 3, pp. 382–398, 1997.
- [101] F. Veiga-López, D. Martínez-Ruiz, E. Fernández-Tarrazo, and M. Sánchez-Sanz, “Experimental analysis of oscillatory premixed flames in a Hele-Shaw cell propagating towards a closed end,” *Combust. Flame*, vol. 201, pp. 1–11, 2019.
- [102] P. Pelcé and D. Rochwerger, “Vibratory instability of cellular flames propagating

- in tubes," *J. Fluid Mech.*, vol. 239, pp. 293–307, 1992.
- [103] S. Kerampran, D. Desbordes, and B. Veyssiere, "Study of the mechanisms of flame acceleration in a tube of constant cross section," *Combust. Sci. Technol.*, vol. 158, no. 1, pp. 71–91, 2000.
- [104] C. Mandilas, M. P. Ormsby, C. G. W. Sheppard, and R. Woolley, "Effects of hydrogen addition on laminar and turbulent premixed methane and iso-octane–air flames," *Proc. Combust. Inst.*, vol. 31, no. 1, pp. 1443–1450, 2007.
- [105] C. Ji, D. Wang, J. Yang, and S. Wang, "A comprehensive study of light hydrocarbon mechanisms performance in predicting methane/hydrogen/air laminar burning velocities," *Int. J. Hydrogen Energy*, vol. 42, no. 27, pp. 17260–17274, 2017.
- [106] X. J. Gu, M. Z. Haq, M. Lawes, and R. Woolley, "Laminar burning velocity and Markstein lengths of methane–air mixtures," *Combust. Flame*, vol. 121, no. 1–2, pp. 41–58, 2000.
- [107] H. Edmondson and M. P. Heap, "The burning velocity of methane-air flames inhibited by methyl bromide," *Combust. Flame*, vol. 13, no. 5, pp. 472–478, 1969.
- [108] C. M. Vagelopoulos, F. N. Egolfopoulos, and C. K. Law, "Further considerations on the determination of laminar flame speeds with the counterflow twin-flame technique," in *Symposium (international) on combustion*, 1994, vol. 25, no. 1, pp. 1341–1347.
- [109] D. Bradley, M. Lawes, and R. Mumby, "Burning velocity and Markstein length blending laws for methane/air and hydrogen/air blends," *Fuel*, vol. 187, pp. 268–275, 2017.
- [110] E. Hu, Z. Huang, J. He, C. Jin, and J. Zheng, "Experimental and numerical study on laminar burning characteristics of premixed methane–hydrogen–air flames," *Int. J. Hydrogen Energy*, vol. 34, no. 11, pp. 4876–4888, 2009.
- [111] D. P. Mishra, *Fundamentals of combustion*. PHI Learning Pvt. Ltd., 2007.
- [112] B. Sakintuna, F. Lamari-Darkrim, and M. Hirscher, "Metal hydride materials for solid hydrogen storage: a review," *Int. J. Hydrogen Energy*, vol. 32, no. 9, pp. 1121–1140, 2007.
- [113] S.-P. Yu *et al.*, "Integration of low-pressure hydrogen storage cylinder and automatic controller for carbon deposit removal in car engine," *Int. J. Hydrogen*

- Energy*, vol. 41, no. 46, pp. 21795–21801, 2016.
- [114] L. Hao *et al.*, “Investigation of cold-start emission control strategy for a bi-fuel hydrogen/gasoline engine,” *Int. J. Hydrogen Energy*, vol. 41, no. 40, pp. 18273–18281, 2016.
- [115] D. B. Lata, A. Misra, and S. Medhekar, “Effect of hydrogen and LPG addition on the efficiency and emissions of a dual fuel diesel engine,” *Int. J. Hydrogen Energy*, vol. 37, no. 7, pp. 6084–6096, 2012.
- [116] T. G. Scholte and P. B. Vaags, “Burning velocities of mixtures of hydrogen, carbon monoxide and methane with air,” *Combust. Flame*, vol. 3, pp. 511–524, 1959.
- [117] F. Halter, C. Chauveau, N. Djebaili-Chaumeix, and I. Gökalp, “Characterization of the effects of pressure and hydrogen concentration on laminar burning velocities of methane–hydrogen–air mixtures,” *Proc. Combust. Inst.*, vol. 30, no. 1, pp. 201–208, 2005.
- [118] B. E. Milton and J. C. Keck, “Laminar burning velocities in stoichiometric hydrogen and hydrogen hydrocarbon gas mixtures,” *Combust. Flame*, vol. 58, no. 1, pp. 13–22, 1984.
- [119] R. T. E. Hermanns, “Laminar burning velocities of methane-hydrogen-air mixtures,” *Submitt. to Combust. Flame*, 2007.
- [120] J.-Y. Ren, W. Qin, F. N. Egolfopoulos, and T. T. Tsotsis, “Strain-rate effects on hydrogen-enhanced lean premixed combustion,” *Combust. Flame*, vol. 124, no. 4, pp. 717–720, 2001.
- [121] Z. Huang, Y. Zhang, K. Zeng, B. Liu, Q. Wang, and D. Jiang, “Measurements of laminar burning velocities for natural gas–hydrogen–air mixtures,” *Combust. Flame*, vol. 146, no. 1–2, pp. 302–311, 2006.
- [122] J.-Y. Ren, W. Qin, F. N. Egolfopoulos, H. Mak, and T. T. Tsotsis, “Methane reforming and its potential effect on the efficiency and pollutant emissions of lean methane–air combustion,” *Chem. Eng. Sci.*, vol. 56, no. 4, pp. 1541–1549, 2001.
- [123] S. Refael and E. Sher, “Reaction kinetics of hydrogen-enriched methane air and propane air flames,” *Combust. Flame*, vol. 78, no. 3–4, pp. 326–338, 1989.
- [124] C. Uykur, P. F. Henshaw, D.-K. Ting, and R. M. Barron, “Effects of addition of

- electrolysis products on methane/air premixed laminar combustion," *Int. J. Hydrogen Energy*, vol. 26, no. 3, pp. 265–273, 2001.
- [125] V. Di Sarli and A. Di Benedetto, "Laminar burning velocity of hydrogen–methane/air premixed flames," *Int. J. Hydrogen Energy*, vol. 32, no. 5, pp. 637–646, 2007.
- [126] F. Halter, C. Chauveau, and I. Gökalp, "Characterization of the effects of hydrogen addition in premixed methane/air flames," *Int. J. Hydrogen Energy*, vol. 32, no. 13, pp. 2585–2592, 2007.
- [127] T. Boushaki, Y. Dhué, L. Selle, B. Ferret, and T. Poinso, "Effects of hydrogen and steam addition on laminar burning velocity of methane–air premixed flame: experimental and numerical analysis," *Int. J. Hydrogen Energy*, vol. 37, no. 11, pp. 9412–9422, 2012.
- [128] N. Syred *et al.*, "Effect of inlet and outlet configurations on blow-off and flashback with premixed combustion for methane and a high hydrogen content fuel in a generic swirl burner," *Appl. Energy*, vol. 116, pp. 288–296, 2014.
- [129] Y. Shoshin, R. J. M. Bastiaans, and L. P. H. de Goey, "Anomalous blow-off behavior of laminar inverted flames of ultra-lean hydrogen–methane–air mixtures," *Combust. Flame*, vol. 160, no. 3, pp. 565–576, 2013.
- [130] S. Hong, R. L. Speth, S. J. Shanbhogue, and A. F. Ghoniem, "Examining flow-flame interaction and the characteristic stretch rate in vortex-driven combustion dynamics using PIV and numerical simulation," *Combust. Flame*, vol. 160, no. 8, pp. 1381–1397, 2013.
- [131] J. Lee, S. Jeon, and Y. Kim, "Multi-environment probability density function approach for turbulent CH<sub>4</sub>/H<sub>2</sub> flames under the MILD combustion condition," *Combust. Flame*, vol. 162, no. 4, pp. 1464–1476, 2015.
- [132] V. Di Sarli, A. Di Benedetto, E. J. Long, and G. K. Hargrave, "Time-Resolved Particle Image Velocimetry of dynamic interactions between hydrogen-enriched methane/air premixed flames and toroidal vortex structures," *Int. J. Hydrogen Energy*, vol. 37, no. 21, pp. 16201–16213, 2012.
- [133] R. W. Schefer, "Hydrogen enrichment for improved lean flame stability," *Int. J. Hydrogen Energy*, vol. 28, no. 10, pp. 1131–1141, 2003.
- [134] i. Yilmaz, A. Ratner, M. Ilbas, and Y. Huang, "Experimental investigation of

- thermoacoustic coupling using blended hydrogen–methane fuels in a low swirl burner,” *Int. J. Hydrogen Energy*, vol. 35, no. 1, pp. 329–336, 2010.
- [135] H. S. Kim, V. K. Arghode, and A. K. Gupta, “Flame characteristics of hydrogen-enriched methane–air premixed swirling flames,” *Int. J. Hydrogen Energy*, vol. 34, no. 2, pp. 1063–1073, 2009.
- [136] T. García-Armingol and J. Ballester, “Operational issues in premixed combustion of hydrogen-enriched and syngas fuels,” *Int. J. Hydrogen Energy*, vol. 40, no. 2, pp. 1229–1243, 2015.
- [137] S. J. Shanbhogue, Y. S. Sanusi, S. Taamallah, M. A. Habib, E. M. A. Mokheimer, and A. F. Ghoniem, “Flame macrostructures, combustion instability and extinction strain scaling in swirl-stabilized premixed CH<sub>4</sub>/H<sub>2</sub> combustion,” *Combust. Flame*, vol. 163, pp. 494–507, 2016.
- [138] S. Barbosa, M. de L. C. Garcia, S. Ducruix, B. Labegorre, and F. Lacas, “Control of combustion instabilities by local injection of hydrogen,” *Proc. Combust. Inst.*, vol. 31, no. 2, pp. 3207–3214, 2007.
- [139] M. Emadi, K. Kaufman, M. W. Burkhalter, T. Salameh, T. Gentry, and A. Ratner, “Examination of thermo-acoustic instability in a low swirl burner,” *Int. J. Hydrogen Energy*, vol. 40, no. 39, pp. 13594–13603, 2015.
- [140] M. Emadi, D. Karkow, A. Melendez, and A. Ratner, “Parameter variations and the effects of hydrogen: An experimental investigation in a lean premixed low swirl combustor,” *Int. J. Hydrogen Energy*, vol. 38, no. 13, pp. 5401–5409, 2013.
- [141] R. H. Herrera, J. Han, and M. van der Baan, “Applications of the synchrosqueezing transform in seismic time-frequency analysis,” *Geophysics*, vol. 79, no. 3, pp. V55–V64, 2014.
- [142] M. X. Cohen, *Analyzing neural time series data: theory and practice*. MIT press, 2014.
- [143] C. E. Ebieto, N. A. Amaludin, and R. Woolley, “Methane/Hydrogen/Air Flame Oscillations in Open Ended Tubes.”
- [144] I. Daubechies, J. Lu, and H.-T. Wu, “Synchrosqueezed wavelet transforms: An empirical mode decomposition-like tool,” *Appl. Comput. Harmon. Anal.*, vol. 30, no. 2, pp. 243–261, 2011.
- [145] C. Li and M. Liang, “Time–frequency signal analysis for gearbox fault diagnosis

- using a generalized synchrosqueezing transform,” *Mech. Syst. Signal Process.*, vol. 26, pp. 205–217, 2012.
- [146] Y. Hu, X. Tu, and F. Li, “High-order synchrosqueezing wavelet transform and application to planetary gearbox fault diagnosis,” *Mech. Syst. Signal Process.*, vol. 131, pp. 126–151, 2019.
- [147] MathWorks, “Wavelet Synchrosqueezing.” [Online]. Available: <https://uk.mathworks.com/help/wavelet/gs/wavelet-synchrosqueezing.html#bu9sda1-1>. [Accessed: 30-Nov-2020].
- [148] I. Daubechies, *Ten lectures on wavelets*. SIAM, 1992.
- [149] S. Maes, “A nonlinear squeezing of the continuous wavelet transform based on auditory nerve models,” in *Wavelets in medicine and biology*, Routledge, 2017, pp. 527–546.
- [150] C. Li and M. Liang, “A generalized synchrosqueezing transform for enhancing signal time–frequency representation,” *Signal Processing*, vol. 92, no. 9, pp. 2264–2274, 2012.
- [151] K. T. Kim, J. G. Lee, B. D. Quay, and D. A. Santavicca, “The dynamic response of turbulent dihedral V flames: An amplification mechanism of swirling flames,” *Combust. Sci. Technol.*, vol. 183, no. 2, pp. 163–179, 2010.
- [152] K. C. Schadow, E. Gutmark, T. P. Parr, D. M. Parr, K. J. Wilson, and J. E. Crump, “Large-scale coherent structures as drivers of combustion instability,” *Combust. Sci. Technol.*, vol. 64, no. 4–6, pp. 167–186, 1989.
- [153] A. Petchenko, V. Bychkov, V. Akkerman, and L.-E. Eriksson, “Flame–sound interaction in tubes with nonslip walls,” *Combust. Flame*, vol. 149, no. 4, pp. 418–434, 2007.
- [154] K. R. McManus, T. Poinso, and S. M. Candel, “A review of active control of combustion instabilities,” *Prog. energy Combust. Sci.*, vol. 19, no. 1, pp. 1–29, 1993.
- [155] S. Hubbard and A. P. Dowling, “Acoustic resonances of an industrial gas turbine combustion system,” *J. Eng. Gas Turbines Power*, vol. 123, no. 4, pp. 766–773, 2001.
- [156] S. L. Hahn, “Hilbert transforms in signal processing, Artech House,” *Inc., Boston, London*, 1996.

- [157] MathWorks, "Hilbert Transform." [Online]. Available: <https://uk.mathworks.com/help/signal/ref/hilbert.html>. [Accessed: 03-May-2021].
- [158] J. O. Smith III, "Mathematics of the Discrete Fourier Transform: With Audio Applications." [Online]. Available: <https://ccrma.stanford.edu/~jos/st/>. [Accessed: 05-May-2021].
- [159] H. J. Lee, K. T. Kim, J. G. Lee, B. D. Quay, and D. A. Santavicca, "An experimental study on the coupling of combustion instability mechanisms in a lean premixed gas turbine combustor," in *Turbo Expo: Power for Land, Sea, and Air*, 2009, vol. 48838, pp. 749–758.
- [160] Pennington P, "Flames in Tubes [Master Thesis]," University of Sheffield, 2009.
- [161] F. Mossa, "Flames in Tubes [Ph.D. Thesis]," University of Sheffield, 2014.
- [162] M. Wu, M. P. Burke, S. F. Son, and R. A. Yetter, "Flame acceleration and the transition to detonation of stoichiometric ethylene/oxygen in microscale tubes," *Proc. Combust. Inst.*, vol. 31, no. 2, pp. 2429–2436, 2007.
- [163] W. Payman and R. V Wheeler, "A note on 'the uniform movement' during the propagation of flame," *Trans. Faraday Soc.*, vol. 22, pp. 301–306, 1926.
- [164] Vision Research, "Phantom v210 Data Sheet." [Online]. Available: <https://manualzz.com/doc/41859611/v210-data-sheet>. [Accessed: 20-Feb-2020].
- [165] N. I. User Guide, "myDAQ," *National Instruments Company*. [Online]. Available: <https://www.manualslib.com/manual/1602524/National-Instruments-Mydaq.html>. [Accessed: 02-Nov-2017].
- [166] T. Maxworthy, "Flame propagation in tubes," *Phys. Fluids*, vol. 5, no. 4, pp. 407–417, 1962.
- [167] R. J. Kee, F. M. Rupley, and J. A. Miller, "CHEMKIN: The Chemkin Thermodynamic Database. Rep. SAND87-8215," *Sandia Natl. Lab. Livermore (CA), USA*, 1987.
- [168] "Phantom Camera Control." [Online]. Available: <https://phantomhighspeed-service.force.com/servlet/servlet.FileDownload?file=00P1N00000dSuEMUA0&oid=00D1N000002Br2EUAS>. [Accessed: 05-Oct-2017].
- [169] "VirtualDub." [Online]. Available: <https://www.virtualdub.org>. [Accessed: 02-Mar-2018].

- [170] MATLAB, "The MathWorks, Inc., Natick, Massachusetts." [Online]. Available: [https://uk.mathworks.com/campaigns/products/trials.html?ef\\_id=Cj0KCQiAqbyNBhC2ARIsALDwAsBwt-dB1cnsI07cKXSXCInjD8B66GQ4btLBDudIbcRnmDo6QNullelaAhZyEALw\\_wcB:G:s&s\\_kwcid=AL!8664!3!463011314378!b!!g!!%2Bmathworks%2Bmatlab&s\\_eid=ppc\\_6588247642&q=+mathworks+m](https://uk.mathworks.com/campaigns/products/trials.html?ef_id=Cj0KCQiAqbyNBhC2ARIsALDwAsBwt-dB1cnsI07cKXSXCInjD8B66GQ4btLBDudIbcRnmDo6QNullelaAhZyEALw_wcB:G:s&s_kwcid=AL!8664!3!463011314378!b!!g!!%2Bmathworks%2Bmatlab&s_eid=ppc_6588247642&q=+mathworks+m). [Accessed: 05-Oct-2019].
- [171] D. Bradley *et al.*, "Turbulent burning velocity, burned gas distribution, and associated flame surface definition," *Combust. Flame*, vol. 133, no. 4, pp. 415–430, 2003.
- [172] A. V Oppenheim, *Discrete-time signal processing*. Pearson Education India, 1999.
- [173] N. A. bin Amaludin, "Flame Instabilities in Open Ended Tubes." University of Sheffield, 2020.
- [174] MathWorks, "Time-frequency ridges from wavelet synchrosqueezing." [Online]. Available: <https://uk.mathworks.com/help/wavelet/ref/wsstridge.html>. [Accessed: 07-Dec-2020].
- [175] M. Feldman, "Hilbert transform in vibration analysis," *Mech. Syst. Signal Process.*, vol. 25, no. 3, pp. 735–802, 2011.
- [176] T. C. Lieuwen, *Unsteady combustor physics*. Cambridge University Press, 2012.
- [177] N. T. G. Tri, A. K. Dubey, N. Hashimoto, and O. Fujita, "Effect of flame surface area of downward propagating flames induced by single and double laser irradiation on transition to parametric instability," *Combust. Flame*, vol. 223, pp. 450–459, 2021.

## **APPENDICES**

### **Appendix A: Optical calibration**

The optical calibration was crucial in this study as the results would have been directly impacted by any measurement errors. To reduce the potential for imaging errors and enhance the recording quality, the following procedures were implemented:

1. The camera height was set to the level of the tube.
2. The lens focal length was altered to suit the recording range.
3. The camera sampling rate was set to viewable fps under ambient conditions.
4. PCC was used to adjust the image resolution to fit the section of the tube being recorded.
5. The camera was aligned with the tube via the software's horizontal grid display, whereby care was taken to ensure that the tube view was straight.
6. A metal wire was placed within the quartz tube for the camera to focus on; this was removed after focusing.
7. A measurement tap was used to measure the recorded length of the tube to perform pixel-distance conversion during the image post-processing.
8. The sampling rate was altered based on which type of flame was being tested; this was primarily evaluated by performing a test recording: if the flame was excessively bright, the sampling rate was increased, while it was decreased if the flame was overly faint.
9. The lens was closed using a lens cap to achieve de-noising; furthermore, current session referencing (CSR) was done using PCC.

## Appendix B: Pressure measurement settings

The pressure was calibrated using the Kistler Type 5018 Charge Amplifier interface. Although the charge amplifier generally stores the current settings, irregularities cropping up in the pressure readings highlight the need to recheck the settings, as exemplified in Figure B.1. The pressure range should be 1.0 bar, the sensitivity should be -2321 pC/bar (taken from the calibration sheet provided with the Kistler Type 7261 Pressure Transducer), the time constant should be set to short ( $\tau = 0.42\text{s}$ ), and the low pass filter should be turned off. The pressure signal conversion, presented near the bottom of the screen, is 0.1 bar/V.



Figure B.1: Kistler Type 5018 charge amplifier settings

## **Appendix C: Fuel collection procedure**

To avoid a hazard, the fuel was collected from the gas cylinder storage compound in accordance to a strict procedure. The individual who collected the gas was required to have attended a control of substances hazardous to health (CoSHH) gas cylinder handling course, which involved both online and in-person training. A CoSHH form drafted for this task was sent to the departmental safety officer (DSO) for them to review and revise. The fuel collection adhered to the following procedure:

1. An assigned technician who has undergone the necessary training must be present to observe the process.
2. The gas cylinder is inspected and checked to ensure that it is properly secured in the holder.
3. The gas cylinder regulator is inspected visually for signs of damage and to ensure that it has not exceeded its service date.
4. The fuel collection must be stopped if the regulator is damaged or the service date has been exceeded.
5. The gas storage compound is checked to make sure that it is free from all sources of ignition.
6. The cylinder gauges are inspected to ensure they read zero while the regulator and main cylinder valves are closed.
7. If the regulator reading is non-zero, the main cylinder valve is closed and the regulator valve is opened to purge any gas remaining inside the regulator.
8. To maintain the purity of the collected gas, first, the main cylinder valve is opened; then, the regulator valve is opened for approximately ten seconds to purge the cylinder hose.
9. The on/off valve on the gas sampling bag is opened and attached to the cylinder hose.

10. To prevent cross-contamination, only gas sampling bags designated for the intended gas are to be used.
11. The regulator valve is opened until the bag has been filled.
12. The regulator valve is closed; then, the on/off valve and the main cylinder valve are closed.
13. The on/off valve is disconnected from the cylinder hose; then, the regulator valve is opened to purge the regulator.
14. The gas storage compound is properly locked before leaving the place.
15. The gas bag is taken directly to the lab, after first ensuring that there are no significant sources of ignition along the route. If any such sources are present, an alternative route to the lab must be taken.

## Appendix D: Experimental Procedures

The procedure of the flame tube rig is simple to follow, but this simplicity comes with many errors so the procedure must be performed correctly to minimise these errors. The experiments should be performed at room temperature and pressure, 298K and 1 atm. The procedures of experiment are listed below.

- i. Connect the vacuum pump to the rig by opening a one-way valve three times to remove the air and combustion product from previous experiments.
- ii. Attempt to reach the rig pressure reading around -0.95 bar by turning on the pump, and vacuum the rig using the PDCR810 pressure transducer.
- iii. Once the rig pressure reaches -0.95 bar, turn off the vacuum pump and isolate the rig by closing the one-way valve.
- iv. Prepare the required amount of fuels in syringes then inject them into the rig through the injection port.
- v. Open the three-way valve slowly to allow ambient air in and once the rig pressure increases to ambient pressure (0 bar) close the valve.
- vi. Turn on the fans to mix the air and fuel for three minutes to get a homogenous mixture inside the rig.
- vii. Turn off the mixing fans and then turn off the light in the lab.
- viii. Turn off the three-way valves to isolate the quartz tube from the flame tube rig.
- ix. Press the trigger of the data acquisition tool and ignite the mixture by using a lighter in this experiment.
- x. Vacuum the rig by closing the three-way valves and the one-way valve.
- xi. Repeat these steps for the following experiments.

## Appendix E: Procedure for selecting the presented run

The flame position for the three runs of methane and propane was plotted against time to select the suitable run to present the mixture. The figures below showed two cases of flame position trends: 1) Two trends of flames position show similar behaviour or 2) All trends show different behaviours. In the first case, one of the similar trends was selected to present the mixture. In the second case, the middle trend was selected to present the mixture. Figure D.1 shows the three runs of each mixture of methane and propane flames for equivalence ratio, ranging 0.8, 1.0, and 1.2 and  $R_H = 0-0.4$

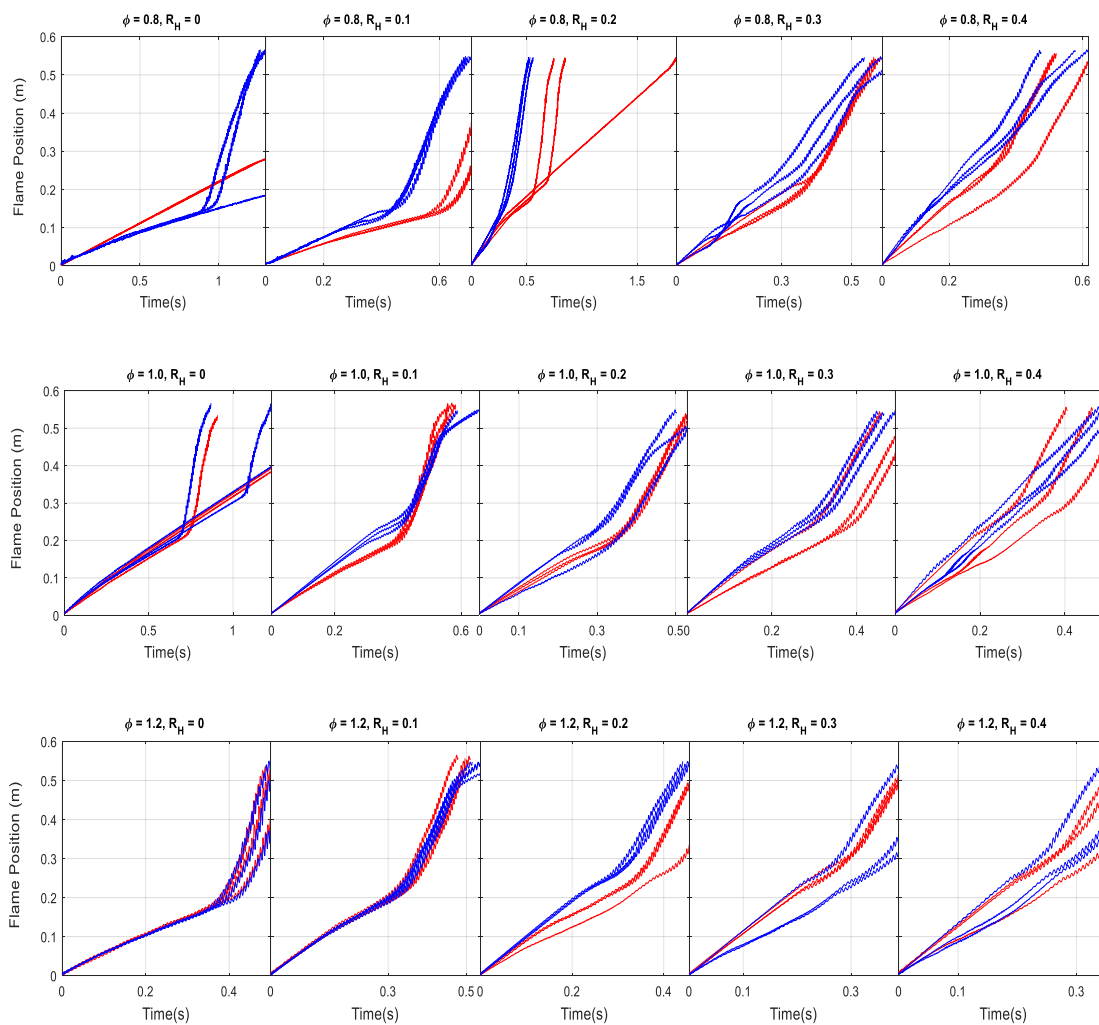


Figure D.1: : Flame front position against time of methane (blue), and propane (red) on  $\phi = 0.8, 1.0$ , and  $1.2$ ,  $R_H = 0-0.4$  flames

## Appendix F: Procedure for selecting reference velocity

Since the laminar burning velocity of propane needs a complicated mechanism to calculate it, the minimum underlying speed was used instead, shown in Figure 6.2 and Figure 6.4. The laminar burning velocity of methane flames in  $\phi = 1.0$  and  $R_H = 0-0.4$  was used to present this method. The underlying velocity was plotted against time, as shown in Figure E.1. Once the underlying velocity was plotted, the laminar burning velocity line was found for comparison with minimum underlying speed. This method showed an uncertainty of 5%, 10%, 16%, 18%, and 36% for  $R_H = 0.4, 0.3, 0.2, 0.1,$  and  $0$ , respectively.

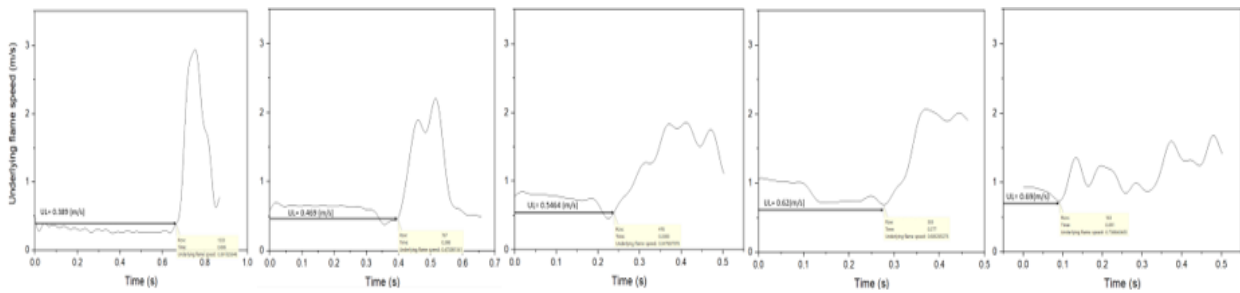


Figure E.1: Underlying flame speed against time of methane on  $\phi = 1.0$ ,  $R_H = 0-0.4$  flames

## Appendix G: MATLAB code for SST and ISST

```
x          = pressure signal;                                % signal of interest
R= 0.1;
Nr = 50;
N=size(x,1);
NR=min(round(N*R),Nr);
x1=2*x(1)-flipud(x(2:NR+1)); % maintain continuity in level and slope
x2=2*x(end)-flipud(x(end-NR:end-1));
x=[x(NR: -1:1);x;x(end: -1:end-NR+1)];

fs = 2000; % original sampling rate
dt = 1/fs; % time per frame
t = 0:dt:numel(x)*dt-dt; % generates the time data for the experimental
data set
[sst,f] = wssst(x,fs);
contour (t,f,abs(sst),50);
grid on;
% title('Phi= 1.2 , RH0.3');
xlabel('Time (s)');
ylabel('Frequency (Hz)');
% ylim([0 750]);

%% SST

R = 8; %number of ridges found based on SST contour plot

subplot (2,2,1)
[fridge,~] = wsstridge(sst,60,f,'NumRidges',R);
contour(t,f,abs(sst));
grid on;
title('Penalty 60');
xlabel('Time (s)'); ylabel('Hz');
hold on;
plot(t,fridge,'k--','linewidth',1);
hold off;
ylim([0 1000]);

subplot (2,2,2)
[fridge,~] = wsstridge(sst,30,f,'NumRidges',R);
contour(t,f,abs(sst));
grid on;
title('Penalty 30');
xlabel('Time (s)'); ylabel('Hz');
hold on;
plot(t,fridge,'k--','linewidth',1);
hold off;
ylim([0 1000]);

subplot (2,2,3)
[fridge,~] = wsstridge(sst,20,f,'NumRidges',R);
contour(t,f,abs(sst));
grid on;
title('Penalty 20');
xlabel('Time (s)'); ylabel('Hz');
hold on;
plot(t,fridge,'k--','linewidth',1);
hold off;
```

```

ylim([0 1000]);

subplot (2,2,4)
[fridge,~] = wsstridge(sst,10,f,'NumRidges',R);
contour(t,f,abs(sst));
grid on;
title('Penalty 10');
xlabel('Time (s)'); ylabel('Hz');
hold on;
plot(t,fridge,'k--','linewidth',1);
hold off;
ylim([0 1000]);

%% Reconstruct

[fridge,iridge] = wsstridge(sst,20,f,'NumRidges',R);
fridge=fridge(NR+1:end-NR,:);

ye = iwsst(sst,iridge); %inverse sst for extracted mode of pressure signal
ye =ye(NR+1:end-NR,:);
t = 0:dt:size(ye,1)*dt-dt;
for i = 1:1:R

subplot (R/2,2,i)
freq = floor (mode (fridge(:,i)));
plot(t,ye(:,i),'r');
grid on;
ylabel(freq);
% xlim([0 (max(t))]);
% xlim([0.08 0.09]);
% ylim([-max(ye(:,1)) (max(ye(:,1)))]);
ylim([-max(ye(:)) (max(ye(:)))]);
title(i);
end

```